Karlsruhe Institute of Technology

Phase-field modeling of microstructural evolution in multicomponent alloy systems

Zur Erlangung des akademischen Grades eines
Doktors der Ingenieurwissenschaften
von der KIT-Fakultät für Maschinenbau
des Karlsruher Instituts für Technologie (KIT)

angenommene **Dissertation**

von

Yuhan Cai

Tag der mündlichen Prüfung:	12. Dezember 2023
Erstgutachter:	Prof. Dr. rer. nat. Britta Nestler
Zweitgutachter:	Prof. Dr. Hans Jürgen Seifert

–

This document is licensed under a Creative Commons
Attribution-ShareAlike 4.0 International License (CC BY-SA 4.0):
https://creativecommons.org/licenses/by-sa/4.0/deed.en

I declare that I have developed and written the enclosed thesis completely by myself, and have not used sources or means without declaration in the text.

PLACE, DATE

. . . . . .

(**Yuhan Cai**)

Abstract

In this thesis, we employ a thermodynamically consistent multi-phase, multi-component phase-field (PF) model to comprehensively investigate the morphological evolution during solidification process in alloys through 2-D and 3-D simulations.

We introduce a methodology for integrating thermodynamic databases into phase-field simulations, specifically for stoichiometric phases, where data is limited. This enables the creation of thermodynamically consistent models for three representative alloy systems: Fe-C, Al-C, and Mo-Si-Ti. These models are rigorously validated through phase-field simulations, encompassing both two- and three-dimensional simulations for all three systems to explore the development of two-phase microstructures.

In our study, we first delve into the peritectic transition in Fe-C binary system, aiming to interpret the isothermal peritectic transition with a liquid supersaturation in alloys. Subsequently, we utilize the phase-field model to study the peritectic transition in the Al-C binary system. In contrast to the emblematic microstructure formed by peritectic transition in Fe-C, the peritectic phase Al_4C_3 grows on the surface of the parent phase graphite with a needle-like structure. Leveraging crystalline anisotropy within the PF model, we depict the formation of this needle-like morphology and investigate the critical orientation angle of a needle-like Al_4C_3 structure on graphite surfaces. Through simulating the diffusion-reaction process in the Al–C system, we elucidate the mechanisms of orientation selection in the phase transition from an energetic perspective, contributing to a better understanding of growth orientation in similar systems.

Additionally, employing the phase-field method, we study the morphological evolution of lamellar eutectics during three-phase eutectic transition in Mo-Si-Ti ternary system. Building on our understanding of fundamental peritectic transitions and eutectic transformations from the prior studies, we scrutinize the quasi-peritectic four-phase reaction in this ternary system and analyze the morphological evolution during this phase transition process. Our computational investigation into this intricate phase reaction sheds light on the underlying growth mechanism for the formation of lamellae pairs in Mo-Si-Ti alloy.

To investigate the influences of various key parameters, we utilize qualitative and quantitative methods to analyze the solidified microstructures in alloys. This work encapsulates a comprehensive investigation, starting from modeling the material systems to conducting representative phase-field simulations, and culminating in the analysis of resulting microstructures.

Zusammenfassung

In dieser Arbeit verwenden wir ein thermodynamisch konsistentes Phasenfeldmethode, um die morphologische Evolution während des Erstarrungsprozesses in Legierungen umfassend durch 2D- und 3D-Simulationen zu untersuchen.

Wir stellen eine Methodik zur Integration von thermodynamischen Datenbanken in Phasenfeldsimulationen vor, insbesondere für stöchiometrische Phasen, bei denen die Daten begrenzt sind. Dies ermöglicht die Erstellung thermodynamisch konsistenter Modelle für drei repräsentative Legierungssysteme: Fe-C, Al-C und Mo-Si-Ti. Diese Modelle werden durch Phasefeldsimulationen validiert, die sowohl zwei- als auch dreidimensionale Simulationen für alle drei Systeme umfassen, um die Entwicklung von Zweiphasen-Mikrostrukturen zu untersuchen.

In unserer Studie gehen wir zunächst auf den peritektischen Übergang im binären System Fe-C ein, mit dem Ziel, den isothermen peritektischen Übergang mit einer Flüssigkeitssättigung in Legierungen zu interpretieren. Anschließend nutzen wir das Phasenfeldmodell, um den peritektischen Übergang im binären System Al-C zu untersuchen. Im Gegensatz zur emblematischen Mikrostruktur, die sich durch den peritektischen Übergang in Fe-C bildet, wächst die peritektische Phase Al_4C_3 auf der Oberfläche der Ausgangsphase Graphit mit einer nadelförmigen Struktur. Unter Verwendung der kristallinen Anisotropie im PF-Modell stellen wir die Bildung dieser nadelförmigen Morphologie dar und untersuchen den kritischen Orientierungswinkel einer nadelförmigen Al_4C_3-Struktur auf den Graphitoberflächen. Durch Simulation des Diffusions-Reaktionsprozesses im Al-C-System klären wir die Mechanismen der Orientierungsauswahl im Phasenübergang aus energetischer Sicht auf, was zu einem besseren Verständnis der Wachstumsorientierung in ähnlichen Systemen beiträgt.

Zusätzlich untersuchen wir mithilfe der Phasenfeldmethode die morphologische Evolution von lamellaren Eutektika während des dreiphasigen eutektischen Übergangs im Mo-Si-Ti-Ternärsystem. Aufbauend auf unserem Verständnis der grundlegenden peritektischen Übergänge und eutektischen Transformationen aus vorherigen Studien, untersuchen wir den quasi-peritektischen Vierphasenprozess in diesem Ternärsystem und analysieren die morphologische Evolution während dieses Phasenübergangsprozesses. Unsere rechnerische Untersuchung dieses komplexen Phasenübergangs wirft Licht auf den zugrunde liegenden Wachstumsmechanismus für die Bildung von Lamellenpaaren in der Mo-Si-Ti-Legierung.

Für die Untersuchung des Einflusses dieser Schlüsselparameter werden so- wohl qualitative als auch quantitative Analysemethoden zur Untersuchung der Mikrostrukturen eingesetzt. Die vorliegende Arbeit umfasst eine vollständige Untersuchungskette von der Modellierung der Materialsysteme über die Durch- führung repräsentativer Phasenfeldsimulationen bis hin zur Analyse der sich entwickelnden Mikrostrukturen.

Acknowledgement

I completed this dissertation during my work as a research assistant at the Institute of Applied Materials-Microstructure Modelling and Simulation (IAM-MMS) within the Karlsruhe Institute of Technology (KIT), under the guidance of Prof. Dr. rer. nat. Britta Nestler. It was a privilege to be a member of this vibrant and diverse research group. The fruition of this thesis was made possible through the generous support of numerous individuals, and I wish to express my heartfelt gratitude to all of them on this occasion.

Foremost, I wish to express my profound appreciation to my supervisor, Prof. Dr. rer. nat. Britta Nestler, for her exceptional guidance, constant encouragement, and invaluable scientific insights. Her constructive critique and unwavering belief in my capabilities have significantly propelled the successful culmination of my doctoral research. I am genuinely grateful for the autonomy she provided, allowing me to explore captivating phenomena within the domain of phase transformation during solidification and for her facilitation of collaborations with researchers from various institutes, especially with Prof. Hans Jürgen Seifert. I hold immense admiration for Hans, appreciating his exceptional guidance and teaching. His profound knowledge and insightful instruction in thermodynamics have significantly enriched my understanding of this fundamental subject. This foundational understanding has proven invaluable in the pursuit of my doctoral research.

In addition, I would like to thank my group leaders Dr. August Anastasia and Dr. Fei Wang for their helpful discussions and our cooperation in cosupervising of students. Particularly, I hold great appreciation for Dr. Fei Wang, acknowledging his fervor, brilliance, and extensive knowledge. The stimulating and in-depth discussions with Fei, Haodong, and Yanchen have been a constant source of inspiration for me. Many thanks to Dr. Michael Kellner, Marco Seiz, and Kaveh Dargahi Noubary for their discussing and supporting. Many thanks for our daily jokes and many pleasures sharing with Fei Wang, Yanchen Wu, Yinghan Zhao, Nico Brandt during lunchtime.

I also thank the secretariat, many thanks to Ms. Inken Heise, Ms. Birgitt Hardt, and Ms. Michelle Ritzinger for helping with all the paper works. Many thanks to Mr. Leon Geisen for the organization of seminars and conference information. Many thanks to Mr. Christof Ratz, Mr. Domenic Frank, Ms. Roxanne Hohl for the technical support of computers and systems.

I extend my deepest gratitude to my parents for their unwavering support and encouragement. In particular, I want to convey my love and appreciation to my girlfriend for her understanding and patience.

Finally, the main part of the research has been carried out through funding by the German Research Foundation (DFG) in the frame of the Research Training Group 2561: Materials Compounds from Composite Materials for Applications in Extreme Conditions, which is gratefully acknowledged. Moreover, a part of work is funded by the European Regional Development Fund (ERDF) and the state of Baden-Wuerttemberg, within the

framework of the Center of Applied Research at Universities of Applied Sciences (ZAFH) 'InSeL—Innovative Foam Structures for Efficient Lightweight Design'. I thank the ERDF and the state of Baden-Wuerttemberg for supporting the project.

Contents

List of Figures

List of Tables

1. Introduction

1.1. Motivation

As schematically illustrated in Fig. 1.1, the linkage between processing, microstructures, and properties forms the foundational principle in material science [1, 2]. Under distinct processing conditions, the materials consisting of multiphase exhibit varying microstructures. The organization and characteristics of distinct phases at the microscopic level

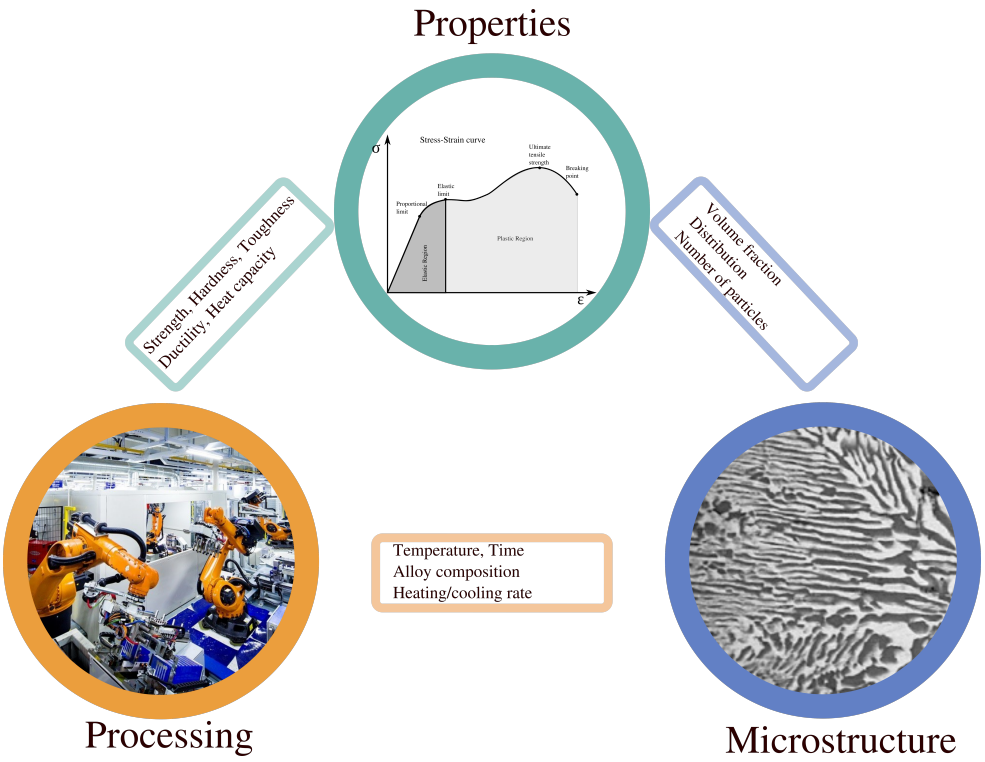

Figure 1.1.: A mutual dependence between the processing, microstructure, and properties. The schematic picture for processing are taken from [3]. The SEM micrograph is from [4].

significantly influence the overall behavior of materials at the macroscopic scale. A comprehensive understanding of the processing-microstructure-property relationship is crucial for industrial applications, aiding in the development of new tailored materials through the design of microstructural morphology.

The wide utilization of alloys across diverse fields, from aerospace to automobile industry (see Fig. 1.2), has led to a sustained focus on the solidification process by numerous

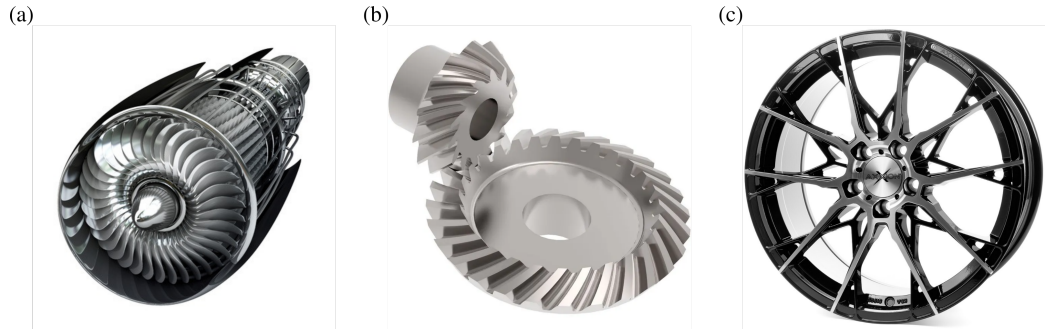

Figure 1.2.: (a) Titanium-based alloy used in aerospace turbine engine components [5]. (b) Steel used in spiral bevel gear [6]. (c) Aluminum-based alloy used in wheel [7].

researchers over several decades. Tang et al. [8] investigated how the presence of superficial Bi and Ga_2O_3 layers affects surface solidification and explained the mechanisms of pattern-formation, involving surface-catalysed heterogeneous nucleation. The observed surface patterns enabled precise nanoscale-infrared and surface-enhanced Raman mapping, hinting at significant potential for applications at the surface and nanoscale. For the tailored Ti-based alloys produced via additive manufacturing, Zhang et al. [9] studied the microstructural evolution behavior on multiple scales of Ti–47Al–2Cr–2Nb powders by aging-treated. Additionally, Shi et al. [10] designed a high-entropy alloy with a hierarchical microstructure that allows reconciliation of crack tolerance and high uniform elongation.

With the development of computer science, the computational material simulation is widely used in material science. In comparison with the experimental studies, the computer simulations include following advantages: (1) Simulations are often more cost-effective than conducting real experiments. (2) Simulations enable precise control over parameters, initial conditions, and variables, which helps to understand the underlying influence of specific parameter. (3) Simulations provide insights into processes or phenomena that are difficult or impossible to be observed directly in experiments. (4) Simulations can be easily repeated to verify results.

Since the early 90's, the phase-field (PF) method has emerged as an outstanding tool for simulating the formation and evolution of microstructures during solidification process [11, 12, 13, 14, 15]. The early phase-field models, proposed by Karma [16] and Wheeler et al. [17], were used to simulate alloy solidification. These models applied a dual phase-field model to describe the solid and liquid phases and coupled with Cahn-Hilliard model for demixing in solid phase. However, they are restricted to emulate the three-phase transition. In order to solve this problem, a multi-phase model was developed [18, 19]. In this multi-phase model, each phase is identified with an individual phase field parameter φ_α. Nestler and Wheeler [20] formulated a phase-field approach based on interpolating the free energy density to simulate the solidification process for binary eutectic and peritectic alloy systems, by setting up suitable values for the latent heats and temperature. This model in combination with a cubic anisotropy function was applied by Choudhury et al. [21] to emulate the solidification in Fe-C. Due to a common idea that the driving force for a phase transformation is the difference in the grand potentials between phases, Choudhury and Nestler reformulated a multi-phase-field model based on the grand-potential func-

tional [22]. Moreover, the anomalous interface effects were observed in several numerical investigations by using the phase-field model, when the interface width was extended artificially and the solute has unequal diffusivities between phases [23, 24, 25]. In order to eliminate these abnormal effects, an anti-trapping current was proposed into the diffusion equation by Karma [26].

The phase-field method has been proven to be a powerful modeling technique to simulate the growth of intermetallic compounds in many alloy systems, e.g. Sn-Cu [27, 28], Al-Au [29], Fe-Cr-Ni [30] and Al-Cu-Mg [31]. Among these mentioned works, more attention is paid to the eutectic transformation [32, 33, 34, 35] and peritectic transformation [36, 37, 38, 39, 40], which commonly occur during the solidification process. Nowadays, several eutectic alloys (such as cast iron [41], Al-Si [42], Nb-Si-Ti [43], etc.) play a crucial role in electronics, automotive, aerospace, and related industries. In the above mentioned studies, the alloys with distinct microstructures obtained under different solidification conditions exhibit diverse properties. Therefore, to understand the processing-microstructure connection is necessary for the industry applications. By using this method, Steinmetz et al. investigated and predicted the undercooling-spacing-velocity relationship for complex pattern arrangements via 2-D and 3-D simulations [44]. Kellner et al. studied the influence of nucleation on the morphological evolution of eutectic colony in NiAl-34Cr [45]. Moreover, Tu et al. explored the eutectic growth in combination with solid-solid boundary anisotropy and analyzed its influence on steady and unsteady lamellar morphologies [46]. The peritectic transition is frequently found in different alloys, e.g. Cu-Sn [47], Ag-Sn and Cd-Ag [48], and Fe-Co [49], and the phase-field method is applied to research this phase transition since quite early on. By using phase-field method, Tiaden et al. [19] studied the engulfing microstructure, in which the peritectic phase grows over the pro-peritectic phase. PhysRevE.63.031504 Lo et al. [50] conducted a study on a specific category of banded microstructures that emerge in peritectic alloy during a directional solidification. Dobler et. al. [51] documented another possible growth morphology in peritectics, namely coupled growth of lamellae or rods like in eutectics, and clarified the main differences between this analogues morphology in peritectics and eutectics. However, the understanding of peritectic transition in alloy solidification, especially from numerical studies, is considerably limited compared to other common phase transitions in alloy, such as eutectic transition. The relatively small amount of numerical investigations on the peritectic transition is likely to be caused by the following reasons: (i) In comparison with eutectic transition, there are much greater variety of growth modes in peritectic transformation, e.g., diffusion control mechanism, δ-ferrite remelting mechanism, and massive transformation mechanism [52, 53]. (ii) According to the previous experimental and numerical observations [54, 21], the growth rate of γ-phase after the complete engulfment of the δ particle decreases significantly, and consequently the simulation of whole process requires a high amount of computational effort, especially for a 3-D simulation. (iii) Most studies focus on directional solidification in peritectic transformation where the steady-state growth is rarely achieved [55]. (iv) The paucity of 3D phase-field modeling of peritectic transition in mesoscopic scale is probably due to the capability of the phase-field model before the invention of the thin interface analysis as well as the decoupling of the interfacial energy from the interface width in the grand potential formalism.

Furthermore, the four-phase reaction in ternary system, namely $L + \alpha \rightarrow \beta + \gamma$, is referred to as a quasi-peritectic reaction. Understanding of quasi-peritectic reactions is based on simple extension of binary peritectic reaction theory [56]. Meanwhile, a eutectic transformation ($L \rightarrow \beta+\gamma$) will consequently take place after α phase was covered by β and γ. Therefore, the microstructural evolution of the alloy during this phase transformation process would be affected by the combination of these reactions and exhibits differences compared with that formed in a primary eutectic transformation. However, there is a paucity of research discussing the quasi-peritectic four-phase reaction, which is likely due to the following reasons: (i) the transient accomplishment of the four-phase reaction. (ii) More attention is paid to the lamellar microstructure caused by the eutectic transformation rather than the similar lamellar microstructure produced by the quasi-peritectic four-phase reaction. (iii) The complexity caused by the potential several phase transitions.

In this work, the microstructure evolution of various alloys in different solidification processes is investigated using phase field methods. Based on already published data sets of the systems Fe-C, Al-C, and Mo-Si-Ti, thermodynamic models are developed and coupled with phase-field equation for simulating these alloy solidification. Using these models, two- and three-dimensional phase field simulations are performed in representative area sizes to explore the influence of different process conditions on the solidified microstructure. First, the study on the peritectic transition in Fe-C system was conducted, in that the peritectic phase γ grows on the surface of the parent phase δ until δ phase is engulfed. Next, we investigated the peritectic transition in Al-C system. Different from that in Fe-C system, the peritectic phase Al_4C_3 shows a needle-like microstructure on the surface of graphite with an orientation angle. Finally, we shed light on the eutectic transformation and quasi-peritectic four-phase reaction in Mo-Si-Ti ternary system. The difference in solidified morphology between the quasi-peritectic reaction and eutectic/peritectic transformation is discussed. Different analytical methods are used individually and jointly to evaluate these microstructures, providing a deeper understanding of microstructure evolution in multicomponent multiphase material systems.

1.2. Synopsis

The outline of this dissertation is as follows. In chapter 2, physical fundamentals and literature review of the study on solidification process for three considered alloy system are given. Subsequently, the phase-field model utilized for simulating the morphological evolution during solidification process is formulated in chapter 3. In chapter 4, the coupling approach of CALPHAD database with the phase-field model for all three alloy systems is discussed. In chapter 5, we shed light on the microstructural evolution of peritectic transition in Fe-C system and propose a new measurement method to determine the dynamic contact angle. By using this phase-field method, we simulate the evolution of γ phase in both 2-D and 3-D simulations under different liquid supersaturations as well as on the δ particle with distinct microstructures. By analyzing the concentration distribution and morphological evolution, we clarify the underlying mechanisms of the peritectic transition in carbon steel. In chapter of Al-C system (chapter 6), we illuminate the growth mechanism of the intermetallic compound Al_4C_3, with different orientation

angles in the Al-C system. The objective of our research is to show how the orientation angles influence the growth behavior of Al_4C_3, and which parameters have an impact on the critical orientation angle. By using this phase-field method, we simulate the evolution of a single intermetallic phase as well as the interaction of two adjacent particles. Through analyzing the concentration distribution, we clarify the underlying physics for the growth behaviors of Al_4C_3 with different orientation angles. Chapter 7 focuses on the lamellae growth during a eutectic transformation and a four-phase reaction in Mo-Si-Ti alloy. By using this phase-field method, we study the evolution of the lamellar pair $Ti(Mo)_5Si_3$ and β(Mo,Si,Ti) in 2-D and 3-D under different melt supersaturations and with various lamellar spacings, in both eutectic transformation and four-phase reaction. In the results section of eutectic transformation, we construct a microstructure selection map via systematic study of the lamellar spacing and the composition of Mo. Moreover, we scrutinize the influence of solid-liquid interfacial energy on the solidification morphology. In the part of four-phase reaction, we obtain lamellae microstructure differing from that in eutectic transformation. In addition, a tilt lamellae microstructure is observed in both phase transformation processes (see Fig. 2.17(b)). A qualitative investigation on this phenomenon will be provided in this work by phase-field simulations. Finally, in chapter 8, a comprehensive summary of the entire work is presented, emphasizing significant achievements and key findings. Furthermore, an outlook on potential future research and the associated challenges is provided.

2. Background

2.1. Solidification morphology

In the past decades, the formation of complex microstructures during solidification of alloys has drawn increasing attention of researchers in materials science. As the result of the change in external conditions in industrial production, the phase transition occurs. During the different phase transitions, metal and alloy solidify in different microstructres and morphologies, resulting in a distinction of properties of alloy. As a bridge, the solidified microstructure connects the production conditions and the properties of alloy [57]. The systematical study on the relationship between the microstructure and the production conditions is helpful for the development of new tailored materials by new designing the microstructural morphology.

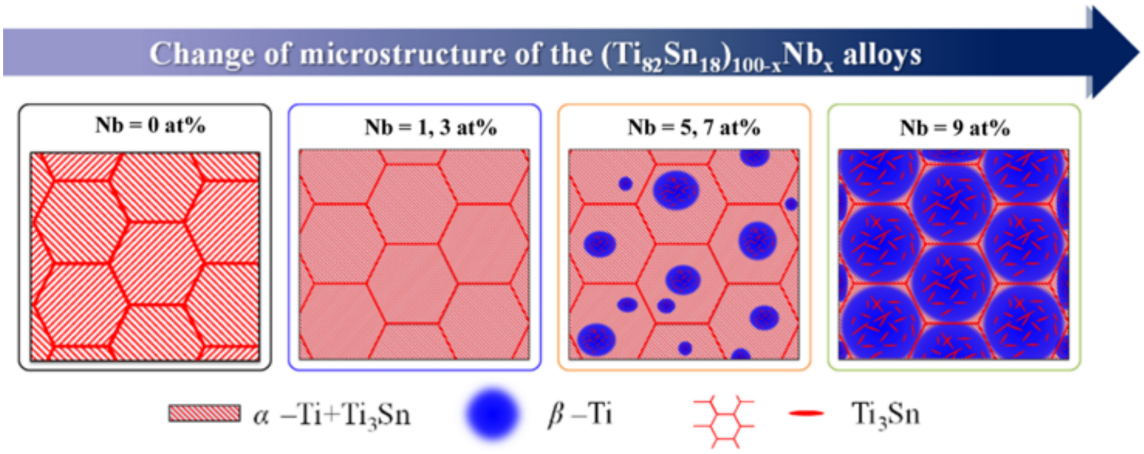

Figure 2.1.: Schematic showing the influence of Nb on the evolution of Ti-Sn eutectic structure [58]

Solidification is the process by which liquid is transformed into crystalline solid [59]. As the common phase transition, the eutectic transformation is widely investigated by experiments and simulations in different alloys, e.g. Al-Ce [60], Mg-Ni [61], Mo-Si [62], Ni-Al-Cr [45], Nb-Si-Ti [43]. The variation of the microstructure with different content of Nb in $(Ti_{82}Sn_{18})_{100-x}Nb_x$ (x = 0, 1, 3, 5, 7, and 9 at.%) alloy is shown in Fig. 2.1. For the case x= 0, the microstructure is composed of lamellar type duplex structure i.e., α−Ti + Ti_3Sn intermetallic compound, which are enclosed by Ti_3Sn. When the Nb constituent is between 1 and 3 at.%, the grain size increases slightly without change of the constituent phases. Further, lath-like Ti_3Sn with size in the range of 80 - 850 nm are embedded in the β-Ti region in case of x = 5 and x = 7. Whereas, the volume fraction of β-Ti(Nb)

phase increases up to 84 vol.% for x = 9. Kellner et al. has also investigated the influence from the concentration on the solidified morphology in Nb-Si-Ti alloy system, as depicted in Fig.2.2. In Fig.2.2 (a)-(f), the finally evolving solidification fronts for different melt compositions are observed in 3D-simulations. The corresponding target concentrations for simulation studies are marked by colored lines shown in Fig.2.2 (g). For the cases (a)-(c), the (Nb, Ti)$_3$Si and Nb$_{sol}$ phases grow with a lamellar-type structures, while the growth of a fibrous structure occurs in other three cases (d)-(f). By the phase-field modeling, Rátkai

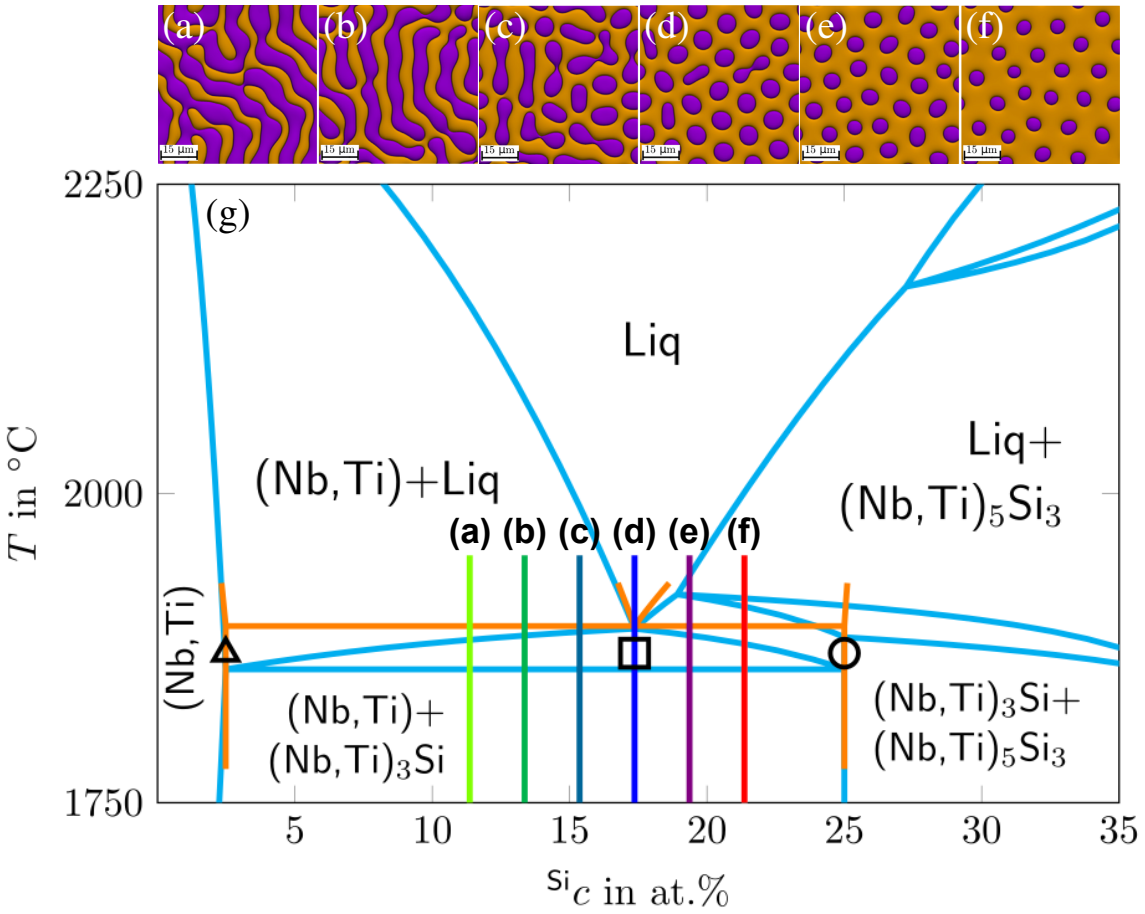

Figure 2.2.: Solidification fronts of the three-dimensional simulations of Nb-Si-Ti with different applied melt concentrations [43].

et al. studied the influence of anisotropy and predicted the morphological evolution of a eutectic transformation during a directional solidification process. Fig .2.3 (a) shows a schematic temperature profile applied in simulations, where the highest and lowest temperature are T_E = 1100 K and $T_E - \Delta T$, respectively. In these simulations, the matter moves downwards, while solidification takes place at the upper front and melting occurs at the lower front. With increasing undercooling, the following sequence of eutectic patterns was observed: (b) lamellae, (c) lamellae mixed with globules, (d) globules and merged horizontal globule pair, (e) merged globules, and (f) a "band-like" structure composed of lamellae parallel with the fronts. Zhu et al. explored the pattern formation of directionally-solidified $MoSi_2/Mo_5Si_3$ eutectic [62]. The 3D simulation results for this eutectic growth

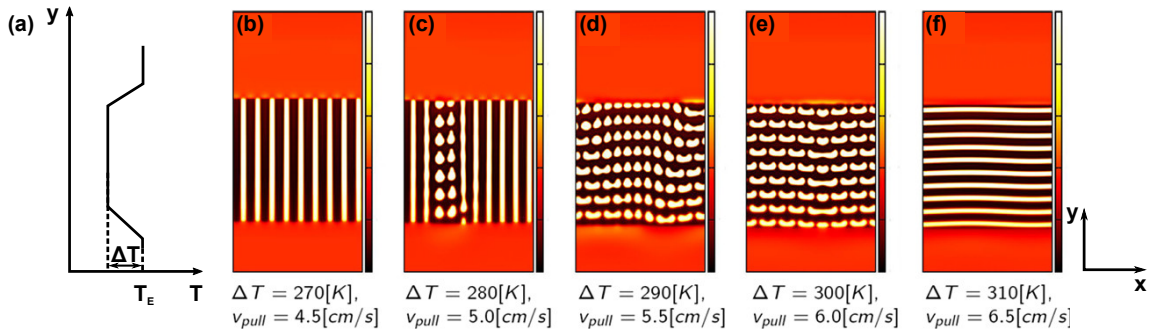

Figure 2.3.: Eutectic patterns predicted by the present phase-field mode at extreme undercoolings at the front. (a) A schematic temperature profile applied in simulations, where the highest and lowest temperatures were T_E =1100 K and $T_E - \Delta T$, respectively. (b)-(f) The concentration field of simulations with different undercoolings, accordingly the color bar indicates changes between c= 0 (black) and 1 (white). With increasing undercooling the following sequence of eutectic patterns was observed: (b) lamellae, (c) lamellae mixed with globules, (d) globules and merged horizontal globule pair, (e) merged globules, and (f) a "band-like" structure composed of lamellae parallel with the fronts. In these simulations, the matter moves downwards, while solidification takes place at the upper front and melting occurs at the lower front [63].

with three different growth rates are shown in Fig .2.4(a). All the simulations are in steady-state. In Fig .2.4(b) and (c), their cross-section images of growth direction and the corresponding experimental results is illustrated, respectively. The simulation results reveal that the larger growth rate gives rise to the finer microstructure. This is in accordance with the experimental results. Shi et al. scrutinize the solidified morphology of eutectic high-entropy alloys (EHEAs) $Al_{19}Fe_{20}Co_{20}Ni_{41}$ (at%) obtained by different manufacturing processes: conventional as-cast and directional solidification shown in Fig. 2.5. In Fig. 2.5(a), the conventionally cast EHEA exhibits a typical lamellar microstructure during a eutectic transformation as a reference material. The dual-phase lamellae consisting of $L1_2$ and B2 varies growth directions in distinct near-equiaxed grains (see Fig. 2.5(b)). During a directional solidification process, this alloy displays a microstructure that columnar grains align along the direction of applied temperature gradient (the DS-direction). As depicted in Fig. 2.5(c) and (d), columnar grains consists of aligned and branched eutectic colonies, both of which involves $L1_2$ and B2 lamellae, respectively. Aligned eutectic colonies grow along the DS-direction, whereas branched colonies are inclined at 30° and 60° to the DS-direction. This directionally solidified EHEA assumes a new type of herringbone microstructure that exhibits an outstanding improvement in ductility.

Furthermore, the solidification of peritectic alloys, such as Cu-Sn [47], Ag-Sn, Cd-Ag [48], and Fe-Co [49], also frequently produces multi-phased microstructures in the bulk [64], which plays a crucial role in alloy properties. Pan et al. studied the peritectic transition in Fe-C alloy using an quantitative multi-phase-field model and compared with the experimental results from [65, 66]. Through this comparison , the phase-field simulation and experimental observation show the same tendency that the increasing

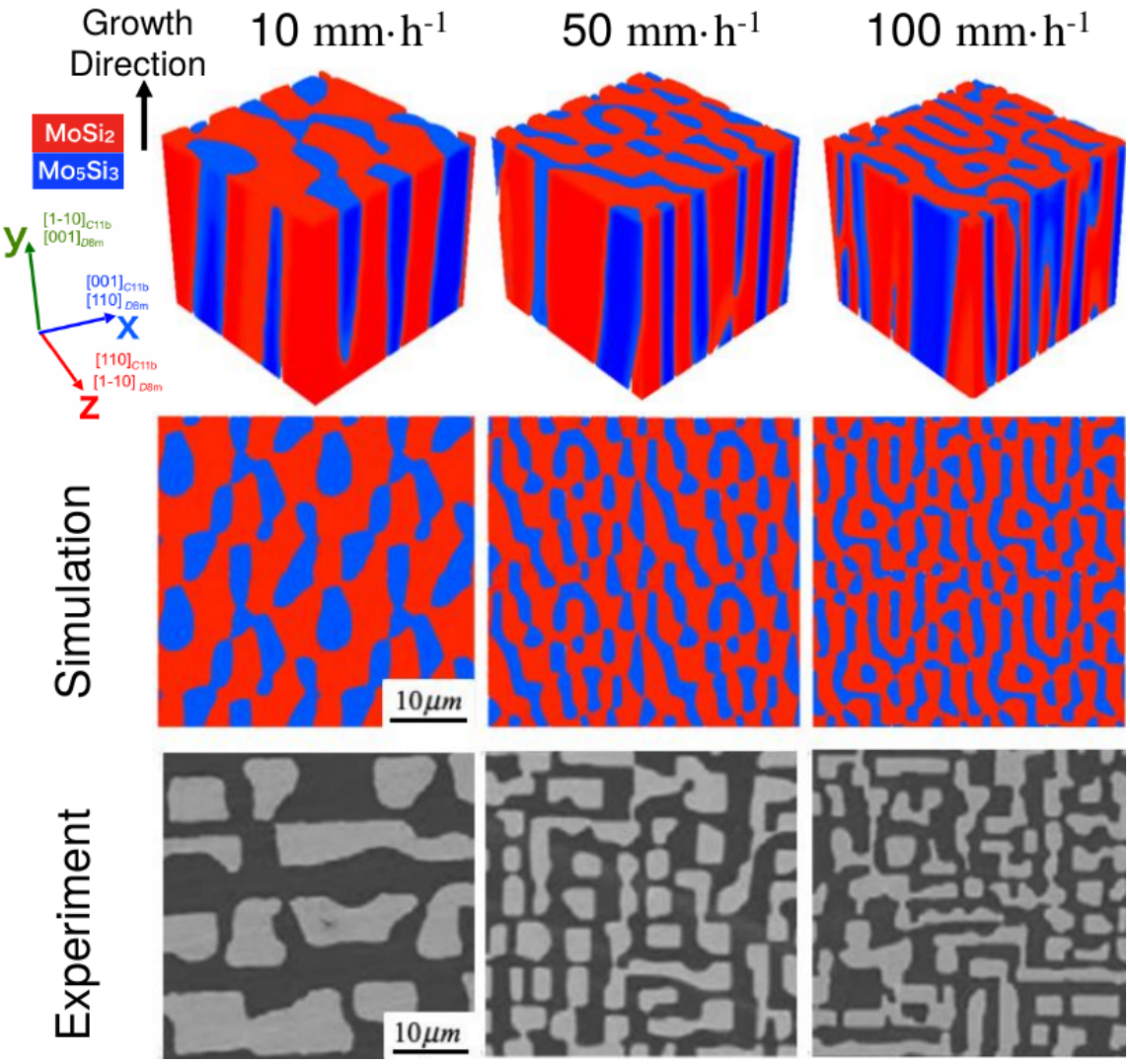

Figure 2.4.: Comparison of solidified microstructure between phase-field simulations and experiments for three growth rates of 10 mm h^{-1}, 50 mm h^{-1}, 100 mm h^{-1}. [62].

tip velocity of γ-platelet gives rise to a decrease of its thickness(see Fig. 2.6). Beside this typical peritectic structure that the δ-phase is surrounded by the γ-phase, Lo et al. also observed several other morpholigies in peritectic solidification by phase-field simulation. A microstructure selection map that summarizes observed morphologies during peritectic solidification is shown in Fig. 2.7(a) and (b). The four different morphologies of β-island banding, coupled growth after transient β-island banding, coupled growth after transient α-island banding, and discrete banding is represented by filled triangles, open circles, open diamonds, and filled squares, respectively. As an exemplary explanation, Fig. 2.7(c) and (f) displays the two basic behaviors of sustained β-island banding and transient island banding leading to stable coupled growth, respectively. In Fig. 2.7(d) and (e), a more complex intermediary case of intermittent island banding interrupted by long periods of oscillatory coupled growth is illustrated. Note that (e) is the successive frame of (d). Aside

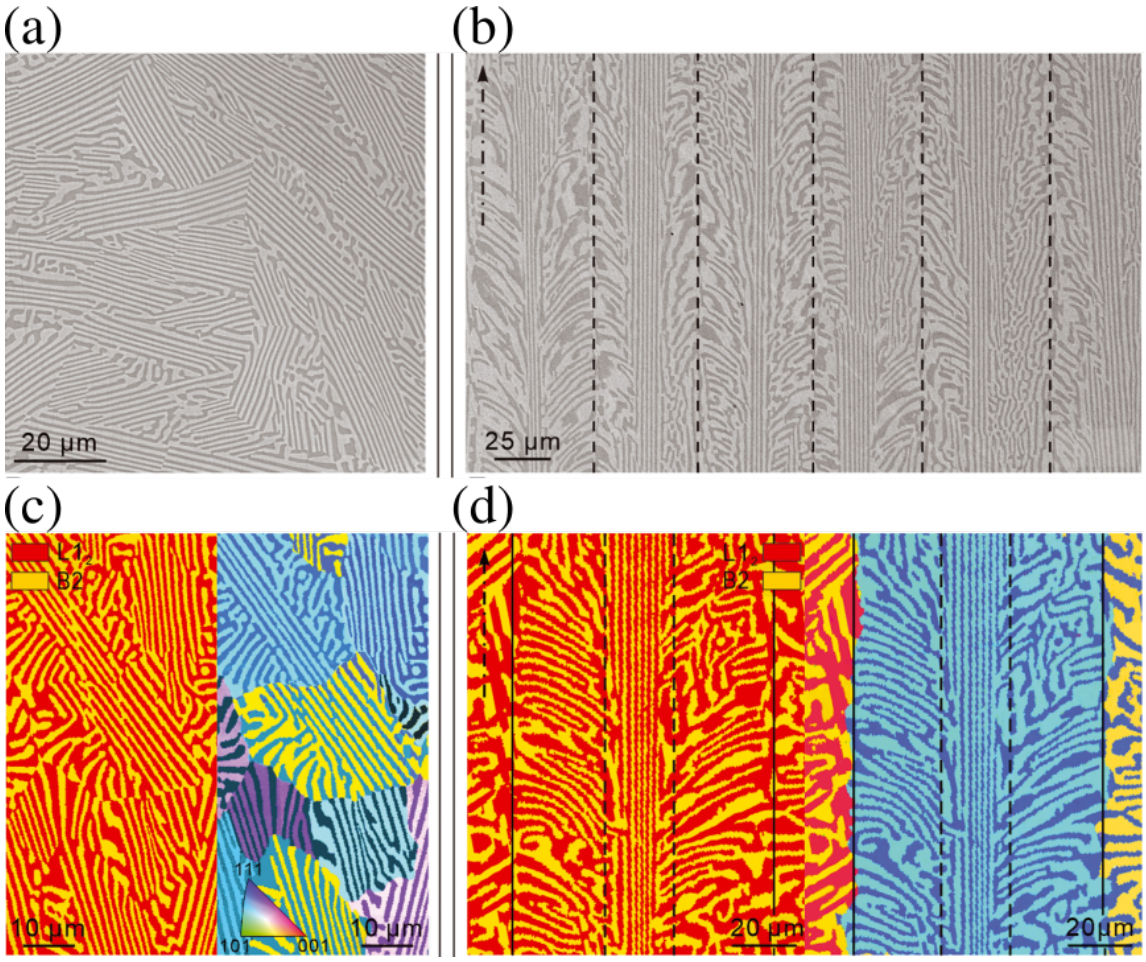

Figure 2.5.: (a) and (c) The Conventionally cast EHEA. (a) SEM backscattered electron image. (c) Electron backscattering diffraction (EBSD) phase map (left) and inverse pole figure (IPF) map (right). (b) and (d) The directionally solidified EHEA. (b) SEM backscatter electron image. (d) Enlarged EBSD phase and IPF maps [10].

from that, as the predominant microstructural constituents of solidified alloys[Trivedi and Kurz 2013], the dendrite formation in the solidification process is observed in many alloys, such as Al-Zn, Al-Cu, Mg-Al, Al-Cu-Mg and Al-Si-Mg, and extensively studied in the past decades. In the following section, the literature review for the solidification process of different phase transformations involving experimental and numerical studies are conducted.

2.2. Eutectic growth

Eutectic solidification is defined as a simultaneous precipitation of two or more solid phases from a liquid phase via a eutectic reaction $L \leftrightarrow \alpha + \beta$ at constant eutectic temperature [68].

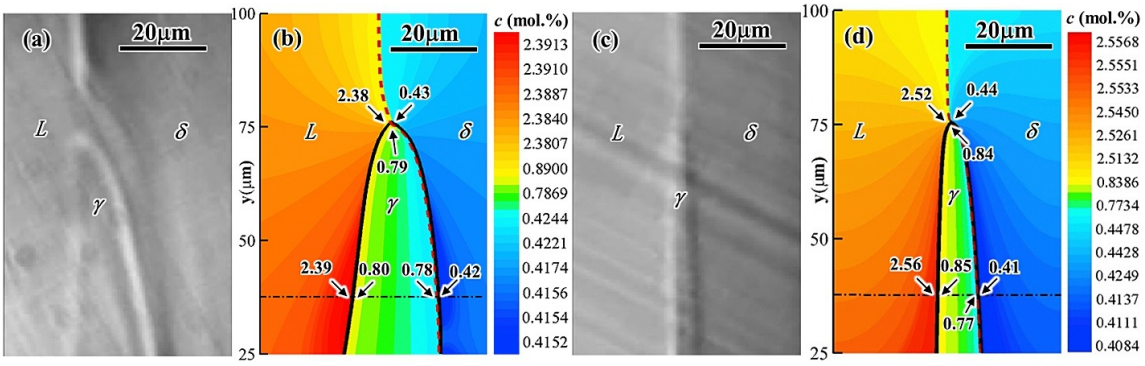

Figure 2.6.: Comparison of the γ-platelet morphologies with different tip velocities obtained by the experiment [65, 66] and PF simulation: (a) experiment, V_{tip}=36 μm s^{-1}; (b) PF simulation, V_{tip}=36.5 μm s^{-1} with ΔT= 0.85 K; (c) experiment, V_{tip}=510 μm s^{-1}; (d) PF simulation, V_{tip}=521 μm s^{-1} with ΔT= 3.17 K (numbers in the figures show the local carbon concentrations). [38].

A schematic phase diagram of a binary alloy A-B is shown in Fig. 2.8(a). The eutectic temperature T_E is always below the the melting temperatures of the components involved.

During the solidification process, eutectic reactions in melt often result in solids with distinct microstructures. According to the different morphologies, eutectic reactions are discriminated and named as lamellar, rod, spiral, and nodular eutectic structures etc.. Some representative examples are shown in Fig. 2.9. Owing to the fact that several morphologies could appear in the same system simultaneously, the eutectic structures are also classified by other ways [69]. One way is to classify the eutectic as normal or degenerate based on its ability to establish cooperation between the two phases during the precipitation. For a normal eutectic reaction, two solid phases grow with a comparable rate forming a common interface. Lamellar- or rod-shaped aggregates are formed in this case. For a degenerate eutectic, a lamellar or rod eutectic cannot be formed, whereas one phase grows ahead of the other determining the eutectic microstructure. The crucial reason is to a large extent the conditions at the interface, i.e. the interface kinetics. Due to the widely industrial applications of lamellar or rod eutectic structure, we focus on this normal eutectic growth in the following study.

As shown in the Fig. 2.8(b), the lamellae consisting of α and β phases grow side by side in the melt. For the lamellar growth, B atoms diffuse from the liquid near to the α phase to the melt ahead of β phase, whereas A atoms move in the opposite direction. Jackson and Hunt[jackson-Hunt theory] have purposed a general theory for the steady-state growth of lamellar and rod eutectics. Based on their research, the interface temperature as well as the difference between the eutectic temperature T_E and the local actual temperature of the interface T_I play a crucial role on its stability. For a nonplanar interface, which are not of eutectic composition and not at equilibrium, the undercooling ΔT based on the Gibbs-Thompson relationship is formulated as

$$\Delta T = T_E - T_I = \Delta T_C + \Delta T_\kappa + \Delta T_k. \tag{2.1}$$

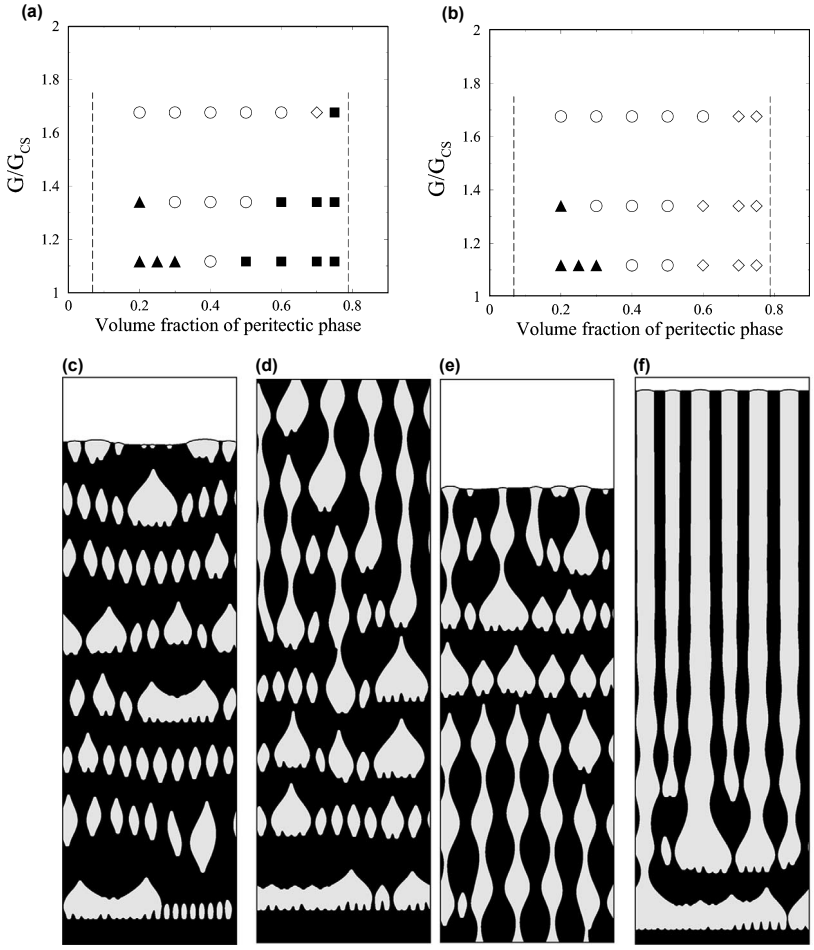

Figure 2.7.: Microstructure selection map extracted from 2D-simulations with different nucleation parameters:(a) $w_0 = 5 \times 10^{43}$ and $A = 0.215$ (high nucleation rate), (b) $w_0 = 5 \times 10^{11}$ and $A = 0.0576$ (low nucleation rate). The pulling rate is kept constant, and the volume fraction of peritectic phase (nominal composition of the sample) and the temperature gradient G are varied. G_{CS} is the critical gradient for onset of morphological instability of the primary phase (constitutional supercooling). Filled triangles: β-island banding; open circles: coupled growth after transient β-island banding; open diamonds: coupled growth after transient α-island banding; filled squares: discrete banding. Vertical dashed lines indicate the limits of the banding window. Examples of simulated (c) persistent; (d)-(e) intermittent; (f) transient β-island banding for $G/G_{CS} = 1.117$ (c)-(e) and $G/G_{CS} = 1.34$ (f). The volume fractions of the peritectic phase: (c) 0.25; (d)-(e) 0.3; and (f) 0.5. Nucleation parameters of all cases are set as in (a). Black: primary α phase; gray: peritectic β phase; white: liquid phase. Note that: (e) is the successive frame of (d) [67].

The first term ΔT_C describes the influence of the concentration, the second term ΔT_κ represents the contribution from the interface curvature, and the third term ΔT_k is the kinetic undercooling. According to this formulation, the analytic relationship between the

undercooling of a macroscopically flat eutectic interface ΔT growing at velocity v, and the eutectic spacing (lamellar spacing) λ can be derived as follow:

$$\Delta T = A\lambda v + \frac{B}{\lambda}, \tag{2.2}$$

where parameters A and B are the constants that only depend on the material system and can be calculated analogously to[Jackson und Hunt]. The two terms on the right-hand side of Eq. (2.2) originate physically from solute diffusion in the liquid and capillarity, respectively. For a given v, ΔT is a function of λ and has an extreme at the point λ_m, which is calculated as

$$\lambda_m = (B/A)^{\frac{1}{2}} v^{-\frac{1}{2}}. \tag{2.3}$$

According to the argument from Jackson-Hunt theory, coupled growth of lamellae should show a morphological instability for $\lambda < \lambda_m$. The key assumption, which Jackson-Hunt attributed to Cahn [Jackson-Hunt theory], is that lamellae grow locally perpendicular to the envelope of the eutectic front. A schematic illustration by considering a concave perturbation of the eutectic front is shown in Fig. This assumption forms a relationship between the lateral displacement of the triple junctions and local slope of the envelope of the eutectic front and indicates that the lamellar spacing decreases in the concave region of the envelope (see Fig.). For the case $\lambda > \lambda_m$, the decrease in λ leads to an increase of the interface temperature and a temporal decrease in perturbation. In contrast, for $\lambda < \lambda_m$, the reduction in the lamellar spacing gives rise to that the front temperature decreases and the lamellae becomes even narrower until its elimination. Based on this argument, the interface is unstable during the lamellar growth when $\lambda < \lambda_m$. However, some experiments, that directly measured the temperature-versus-spacing curve and the relaxation rate of the spacing perturbations, purposed different conclusion. They fund that the lamellae can be stable for the spacing as low as $0.8\lambda_m$. This overstability was also confirmed by phase-field simulations and was also observed in the current work. As above mentioned in this well-known relationship, the lamellar spacing λ and the growth velocity v have a crucial influence on the temperature of interface, consequently on the stability of the morphology.

2.3. Peritectic growth

In many binary alloy systems, the occurrence of the peritectic transition is often observed, in which one solid phase reacts with a liquid phase to produce a second solid phase, i.e. $\alpha + L \rightarrow \beta$. The most important example is the Fe-C system, in which at about 1767 Kelvin delta ferrite and liquid phase are in equilibrium with austenite. A similar reaction is found in other different alloys, e.g. Cu-Sn [47], Ag-Sn and Cd-Ag [48], and Fe-Co [49]. The growth of the peritectic phase is usually divided into three parts [70]: (p_1) the direct interaction of the primary solid and the liquid phases; (p_2) the transformation by solid state diffusion; (p_3) the direct solidification on the primary phase. A schematic diagram of the three growth stages of peritectic solidification is depicted in Fig. 2.10.

As shown in Fig. 2.11(a), a peritectic reaction as part of a schematic binary phase diagram takes place at the temperature T_P. In analogous to the eutectic composition in eutectic

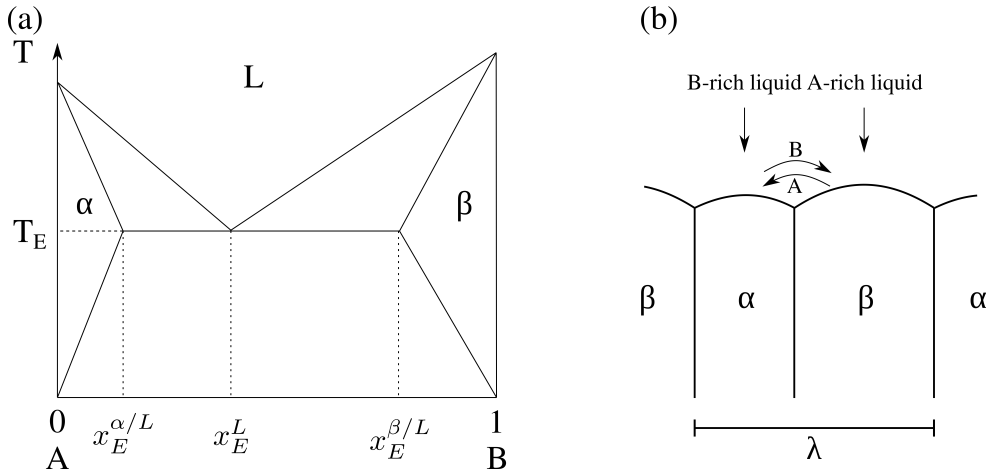

Figure 2.8.: Schematic phase diagram of a binary alloy.

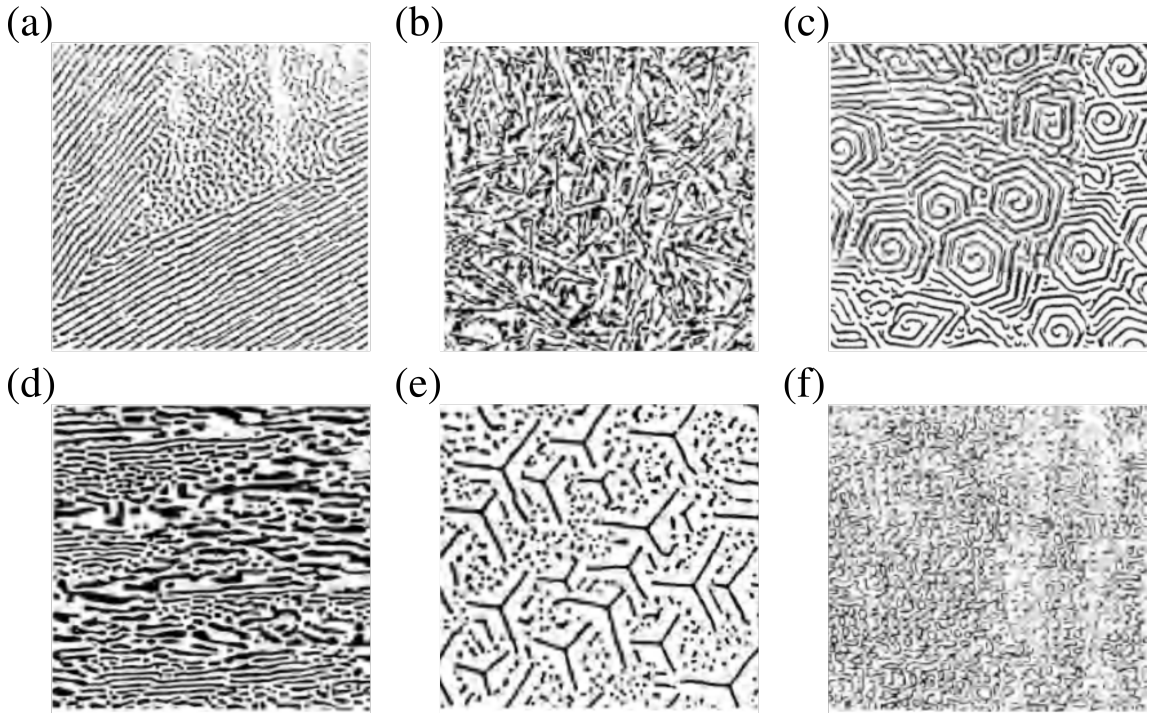

Figure 2.9.: (a) Rod-like and plate-like eutectic structures in Cu-Ag. (b) Irregular plate-like eutectic structure in Al-Si. (c) Spiral eutectic structure in Zn-Mg-Zn_2, (d) Irregular plate-like eutectic structure in Cd-Bi, (e) Irregular eutectic structure in Co-TaC, and (f) Rod-like eutectic structure in $FeFe_2B$ [69].

systems, the peritectic composition C_P of the peritectic phase (β) indicates that only at this composition the high temperature phases α and liquid can be replaced completely by the lower temperature β phase. C_α and C_L are the compositions of α and liquid phases in equilibrium with β phase at peritectic temperature. The phase diagram in Fig. 2.11(a) is similar to the Fe-C system. The equilibrium distribution coefficients k_e of the solutes is defined as $k_e = C_s/C_l$, where C_s and C_l are the concentrations of the solid and liquid

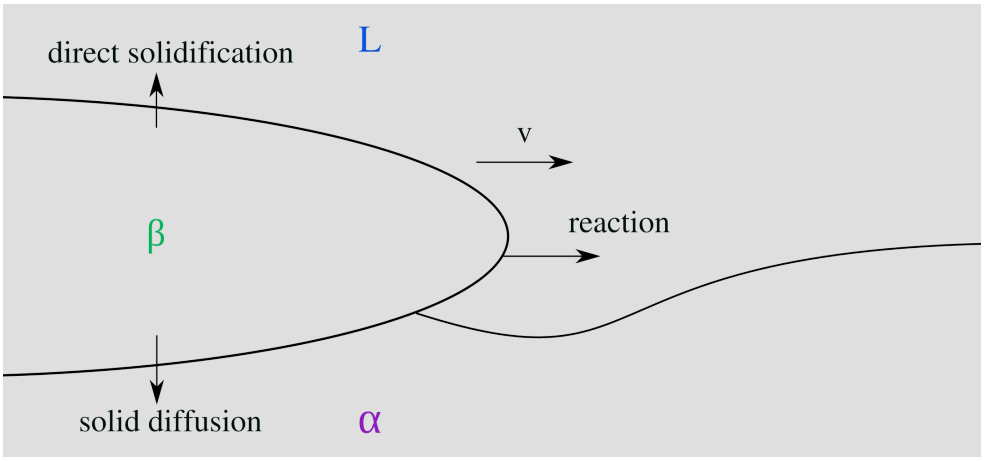

Figure 2.10.: A schematic diagram of the three growth stages of peritectic solidification.

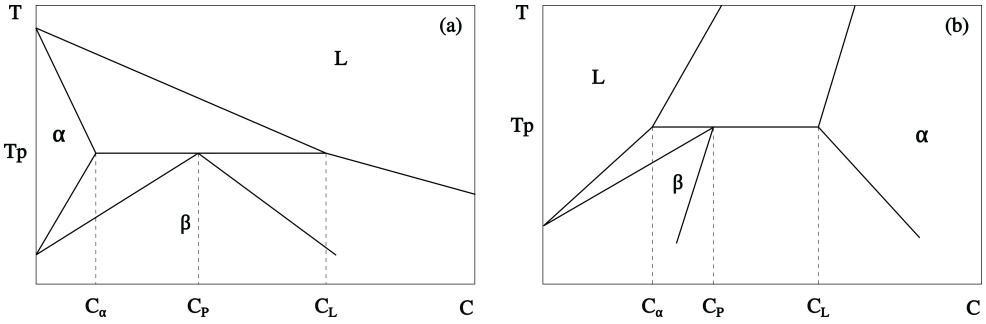

Figure 2.11.: Schematic peritectic phase diagrams with different equilibrium distribution coefficients k_e: (a) $k_e < 1$ and (b) $k_e > 1$.

phases in equilibrium at the given temperature. In this case, k_e are less than one in both parent and peritectic phases. In contrast, another kind of peritectic transition has been observed in many Al-based alloys, in which $k_e > 1$ in both solid phases (see Fig. 2.11(b)). The hypoperitectic alloy in these system should contain the liquid and β phases below T_P, rather than α and β phases as in hypoperitectic alloy with $k_e < 1$. Similarly, the non-peritectic alloys, in which the peritectic phase solidifies directly from the liquid, are with concentration less than C_L of $k_e > 1$ systems, whereas bigger than C_L of $k_e < 1$ systems. For these two kinds of peritectic transitions, the main differences are summarised in Table 2.1.

	k< 1	k> 1
Non-peritectic	$C_0 > C_L$	$C_0 < C_L$
Peritectic alloys	$C_\alpha < C_0 < C_L$	$C_L < C_0 < C_\alpha$
Hypoperitectic	$C_\alpha < C_0 < C_P$	$C_L < C_0 < C_P$

Table 2.1.: Comparison of two different peritectic systems: k< 1 and k> 1.

As above-mentioned, three different parts have been identified in the growth of the peritectic transition (see Fig. 2.10). However, it should be noted that the whole growth process cannot be clearly divided into three distinct stages, since once the reaction occurs and the primary phase is covered by the peritectic phase, both the solid transformation and direct β solidification take place simultaneously. During the liquid-solid peritectic reaction, the three phases contact with each other at the triple junction, as schematically shown in Fig. 2.10. Several models are proposed to describe this process. Hillert [71] pointed out that if the surface energies of the three phases are assumed to balance where they intersect, then during the growth of the β-phase over the α-phase both dissolution and some resolification of the α-phase is required. The concentration difference $C_L^\beta - C_L^\alpha$ leads to the diffusion of atoms in liquid ahead of advancing β-phase. Fredriksson and Nylen extended this model with assumption that the β-phase is a flat platelike surface layer with a radius of curvature R at its tip. In addition, they assume that the β platelet reaches the steady state with the maximum velocity, giving a thickness 2R. They applied a model proposed by Bosze and Trivedi [72] for describing this platelike growth. The velocity of the platelike β is written as a function of the supersaturation Ω defined as

$$\Omega = \frac{C_L^\beta - C_L^\alpha}{C_L^\beta - C_\beta^L}, \tag{2.4}$$

where C_L^β is the concentration of β in equilibrium with the liquid phase at the growth temperature (see Fig. 2.11(a)). At low undercoolings, the β growth velocity is given by

$$V = \frac{9}{8}\frac{D_L}{R}\Omega'^2, \tag{2.5}$$

where

$$\Omega' = \frac{\Omega}{1 - \frac{2}{\pi}\Omega - \frac{1}{2\pi}\Omega^2} \tag{2.6}$$

Bosze and Trivedi has simplified this model and obtained the ratio of the critical radius for nucleation R_c to the actual radius R for the case with small Peclet number ($\frac{VR}{2D_L}$) is

$$\frac{R_c}{R} = \frac{3}{32}\Omega \tag{2.7}$$

For the peritectic reaction, Fredriksson and Nylen estimated the critical thickness of the platelike peritectic phase as

$$R_c = \frac{\sigma}{\Delta G_m} V_m \tag{2.8}$$

where $\sigma = \sigma_{\beta L} + \sigma_{\alpha\beta} - \sigma_{\alpha L}$ and $\sigma_{\beta L}$, $\sigma_{\alpha\beta}$, $\sigma_{\alpha L}$ are the surface energies of β/liquid, α/β, and α/liquid interfaces, respectively, ΔG_m represents the driving force, and V_m is the molar volume of the liquid. However, the predicted value and the thickness observed in experiments show a good consistent only for the case with unreasonable high values of σ. These differences in thickness between the prediction by model and the experiment are likely caused by the following various factors [73]: the effect of the thermal gradient, errors in thermodynamic data, and the solid diffusion through the β phase. The contact between

liquid and α phase is prevented by the formation of the peritectic β phase during the peritectic reaction. Hence the further movement of α/β interface towards α phase requires the atom diffusion through the β layer. This diffusion is driven by the compositional difference between the α/β and β/liquid interfaces. Via a one-dimensional analysis, the thickness Δ of the β layer for isothermal conditions is described by the following equation

$$\frac{\Delta^2}{2t} = D_\beta \frac{(C_\beta^L - C_\beta^\alpha)(C_L^\beta - C_\alpha^L)}{(C_L^\beta - C_\beta)(C_\beta - C_\beta^\alpha)}, \tag{2.9}$$

where D_β is the average interdiffusion coefficient in the β-phase, t is the time of isothermal annealing, C_β^α and C_β^α are the equilibrium concentration of β with respect to α and of α with respect to β, respectively. The relationship between the thickness of peritectic phase and the time can be simplified as $\Delta = At^n$. In the study by Titchener and Spittle [74], they examined the time dependence of the thickness β phase for different undercooling and found that n varied from 0.35 to 0.57, almost consistent with the diffusion-controlled growth of n= 0.5. This model is also applicable to the other diffusion-controlled process, such as peritectoid transformation. Except the liquid-solid reaction and solid-solid transformation, the direct solidification of β phase from liquid has also the contribution to its thickness. By employing the Scheil equation, Fredriksson and Nylen calculated the fraction of β formed by direct solidification, which obey the following equation

$$C_\beta^L = C_L^0 f_L^{(k_e - 1)}. \tag{2.10}$$

In this case, k_e is the distribution coefficient of B in the β phase and C_L^0 is the average composition of the liquid at the start of direct solidification.

For the peritectic transition in a binary system, the combined effects of the reaction, transformation and direct solidification on the growth kinetic should be taken into consideration and is used to analyze the 2D and 3D simulations of the peritectic transition in Fe-C in chapter 5.

Extension to the ternary system, peritectic type reactions are expected over a range of temperatures. On the liquidus projection of a ternary system, the composition of peritectic liquid C_L moves along a monovariant line. At a given temperature, the peritectic reaction involves the liquid in equilibrium with both solid phases. In some ternary systems, the monovariant peritectic line lead to an invariant reaction involving four phases [70]. This four-phase reaction can be classified into two different cases: (p_i) the quasi-peritectic reaction, in which a liquid reacts with a primary solidified solid phase to form two new solid phases ($\alpha + liquid \rightarrow \beta + \gamma$), and ($p_{ii}$) the ternary peritectic reaction, in which a liquid reacts with two solid phases to produce a new solid phase ($liquid + \alpha + \beta \rightarrow \gamma$).

2.4. Thermodynamic fundamentals

In this section, the thermodynamic fundamentals related in the following investigations are briefly summarised, such as nucleation theory, growth mechanism of the intermetallic phase, as well as the derivation of the thermodynamic potentials.

2.4.1. Nucleation theory

Solidification of alloy melts is a phase transformation process, in which a melt of alloy turns into a solid phase at the temperature lower than the melting point. In general, solidification requires a heat flow that changes the free energies and therefore the relative thermodynamic stability, of the phases present. In comparison with thermodynamically stable phases, the transformation process of one phase to another requires the rearrangement of the atoms. For a pure substance, this transformation may involve a relatively short-range (atomic) rearrangement to form a new crystal structure. The atomic movement are required over much larger, but still microscopic, distances for alloy solidification, where mass diffusion controls the transformation. Due to the atomic movements, solidification can never be an equilibrium process and some irreversible departure from the equilibrium provides the driving force for this process [75].

In solidification, the phase transformation process cannot occur at any arbitrarily small undercooling. The large curvature related to a crystal in atomic dimension gives rise to this phenomena. Fig. 2.12 schematically illustrates the temperature-dependent Gibbs energy of a pure substance in liquid and solid phases. When the temperature at the melting point T_M,

$$g_L = g_S, \tag{2.11}$$

and the system is in thermodynamic equilibrium. With the decreasing temperature, the system deviates from the equilibrium and the difference in Gibbs energy between solid and liquid phases Δg increases. Consequently, the nucleation occurs and the liquid solidifies into a solid. The nucleation process is determined by two factors: one is the difference in the bulk free energy between solid and liquid phases, that provides the driving force for the phase transformation, and the other is the surface energy against nuclei growth. For a

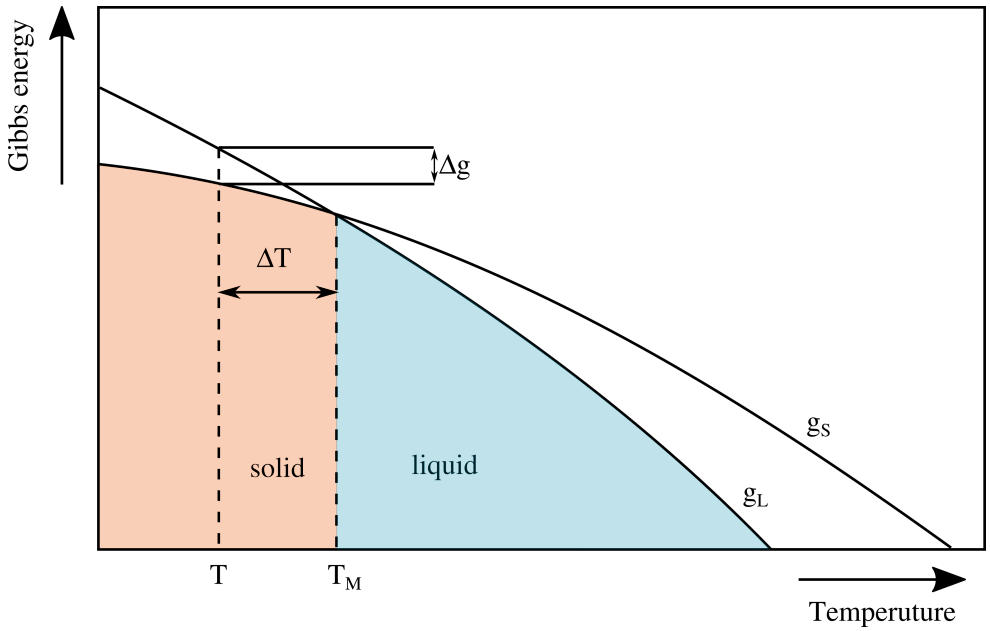

Figure 2.12.: The Gibbs energies of a solid and a liquid phase of a pure substance as a function of temperature.

homogeneous nucleation, the total free energy of a particle E can be written as the sum of a bulk term, which is proportional to the volume of the nucleus, and as a surface term, which is proportional to its surface area

$$E(r) = \frac{4}{3}\pi r^3 \Delta g + 4\pi r^2 \sigma, \tag{2.12}$$

which is in accordance with the CNT. Here, Δg is the difference in the free energy density, and σ is the surface tension. The former one is negative, whereas the latter one is always positive. As a schematic illustration in Fig. 2.13, with an increase in the radius r, the total free energy firstly increases and then passes through a maximum. Thus we obtain the critical radius r_c written as

$$r_c = \frac{2\gamma}{\Delta g}, \tag{2.13}$$

where $\frac{dE}{dr} = 0$. A nucleus with radius greater than r_c grows decreasing the free energy while growing. The nucleus, which is smaller than r_c, cannot surmount the "energy barrier" and will eventually disappear [76]. This "energy barrier" is the minimum energy for the nuclei growth, namely the critical activation energy Δg_c, which is formulated as

$$\Delta g_c = \frac{16\pi\gamma^3}{3\Delta g^2}. \tag{2.14}$$

The heterogeneous nucleation is similar to the homogeneous nucleation and we set up an orientation angle to the nucleus. The free energy E^* can be reformulated as

$$E^*(r,\theta) = \int_V \Delta g f(\theta) dv + \int_S \sigma h(\theta) ds, \tag{2.15}$$

where $f(\theta)$ and $h(\theta)$ are the functions of the orientation angle. When $\frac{\partial E^*}{\partial \theta} = 0$ and $\frac{\partial E^*}{\partial r} = 0$, a critical orientation angle is achieved, which is equal to the CNT.

2.4.2. Thermodynamic potentials

In order to describe the total energy of a system correctly, the thermodynamic potential of the internal energy of the system is used as the basis for the numerical study. As defined in the first law of thermodynamics, the internal energy U is expressed as a function of the state variables the entropy S and the volume V: $U = U(S,V)$ and the change of the internal energy of a closed system is formulated as

$$\begin{aligned} dU =& \delta Q + \delta W \\ =& TdS - pdV, \end{aligned} \tag{2.16}$$

where $\delta W = -pdV$ is mechanical work and $\delta Q = TdS$ represents the quantity of heat added to the system. When the system is in thermodynamic equilibrium, the internal energy remains constant, $dU = 0$.

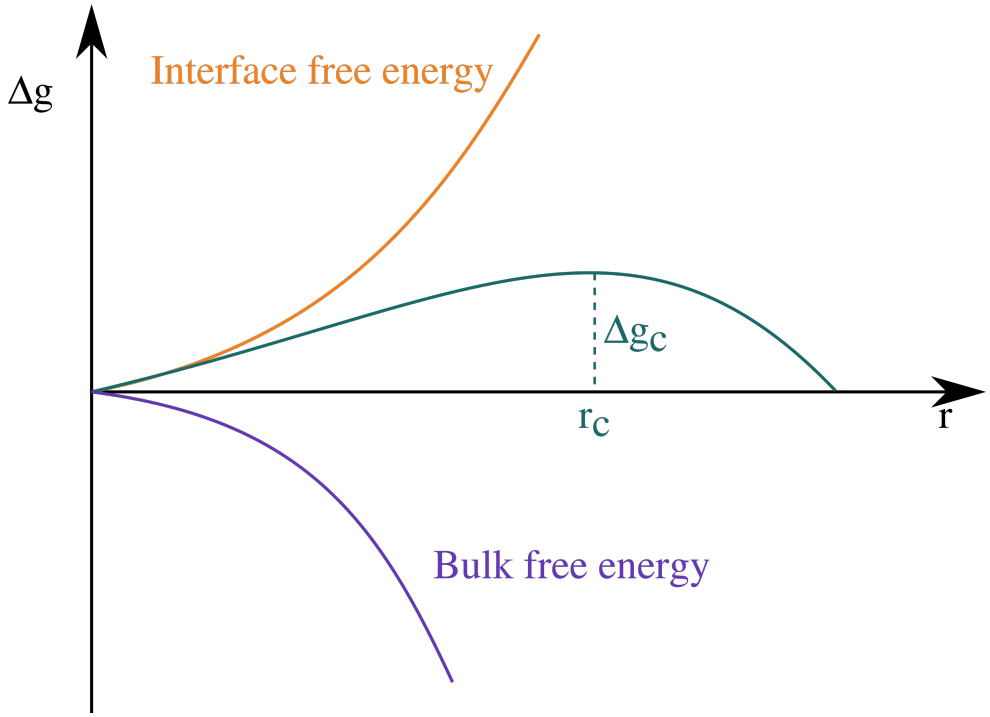

Figure 2.13.: Schematic illustration of the total free energy as a function of nucleation radius.

In the case of a closed system in which the particles of the system are of different types and, because chemical reactions may occur, the fundamental thermodynamic relation for dU becomes

$$dU = TdS - pdV + \sum_i \mu_i dN_i, \tag{2.17}$$

where dN_i is the increase in number of i-th particles. The change of the internal energy is related to the change in the state variables S and V, to the change in amount of substance as well as to the pressure p and to the chemical potential for i-th component μ_i. By use of a Legendre transformation of the internal energy $U(Ni, T, V)$ with respect to the S, the free energy $F(Ni, T, V)$ can be obtained

$$\begin{aligned} F(Ni, T, V) =& U(Ni, S(Ni, T, V), V) - \left.\frac{\partial U}{\partial S}\right|_{V,N_i} S(Ni, T, V) \\ =& U(S(Ni, T, V)) - TS(Ni, T, V). \end{aligned} \tag{2.18}$$

The change in free energy dF considering Eq. 2.17 is formulated as

$$\begin{aligned} dF =& dU - TdS - SdT \\ =& TdS - pdV + \sum_i \mu_i dN_i - TdS - SdT \\ =& -pdV + \sum_i \mu_i dN_i - SdT. \end{aligned} \tag{2.19}$$

The free energy F is an extensive state variables, the change of which is related to the temperature T, the volume V, and amounts of constituents N_i. By a further Legendre transformation with respect to the amounts of constituents N_i, the fee energy can be converted into the grand chemical potential Ψ

$$\begin{aligned}\Psi(\mu_i, T, V) =& F(N_i(\mu_i, T, V), T, V) - \left.\frac{\partial F}{\partial N_i}\right|_{T,V} N_i(\mu_i, T, V) \\ =& F(N_i(\mu_i, T, V), T, V) - \sum \mu_i N_i(\mu_i, T, V).\end{aligned} \tag{2.20}$$

The chemical potential μ_i is defined as

$$\mu_i = \left.\frac{\partial F}{\partial N_i}\right|_{T,V} \tag{2.21}$$

for the case with constant T and V. When a system with constant amount of substance of

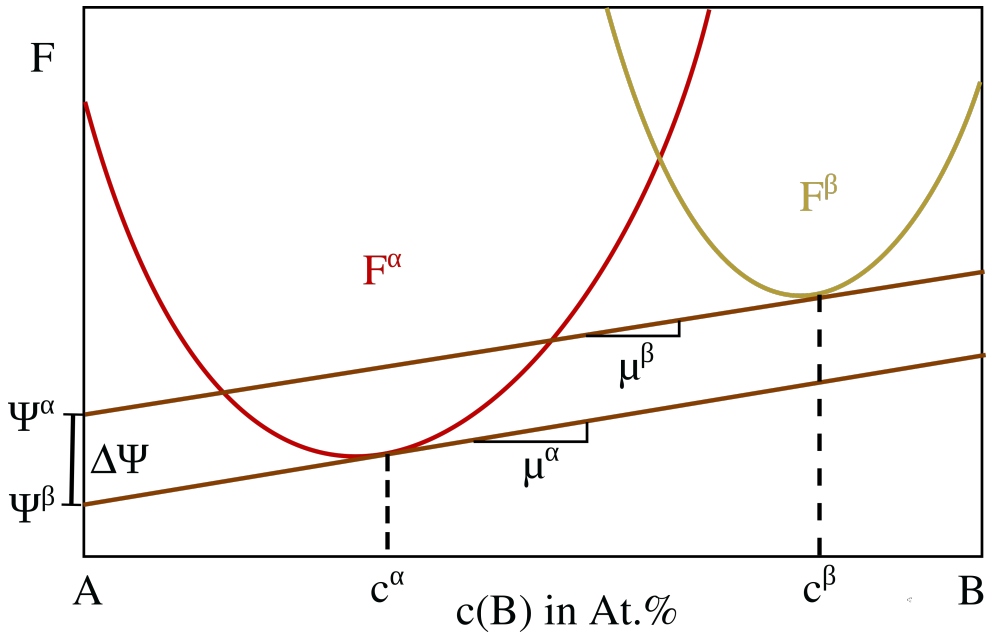

Figure 2.14.: A schematic illustration of the relationship between the free energy F, the chemical potential μ, the concentration c^α, and the grand chemical potential Ψ in a binary system with two phases in non-equilibrium.

one mole, the concentration of i-th component c_i^α in one phase can be used to calculate the chemical potential of this phase μ_α

$$\mu_i^\alpha = \left.\frac{\partial F}{\partial c_i^\alpha}\right|_{T,V}. \tag{2.22}$$

The chemical potential thus defines the slope of tangent at a given concentration in the free energy curve. And the grand chemical potential of one phase in a system is reformulated as

$$\Psi(\mu_i, T, V) = F(c_i^\alpha(\mu_i), T, V) - \sum \mu_i c_i^\alpha(\mu_i). \tag{2.23}$$

A schematic illustration of the relationship between the free energy F, the chemical potential μ, the concentration c^{α}, and the grand chemical potential Ψ in a binary system with two phases is depicted in Fig. 2.14. The chemical potential μ_{α} and μ_{β} describe the slope

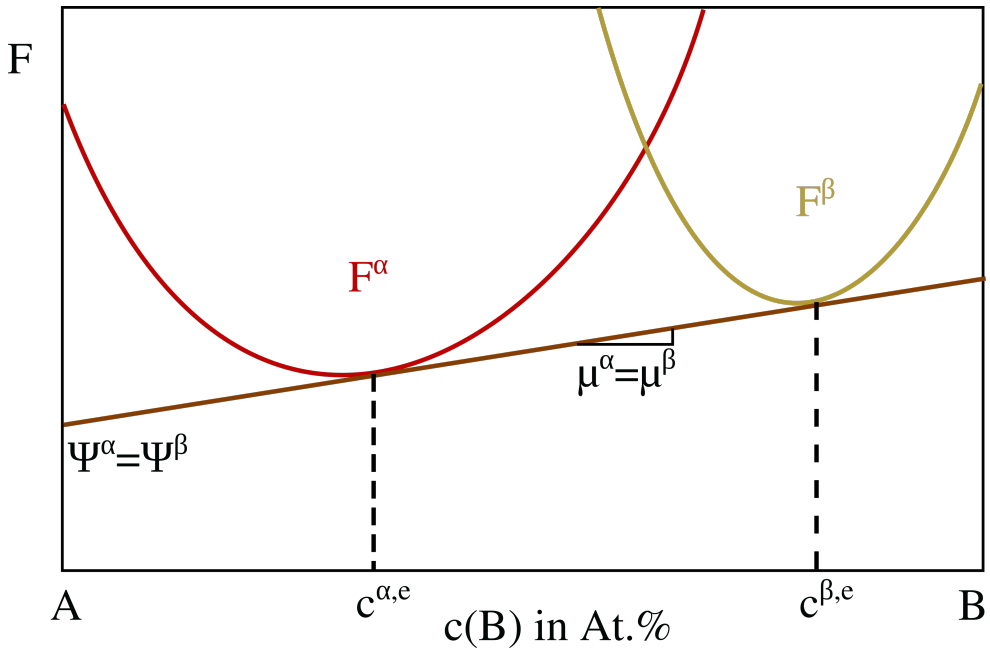

Figure 2.15.: A schematic illustration of the relationship between the free energy F, the chemical potential μ, the concentration c^{α}, and the grand chemical potential Ψ in a binary system with two phases in equilibrium.

of tangent in individual free energy curve at the concentration c^{α} and c^{β}, respectively. The y-intercept of tangent is the grand chemical potential Ψ and the difference in Ψ between two phases $\Delta\Psi$ provides the driving force for the phase transformation between them. During the phase transformation, $\Delta\Psi$ decreases, and until $\Delta\Psi = 0$, two phases will reach equilibrium. As illustrated in Fig. 2.15, the free energy curves of two phases have a common tangent. It indicates the conditions for two phases in equilibrium:

$$\mu^{\alpha}(c^{\alpha,e}) = \mu^{\beta}(c^{\beta,e}) \tag{2.24}$$

$$\Psi^{\alpha} = \Psi^{\beta} \tag{2.25}$$

Through the twice Legendre transformations, the internal energy $U(Ni, S, V)$ was transferred via the free energy $F(T, V, Ni)$ to the grand chemical potential $\Psi(T, V, \mu)$. This transfer from one thermodynamic potential to another enables the efficient calculation of the total energy of a system using thermodynamic data sets.

2.5. Literature review

In the following, a literature review of the numerical and experimental studies on the solidified microstructure of three alloy systems considered in the present work is given. The

focus is placed on recent studies of microstructural evolution during a eutectic transformation or peritectic transition and their underlying mechanisms. In addition, some current challenges in the study of phase field simulations on these two phase transformation processes are mentioned as well.

2.5.1. High-strength steel (Fe-based alloy)

High-strength steels (HSS) within the peritectic composition range are used in a broad variety of engineering applications due to its outstanding mechanical properties [77, 78, 79]. However, the defects generated by the peritectic transition during solidification, such as surface depressions, cracks, and breakouts, have a crucial damage on mechanical properties and thereby limit the utilization of steels [80, 81, 82, 83]. In order to avoid these defects in steels, numerous investigations on the microstructural evolution in peritectic transition have been conducted in the past decades.

The peritectic phase transition in carbon steel involves the peritectic reaction ($L+\delta \rightarrow \gamma$) and subsequent peritectic transformations ($L \rightarrow \gamma$ and $\delta \rightarrow \gamma$). Many different mechanisms have been proposed via experimental observations to explain the details of this phase transition. Shibata et al. [54] investigated the peritectic transition in carbon steel by using a confocal scanning laser microscope (CSLM) and proposed that the growth of the γ phase is not controlled by carbon-diffusion but by either a massive transformation or solidification direct from the liquid. In the study of peritectic transition, Griesser et al. observed three different modes, including a diffusion controlled mode, a cellular/dendritic peritectic transformation mode, and a massive transformation mode, by the use of a concentric solidification technique [53]. Nassar et al. [84] experimentally observed that surface tension plays a vital role in the governing mechanism of γ phase. Owing to the complexity of the peritectic transition, the explanation about the growth mechanisms is not entirely consistent.

Considering the daunting task of statistical and theoretical investigations by precisely controlled experiments, it is of great significance and feasibility to gain insight into the peritectic transition by using computational materials simulations. The phase-field model has been proven to be a powerful modeling technique to simulate the microstructural evolution in many alloy systems [29, 85, 45], including peritectic alloys. In addition, the peritectic transition in carbon steels is explored by phase-field modeling to clarify its underlying growth mechanism [37, 86, 36]. Ohno and Matsuura [39] investigated the γ growth at different undercoolings by using phase-field model and confirmed previous experimental observations proposed by Hillert [71] that the re-melting of δ phase in the vicinity of triple junction affects the peritectic reaction rate. This phenomenon has been also confirmed by other phase-field modeling studies [87, 38]. Owing to their focus on the mechanisms of peritectic reaction, these studies investigated the growth of γ phase on a planar δ phase at different undercoolings in 2-D simulations. However, there is a paucity of researches discussing the curvature effect of δ particle on the growth of γ phase as well as on the growth process after the complete engulfment of δ particle. Moreover, in comparison with 2-D simulations, the curvature effect in an extra direction in 3-D should also be taken into consideration. As a supplement to the work of Ohno et al, we presently explore the morphological evolution of γ phase on a spherical δ particle in 2-D and 3-D

simulations. In the most of above mentioned studies, more attention were paid to the peritectic transition at different undercoolings, while there is still a gap in research on the peritectic transition caused by supersaturation. In the past decades, the static contact angle is determined by the thermodynamic equilibrium at the triple junction between three distinct phases, described by Young's law. However, the dynamic contact angle deviates from the Young's law under the influence of the interface motion, which is observed in several experimental and numerical observations about spreading of fluids [88, 89, 90]. Similarly, the occurrence of the phase transition is accompanied with the movement of interfaces. Hence, the dynamic contact angle may also deviate from Young's law during the phase transition. In the previous study by Ohno and Matsuura, the measurement methods of the dynamic contact angle cannot determine the contact angle precisely, e.g. the value of the contact angle is significantly affected by the different selecting criteria [39]. In order to better explore the dynamic contact angle in peritectic transition, a novel measurement method for a dynamic contact angle should be proposed.

2.5.2. Lightweight and recyclable materials (Al-based alloy)

Modern lightweight and recyclable metals show a great potential for a broad variety of engineering applications [91]. Because of the outstanding thermodynamic and lightweight properties, as well as the economic cost, Al-based alloys play a crucial role in railway, shipbuilding, automotive and aerospace industries [92, 93, 94, 95]. However, the utilization of the Al-based alloys is limited by their inferior mechanical properties. To cope with this limitation, a number of methods, such as structure design [95, 96, 97] and solid solution strengthening [98, 99, 100, 101], have been reported over the past years. In some references, for instance, Al-alloys have been fabricated into hollow structures [96, 97] and sandwich panels [95], while other researchers have mixed the Al-matrix with a solid solution, such as a carbon nanotube [98, 99], silicon carbide [100] or graphite [101] for microstructural enhancement. In the present study, we focus on an Al-alloy, which is enhanced with graphite particles. The mechanical properties of the alloy are influenced by the interfacial microstructure and the production of intermetallic compounds. In this binary Al-C system, which functions as a sole intermetallic compound, the aluminum carbide (Al_4C_3) appears at the graphite-aluminum interface, with an orientation angle, caused through the reaction between aluminum and carbon.

As observed in a large amount of experiments in literature [98, 102, 103, 104, 105], the aluminum carbide has a needle-like morphology at the graphite-aluminum interface. Owing to the influence of this needle-like structure, the aluminum carbide crystal becomes brittle. In addition, the aluminum carbide is recognized as highly sensitive to moisture contact [102], which gives rise to a degeneration of the microstructural properties of this composite. Thus, the formation of Al_4C_3 should be avoided [106, 107]. Pech-Canul et al. have reported that Si, as an addition to the Al-C system, is known to reduce the tendency towards the formation of aluminum carbide in C-Al-Si composites [108]. Furthermore, Zhang et al. and Lacom et al. have proposed that a high degree of graphitisation of the fibers leads to a suppression in the nucleation of Al_4C_3 [105, 109]. However, from the experimental results [98, 102, 110, 111], the formation and growth of Al_4C_3 are always with an unknown and seemingly random orientation (see Fig. 2.16(b)) at the Al-C interface.

In previous studies, more attention was paid to the formation of this intermetallic phase and to the influence on the mechanical properties, but the mechanisms of the growth orientation as well as the influence of this special morphology on the microstructural properties were not fully revealed. It is noteworthy that Bakshi et al. [98] provided an explanation for the orientation angle of Al_4C_3 in aluminum-carbon composites. By analyzing the crystal structure of Al_4C_3, it was clarified that there is no evident orientation relationship between Al_4C_3 and CNTs (carbon nanotubes). Kleiner et al. [112] studied the dependence of the aluminum carbide formation on the diamond crystallographic orientation. According to the two researches above, the underlying causes for the selection of the orientation angle of the intermetallic phase are still not clear. For other similarly oriented composites, such as TiO_2, the growth orientation was explored by Liu and Aydil [113]. In the FESEM (field emission scanning electron microscopy) images, they observed that the orientation of TiO_2 nanorods is in a narrow range close to the normal direction of the substrate. Yet, the clarification about this orientation angle was not further addressed in their study. In the investigations on the dendrite in directional solidification, Akamastsu and Ihle [114] focused on the quantitative dependence of the tilt angle on various relevant parameters, such as temperature gradients, pulling velocities, dendrite spacings, and the orientation of the crystal. Deschamps et al. reported that the growth directions of cellular or dendritic microstructures stand between the temperature gradient and a preferred crystalline orientation [115]. However, every dendrite in these directional solidification samples grows with the same tilt angle, which is in sharp contrast to the diverse orientations of Al_4C_3 [98], which are less clearly understood.

Due to the difficulty of statistical and theoretical investigations by carefully controlled experiments, it is of great significance and feasibility to shed light on the formation of Al_4C_3, by using computational material simulations. Monte Carlo [116] and front-tracking [117, 118] methods have been used for the research on the intermetallic alloys. Molecular dynamics (MD) investigates the intermetallic particle on the microscale and requires a high amount of computational effort. Beyond these approaches, phase-field (PF) models are capable of quantitatively analyzing the complex dynamics of the interface. In the present work, we use a phase-field model with inputs from thermodynamical databases to investigate the growth of the aluminum carbide at the graphite-aluminum interface [22]. In the past years, the phase-field method has proved to be a powerful modeling technique to simulate the growth of the intermetallic phase [27, 119, 120, 121, 122]. Wang et al. studied the evolution of the Mg_2Si from two aspects: diffusion and reaction, by using a phase-field model [123]. Park et al. investigated intermetallic compounds in the Cu/Sn system under electromigration [124]. In combination with an appropriate anisotropic equation, this simulation method can be applied to study the orientation selection in the phase evolution. Haxhimali et al. investigated the dendritic evolution in the Al/Zn system and demonstrated from the crystallographic aspect, that primary dendritic growth directions are a function of the composition-dependent anisotropy parameters [125]. As a supplement to the work of Haxhimali et al., we presently clarify the orientation selection in the phase transition by using thermodynamic and kinetic analyses. Xing et al. scrutinized the orientation of columnar dendritic growth in directional solidification [126]. In their investigation, the effect of primary dendrite orientation on the growth behavior of secondary sidebranches was discussed in detail. Tourret et al. [127] systematically investigated the grain growth

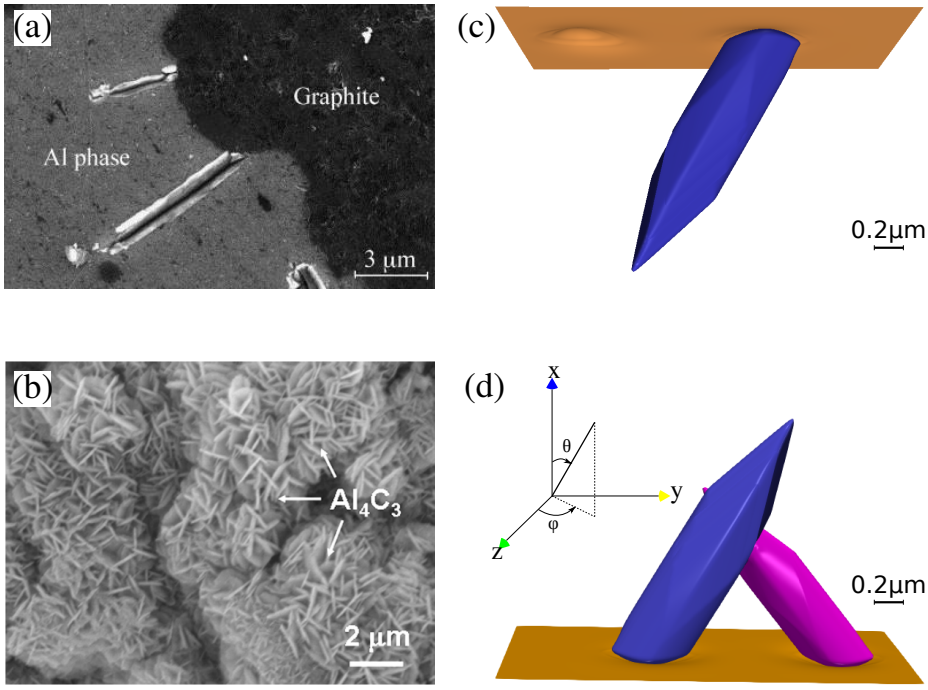

Figure 2.16.: (a) SEM micrograph of Al_4C_3 phases in an Al/C composite [102], reuse with permission, copyright 2007, Elsevier. (b) SEM image of a fracture surface of an Al-C-Si composite, showing clusters of Al_4C_3 needles [98], reuse with permission, copyright 2009, Elsevier. (c) and (d) are the simulation results of the needle-like Al_4C_3 phase, with an orientation angle on the Al/C interface, as part of the present work.

competition arising from different orientations. But the mechanism, which is responsible for the grain orientation, is not elaborated in detail. Demange et al. simulated the ice needle in three dimensions, using a modified phase-field model [128]. In their study, a surface tension anisotropy function is adopted to simulate the needle-like structure with a smooth tip. In contrast to the ice needle, the tip of the needle-like structure of Al_4C_3 is sharp. The equilibrium shape of this needle-like structure in principle can be determined in principle by constructing a crystalline anisotropy for the interfacial energy. In addition to the surface energy anisotropy, the kinetic anisotropy also has an impact on the crystal growth, as reported particularly by Karma and Rappel [129], McFadden et al. [130], and Sekerka [131]. Therefore, we use the phase-field method in combination with both surface and kinetic anisotropies to simulate the intermetallic phase growth.

In the present work, we cast light on the growth mechanism of the carbide Al_4C_3, with different orientation angles in the Al–C system, by using a PF method. The objective of our research is to show how the orientation angles influence the growth behavior of Al_4C_3, and which parameters have an impact on the critical orientation angle. By using the PF method, we simulate the evolution of a single intermetallic phase as well as the interaction of two adjacent particles. Through analyzing the concentration distribution, we clarify the underlying physics for the growth behaviors of Al_4C_3 with different orientation angles.

2.5.3. High-temperature structural materials (Ti-based alloy)

In past decades, Mo-Si-based alloys have drawn increasing attention due to its potential as alternative materials to Ni-based superalloys for high temperature structural applications [132, 133]. Besides good creep resistance and high melting point, Mo-Si-based alloy exhibits a significant reduction in density, which is a considerable advantage compared to Ni-based alloy [134]. However, inadequate oxidation resistance, especially at intermediate temperature below 1000 °C, is still a challenge for its industrial utilization. To address this issue, Schliephake et al. developed a two-phase eutectic Mo-Si-Ti alloy that shows great potential [4] for industrial application. On the basis of the work [4], Obert et al. found a novel eutectic-eutectoid two-phase Mo-Si-Ti alloy that shows both outstanding oxidation resistance and sufficient creep resistance [135]. In these alloys, the $Ti(Mo)_5Si_3$ and β(Mo,Si,Ti) lamellae, formed during the solidification process, play a vital role in the oxidation as well as in the creep behavior. Therefore, it is meaningful to systematically study the morphological evolution of lamellae in Mo-Si-Ti alloy. According to the previous work by Yang et al. [136], lamellae microstructures can be produced either by eutectic transformation ($L \rightarrow Ti(Mo)_5Si_3 + \beta(Mo,Si,Ti)$) or by a quasi-peritectic four-phase reaction ($L + Mo(Ti)_3Si \rightarrow Ti(Mo)_5Si_3 + \beta(Mo,Si,Ti)$). Hence, in the present study, we focus on this lamellae growth produced by an eutectic transformation as well as by a four-phase reaction. It is a daunting task to investigate the phase transformation statistically and theoretically by carefully controlled experiments. Therefore, it is of great significance and feasibility to shed light on the growth of the $Ti(Mo)_5Si_3$ and β(Mo,Si,Ti) lamellae, by using computational materials simulations. In the current work, we investigate the microstructural evolution of eutectic lamellae in Mo-Si-Ti alloy under different supersaturation of melt and with various lamellar spacings by using phase-field modeling. The aim is to construct a microstructure selection map for different growth morphologies. In addition, the understanding of the influence of interfacial energy on the solidification morphology, especially from experimental studies, is considerably limited, since an accurate measurement of interfacial energy is almost impossible in experiments. The role of interfacial energy in solidification morphology will be studied in the present work by simulations.

The lamellar microstructure of $Ti(Mo)_5Si_3$ and β(Mo,Si,Ti) can also form via a four-phase reaction. Based on the organic alloy solidification experiments [137], Podolinsky et al. proposed a two-step eutectic formation mechanism: initially two different phases nucleate independently in the melt and then the eutectic structures form after the neighboring nuclei contact with each other. In analogy with this eutectic mechanism, it is very likely that the four-phase reaction consists of following steps: (i) Two solid phases ($Ti(Mo)_5Si_3$ and β(Mo,Si,Ti)) nucleate at the surface of $Mo(Ti)_3Si$ independently. (ii) Two peritectic transitions occur in the vicinity of two triple junctions, namely $L/Ti(Mo)_5Si_3/Mo(Ti)_3Si$ and L/β(Mo,Si,Ti)/$Mo(Ti)_3Si$. When $Ti(Mo)_5Si_3$ and β(Mo,Si,Ti) are close together, the four-phase reaction takes place subsequently. (iii) The four-phase reaction ends after these two phases contact with each other and the eutectic transformation happens. Therefore, the lamellae microstructure resulting from the combined effect of these reactions exhibits differences compared with that formed in a primary eutectic transformation. In the recent decades, multi-phase-field (MPF) method is employed to investigate the morphological evolution during the solidification process, such as ternary eutectic transformation [138, 139,

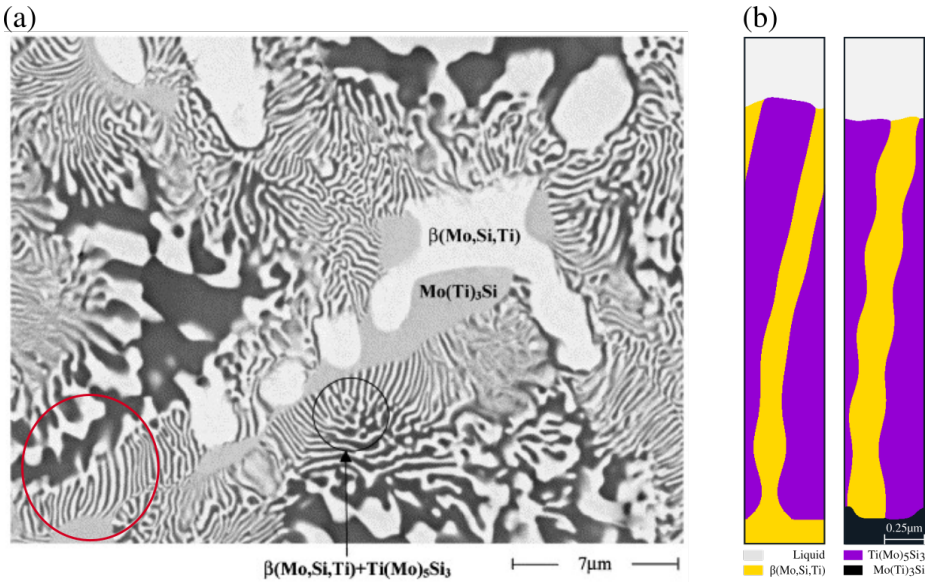

Figure 2.17.: (a) A back scattered image of the as-cast microstructure of the $Mo_{40}Si_{20}Ti_{40}$ alloy. Reprinted from [136]. (b) The simulation results of a bending growth of lamellae, as part of the present work.

140]. Rahul et al. studied the microstructural evolution in the solidification of undercooled high entropy alloys by using MICRESS [141]. In addition, MPF method is widely applied for the study of grain growth. Using the same MPF approach, Park et al. investigated the epitaxial effect on the grain structure of an additively manufactured AlSi10Mg alloy [142]. Apel et al. explored the motion of grain boundary under the particle pinning effect [143]. Eiken proposed a precise analytical solution to the tri-crystal problem and predicted anisotropic grain growth by MPF simulations [144]. Kundin et al. [145] scrutinized a four-phase reaction in Al-Cu-Ni system. They focused on the effect of heterogeneous nucleation of fourth phase on the final morphology. The microstructural evolution of lamellae produced by four-phase reaction and the differences of lamellae growth between eutectic transformation and four-phase reaction have not yet been examined. Moreover, from results in experiments, some lamellar pairs are observed to show a bending growth at the surface of $Mo(Ti)_3Si$, as marked by a red circle in Fig. 2.17(a). The mechanism behind this phenomenon is unknown and worth being explored in detail. The objective of our research is to explore the influence of different solidification conditions on the lamellae microstructure in these two distinct phase transformation processes.

3. Phase-field method

3.1. Historical development of phase-field method

The fundamental concept of describing the transition region between two phases with a diffuse area was first proposed by van der Waals approximately 140 years ago [146]. This notion was further extended in the middle of the last century through the use of an order parameter to describe superconductors, leading to the Ginzburg-Landau functional theory [147]. The order parameter describes the state of the respective phase. The evolution of the order parameter was derived by Cahn and Hilliard [148, 149, 150, 151] and later by Allen and Cahn [152] based on the Ginzburg-Landau-type energy functional. The evolution equation is a partial differential equation that describes the transformation from one phase to another due to the minimization of the total energy in the system.

A precursor version of the phase-field method can be attributed to the models by Halperin et al. [153] from 1974. These models describe the temporal evolution of conserved and non-conserved order parameters based on the Ginzburg-Landau functional. In particular, the approach described as "case C" or "model C" in [153, 154] forms the basis for current phase-field models. Wheeler and his co-authors extended the existing one-dimensional models for pure materials to two dimensions, both for calculating spinodal phase separations [155] and for the growth of thermal dendrites [156]. In 1985, Collins and Levine [157] linked the evolution equation of the order parameter to the diffusion equation of temperature, enabling the simulation of temporal and spatial growth of a thermal dendrite in subsequent works. Based on their work, Kobayashi [158] published the first large-scale simulation of a thermal dendrite in a two-dimensional domain of 300 $\times$ 300 cells in 1993. Through an extension to a binary system and coupling the evolution equation of the order parameter with the diffusion equation of concentration, Karma et al. [16] simulated binary eutectic growth using the phase-field method. Various thermodynamically consistent models for multiphase systems have been developed throughout this progress. In [17], Wheeler and his co-authors draw a comparison between their thermodynamically consistent phase-field model and their own earlier works [155, 156]. In [19], Tiaden et al. compare their multiphase approach for solid-phase diffusion with an earlier work by Wheeler et al. for a binary two-phase model and demonstrate the equivalence of the two approaches for specific special cases. Further multiphase field models have been published by Steinbach et al. [18], Garcke et al. [159], and Nestler et al. [20], allowing the simulation of the interrelationship between two different phases. As a subsequent extension of multiphase field models, models for the solidification of systems with multiple components were developed [160, 139, 161, 162, 163]. Garcke et al. demonstrate the validity of their approach [160] for special cases through a comparison with classical models featuring a sharp phase transition, as well as with earlier works by

Penrose et al. [164] and Caginalp et al. [165]. In their work from 2005 [139], Nestler et al. present a thermodynamically consistent multi-component multiphase field model and demonstrate its applicability for ternary systems in a three-dimensional domain. This model encompasses formulations for interfacial energy anisotropy as well as for kinetics.

The increasingly complex models to describe phase transformation processes demand growing computational resources. The size of simulation domains is constantly increasing to represent multicomponent and multiphase systems in representative volume elements. The influence of the domain size on simulation results is demonstrated in [166]. To reduce the computational effort required, numerous optimizations of the published models have been conducted [167, 129, 26, 168, 169].

In addition to these and further optimizations for more efficient model computations, the investigated models have also been advanced, bringing model-specific effects increasingly into focus. For instance, Wheeler et al. [156], Boettinger et al. [170], and several other authors [171, 172, 173] examined the 'solute trapping effect' arising due to artificially enlarged boundary regions, particularly pronounced at the solidification front where diffusion coefficients between solid and liquid phases often significantly differ by several orders of magnitude. To minimize the deviations caused by this model-induced effect compared to models with a sharp phase transition, an 'anti-trapping current' is introduced into the evolution equation responsible for mass flow [26, 174, 175, 176]. However, this additional term, due to its complexity, leads to higher computational demands. In their works, Mullis [177] and Nestler et al. [178] investigate the occurrence of unphysical anisotropic effects, attributable to the discretization of simulation grids. On the other hand, McFadden et al. [179] and Garcke et al. [180] present a physically motivated model for the behavior of anisotropic surfaces.

Throughout the advancements, various thermodynamic potentials have been employed as driving force for phase transformation in different phase-field models. One frequently used approach is based on minimizing free energy, employed in publications such as [181, 182, 155, 183]. Another approach, pursued in [184, 164, 21], is based on maximizing entropy in the system as described by Penrose and Fife [164]. Another approach defines the driving forces for phase transformation using differences in the grand chemical potentials [185, 22]. This is caused by the fact that the chemical potentials of the involved phases are equal during a phase transition close to thermodynamic equilibrium [32, 40, 186]. By considering the grand chemical potentials, the interfacial energy and width can be described independently. This advantage allows the computationally intensive interface to be calculated with lower grid resolution and reduced computational effort. Additionally, the formulation using the grand canonical potential does not introduce additional energies in the interfacial region that could influence the results.

3.2. Phase-field model

In the present study, a phase-field model with the grand-potential formulation, which is proposed by Choudhury and Nestler [20], is used to investigate the microstructural evolution during solidification process. For an N-phase and K-component system, the bulk

free energy density of the phase α is formulated as

$$f^{\alpha} = f^{\alpha}(c_1^{\alpha}, ..., c_k^{\alpha}, ..., 1 - \sum_{i=1}^{K-1} c_i^{\alpha}), \alpha \in [1, N], k \in [1, K]. \tag{3.1}$$

The chemical potential for the α phase is written as:

$$\mu_k^{\alpha} = \frac{\partial f^{\alpha}}{\partial c_k^{\alpha}}. \tag{3.2}$$

The grand chemical potential is given by the following equation:

$$\Psi^{\alpha}(\boldsymbol{\mu}) = f^{\alpha}(\boldsymbol{c}^{\alpha}(\boldsymbol{\mu})) - \langle \boldsymbol{\mu}^{\alpha}, \boldsymbol{c}^{\alpha} \rangle, \tag{3.3}$$

where the concentration vector is defined as $\boldsymbol{c}^{\alpha} = (c_1^{\alpha}, ..., c_{K-1}^{\alpha})$ and the chemical potential vector is written as $\boldsymbol{\mu}^{\alpha} = (\mu_1^{\alpha}, ..., \mu_{K-1}^{\alpha})$. When the phases are in thermodynamic equilibrium, the chemical potential of each phase is equal to each other, hence the chemical potential vector can be described as $\boldsymbol{\mu}^{\alpha} = \boldsymbol{\mu} = (\mu_1, ..., \mu_{K-1})$. The mathematical symbol $\langle , \rangle$ represents a scalar product.

In this model, we introduce an order parameter φ_{α} to represent the local volume fraction of the α phase, whose value characterizes the phase state of the system temporally and spatially. In addition, a diffuse interface is used to separate two distinct phases α and β. Therefore, we set the order parameter $\varphi_{\alpha} = 1$, $0 < \varphi_{\alpha} < 1$, $\varphi_{\alpha} = 0$ in the bulk phase α, in the diffuse interface, and in other phases, respectively. The phase-field vector $\boldsymbol{\varphi} = (\varphi_1, ..., \varphi_N)$ is applied to characterise the phase state of the system. The grand chemical potential in the diffuse interface is interpolated in terms of the individual phases as

$$\Psi(\boldsymbol{\varphi}, \boldsymbol{\mu}) = \sum_{\alpha=1}^{N} \Psi^{\alpha}(\boldsymbol{\mu}) h(\varphi_{\alpha}), \tag{3.4}$$

where $h(\varphi_{\alpha})$ is a cubic interpolation function defined as $h(\varphi_{\alpha}) = \varphi_{\alpha}^2(3 - 2\varphi_{\alpha})$ and satisfies $h(0) = 0$ and $h(1) = 1$. With the aid of Eq. (3.3), we differentiate both sides of Eq. (3.4) with respect to μ_i yielding

$$\boldsymbol{c}(\boldsymbol{\varphi}, \boldsymbol{\mu}) = \sum_{\alpha=1}^{N} \boldsymbol{c}^{\alpha}(\boldsymbol{\mu}) h(\varphi_{\alpha}), \tag{3.5}$$

where the concentration vector is defined as $\boldsymbol{c} = (c_1, ..., c_{K-1})$.

In accordance with the basic thermodynamic law, the fundamental idea of using the phase-field method to illustrate the phase transition process in a multiphase system is such as to minimize the grand potential functional $d\Omega/dt \leq 0$, which is achieved with the following formulation:

$$\Omega(\boldsymbol{\varphi}, \boldsymbol{\mu}) = \int_V \left[\epsilon a(\boldsymbol{\varphi}, \nabla \boldsymbol{\varphi}) + \frac{1}{\epsilon} w(\boldsymbol{\varphi}) + \Psi(\boldsymbol{\varphi}, \boldsymbol{\mu}) \right] dx. \tag{3.6}$$

Here, V is the volume occupied by the system, and ϵ is a length parameter, which determines the width of the diffuse interface.

The first term in Eq. (3.6) represents the gradient energy density that is formulated as

$$a(\boldsymbol{\varphi}, \nabla\boldsymbol{\varphi}) = \sum_{\alpha<\beta} \gamma_{\alpha\beta}[a_{\alpha\beta}(\boldsymbol{q_{\alpha\beta}})]^2 |\boldsymbol{q_{\alpha\beta}}|^2, \tag{3.7}$$

where $\gamma_{\alpha\beta}$ is a coefficient defining the surface energy of the α-β interface, and $\boldsymbol{q_{\alpha\beta}}$ is the generalized asymmetric gradient vector, which is written as: $\boldsymbol{q_{\alpha\beta}} = \varphi_\alpha \nabla\varphi_\beta - \varphi_\beta \nabla\varphi_\alpha$. Anisotropy of the surface energy is modelled by the factor $a_{\alpha\beta}$. In some alloy systems, the solid phase shows isotropic microstructure, hence $a_{\alpha\beta}(\boldsymbol{q_{\alpha\beta}})$ is set as 1.

The second term in Eq. (3.6) is an obstacle potential, which is expressed as

$$w(\boldsymbol{\varphi}) = \begin{cases} \frac{16}{\pi^2} \sum_{\alpha<\beta} \gamma_{\alpha\beta}\varphi_\alpha\varphi_\beta + \sum_{\alpha<\beta<\delta} \gamma_{\alpha\beta\delta}\varphi_\alpha\varphi_\beta\varphi_\delta & \varphi \in G \\ \infty & sonst, \end{cases} \tag{3.8}$$

where G is Gibbs simplex and defined as $G = \{\varphi \in \mathbb{R}^N : \sum_\alpha \varphi_\alpha = 1, \varphi_\alpha \geq 0\}$.

Here, the higher order term $\gamma_{\alpha\beta\delta}$ suppresses spurious contributions of third phases in the binary interfaces. The temporal phase-field evolution equation is derived by the variational approach and writes as

$$\begin{aligned} \tau_{\alpha\beta}\epsilon\frac{\partial\varphi_\alpha}{\partial t} =& \epsilon\left[\frac{\partial a(\boldsymbol{\varphi}, \nabla\boldsymbol{\varphi})}{\partial\varphi_\alpha} - \nabla\cdot\frac{\partial a(\boldsymbol{\varphi}, \nabla\boldsymbol{\varphi})}{\partial\nabla\varphi_\alpha}\right] - \frac{1}{\epsilon}\frac{\partial w(\boldsymbol{\varphi})}{\partial\varphi_\alpha} \\ & - \left[\Psi^\alpha(\boldsymbol{\mu}) - \Psi^\beta(\boldsymbol{\mu})\right]h'(\varphi_\alpha) - \lambda, \\ \alpha =& 1, \ldots N, \beta \neq \alpha, \end{aligned} \tag{3.9}$$

whereby λ is a Lagrange multiplier ensuring $\sum_{\alpha=1}^N \varphi_\alpha = 1$. The parameter $\tau_{\alpha\beta}$ is a relaxation constant at the α/β interface. Furthermore, the total amount of solute in the system is conserved. Therefore, we introduce a diffusion equation, which follows Fick's law. As the flux in the diffuse interface of phase-fields differ from the sharp interface limit, an anti-trapping current is added in this solute conservation equation. The evolution equation for the concentration fields is derived as [187, 22]

$$\frac{\partial \boldsymbol{c}}{\partial t} = \nabla\cdot\left[\boldsymbol{M}(\boldsymbol{\varphi}, \boldsymbol{\mu})\nabla\boldsymbol{\mu} - \boldsymbol{J}_{at}\right], \tag{3.10}$$

where $\boldsymbol{M}(\boldsymbol{\varphi}, \boldsymbol{\mu}) = \sum_{\alpha=1}^N \boldsymbol{M}^\alpha(\boldsymbol{\varphi}, \boldsymbol{\mu})h(\varphi_\alpha)$ is the mobility. The mobility of atoms in α phase $\boldsymbol{M}^\alpha$ is defined as

$$\boldsymbol{M}^\alpha = \frac{\boldsymbol{D}^\alpha}{\frac{\partial\boldsymbol{\mu}}{\partial\boldsymbol{c}^\alpha}}, \tag{3.11}$$

where $\boldsymbol{D}^\alpha$ is the diffusivity matrix in α phase. In this paper, we state the result as the anti-trapping current in the phase-field simulation and refer to another paper for details of the asymptotic and derivation [22]. The anti-trapping current is defined as

$$\boldsymbol{J}_{at} = \frac{\pi\epsilon}{4}\sum_{\alpha=1}^N \frac{h(\varphi_\alpha)(1-h(\varphi_\alpha))}{\sqrt{\varphi_\alpha^0(1-\varphi_\alpha^0)}}\frac{\partial\varphi_\alpha}{\partial t}\left(\frac{\nabla\varphi_\alpha}{|\nabla\varphi_\alpha|}\cdot\frac{\nabla\varphi_L}{|\nabla\varphi_L|}\right)\left((\boldsymbol{c^L}(\boldsymbol{\mu}) - \boldsymbol{c^\alpha}(\boldsymbol{\mu}))\otimes\frac{\nabla\varphi_\alpha}{|\nabla\varphi_\alpha|}\right), \tag{3.12}$$

where φ_α^0 is the lowest order solution of the phase-field equation, $\boldsymbol{c}^L$ and $\boldsymbol{c}^\alpha$ are the concentrations in liquid and solid phases, respectively.

According to Eq. (3.5), the time derivative of the concentration is written as

$$\begin{aligned}\frac{\partial \boldsymbol{c}}{\partial t} &= \sum_{\alpha=1}^{N} \boldsymbol{c}^\alpha(\boldsymbol{\mu}) \frac{\partial h(\varphi_\alpha)}{\partial t} + \sum_{\alpha=1}^{N} \frac{\partial \boldsymbol{c}^\alpha(\boldsymbol{\mu})}{\partial t} h(\varphi_\alpha) \\ &= \sum_{\alpha=1}^{N} \boldsymbol{c}^\alpha(\boldsymbol{\mu}) h'(\varphi_\alpha) \frac{\partial \varphi_\alpha}{\partial t} + \sum_{\alpha=1}^{N} \frac{\partial \boldsymbol{c}^\alpha}{\partial \boldsymbol{\mu}} h(\varphi_\alpha) \frac{\partial \boldsymbol{\mu}}{\partial t}.\end{aligned} \tag{3.13}$$

Through a combination of Eqs. (3.10) and (3.13), the evolution equation for the chemical potential is formulated as

$$\begin{aligned}\frac{\partial \boldsymbol{\mu}}{\partial t} =& \left[\sum_{\alpha=1}^{N} \frac{\partial \boldsymbol{c}^\alpha(\boldsymbol{\mu})}{\partial \boldsymbol{\mu}} h(\varphi_\alpha) \right]^{-1} \\ & \cdot \left[(\nabla \cdot (\boldsymbol{M}(\boldsymbol{\varphi}, \boldsymbol{\mu}) \nabla \boldsymbol{\mu} - \boldsymbol{J}_{at})) - \sum_{\alpha=1}^{N} \boldsymbol{c}^\alpha(\boldsymbol{\mu}) h'(\varphi_\alpha) \frac{\partial \varphi_\alpha}{\partial t} \right].\end{aligned} \tag{3.14}$$

3.2.1. Anisotropy: needle-like structure

The first term in Eq. 3.6 represents the gradient energy that is formulated as

$$a(\boldsymbol{\varphi}, \nabla \boldsymbol{\varphi}) = \sum_{\alpha<\beta} \gamma_{\alpha\beta} [a_{\alpha\beta}(\boldsymbol{q_{\alpha\beta}})]^2 |\boldsymbol{q_{\alpha\beta}}|^2, \tag{3.15}$$

where $\gamma_{\alpha\beta}$ is a coefficient defining the surface energy of the α-β interface, and $\boldsymbol{q_{\alpha\beta}}$ is the generalized asymmetric gradient vector, which is written as: $\boldsymbol{q_{\alpha\beta}} = \varphi_\alpha \nabla \varphi_\beta - \varphi_\beta \nabla \varphi_\alpha$.

The anisotropy of the surface energy density is modeled by the factor $[a_{\alpha\beta}(\boldsymbol{q_{\alpha\beta}})]^2$. In this study, we define

$$a_{\alpha\beta}(\boldsymbol{q_{\alpha\beta}}) = \max_{1 \le q \le Q} \{ \frac{\boldsymbol{q_{\alpha\beta}}}{|\boldsymbol{q_{\alpha\beta}}|} \cdot \boldsymbol{\eta}_a^q \} \tag{3.16}$$

to simulate the needle-like structure, which is elaborated in the literature [184, 188]. The vectors $\boldsymbol{\eta}_a^q$ in Eq. 3.16 are the corners of the Wulff shape and allow to model arbitrary crystal formations. In a 2D simulation, a hexagonal structure is used to simulate this needle-like structure, and the vectors of 6 corners are written as a 2×6 matrix

$$\begin{aligned}T &= \begin{bmatrix} \eta_x^1 & \eta_x^2 & \eta_x^3 & \eta_x^4 & \eta_x^5 & \eta_x^6 \\ \eta_y^1 & \eta_y^2 & \eta_y^3 & \eta_y^4 & \eta_y^5 & \eta_y^6 \end{bmatrix} \\ &= \begin{bmatrix} 1 & 1 & 0 & -1 & -1 & 0 \\ -2.5 & 2.5 & 5.5 & 2.5 & -2.5 & -5.5 \end{bmatrix}.\end{aligned} \tag{3.17}$$

For each orientation angle, we perform a matrix multiplication with a rotation matrix

$$T_{rot} = \begin{bmatrix} \cos(\theta) & \text{-}\sin(\theta) \\ \sin(\theta) & \cos(\theta) \end{bmatrix} \cdot T. \tag{3.18}$$

The ratio of long/short diagonals of this hexagon is set close to the value from the experimental observation (Fig. 2.16(a)).

3.2.2. Interface width

The width of the diffuse interface resulting from the present formalism is discussed in this section. The grand potential functional of the binary system for two phases α and β, where $\varphi_\alpha + \varphi_\beta = 1$ and $\boldsymbol{\mu}$ is expressed as μ for this binary system, is written as

$$\Omega(\varphi_\alpha, \mu) = \int_V \left[\gamma_{\alpha\beta}\epsilon|\nabla\varphi_\alpha|^2 + \frac{16}{\pi^2}\frac{\gamma_{\alpha\beta}}{\epsilon}\varphi_\alpha(1-\varphi_\alpha) + \Psi^\alpha(\mu)h(\varphi_\alpha) + \Psi^\beta(\mu)h(1-\varphi_\alpha) \right] dx. \quad (3.19)$$

In equilibrium, the movement speed of the interface is zero, reading

$$\tau_{\alpha\beta}\epsilon\frac{\partial\varphi_\alpha}{\partial t} = -\frac{\delta\Omega}{\delta\varphi_\alpha} \equiv 0, \quad (3.20)$$

For an one-dimensional setup, the equilibrium equation writes

$$2\gamma_{\alpha\beta}\epsilon\frac{d^2\varphi_\alpha}{dx^2} = \frac{16}{\pi^2}\frac{\gamma_{\alpha\beta}}{\epsilon}(1-2\varphi_\alpha) + \left(\Psi^\alpha(\mu) - \Psi^\beta(\mu)\right)\frac{dh(\varphi_\alpha)}{d\varphi_\alpha}, \quad (3.21)$$

Both sides of Eq. (3.21) multiplying by $\frac{d\varphi_\alpha}{dx}$ and integrating from $-\infty$ to x yield

$$\int_{-\infty}^{x}\frac{d\varphi_\alpha}{dx}\frac{d^2\varphi_\alpha}{dx^2}dx = \int_{-\infty}^{x}\left[\frac{16}{\pi^2}\frac{1}{\epsilon^2}\frac{1-2\varphi_\alpha}{2} + \frac{1}{2\gamma_{\alpha\beta}\epsilon}\left(\Psi^\alpha(\mu) - \Psi^\beta(\mu)\right)\frac{dh(\varphi_\alpha)}{d\varphi_\alpha}\right]\frac{d\varphi_\alpha}{dx}dx \quad (3.22)$$

Upon integrating with the conditions $\frac{d\varphi_\alpha}{dx} = 0, x \to -\infty$ and $h(\varphi_\alpha) = 0$ when $\varphi_\alpha = 0$, the following equation is obtained

$$\left(\frac{d\varphi_\alpha}{dx}\right)^2 = \frac{16}{\pi^2}\frac{1}{\epsilon^2}\varphi_\alpha(1-\varphi_\alpha) + \frac{1}{\gamma_{\alpha\beta}\epsilon}\left(\Psi^\alpha(\mu) - \Psi^\beta(\mu)\right)h'(\varphi_\alpha). \quad (3.23)$$

The interface width $\Lambda_{\alpha\beta}$ is estimated by

$$\Lambda_{\alpha\beta} = \int_{-\infty}^{\infty} dx = \int_0^1 \frac{1}{\frac{d\varphi_\alpha}{dx}}d\varphi_\alpha. \quad (3.24)$$

Based on Eq.3.23, the interface width is derived as

$$\Lambda_{\alpha\beta} = \epsilon\int_0^1 \frac{d\varphi_\alpha}{\sqrt{\left[\frac{16}{\pi^2}\varphi_\alpha(1-\varphi_\alpha) + \frac{\epsilon}{\gamma_{\alpha\beta}}\left(\Psi^\alpha(\mu) - \Psi^\beta(\mu)\right)h'(\varphi_\alpha)\right]}}. \quad (3.25)$$

When there is no driving force between the phases α and β, the difference of the grand chemical potential of two phases $\Delta\Psi = \Psi^\alpha(\mu) - \Psi^\beta(\mu) = 0$ and the interface width is expressed as

$$\Lambda_{\alpha\beta} = \epsilon\frac{\pi^2}{4}. \quad (3.26)$$

The above expression of the interface width is also valid for the phase transition with small driving force. In the same manner, the interfacial energy $\sigma_{\alpha\beta}$ is derived from Eq. (3.21) and written as

$$\sigma_{\alpha\beta} = 2\gamma_{\alpha\beta} \int_0^1 \sqrt{\left[\frac{16}{\pi^2}\varphi_\alpha(1-\varphi_\alpha) + \frac{\epsilon}{\gamma_{\alpha\beta}}\left(\Psi^\alpha(\mu) - \Psi^\beta(\mu)\right)h'(\varphi_\alpha)\right]} d\varphi_\alpha. \tag{3.27}$$

When there is no driving force $\Delta\Psi = 0$ or the contribution from the latter term in Eq. (3.27) is far less than the one from the former term, which is the typical case of equilibrium solidification, we obtain that the physical parameter interfacial energy $\sigma_{\alpha\beta}$ equals the simulation parameter $\gamma_{\alpha\beta}$. For such two cases, the parameters $\sigma_{\alpha\beta}$ and $\Lambda_{\alpha\beta}$ are independent from each other. Hence, for the sake of convenience, we set the interface width of all three interfaces with the same value in the present simulations without interfering with the physical values of the interfacial energies.

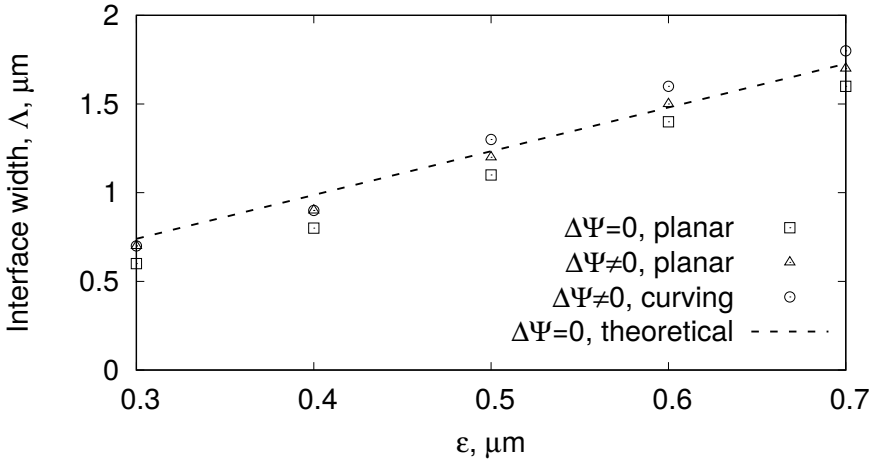

Figure 3.1.: The interface width as a function of ϵ.

In the following, we perform 1D simulations to validate the derived equation, Eq. (3.25) with ($\Delta\Psi \neq 0$) and without ($\Delta\Psi = 0$) driving force. Aiming to prove the above theoretical calculation, we simulate a binary phase transition between γ and liquid phases, as an exemplary validation. Considering the influence of the driving force on the interface width, we choose its largest value $\Delta = 0.352$ considered in the present work for the validation. Furthermore, the theoretical derivation is based on the one-dimensional setup, where the curvature effect has not been considered. In particular, non-uniform curvature may lead to different driving force during the time evolution and thus engenders a deviation of interface width from that of a planar interface. In order to show this deviation, we conduct simulations with curving L/γ interface, where the γ phase is set as a circle in the liquid phase with the smallest radius 3 µm, corresponding to the largest curvature in the current work. Fig. 3.1 illustrates the relationship between the interface width and the modeling parameter ϵ. The black dashed lines is obtained by the theoretical calculation based on Eqs. (3.26) for $\Delta\Psi = 0$. The triangle and the square symbols correspond to a planar L/γ interface with $\Delta = 0.352$ and $\Delta = 0$, respectively. The circle depicts the cases of curving L/γ interface with $\Delta = 0.352$. Under the influence of the driving force and curvature, the

interface width for the cases with same ϵ shows a relatively small difference of 0.1-0.2 μm, corresponding to 1-2 grid cells in our simulations. Good agreement between theoretical calculation and simulation results suggests that the present model can simulate the phase transformation with a specified interface width for a fixed ϵ, when the driving force is relatively small.

4. Phase diagram

For the thermodynamic consistency of phase-field simulations, correctly thermodynamic input of considered alloy system is the central task. Nowadays, the coupling to the CALPHAD (CALculation of PHAse Diagrams) database becomes a common and standard method to provide reasonable thermodynamic information, such as the bulk free energy and its derivatives, chemical potential, and thermodynamic factor, used in phase-field simulations [189, 190]. A variety of coupling approaches have been proposed in phase-field simulations of solidification process. Those coupling methods can be roughly split into two classes [191]. One is called as the "indirect method", including: i) with the help of an external CALPHAD software package to calculate the required thermodynamic information, such as the free energy density, the chemical potential as well as the equilibrium concentrations [192]; ii) approximate description of free energy curve via polynomial functions, e.g. parabolic function or Landau polynomials [193]; and iii) the use of locally linearized phase diagrams [163]. The other approaches can be addressed as the "direct method" in which the free energy functions stored in CALPHAD database are directly incorporated in phase-field equation. This method is applied in substitutional system, where the mole fraction is directly related to the concentration via a given mole density [194]. For the intermetallic compounds and interstitial diffusion, a sublattice model is used to describe its free energy [191].

In the following study, for the coupling of CALPHAD database with the phase-field model, we use a parabolic function to describe the free energy density of each phase [195, 196, 85].This coupling approach is chosen for the following reason: In CALPHAD database, the free energy density f^{α} of a single phase is written by a Redlich-Kister polynomial [197] in the form of $\sum_{i=1} c_i^{\alpha} \ln c_i^{\alpha} + \sum_{i,j}^{K} c_i^{\alpha} c_j^{\alpha}$. In the simulation, we have to calculate $\boldsymbol{c}^{\alpha}$ as a function of the diffusion potential $\boldsymbol{\mu}$ as well as the derivative of $\boldsymbol{c}^{\alpha}$ with respect to $\boldsymbol{\mu}$ in Eq. (3.14). For the free energy density written in CALPHAD approach, $\boldsymbol{c}^{\alpha}(\boldsymbol{\mu})$ has to be solved implicitly, while $\boldsymbol{c}^{\alpha}(\boldsymbol{\mu})$ is an explicit function when the free energy is written in a parabolic form. The latter one can significantly increase the computational efficiency. For a detailed comparison of the computational effort between these two approaches, we refer to Ref. [198], where an acceleration of about 10 times is achieved via the parabolic approximation for a ternary system.

For the alloy system without stoichiometric phases, such as Fe-C system, direct coupling method via a parabolic function shows a good accuracy, discussed in section 4.1. However, this coupling approach for the phase with stoichiometric composition is still challenging due to its limited data in CALPHAD database. How to correctly describe of stoichiometric phases is an open question in phase-field modeling. As two examples, we will also shed light on the coupling process of the stoichiometric phase to the thermodynamic database in Al-C, and Mo-Si-Ti system, respectively (see sections 4.2 and 4.3). By comparing the thermodynamic information from this coupling process with the data in CALPHAD

database, this coupling method shows a good thermodynamic consistency for both kinds of alloy systems with or without stoichiometric phase. The free energy functions in parabolic form obtained by the coupling approach will be used in the following phase-field simulations.

4.1. Fe-C binary system

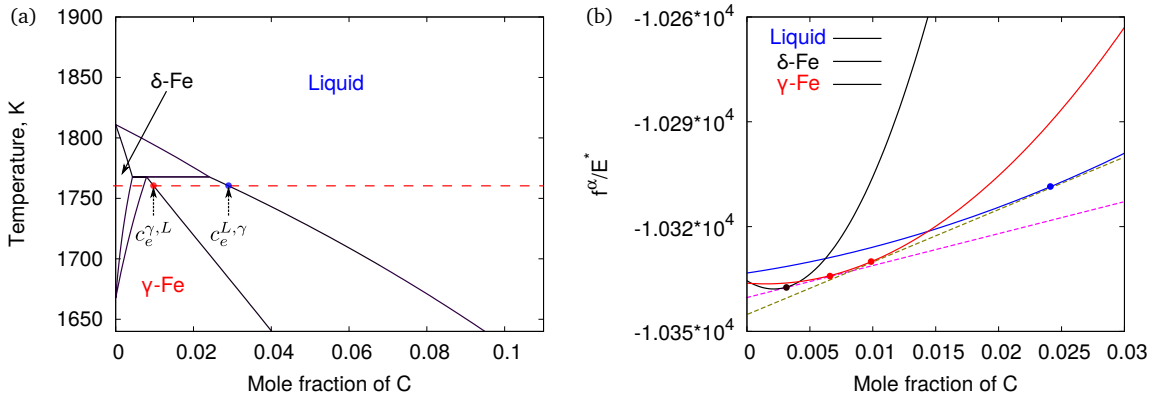

Figure 4.1.: (a) Phase diagram of the Fe-C system. We consider the reaction at the temperature $T = 1757$ K, as indicated by the red dashed line. (b) The fitted dimensionless free energy f^{α}/E^* as a function of concentration, at a fixed temperature $T = 1757$ K, where $E^* = 1 \times 10^6$ J/m^3. α = liquid, δ-Fe, and γ-Fe, respectively.

Fig. 4.1(a) shows the reconstructed Fe-C binary phase diagram based on the thermodynamic database published in Ref [199]. According to this phase diagram, γ-Fe is produced by a peritectic reaction between liquid and δ-Fe phases at the peritectic temperature $T_p = 1767$ K, $L + \delta\text{-Fe} \rightarrow \gamma\text{-Fe}$. In the present study, we simulate this peritectic reaction at the temperature T = 1757 K, which is 10 K below T_p, as displayed by the red dashed line in Fig. 4.1(a). Here, $c_e^{\gamma,L}$ and $c_e^{L,\gamma}$ represent the equilibrium concentration in γ phase with respect to liquid phase and the equilibrium concentration in liquid phase with respect to γ phase at T = 1757 K, respectively. In order to simulate this peritectic transition, we fit the Gibbs free energies of liquid-, γ-, and δ-phases based on the CALPHAD database [199], by using the least square method. The free energy functions of these three phases are written as

$$f^i = a^i c_C^2 + b^i c_C + d^i, \tag{4.1}$$

where the superscript i represents the three different phases (liquid, γ, and δ phases) and c_C is the only independent carbon concentration in this binary system. The coefficients in these fitted functions are listed in Table 4.1 and the corresponding free energy curves are displayed in Fig. 4.1(b). The thermodynamic equilibrium between two phases is given by

Phase \ Coefficients	a	b	d
Liquid	201.383	5.39038	-103.333
γ	903.633	-2.69495	- 103.362
δ	5193.1	-22.2056	-103.355

Table 4.1.: Parameters for the fitted free energy functions in Fe-C system.

the common tangent construction between two Gibbs energy curves, as illustrated by the pink or olive dashed line in Fig. 4.1(b). The equilibrium chemical potentials correspond to the slopes of the common tangent lines. This fitting method results in exact equilibrium concentrations between each pairwise phases (L/γ- and δ/γ-phase), which are in accordance with experimental data.

4.2. Al-C binary system

Fig. 4.2(a) shows the constructed Al-C binary phase diagram based on the database, which is published in Ref. [200]. According to this phase diagram, Al_4C_3 exists as a stoichiometric compound and is produced by a peritectic reaction between liquid and graphite phases, at the temperature $T_p = 2429$ K, $L + \text{Graphite} \longrightarrow Al_4C_3$. In the present case, we simulate this peritectic reaction at a temperature $T = 2423$ K, which is 6 K below T_p, as represented by the red dashed line in Fig. 4.2(a). As observed in the phase diagram, the solubility of Al in the graphite phase is almost zero at the considered temperature. Likewise, as characterized in the phase diagram, the intermetallic phase Al_4C_3 is exactly stoichiometric, and the fixed concentration of C in this phase is 3/7. The assumption of a purely stoichiometric phase leads to a "diffusion barrier", wherein the concentration is uniform and the establishment of concentration gradients is impossible, because the diffusion through this phase is prevented. According to this ideal assumption, the growth of the stoichiometric intermetallic phase therefore cannot occur. Here, we do not consider the vacancy diffusion, because of the relatively low vacancy concentration in both solid phases, typically with a value from 10^{-4} to 10^{-6} [201]. Moreover, there are no vacancies in the liquid phase.

To address the question that how the diffusion occurs in the intermetallic phase, which leads to the growth or shrinkage of this phase, we assume that there is a miscibility gap in this phase. The Gibbs free energy of the liquid phase is written as

$$f^L = a^L c^2 + b^L c + d^L, \tag{4.2}$$

where c is carbon concentration, and fitted using the least square method based on the CALPHAD database [200]. In the present phase-field model, the mobility of atoms M is illustrated as

$$M = \frac{D}{\frac{\partial^2 f}{\partial c^2}}, \tag{4.3}$$

where D is the diffusivity of atoms, f is the Gibbs free energy and c represents the concentration [202]. The Gibbs free energy functions of the graphite and Al_4C_3 phase are individually written as

$$\begin{aligned} f^G(c) =& a^G(c - c^G)^2 + d^G \\ f^A(c) =& a^A(c - c^A)^2 + d^A, \end{aligned} \tag{4.4}$$

in order to calculate the second derivative of the Gibbs free energy. Here, we assume that $c^G = 0.998$ and $c^A = 0.4143$, which is a little bit smaller than the equilibrium concentration of the graphite phase, c_e^G, and the Al_4C_3 phase, c_e^A, respectively. There are 4 unknown parameters which can be solved by the following 4 conditions: (a) $f^G|_{c=c_e^G} = f^G_{CALPHAD}$, (b) $\frac{df^G}{dc}|_{c=c_e^G} = \mu^G|_{c=c_e^G} = \mu^G_{CALPHAD}$, (c) $f^A|_{c=c_e^A} = f^A_{CALPHAD}$, and (d) $\frac{df^A}{dc}|_{c=c_e^A} = \mu^A|_{c=c_e^A} = \mu^A_{CALPHAD}$. The values of $f^G_{CALPHAD}$, $\mu^G_{CALPHAD}$, $f^A_{CALPHAD}$, and $\mu^A_{CALPHAD}$ are taken from the CALPHAD database [200]. The coefficients in the free energy functions of all three phases are listed in Table The fitted Gibbs free energy curves of the three phases are displayed in Fig. 4.2(b). The equilibrium chemical potentials correspond to the slopes of the straight lines that are obtained by connecting the circles. This fitting method results in a very small

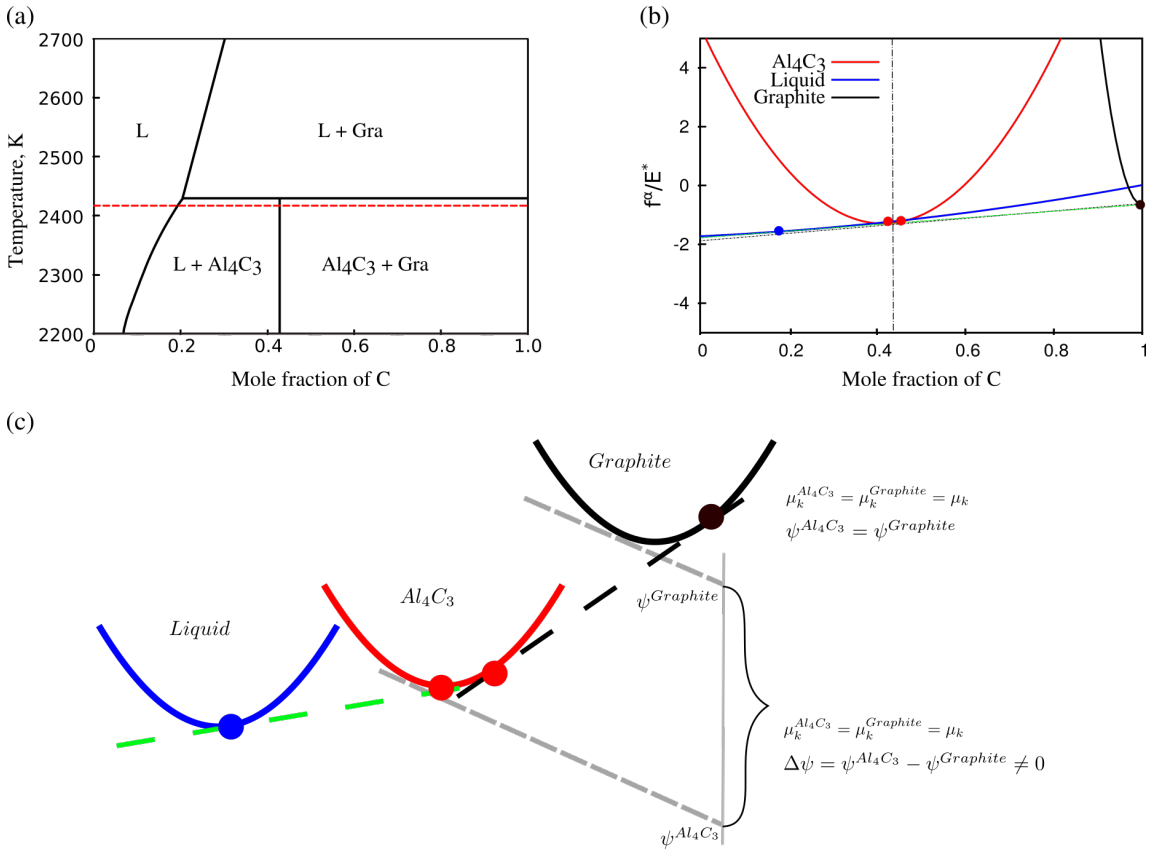

Figure 4.2.: (a) Phase diagram of the Al-C system. We consider the reaction at the temperature of 2423 K, as indicated by the red dashed line. (b) The fitted free energy f^α as a function of concentration, at a fixed temperature of 2423 K. α = liquid, Al_4C_3, and graphite, respectively. (c) Schematic illustration for the common and parallel tangent rules.

solubility range in the intermetallic layer, wherein concentration gradients are permitted. The width of this solubility range, which is controlled by c^G and c^A, affects the curvature of the parabolic curves. As mentioned in Eq. 4.3, the mobility is related to the curvature of the parabolic curves $\frac{\partial^2 f}{\partial c^2}$. Hence, the selected values of c^G and c^A impact the kinetics of the phase transition. The width of the solubility range can be optimized by comparing with the kinetic data from experiments. In addition, the concentration gradients, which are small enough, are almost in accordance with the assumption of the stoichiometric phase.

For a better understanding of the phase transition, a schematic illustration for the common and parallel tangent rules is depicted in Fig. 4.2(c). When two phases are in thermodynamic equilibrium, there is a common tangent between two Gibbs energy curves, which is given by the black or green dashed line in Fig. 4.2(c). It indicates that both the chemical potential and the grand chemical potential for the two phases are equivalent. When the two phases are not in equilibrium, the temporal movement of the interface occurs, and the corresponding driving force is the difference in the grand chemical potential, $\Delta\Psi = \Psi^\alpha - \Psi^\beta$, as illustrated by the gray dashed line in Fig. 4.2(c).

Phase \ Coefficients	a	b	d
Liquid	1.0327	0.70760	-1.7224
Al_4C_3	38.993	—	-1.2929
Graphite	684.1	—	-0.64276

Table 4.2.: Parameters for the fitted free energy functions in Al-C system.

4.3. Mo-Si-Ti ternary system

4.3.1. Isothermal solidification

According to the thermodynamic database published in Ref. [203], $Ti(Mo)_5Si_3$ and β(Mo,Si,Ti) are produced simultaneously by a four-phase reaction involving liquid and $Mo(Ti)_3Si$ phase at the temperature T_{4p} = 2221 K, L + $Mo(Ti)_3Si \rightarrow Ti(Mo)_5Si_3 + \beta$(Mo,Si,Ti). When the temperature is lower than T_{4p}, a eutectic transformation takes place forming the lamellae of $Ti(Mo)_5Si_3$ and β(Mo,Si,Ti), L $\rightarrow Ti(Mo)_5Si_3 + \beta$(Mo,Si,Ti). The formation and development of the lamellae $Ti(Mo)_5Si_3$ and β(Mo,Si,Ti) via the four-phase reaction and the eutectic transformation will be focused in this work by phase-field simulations. The corresponding thermodynamic database (tdb-file) is provided by the authors of [136, 203] (Y. Du) and used in present work. The dataset will be cross-checked in this work by calculating isothermal sections, temperature-sections, liquidus surface, and corresponding thermodynamic functions. In the following sections, we use the notations TS, MS, and β to represent $Ti(Mo)_5Si_3$, $Mo(Ti)_3Si$ and β(Mo,Si,Ti) phase, respectively. For the coupling of CALPHAD database with the phase-field model, we use a parabolic function to describe the free energy density of each phase in the present study [195, 196, 85]. However, the stoichiometric phase in CALPHAD database has a fixed composition and thus the value of the second derivative is missing in the CALPHAD database. In order to solve this problem, we assume a solid solubility in the stoichiometric phase. This assumption has been proven by several experiments. For the two considered stoichiometric solid phases in the present study, the silicon content in TS phase is not fixed at 0.375 but varies around the experimental value [204, 205]. For the MS phase, a deviation of silicon concentration from 0.25 has also been observed [205]. Therefore, the assumption of a certain solid solubility in these two phases is reasonable.

In the following study, the free energy density of liquid phase is expressed by the following function:

$$f^L = a(T)^L c_{Mo}^2 + b(T)^L c_{Mo} + d(T)^L + e(T)^L c_{Ti}^2 + g(T)^L c_{Ti} + h(T)^L c_{Mo} c_{Ti}, \qquad (4.5)$$

and fitted by the least square method in the temperature range from 2196 K to 2219 K based on the thermodynamic data in CALPHAD database. The intermetallic phase TS is exactly stoichiometric with a constant Si concentration 0.375 in CALPHAD database. Presently, we model a temperature dependent of silicon solubility in TS phase by the

following expression

$$f^{TS} = \left[a(T)^{TS}(c_{Mo} + b(T)^{TS})^2 + d(T)^{TS}\right] + n^{TS}a(T)^{TS}(0.625 - c_{Mo} - c_{Ti})^2. \quad (4.6)$$

The formulation of Eq. (4.6) consists of two parts. The first part is fitted by the least square method based on the data from CALPHAD and depicts the free energy density as a function of Mo concentration c_{Mo}. The second part models a temperature dependent solubility of Si in the TS phase, differing from other fitting methods. In the similar manner, the free energy densities of MS and β phases are written as:

$$f^{MS} = \left[a(T)^{MS}(c_{Mo} + b(T)^{MS})^2 + d(T)^{MS}\right] + n^{MS}a(T)^{MS}(0.75 - c_{Mo} - c_{Ti})^2. \quad (4.7)$$

and

$$f^{\beta} = \left[a(T)^{\beta}(c_{Mo} + b(T)^{\beta})^2 + d(T)^{\beta}\right] + n^{\beta}a(T)^{\beta}(0.9797 - c_{Mo} - c_{Ti})^2. \quad (4.8)$$

The solubility of the silicon in the β phase varies between 0 and 0.04 in the considered temperature range. The variation of the temperature dependent solubility is achieved by the n^{β}-related term. For an illustration of the thermodynamic consistency of the fitting

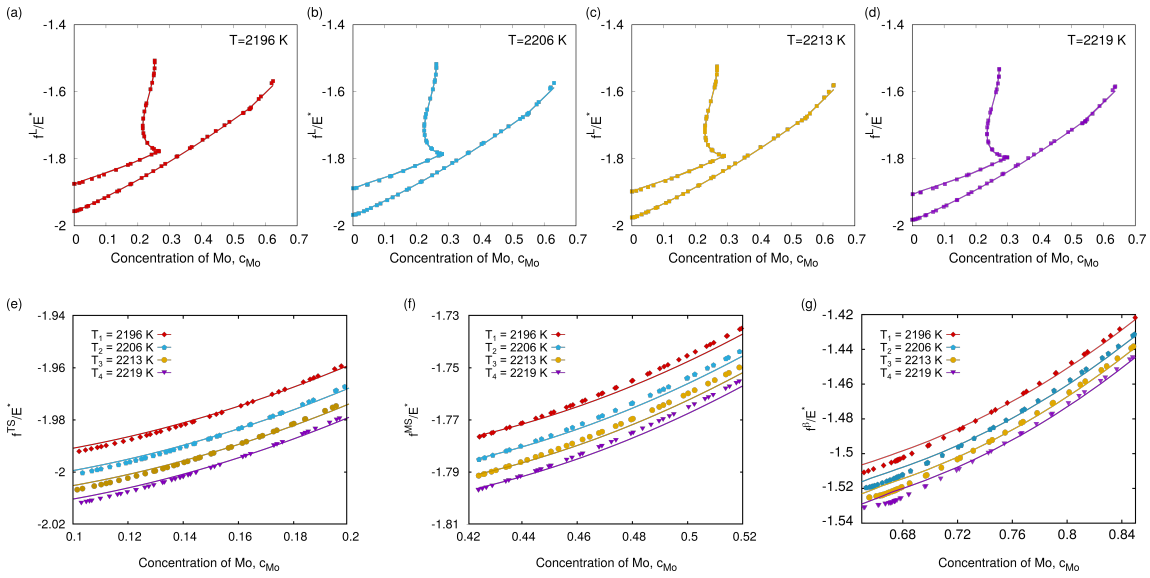

Figure 4.3.: (a) and (b) are the free energy density of TS and MS phases as a function of molybdenum for different temperatures.

method, the free energy densities of liquid phase as a function of c_{Mo} for four exemplary temperatures are shown in Fig. 4.3(a)-(d), respectively. Fig. 4.3(e) illustrates the free energy densities of TS phase for these four temperatures, while the free energy densities of MS and β phases are depicted in Fig. 4.3(f) and (g), respectively. The filled symbols represent the data from CALPHAD database and the fitted functions are depicted by solid lines. The good consistency between the fitted free energy and the CALPHAD dataset demonstrates the capability of the present fitting method in the considered temperature range. After

Phase	a	b	d	e	g	h	n
Liquid	1.994	-1.787	-1.264	2.382	-2.617	3.644	—
$Ti(Mo)_5Si_3$	1.237	-0.022	-2.015	—	—	—	10
$Mo(Ti)_3Si$	1.657	-0.349	-1.802	—	—	—	10
β(Mo,Si,Ti)	1.051	-0.544	-1.541	—	—	—	1000

Table 4.3.: Parameters for the fitted free energy functions in Mo-Si-Ti system.

the calibration of the temperature and composition dependent thermodynamic data with respect to the CALPHAD database, we apply this result to the growth of the eutectic lamellae during isothermal solidification at the temperature T = 2216 K. At this temperature, all unknowns in the free energy functions are listed in Table 4.3. The free energy landscapes of the considered phases are shown in Fig. 4.4(a)-(d) at the temperature of T = 2216 K. For a better visualization, the free energy density of the liquid phase along a particular trajectory in the ternary plot is shown in Fig. 4.4 as an example. Fig. 4.4(e) illustrates the fitted free

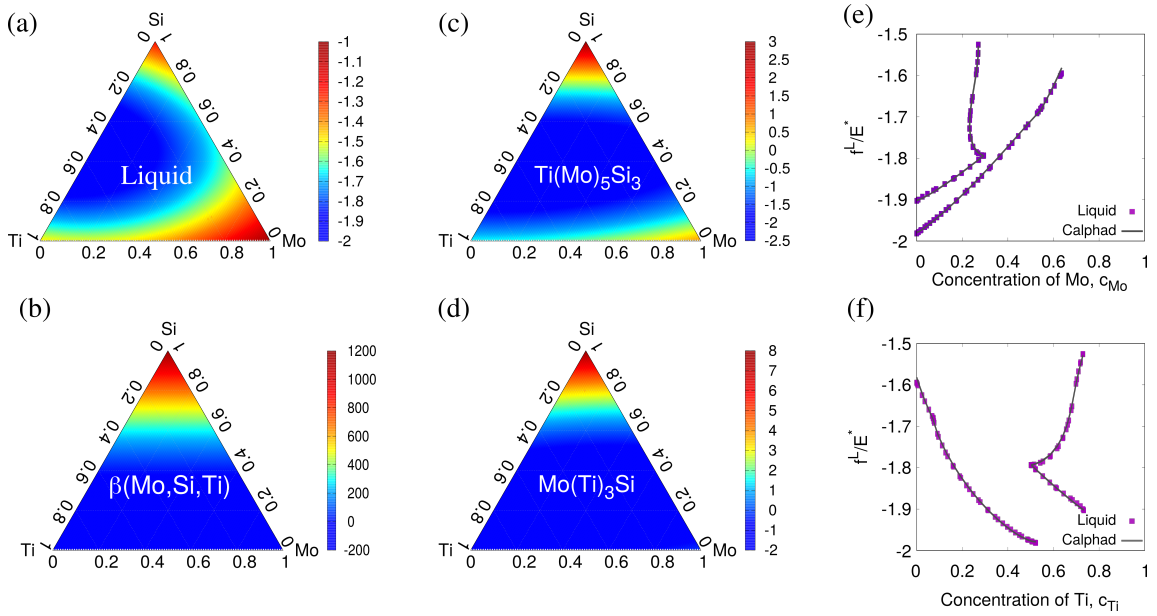

Figure 4.4.: (a)-(d) The free energy density landscape of liquid, β(Mo,Si,Ti), $Ti(Mo)_5Si_3$, and $Mo(Ti)_3Si$ phase, respectively, based on the fitted free energy functions in Eqs. (4.5)-(4.8) (red: high, blue: low). (e) and (f) display the free energy density f/E^* for the liquid phases at the temperature T = 2216 K as a function of concentration of molybdenum and of concentration of titanium, respectively, where $E^* = 1 \times 10^{10}$ J/m^3. The dashed curves represent the fitted free energy functions and the black lines corresponding to the data from CALPHAD database.

energy density for the liquid phase as a function of the concentration of molybdenum c_{Mo} by violet points. In the similar manner, the relationship between the fitted free energy and the concentration of titanium c_{Ti} is portrayed in Fig. 4.4(f). In Fig. 4.4(e) and (f), data

from CALPHAD database are represented by a gray line to verify the reliability of the fitted function for liquid phase. To further prove the thermodynamic consistency of the present method, we calculate the free energy density f/E^*, the diffusion potential with respect to molybdenum μ_{Mo}/E^* and titanium μ_{Ti}/E^*, and the grand chemical potential Ψ/E^* of the liquid phase, in comparison with the CALPHAD database, for six considered compositions, as listed in Table 4.4. In addition, we also calculated the equilibrium concentrations between three solid phases as well as the corresponding values f/E^* and Ψ/E^*, and compared them with the data from CALPHAD, as listed in Table 4.5. Fig. 4.5(a)

Composition	f/E^*			μ_{Mo}/E^*			μ_{Ti}/E^*			Ψ/E^*		
	fitted	exp.	error	fitted	exp.	error	fitted	exp.	error	fitted	exp.	error
23Mo-56Ti-21Si	-1.819	-1.819	0	1.170	1.224	4.35%	0.889	0.951	6.48%	-2.587	-2.632	1.72%
24Mo-55Ti-21Si	-1.817	-1.817	0	1.174	1.225	4.16%	0.878	0.948	7.35%	-2.581	-2.631	1.90%
25Mo-54Ti-21Si	-1.814	-1.814	0	1.177	1.226	3.98%	0.867	0.945	8.22%	-2.576	-2.629	2.02%
26Mo-53Ti-21Si	-1.810	-1.809	0.06%	1.181	1.228	3.86%	0.856	0.938	8.75%	-2.571	-2.626	2.10%
28Mo-51Ti-21Si	-1.804	-1.799	0.28%	1.188	1.231	3.54%	0.833	0.923	9.74%	-2.561	-2.619	2.22%
30Mo-49Ti-21Si	-1.796	-1.794	0.13%	1.195	1.232	3.04%	0.811	0.916	11.49%	-2.552	-2.616	2.44%

Table 4.4.: The calculated free energy density f/E^*, diffusion potentials of molybdenum μ_{Mo}/E^* and titanium μ_{Ti}/E^*, as well as grand chemical potential Ψ/E^* for liquid phase and the corresponding experimental data from [203].

	TS				MS				β			
	c_{Mo}	c_{Ti}	f/E^*	Ψ/E^*	c_{Mo}	c_{Ti}	f/E^*	Ψ/E^*	c_{Mo}	c_{Ti}	f/E^*	Ψ/E^*
fitted	0.139	0.525	-1.980	-2.661	0.461	0.313	-1.773	-2.559	0.682	0.298	-1.521	-2.336
exp.	0.140	0.485	-1.999	-2.609	0.424	0.326	-1.794	-2.609	0.674	0.285	-1.524	-2.609
error	0.660%	8.230%	0.953%	1.964%	8.64%	3.89%	1.194%	1.923%	1.152%	4.584%	0.195%	10.485%

Table 4.5.: The calculated equilibrium concentration, the free energy density as well as the grand chemical potential for three solid phases and the corresponding experimental data from [203].

shows the reconstructed isothermal section of L-TS-MS-β phase region in the Mo-Si-Ti system at temperature T = 2216 K. The violet, blue, yellow, and red lines correspond to the liquid, TS, MS, and β phases, respectively. The equilibrium concentrations calculated by the fitted free energy functions are illustrated by dashed lines. The data from CALPHAD database [203] is represented by solid lines for a comparison. As shown in Fig. 4.5(a), the β single phase region calculated by the parabolic free energy function almost overlaps with the one from CALPHAD. It implies that our fitted free energy density of the β phase in the parabolic form reproduces the silicon solubility in the CALPHAD database. As the TS and MS phases both are exactly stoichiometric in the CALPHAD database a direct reproduction of the silicon solubility in these two phases is almost impossible. In the current study, the calculated silicon concentrations in the TS and MS phase are 0.363±0.036 and 0.243±0.023, respectively, which are within the range of the experimental observation [204, 205]. However, a more quantitative calculation of the solubility in the TS and MS phases is challenging due to the lack of the sufficient experimental data.

The initial mole fractions of Mo, Ti, and Si in the TS, β, and MS phases are indicated by the black circles in Fig. 4.5(a). For the phases TS and β, their initial composition

deviates from the equilibrium concentration providing a solutal driving force for the phase

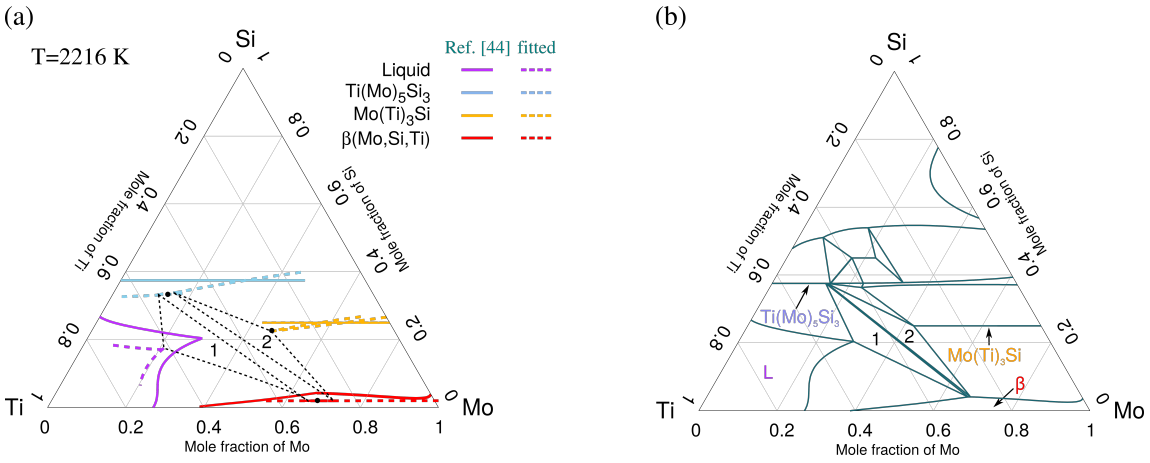

Figure 4.5.: (a) The reconstructed isothermal section of L-TS-MS-β phase region in the Mo-Si-Ti system at temperature T = 2216 K. (b) The isothermal section of Mo-Si-Ti phase diagram at temperature T = 2216 K based on the thermodynamic database [203].

transformation in the present study. The initial composition of MS phase is the equilibrium concentration of three-phase eutectoid. It is noteworthy that the difference between the fitted value and the data from CALPHAD database is caused by the assumption of the solute solubility in stoichiometric phases. The black triangles 1 and 2 in Fig. 4.5(a) depict the L-TS-β and MS-TS-β phase region, respectively, corresponding to the triangles 1 and 2 in the isothermal section of Mo-Si-Ti phase diagram in Fig. 4.5(b). A comparison between the Fig. 4.5(a) and (b) reveals that the fitted free energy functions can be used in the phase-field simulations to describe the four-phase reaction and the three-phase eutectic transformation quantitatively.

4.3.2. Directional solidification

To investigate phase transformation during a directional solidification process, the temperature-dependent free energy function of each phase need to be coupled with phase-field model. In the following section, we focus on the three-phase eutectic reaction (L $\longrightarrow$ $Ti(Mo)_5Si_3$ + β(Mo,Si,Ti)) in the temperature range from 1893 K to 1923 K.

Based on Eq. 4.5, the free energy density of liquid phase is written in a parabolic form and fitted by the least square method based on the thermodynamic data at the temperature 1893 K, 1898 K, 1903 K, 1913 K, 1918 K, and 1923 K, respectively. Similarly to the Eq. 4.6 and 4.8, the free energy function of TS and β phases in this temperature range are rewritten as

$$f^{TS} = \left[a(T)^{TS}(c_{Mo} + b(T)^{TS})^2 + d(T)^{TS}\right] + n^{TS}(0.625 - c_{Mo} - c_{Ti})^2 \tag{4.9}$$

and

$$f^{\beta} = \left[a(T)^{\beta}(c_{Mo} + b(T)^{\beta})^2 + d(T)^{\beta}\right] + n^{\beta}(0.963 - c_{Mo} - c_{Ti})^2. \tag{4.10}$$

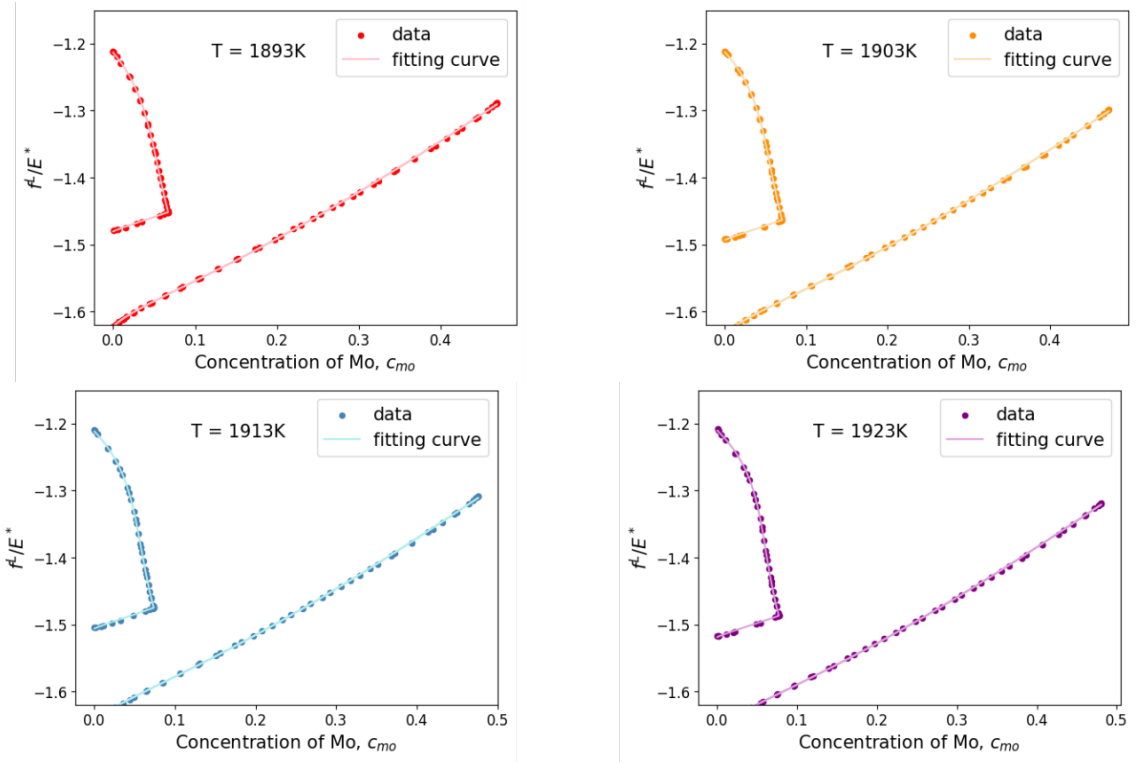

Figure 4.6.: The free energy density of liquid phase as a function of molybdenum concentration for four different temperatures:1893 K, 1803 K, 1913 K, and 1923 K.

Fig. 4.6 illustrates the free energy densities of liquid phase as a function of c_{Mo} for four exemplary temperatures. The corresponding free energy density of TS and β are shown in Fig. 4.7. A good agreement between the fitted free energy and the CALPHAD dataset reveals the capability of the present fitting method. Next, the unknown parameters in free energy functions need to be described as a function of temperature. In order to better describe the temperature-dependence of the parameters, the Eq. 4.9 need to be expanded and combined like terms

$$f^{TS} = a^{TS*}(T)c_{Mo}^2 + b^{TS*}(T)c_{Mo} + d^{TS*}(T) + e^{TS*}(T)c_{Ti}^2 + g^{TS*}(T)c_{Ti} + h^{TS*}(T)c_{Mo}c_{Ti}, \quad (4.11)$$

where

$$\begin{aligned} a^{TS*} &= a^{TS} + n^{TS} \\ b^{TS*} &= 2a^{TS}b^{TS} - 1.25n^{TS} \\ d^{TS*} &= a^{TS}b^{TS2} + d^{TS} + 0.625^2 n^{TS} \\ e^{TS*} &= n^{TS} \\ g^{TS*} &= -1.25n^{TS} \\ h^{TS*} &= 2n^{TS}. \end{aligned} \quad (4.12)$$

Here, every parameter in free energy functions is written as a power series in temperature. In the present work, two cases are considered: (c_i) in a relatively small temperature range

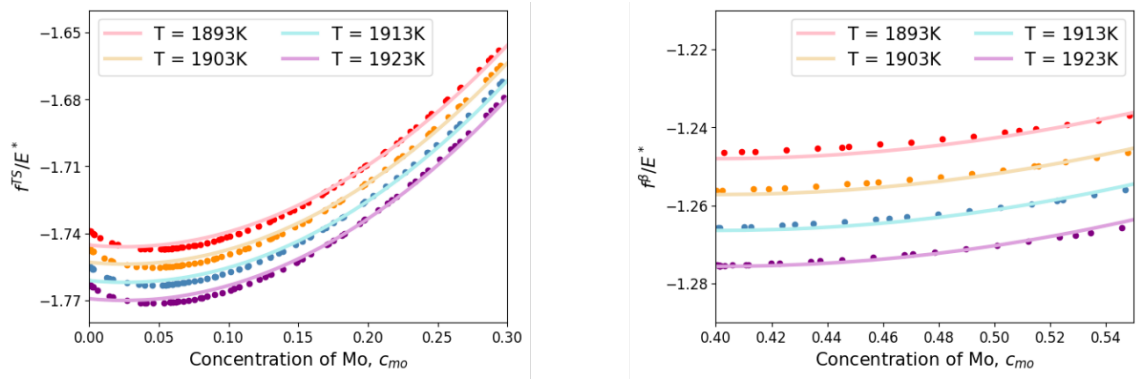

Figure 4.7.: (a) and (b) are the free energy density of TS and MS phases as a function of molybdenum concentration for different temperatures.

(about 10 K) and (c_{ii}) in a relatively large temperature range (about 30 K)), respectively. For case c_i, the temperature dependence of the parameters are fitted by a linear function,

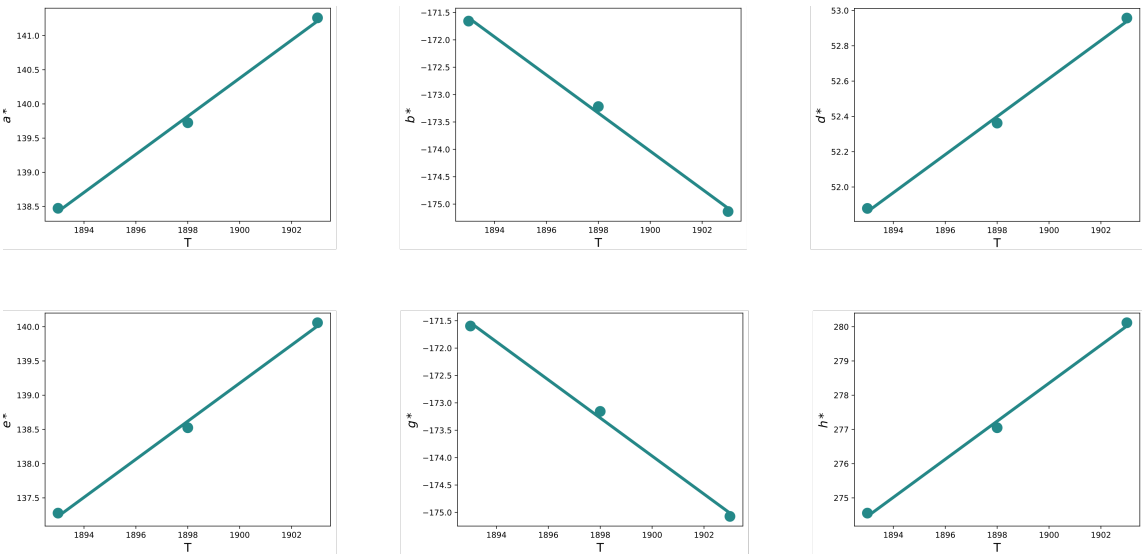

Figure 4.8.: The six coefficients in free energy function of TS phase as a function of temperature.

namely the exemplary parameter a^{TS*} is formulated as

$$a^{TS*}(T) = a_0 + a_1 T. \tag{4.13}$$

Other parameters are expressed similarly. As an example, all six coefficients in free energy expression of TS phase as a function of temperature are depicted in Fig. 4.8. In this relatively small temperature range, this fitting method by linear function exhibits a good agreement. If we consider the occurrence of this eutectic transformation in a relatively large temperature range (case c_{ii}), a higher order polynomial need to be used to describe the relationship between parameters with temperature. For this case, the exemplary parameter

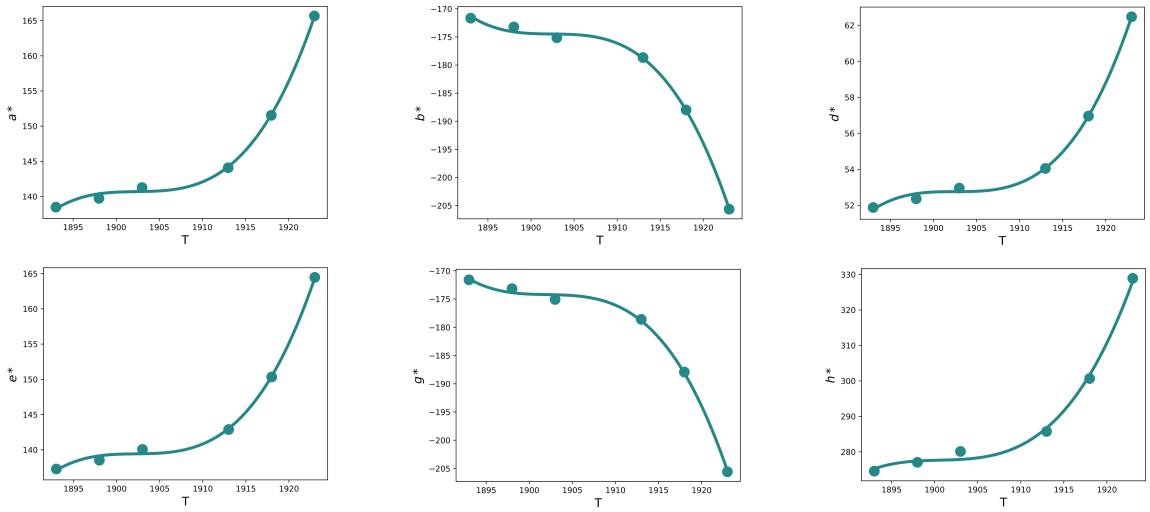

Figure 4.9.: The six coefficients in free energy function of TS phase as a function of temperature.

a^{TS*} is formulated as

$$a^{TS*}(T) = a_0 + a_1 T + a_2 T ln(T) + a_3 T^2 + a_4 T^3, \tag{4.14}$$

and all parameters of TS phase as function of temperature are illustrated in Fig. 4.9. A good consistency of this fitting process provides a reliable thermodynamic information for the forthcoming phase-field simulations. The relationship between the parameters in energy functions and the temperature for the liquid and β phases are obtained similarly and shown in Appendix. Based on these fitted free energy functions, the reconstructed isothermal section of L-TS-β phase region in Mo-Si-Ti system at temperature 1893 K, 1898 K, and 1903 K are shown in Fig. 4.10(a)-(c), respectively. The blue, yellow, and red lines correspond to the TS, liquid, and β phases, respectively. The equilibrium concentrations calculated by the fitted free energy functions are illustrated by open circle. The data from CALPHAD database [203] is represented by full circle for a comparison. As shown in Fig. 4.10(a)-(c), at every temperature the single phase regions of these three phases, which are calculated by the parabolic free energy functions, almost overlaps with the one from CALPHAD. The L-TS-β three phase region is marked by the black triangle, corresponding to the triangle in the isothermal section of Mo-Si-Ti phase diagram at 1893 K, 1898 K, and 1903 K, depicted in Fig. 4.10(d)-(f), respectively. It implies that the present fitted energy functions can be used in the phase-field simulations to investigate this three-phase eutectic transformation quantitatively.

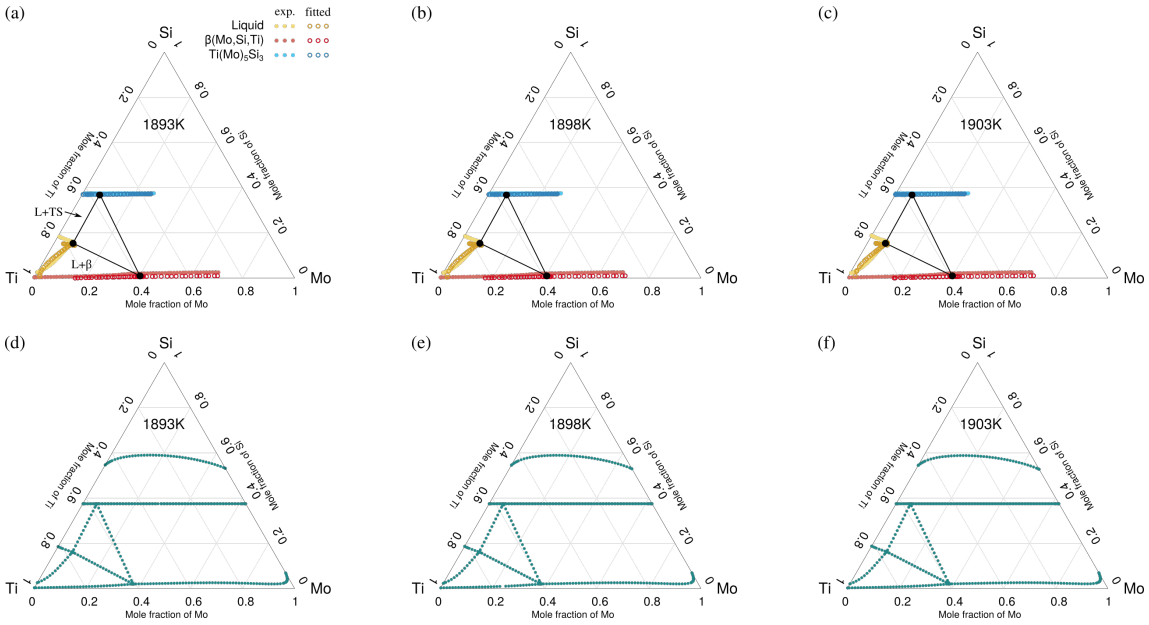

Figure 4.10.: (a)-(c) The reconstructed isothermal section of L-TS-β phase region in the Mo-Si-Ti system at temperature T = 1893 K, 1898 K, and 1903 K, respectively. (d)-(f) The isothermal section of Mo-Si-Ti phase diagram at temperature T = 1893 K, 1898 K, and 1903 K, respectively, based on the thermodynamic database [203].

5. Fe-C binary system: peritectic transition

As observed in experimental microstructures, the austenite platelet (γ) grows along the ferrite (δ)/liquid (L) interface. Aiming to explore the influencing factors of this microstructural evolution during the peritectic transition in carbon steel, we simulate isothermal peritectic solidification of the Fe-C alloy by using the phase-field model in 2-D and 3-D domains. A common agreement is reached through several studies that the peritectic transition in Fe-C alloys at low driving force (e.g. at low undercoolings) is controlled by carbon diffusion [53, 84, 206]. Therefore, the phase-field model formulation in 3-D, added with an anti-trapping current and coupled with a diffusion-equation is applied to simulate the occurrence of phase transition and the growth of intermetallic compound. In the 2-D simulations, we investigate the peritectic solidification for the following two cases: (i) on the δ phase with a planar surface and (ii) on the δ phase with a circular surface. In the 3-D simulations, we explore the peritectic transition on the δ phase with different geometries: (a) spherical structure, (b) cylinder structure, and (c) sandglass-shaped structure. In the following study, we set the initial carbon concentration in the liquid phase c_0^L less than the equilibrium concentration $c_e^{L,\gamma}$ at the temperature $T = 1757$ K, which provides a driving force for the peritectic phase transition. All large domain simulations in 2-D and 3-D are performed in parallel computing on high performance computers. The main part of this chapter was published in Ref. [40].

5.1. Simulation setup

We initially fill a semicircular γ nucleus at the interface between the liquid and δ phases. The interface thickness is set to be 1.5 μm in order to keep the simulation stable. The concentration of C in γ is set to be 0.006785, which is the equilibrium concentration with δ phase at the temperature of 1757 K. The carbon concentration in the δ phase is 0.003159 implying a supersaturation of $\Delta_{\gamma/\delta} = 0.027$. Due to the constant concentration in δ phase, all supersaturation hereafter refers specifically to the supersaturation in liquid. The other simulation parameters are tabulated in Table 5.1. In the following discussion, we simulate the growth of γ-phase with different supersaturations in liquid and its development on the δ-particle in various size. Neumann boundary conditions are applied in the present simulations. The supersaturation in liquid is defined as

$$\Delta = \frac{c_0^L - c_e^{L,\gamma}}{c_e^{\gamma,L} - c_e^{L,\gamma}}, \tag{5.1}$$

where $c_e^{L,\gamma}$ is the solute concentration in the liquid phase in equilibrium with the γ-phase and $c_e^{\gamma,L}$ is the carbon concentration in the γ phase in equilibrium with the liquid (see

Symbol	Description	Value
Δt	Time step	1×10^{-6} s
Δx	Space step	1×10^{-7} m
$\sigma_{\gamma\delta}$	Interfacial energy of the γ/δ interface	$0.370\,\mathrm{J\,m^{-2}}$
$\sigma_{\gamma L}$	Interfacial energy of the γ/L interface	$0.319\,\mathrm{J\,m^{-2}}$
$\sigma_{\delta L}$	Interfacial energy of the δ/L interface	$0.204\,\mathrm{J\,m^{-2}}$
D_L	Diffusion coefficient in the L-phase	$5.2 \times 10^{-7}\exp(-5.0 \times 10^4/(RT))$ m^2 s^{-1} [39]
D_γ	Diffusion coefficient in the γ-phase	$\mathrm{D}_L \times 0.01$
D_δ	Diffusion coefficient in the δ-phase	$\mathrm{D}_L \times 0.01$
R	Gas constant	$8.314\,\mathrm{J/(molK)}$

Table 5.1.: Parameters for the phase-field simulations in Fe-C system.

Fig. 4.1(a)). c_0^L represents the initial carbon concentration in liquid phase. In the following discussion, the supersaturation Δ of 0.352, 0.281,0.211, 0.141, and 0.071 corresponds to the initial carbon concentration in liquid c_0^L of 0.019, 0.020, 0.021, 0.022, and 0.023, respectively.

5.2. Measurement methods

In the present study, we investigate the microstructural evolution of peritectic transition in Fe-C system. Because of the typical peritectic structure that the δ-phase is surrounded by the γ-phase, we measure the temporal change of two parameters: the dynamic contact angle and the equivalent thickness of γ-phase.

In order to facilitate an effective measurement of the contact angle, a sharp-interface analogue is needed. In experiments, the three interface curves between δ-, γ-, and liquid-phases are crossed at a joint point via graphical treatment of the experimental pictures. The three tangent lines at this crossing point for the three interface lines give rise to the contact angle between phases. This is a sharp interface treatment. However, the model in the present study assumes that all interfaces involved are diffuse interfaces with a finite thickness. The phase-field variable (φ_α) varies smoothly from 0 to 1 within the interface. Hence, in this model, the triple junction is extended to a triple point area, as shown in Fig. 5.1(a). The interface between phases is given by the contour line of $\varphi_i = 0.5$ ($i = \delta, \gamma$, and L). Mostly, the three contour lines between δ-, γ-, and liquid-phases or the extension of the contour lines cannot pass a single point inside the triple point area and thus, the determination of the contact angle is ambiguous. In literatures [39, 207], a circle with the center at the point $\varphi_\delta = \varphi_\gamma = \varphi_L = 1/3$ is drawn and this circle crosses with each interface lines with an intersection point. The contact angle can be measured by connecting the center and each intersection point. But this measurement method is very sensitive to the radius of the selected circle. For this reason, we use the following way to locate a sharp interface from the diffuse-interface profiles. Firstly, we take the level 0.5 contours of all the phase-field variables, which are defined as the interface between each two adjacent phases (see Fig. 5.1(a)). The three diffuse interfaces form a diffuse triple junction region. The three vertices of this region p_1, p_2 and p_3 in Fig. 5.1(a) are identified by the intersections between the contour lines of 0.5. For instance, the point p_1 is the crossing point of the

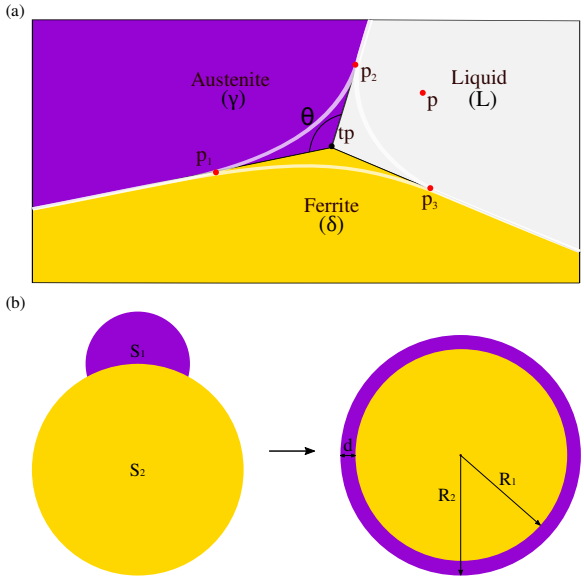

Figure 5.1.: (a) Level 0.5 contours of all the phase-field variables (white lines) identify a triple region. The three boundary points of this region are marked by red circles and called p_1, p_2, and p_3. The triple junction (tp) is the point where $\varphi_1 = \varphi_2 = \varphi_3 = 1/3$. The dynamic contact angle of γ-phase, θ is defined as the angle between two lines, which are obtained by separately connecting the triple junction with two boundary points. The point p and the triple point tp are symmetric with respect to the connecting line between p_2 and p_3. (b) Schematic illustration of equivalent thickness of γ phase.

contour lines of $\varphi_\delta = 0.5$ and $\varphi_\gamma = 0.5$.
The black point in the Fig. 5.1(a), where $\varphi_\delta = \varphi_\gamma = \varphi_L = 1/3$, is defined as the triple junction (tp). The dynamic contact angle of γ-phase θ is defined as the angle between two lines, which are obtained by separately connecting the triple junction with two vertices (see Fig. 5.1(a)). It is noteworthy that the phase-field variables are located in the center of each grid cell, which are assigned to be integer values. The exact positions for $\varphi_\delta = \varphi_\gamma = \varphi_L = 1/3$ or $\varphi_i = 1/2$ ($i = \delta, \gamma$, and L) may not locate at the center of the grid cells. In 2D, a bilinear interpolation based on the values of the phase-field variables of four neighbouring cells is used to determine the position of the points p_1, p_2, p_3, and tp (trilinear interpolation in 3D). The resulting points for $\varphi_i = 0.5$ are connected to form the contour line, as schematically illustrated by the white lines in Fig. 5.1(a). In addition, in the following discussion, we explore the underlying mechanisms of the peritectic transition by analyzing the concentration of the point p, which is chosen to characterise the local liquid concentration in the vicinity of triple point. The point p and the triple point tp are symmetric with respect to the connecting line between p_2 and p_3 (see Fig. 5.1(a)).
In the peritectic transition process, the γ-particle grows along the interface between liquid and δ-phase. Because of its inhomogeneous distribution on the δ-phase, we investigate its development by using an equivalent thickness d.

In Fig. 5.1(b), the violet γ-phase with an instantaneous surface area of $S_1(t)$ locates on the gold δ-phase at the time step t. The γ-phase is equivalently converted to a ring around

the δ-phase with the same area. The equivalent thickness d is calculated by the following equation:

$$\begin{aligned} d(t) =& R_2(t) - R_1(t) \\ =& \sqrt{\frac{S_1(t) + S_2(t)}{\pi}} - \sqrt{\frac{S_2(t)}{\pi}}, \end{aligned} \tag{5.2}$$

where $S_1(t)$ and $S_2(t)$ are functions of time and represent the surface area of γ- and δ-particle, respectively.

5.3. Numerical convergence

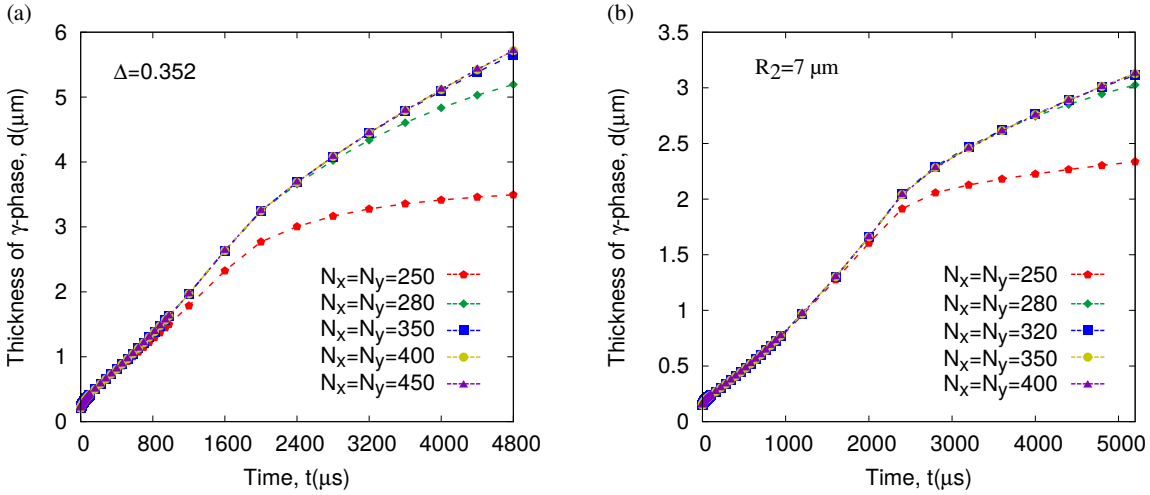

Figure 5.2.: (a) The thickness of the γ-phase as a function of time for different domain sizes under the same supersaturation $\Delta = 0.352$. (b) The thickness of the γ-phase as a function of time for different domain size, while fixing the size of the δ particle.

In order to eliminate the influence of Neumann boundary in simulations on the microstructural evolution, we explore the variations in domain size in this section, while keeping the other simulation conditions fixed.

Fig. 5.2(a) portrays the time evolution of γ-phase thickness with different domain sizes from $250\Delta x \times 250\Delta y$ to $450\Delta x \times 450\Delta y$ for a constant supersaturation ($\Delta = 0.352$). The space scale of the simulation is $\Delta x = \Delta y = \Delta z = 1 \times 10^{-7}$ m and the physical length is given by $N_x \times \Delta x$. The red, black, blue, yellow, and dark-green lines represent the simulation with domain size of $N_x = N_y = 250$, 280, 350, 400, and 450, respectively. In all cases, the thickness of the γ-phase layer increases exponentially with time. The underlying physical reason will be discussed later in this paper. With the magnified domain size, a convergence emerges in the simulation results and the simulations with $N_x = N_y \geq 400$ are well converged. It is noteworthy that among all the considered supersaturation, the supersaturation $\Delta = 0.352$ for testifying the convergence of the simulations is the largest

one, which represents the strongest driving force for the particle growth. The boundary influence recedes with decreasing the driving force. Therefore, we set the domain size with $N_x = N_y = 400$ cells for investigating the influence of liquid supersaturation on the γ-phase thickness. A similar validation is also performed for the study with distinct radius (R_2) of the δ-particle. For the case of δ with the largest initial size ($R_2 = 70$), the simulation results with $N_x = N_y \geq 350$ are converged, which are illustrated in Fig. 5.2(b). The effect of Neumann boundary weakens with decreasing the initial radius of the δ particle, thereby we explore the γ growth with different initial radii of δ particle in a domain with 350×350 cells.

5.4. 2-D simulation: peritectic transition on a planar δ-phase

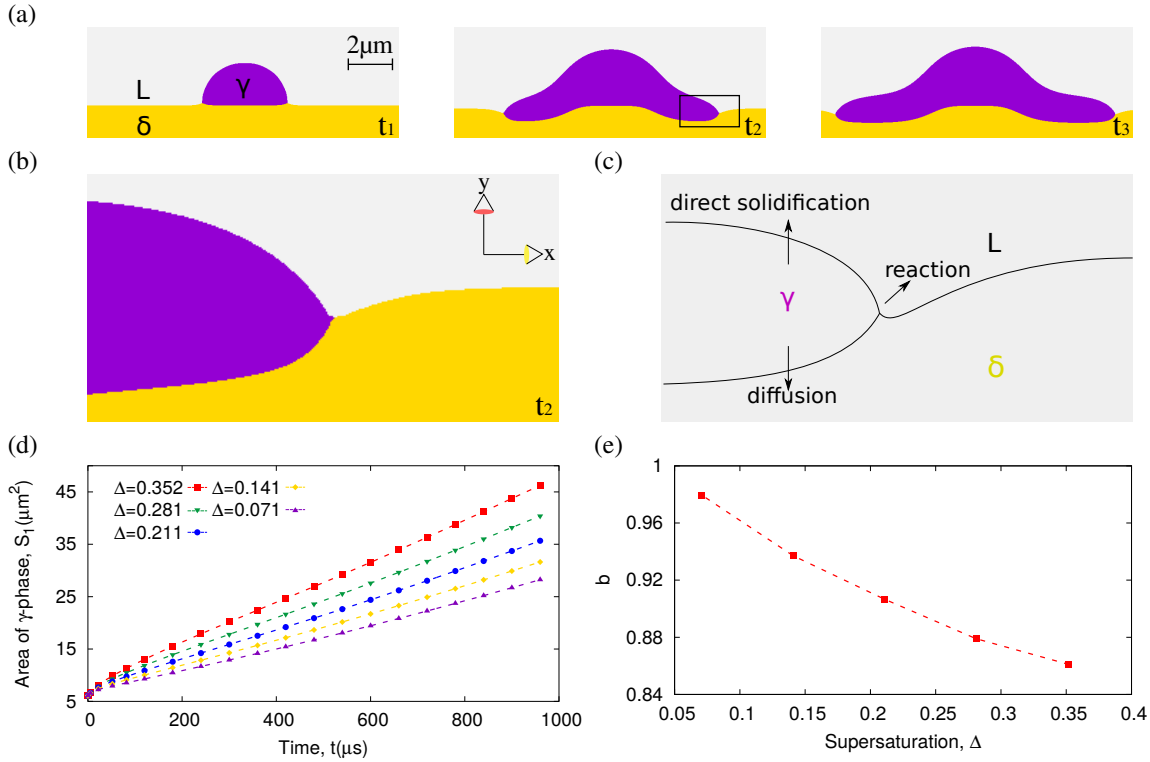

Figure 5.3.: (a) Microstructural evolution of γ-phase on a planar δ-phase during peritectic phase transition from t_1 to t_3, where t_1, t_2, t_3 represent the time 0, 400 μs, 600μs, respectively. (b) A magnified region in the vicinity of the triple point which is highlighted in the middle of (a). (c) Schematic diagram for the microstructure of peritectic phase transition near the triple point. (d) The area of γ phase as a function of time for different supersaturation Δ. (e) The growth exponent b for the relation $S_1 = at^b + g$ as a function of Δ.

In 2-D simulations, we focus on the growth of austenite on a flat and a circular δ-particle. Fig. 5.3(a) portrays the microstructural evolution of the peritectic transition on a flat δ-particle. A semicircular nucleus of the austenite phase with a radius of 2 μm is initially

Δ	0.352	0.281	0.211	0.141	0.071
a	0.104	0.078	0.055	0.038	0.025
b	0.861	0.879	0.907	0.937	0.979
g	6.388	6.427	6.448	6.445	6.435

Table 5.2.: The fitted coefficients for different supersaturation.

placed at the δ-L interface. With time, the austenite phase grows along the δ/L interface in the horizontal direction and its thickenness increases in the vertical dimension. Since the austenite phase grows at the expense of the δ and L phases and the δ phase remelts at the δ/L interface, the γ/δ interface sinks in the vicinity of the triple point, which is a typical characteristic of peritectic transition. Meanwhile, due to the initial quasi equilibrium setup between the γ and δ phase as well as the relatively small diffusivity in these two solid phases, the interfacial region where the γ and δ phases are in contact at the beginning does not evolve with time. This results in a platform in the middle of the γ phase close to the δ phase.

In order to better explore the mechanism of peritectic transition, we magnify the region in vicinity of the triple junction (see Fig. 5.3(b)). At the front of the austenite phase, the L/δ interface is bent towards the δ-phase. This curved interface indicates the melting of the δ phase during the reaction near the L/δ/γ triple point. This phenomenon is well consistent with previous studies [39, 38]. The corresponding schematic diagram of the microstructure near the triple junction is shown in Fig. 5.3(c). The peritectic solidification involves the peritectic reaction, namely $L+\delta \rightarrow \gamma$ and the subsequent peritectic transformation, namely $\delta \rightarrow \gamma, L \rightarrow \gamma$ [208, 209]. Fig. 5.3(d) depicts the area of the γ phase S_1 as a function of time for different supersaturation Δ. The red, green, blue, yellow, and violet lines represent the cases with Δ = 0.352, 0.281, 0.211, 0.141, and 0.071, respectively. In all these 5 cases, S_1 increases exponentially with time, which follows an empirical formulation as

$$S_1 = at^b + g. \tag{5.3}$$

The fitted coefficients a, b, and g are tabled in Table 5.2. A comparison between the five cases shows that a higher supersaturation leads to a faster growth. In order to provide insight into the underlying growth mechanisms, the relationship between the growth exponent b and the supersaturation Δ is shown in Fig. 5.3(e). With an increase in Δ, b decreases from 0.96 to 0.84. This result indicates that the coefficient b in the case with a higher supersaturation is closer to the theoretical exponent of 0.5 for diffusional growth [210]. A higher supersaturation, as defined in previous section, means a lower carbon concentration in the liquid phase, which provides a larger driving force for the phase transformation at the L/γ interface. With the diminishing supersaturation, the direct solidification of austenite from liquid is inhibited. The whole process is determined by the peritectic reaction. As a result, the coefficient b for the case with supersaturation 0.071 is very close to the exponent of 1 for reaction-controlled limit.

The growth of γ-platelet involves the contributions from peritectic transformation between L/γ and δ/γ interfaces, and from peritectic reaction in the vicinity of the triple point. By analyzing the tip velocity of γ-platelet growing along the L/δ interface, we

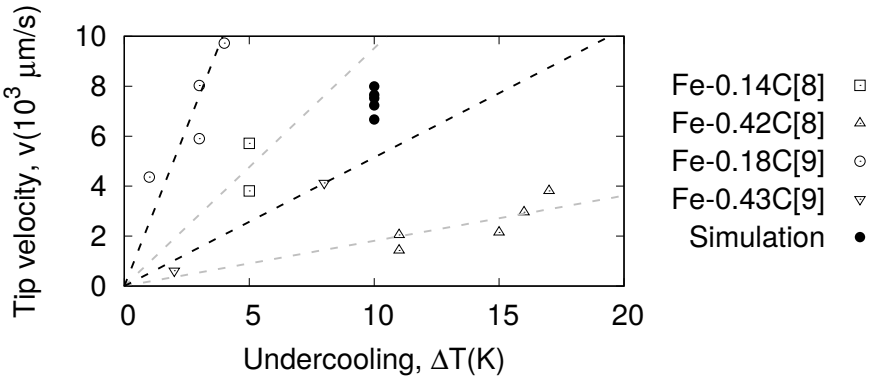

Figure 5.4.: Tip velocity of γ-phase as a function of undercooling in different Fe-C alloys

clarify the influence of various supersaturations on the movement of the triple point, caused by peritectic reaction. Fig. 5.4 demonstrates the tip velocity of γ-platelet as a function of undercooling in Fe-C alloys with different compositions. Five filled circles, from bottom to top, are obtained by the present simulation and correspond to the five cases with increasing supersaturations shown in Fig. 5.3(d). The open symbols are the experimental data from Shibata et al. [54] and Grisser et al. [53], which are shown for the sake of comparison. As aforementioned, the present study focuses on the isothermal peritectic solidification at the 1757 K, which is 10 K below the peritectic temperature (T_p). In order to better compare with experimental data, the mole concentrations for the cases with different supersaturations are converted to the composition in weight percentage of carbon (wt٪) based on the initial concentration and volume fraction of each phase in the system, hence the cases with supersaturation of $\Delta = 0.352$, 0.281, 0.211, 0.141, and 0.071 represent Fe-0.341 wt٪C, Fe-0.359C, Fe-0.376C, Fe-0.394C, and Fe-0.411C steels, respectively. All five numerical measured values fall within the range of experimental data and the tip velocity of γ-platelet increases with a decrease in the carbon concentration. Good agreement between the numerical results and the experimental data indicates that the present PF-model is capable of quantitatively analyzing the peritectic transition.

5.5. 2-D simulation: peritectic transition on a circular δ-phase

As an emblematic peritectic microstructure, austenite surrounds δ-iron, forming a sandwich microstructure: liquid/austenite/δ. When the δ-phase has a spherical shape, the effect of its curvature on the austenite growth needs to be considered. In this section, we investigate the growth of austenite under different supersaturation and its morphological evolution on ferrite in various sizes.

Fig. 5.5(a) presents the microstructural evolution of austenite on a δ-particle. Austenite grows along the L/δ interface and thickens gradually with time. When δ-phase is completely encircled by the γ-phase, the L/δ/γ triple point disappears, which leads to the end of peritectic reaction. Subsequently, the peritectic transformation occurs. As a result, γ-phase engulfs the δ-phase and grows in the liquid phase. The whole process is divided into two stages: before (stage 1) and after (stage 2) the disappearance of triple

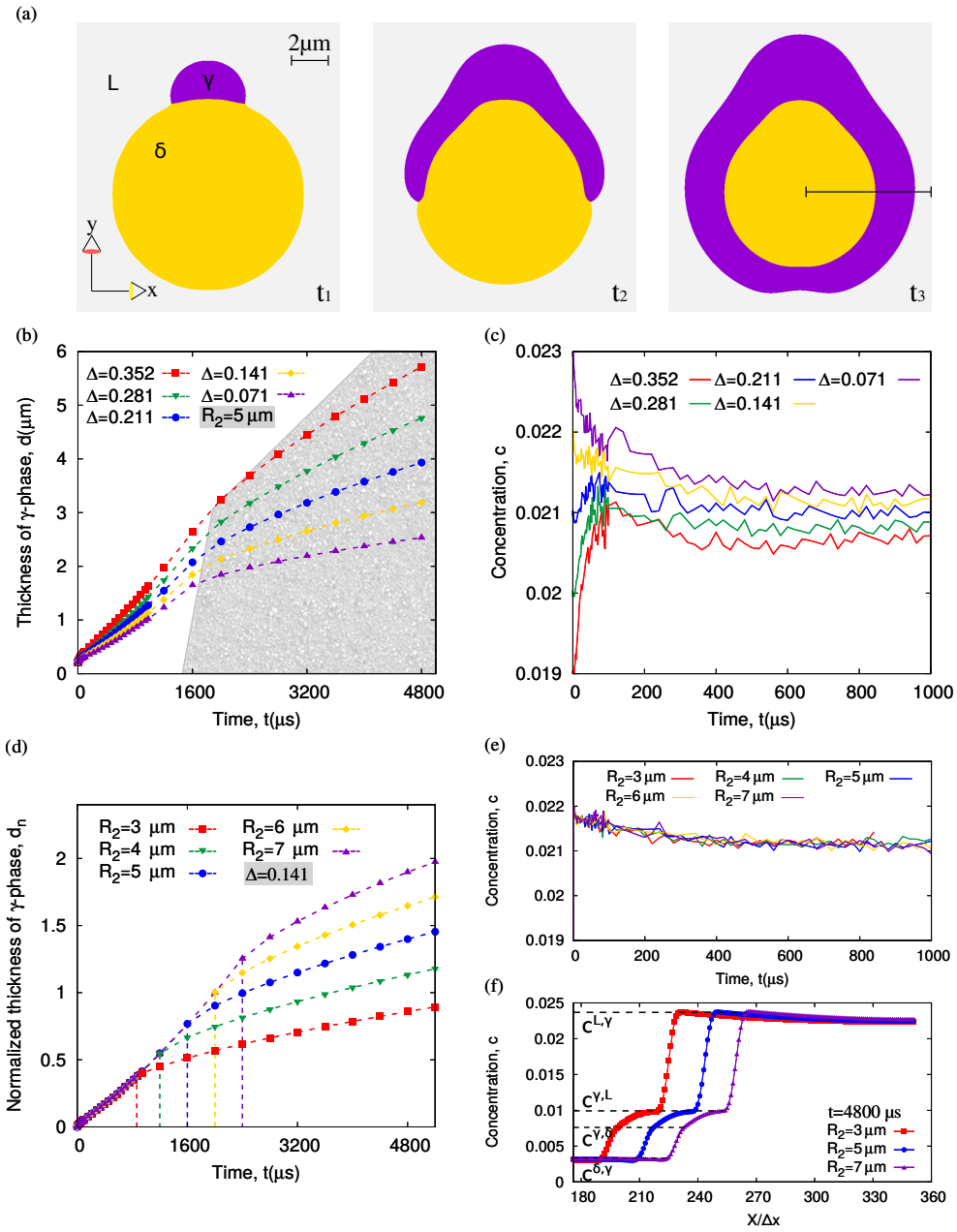

Figure 5.5.: (a) Morphological evolution of austenite on a circular δ-particle. (b) The thickness d of the γ-phase as a function of time for different supersaturation Δ, where the radius of the δ phase is 5 μm. (c) The liquid concentration of the point p as a function of time for different values of Δ. (d) The normalized thickness d_n of the γ-phase as a function of time for different initial radii of the δ particle, where Δ is set as 0.141. (e) The liquid concentration of the point p as a function of time for different initial radii of the δ particle. (f) The concentration distribution at the time t=4800 μs for different initial radii of δ particle. The concentration $c^{i,j}$ represents the concentration of carbon in the i-phase at the i/j interface (i, j = γ, δ, and L).

point. Fig. 5.5(b) illustrates the thickness d of γ-phase, as defined in Eq. (5.2), as a function of time. The red, green, blue, yellow, and violet dashed lines correspond to the liquid with supersaturation of 0.352, 0.281, 0.211, 0.141, and 0.071, respectively. In all five cases, the size of δ-particle is fixed and the thickness of γ-particle d increases exponentially with time. For each case, d shows two different exponents, by which we classify this process into two stages. For a better discrimination, the stage 2 is indicated by a shading region in Fig. 5.5(b). A comparison between these five cases shows that with an increase in Δ, the growth rate of the γ-phase enlarges and the dividing point between stage 1 and 2 slightly delays. As discussed in previous section, the supersaturation denotes the deviation of the composition in the liquid from the equilibrium value. This deviation leads to a difference in the grand chemical potential, which provides the driving force for the phase transition. In the following, we define two concentration differences to represent the driving force for the phase transformation at the respective interface. One is $\Delta c^{L,\gamma} = c^L - c_e^{L,\gamma}$ at the L/γ interface; the other is $\Delta c^{L,\delta} = c^L - c_e^{L,\delta}$ at the L/δ interface. Here, $c_e^{L,\gamma} = 0.024032$ and $c_e^{L,\delta} = 0.0203904$ is the equilibrium concentration in liquid phase with respect to γ and δ phase, respectively. c^L is the carbon concentration in the liquid phase. As illustrated in Fig. 5.5(c), we use the liquid concentration of the point p, which is defined in section 4 (see Fig. 5.1(a)), to characterize the driving force for the morphological evolution of the γ-phase. The red, green, blue, yellow, and violet lines correspond to the five cases in Fig. 5.5(b). In all these five cases, the composition c oscillates during the peritectic transition and converges after an initial transient time. The convergence of the concentration signifies that the peritectic transition reaches a steady state. At the steady state, the concentration differences $\Delta c^{L,\gamma} < 0$ and $\Delta c^{L,\delta} > 0$ lead to the phase transformation of $L \rightarrow \gamma$ and $\delta \rightarrow L$, respectively. It is noteworthy that the melting of δ ($\delta \rightarrow L$) occurs just ahead of the γ phase due to the local enrichment of concentration in liquid. Comparing these five cases, we find that an increase in Δ leads to an increase in $\Delta c^{L,\gamma}$ and a reduction in $\Delta c^{L,\delta}$. The increase in $\Delta c^{L,\gamma}$ provides a relatively large driving force for the austenite growth towards liquid. The reduction in $\Delta c^{L,\delta}$ inhibits the melting of δ phase, decreasing the rate of the peritectic reaction and thereby delaying the disappearance of the triple junction.

Next, we focus on the influence of the initial radius of δ phase on the peritectic transition. Fig. 5.5(d) illustrates the normalized thickness of γ phase d_n as a function of time. The red, green, blue, yellow, and violet dashed lines correspond to the δ particle with radius R_2 of 3 μm, 4 μm, 5 μm, 6 μm, and 7 μm, respectively. The supersaturation for these five cases is fixed at $\Delta = 0.141$. The thickness d_n is defined by the following formulation:

$$d_n = \frac{d - d_0}{d_0}, \tag{5.4}$$

where d is given by Eq. (5.2) and d_0 represents the initial value at t=0. In all five cases, d_n increases with time and the whole process is divided into two stages, which is similar to the previous discussion. In stage 1, these five lines overlap with each other. In stage 2, the five lines separate from each other and are almost parallel, which indicates the same growth rate during the whole peritectic transition. The dividing points between the two stages are marked by the vertical dashed lines. A comparison between these five cases shows that an enlargement of the initial radius of the δ-particle leads to an increase in the migration distance of the triple point, which results in a temporal prolongation of stage 1.

In addition, the growth rate of stage 1 is greater than that in stage 2. An increment in d_n is caused by the difference in the growth rate in combination with the extending stage 1, when the δ particle is with a larger initial radius.

In a similar way, Fig. 5.5(e) depicts the liquid concentration of the point p as a function of time. The red, green, blue, yellow, and violet dashed lines represent the five cases in Fig. 5.5(d). In all five cases, the concentration almost overlaps with each other, which implies the same driving force for the austenite growth on the δ particle in various radii. When the initial size of the γ phase is fixed, the capillary force remains constant. Therefore, the γ phase grows with the same rate in stage 1 for the δ particle with different radii. Due to the complete encirclement of the δ particle by the γ phase, the triple point disappears. Fig. 5.5(f) shows the profile of concentration along the black line in Fig. 5.5(a), corresponding to the three cases with $R_2 = 3$ µm, 5 µm, and 7 µm, respectively. In Fig. 5.5(f), the concentration $c^{i,j}$ represents the concentration of carbon in the i-phase at the i/j interface (i, j = γ, δ, and L). As an exemplary explanation, we choose the concentration profile at the time $t = 4800$ µs. The concentration distribution for these three cases displays a similar characteristic. As shown in Fig. 5.5(f) by the black dashed lines, the local γ concentrations at the γ/L and γ/δ interfaces ($c^{\gamma,L}$ and $c^{\gamma,\delta}$) are the same for these three cases, which is responsible for the same growth rate shown in Fig. 5.5(d).

5.6. 2-D simulation: the dynamic contact angle in peritectic transition

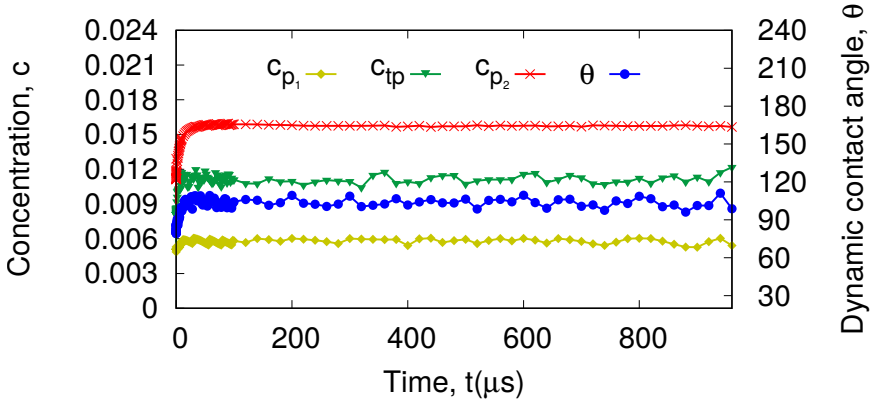

Figure 5.6.: The dynamic contact angle and the concentrations of the three points p_1, p_2, and p_3 as a function of time for the peritectic transition with $\Delta = 0.352$.

According to the previous studies [71], the contact angle between interfaces at a triple junction should follow the thermodynamic equilibrium relation, which is described by Young's law. Typical examples are eutectic and monotectic solidification. However, this is different in the peritectic transition process. In this section, we investigate the dynamic contact angle during the peritectic transition, which is influenced by two factors: the supersaturation Δ and the initial radius R_2 of the δ particle.

Fig. 5.6 illustrates the time evolution of the dynamic contact angle and the concentration for the peritectic transition on a circular δ-particle ($R_2 = 5$ μm) with $\Delta = 0.352$. The dynamic contact angle (the blue line) increases transiently at the beginning and subsequently converges to about 103°, implying that the peritectic transition reaches a steady state after a certain time. As discussed in section 3, the dynamic contact angle θ is determined by the positions of the three points, p_1, p_2, and tp, which are affected by their relative movement caused by the phase transformation. The concentrations of these three points, which are responsible for the transformation, are depicted in Fig. 5.6. The yellow, red, and green lines represent the time evolution of the concentration for p_1, p_2, and tp, respectively. The concentrations of three points increase simultaneously at the beginning and converge to constants after reaching the steady state, which shows a quite similar trend to that of the dynamic contact angle. In contrast to the concentration of the other two points, c_{p_2} has a relatively large increase at the beginning. This large increase of c_{p_2} leads to a farther movement of p_2 towards the liquid phase. As a result, the dynamic contact angle θ increases with an enlarging c_{p_2}.

Fig. 5.7(a) shows the average dynamic contact angle $\bar{\theta}$ as a function of Δ for cases (i) and (ii). In order to eliminate the error caused by the initial setup, we only consider the data at the steady state for the calculation of $\bar{\theta}$. In both cases, $\bar{\theta}$ increases with increasing Δ. As discussed in section 5.4, the increasing supersaturation results in an enlarging phase transformation rate at the L/γ interface towards liquid phase. Meanwhile, the slight increase in the movement rate of the triple point is negligible. Therefore, the dynamic contact angle increases with the supersaturation Δ. The dependence of $\bar{\theta}$ on the initial radius of δ particle R_2 is depicted in Fig. 5.7(b). With increasing R_2, $\bar{\theta}$ almost remains constant, which is consistent with the overlapping of concentrations for different R_2 in Fig. 5.5(e).

5.7. 3-D simulation: peritectic transition on δ particle with different geometries

3D simulations are more close to the reality where the mean curvature has an additional contribution. In this section, we simulate the microstructural evolution of γ phase in 3-D domains and investigate the thickness of the production phase and the dynamic contact angle at the triple junction during the peritectic transition. The differences between 2-D simulation and 3-D simulation are discussed.

Fig. 5.8 portrays the morphological evolution of peritectic transition on the δ phase with different geometries: (a) spherical structure, (b) cylinder structure, and (c) sandglass-shaped structure. In all three cases, the γ phase is initially set as a semisphere with a radius of 2 μm. In (a) and (b), the initial radius of the spherical δ particle and the cylinder δ phase both are 3 μm. In (c), the shape of the δ phase in the longitudinal dimension is depicted by a cosinusoidal function and the cross section through the center of sandglass is a circle with a radius of 3 μm.

In order to compare the simulation results with the cases (i) and (ii) in 2-D simulations, which are previously defined in section 5, we explore the peritectic transition in 3-D for the

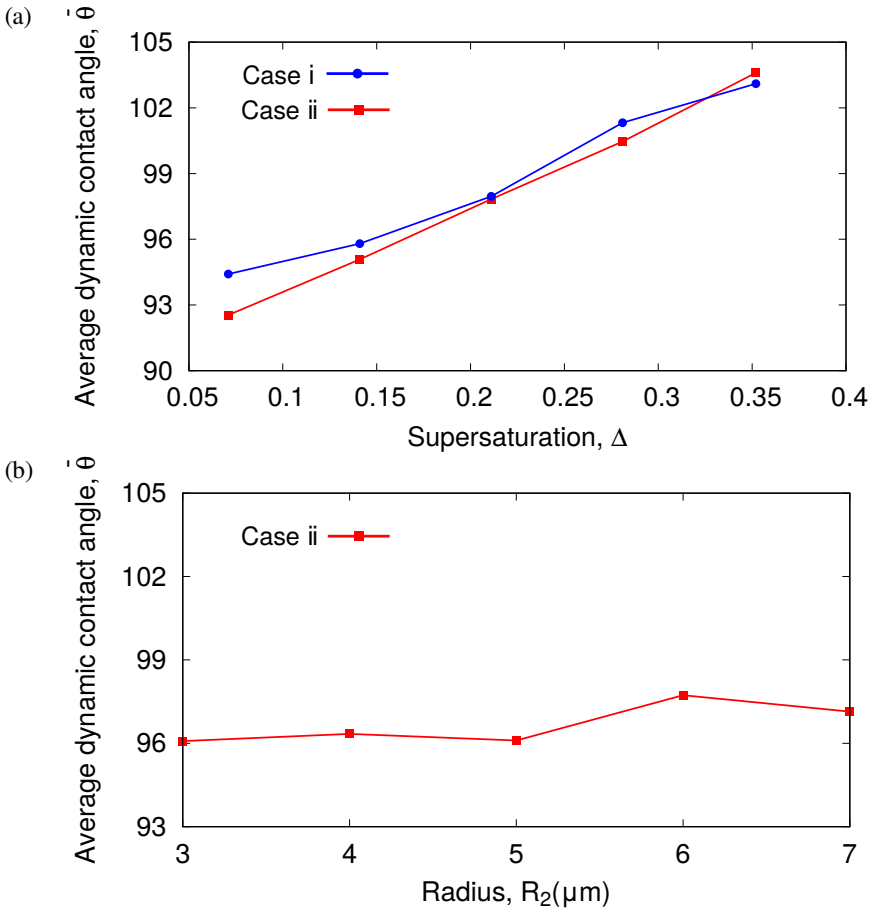

Figure 5.7.: (a) The average dynamic contact angle as a function of the supersaturation for cases 1 and 2. (b) The average dynamic contact angle as a function of the initial radius R_2 of the δ particle.

following five cases: (iii) δ phase with a spherical structure in the x-y plane (Fig. 5.8(a)), (iv) δ phase with a cylinder structure in the x-y plane (Fig. 5.8(b)), (v) δ phase with a cylinder structure in the y-z plane (Fig. 5.8(b)), (vi) δ phase with a sandglass-shaped structure in the x-y plane (Fig. 5.8(c)), (vii) δ phase with a sandglass-shaped structure in the y-z plane (Fig. 5.8(c)). In all the cases (iii)-(vii), the γ phase grows on a planar or quasi-planar δ phase in the y-z plane and on a circular δ particle in the x-y plane. The former one is similar to case (i) and the latter one is comparable with case (ii). In all the cases (i)-(vii), the γ phase gradually covers the outer surface of δ phase.

Fig. 5.9(a) depict the area S_1 of the γ phase as a function of time t for the cases (i), (iii), (v), and (vii). It is noted that case (iii) represents the result in the x-y plane on a circular particle, which differs from the one on a flat δ phase in the cases (i), (v), and (vii). Hence, the green line shows a different exponent b of t^b from the other three lines. This difference is an evident effect of the curvature. In the cases (i), (v), and (vii), the area S_1 increases with time with an almost identical exponent b. A comparison between these four cases shows that S_1 in 3-D increases faster than the one in 2-D and on a circular surface faster than that on a planar surface.

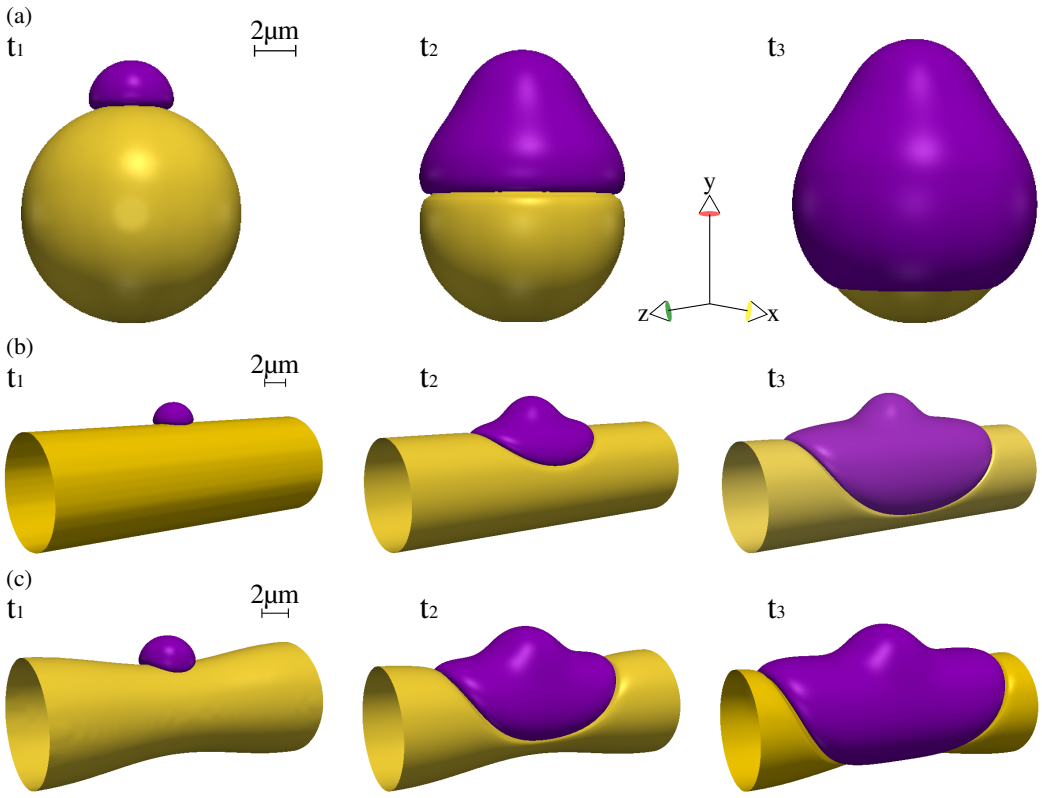

Figure 5.8.: Morphological evolution of γ phase on δ particle with three different geometries: (a) spherical structure, (b) cylinder structure, and (c) sandglass-shaped structure.

In Fig. 5.9(b), the blue, green, red, and yellow lines depict the cases (ii), (iii), (iv), and (vi), respectively. In all four cases, S_1 increases with time and shows obviously different exponents of time in two distinct growing stages, similar to the observation in the Fig. 5.5(d). A comparison between these four cases demonstrates a similar result that γ phase in 3-D has a larger growth rate than in 2-D. In the 3-D simulations, the γ nucleus is set as a semisphere with a surface-to-volume ratio (SVR) of 3/R, whereas in 2-D simulations, the SVR of the semicircular γ particle is 2/R. Here, R is the radius of the γ particle and is fixed in 2-D and 3-D. The bigger SVR facilitates the peritectic reaction and hence leads to a larger growth rate in 3-D. The red and yellow lines almost overlap with each other, which both are lower than the green line. This implies that the γ phase grows on a cylinder and a sandglass-shaped δ phase with a nearly same rate, which is slower than that on a spherical δ phase. After entering into the stage 2 for the cases (iii), (iv), and (vi), the area S_1 increases with the same growth rate, which is caused by the identical supersaturation. The red and blue lines in Fig. 5.9(c) represent the cases (iv) and (v), respectively. A comparison between these two cases shows a difference in the growth rate for the γ phase in the x-y and y-z planes.

We explain the underlying mechanism of the difference in the growth rate for different cases by analyzing the concentration of the point p. Fig. 5.9(d) exemplifies the concentration as a function of time for the cases (iii), (iv), and (v), which are shown by green, red, and

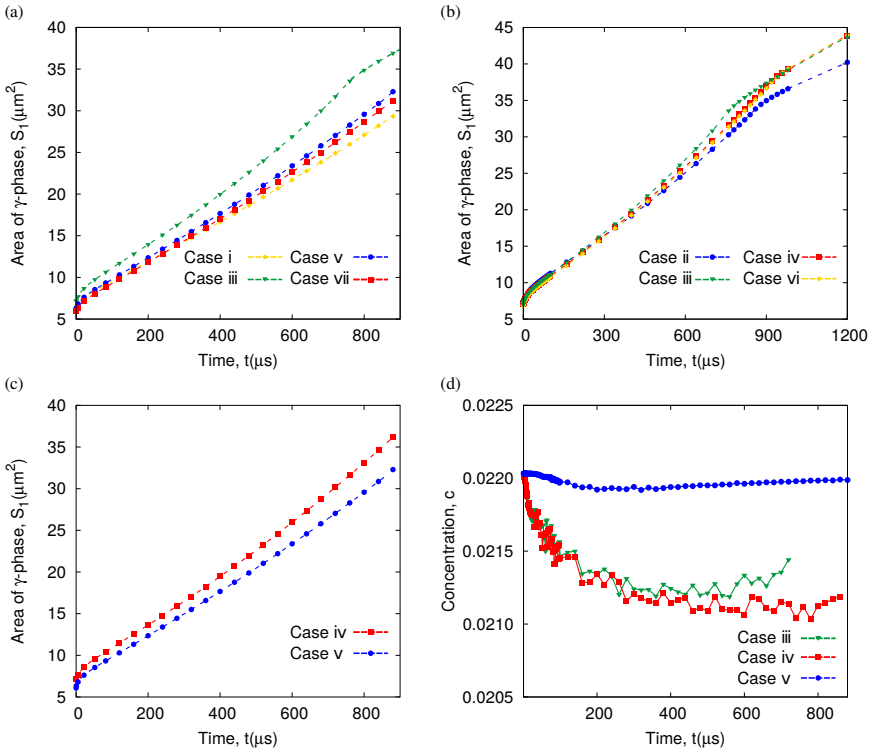

Figure 5.9.: (a)-(c) The area of the γ phase as a function of time for different cases. (d) The concentration of the point p (see Fig. 5.1(a)) as a function of time for the cases (iii), (iv), and (v).

blue lines, respectively. The concentration for case (v) remains almost constant, whereas the concentrations for the cases (iii) and (iv) oscillate around a particular value after an initial transient stage. According to the previous discussion, the growth of the γ phase is controlled by the remelting of δ phase in the vicinity of triple point. The concentration difference $\Delta c^{L,\gamma}$ for the cases (iii) and (iv) is greater than that for case (v), which results in a larger driving force for the phase transformation $L \rightarrow \gamma$. As a result, in cases (iii) and (iv), γ phase grows faster than that in case (v). However, the concentration difference $\Delta c^{L,\delta}$ in the first two cases is smaller than that in the last case and consequently the phase transformation $\delta \rightarrow L$ is inhibited in the former two cases. Fig. 5.10(a) and (c) depict the microstructure in the vicinity of triple point at the time $t = 700$ µs for the cases (v) and (iv), respectively. Fig. 5.10(b) and (d) illustrate the calculated shape of interfaces corresponding to Fig. 5.10(a) and (c), respectively. In each figure, the violet, yellow, and gray lines represent the contour lines of $\varphi_\gamma = 0.5$, $\varphi_\delta = 0.5$, and $\varphi_L = 0.5$ phase, respectively. In order to facilitate the comparison between the cases (iv) and (v), the shape of interfaces in Fig. 5.10(d) is rotated until the two points at the γ interface, which are farthest from the triple point, fall on the y-axis. The triple point situates at the x-axis for both cases. In the vicinity of the triple point, a triangular shaped region is surrounded by the interfaces, because the isolines of $\varphi_\alpha = 0.5$ cannot intersect at the triple point. The L/δ interface, which is defined by the coincidence part of yellow and gray lines, curves towards δ phase in Fig. 5.10(b), indicating the melting of δ, whereas in Fig. 5.10(d), this interface shows

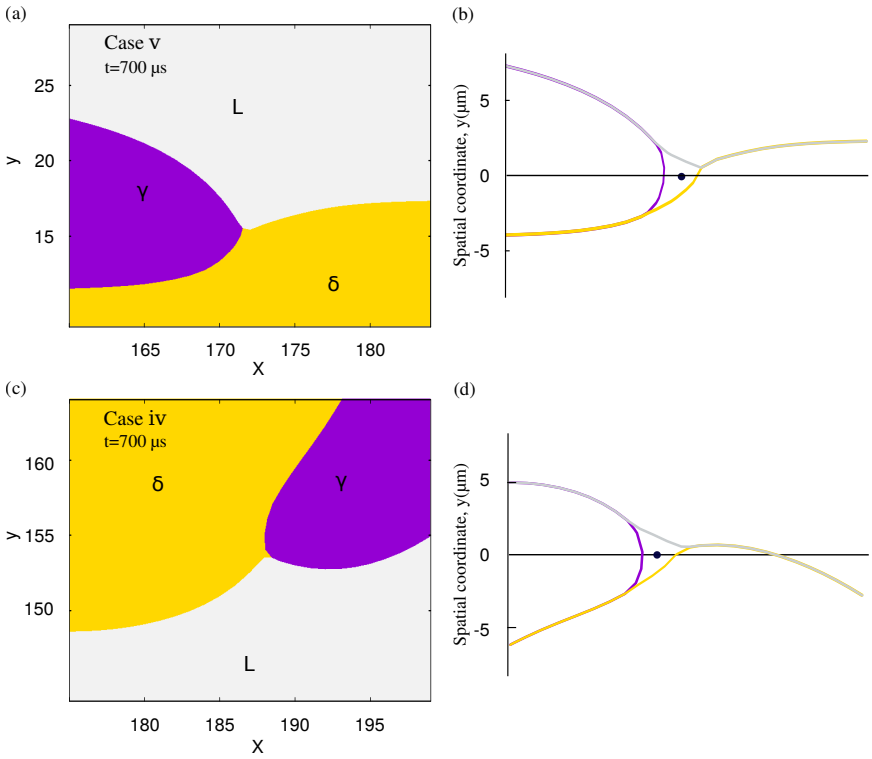

Figure 5.10.: (a) and (c) The microstructure in the vicinity of triple point at the time t = 700 μs for the cases (v) and (iv), respectively. (b) and (d) The calculated shape of interfaces corresponding to Fig. 5.10(a) and (c), respectively.

	Case (iii)	Case (iv)	Case (v)	Case (vi)	Case (vii)
$\bar{\theta}(^\circ)$	94.18	95.44	96.9	95.12	97.24

Table 5.3.: Average dynamic contact angle for cases (iii)-(vii).

no evident change. This difference in microstructure is attributed to the larger solute enrichment in the vicinity of triple point in case (v), as shown in Fig. 5.9(d).

The average dynamic contact angle $\bar{\theta}$ is calculated by using the data in the steady state. The angles $\bar{\theta}$ for the cases (iii)-(vii) are tabulated in Table 5.3. A comparison between these five cases shows that the shape of δ particle has no evident influence on the dynamic contact angle under the same supersaturation.

5.8. Summary

By using the phase-field method, we have systematically investigated the morphological evolution of peritectic transition in Fe-C binary system through 2-D and 3-D simulations, with inputs from the CALPHAD database. A novel measurement method is proposed to more precisely determine the dynamic contact angle.

The simulation results show that the growth of γ phase on a planar δ phase is affected by the supersaturation Δ and the growth rate increases with Δ. Due to the supersaturation,

the migration distance of L/γ interface is larger than that of the δ/γ interface. The tip velocity of γ-platelet, obtained in our simulations, is in concordance with the experimental data, which indicates that the present PF-model can quantitatively investigate the peritectic transision. In addition, the δ/L interface near the L/γ/δ triple point deflects towards the δ phase region, indicating that the melting of δ phase occurs in the vicinity of triple point. The reason is that the local liquid concentration at the triple point is greater than the equilibrium concentration of the liquid phase with respect to the δ phase, but less than the equilibrium concentration of the liquid phase with respect to the γ phase.

Furthermore, we have elucidated that when the γ phase grows on a circular δ particle, the growth rate of γ phase enlarges with Δ and remains constant with an increase in the size of the δ particle. Differing from the γ growth on a planar δ phase, the growth process on a circular δ particle is divided into two stages by the complete engulfment of the δ particle.

In addition, we have measured the dynamic contact angle and found that the average dynamic contact angle increases with the liquid supersaturation and remains almost constant with increasing the radius of the δ phase.

Through the comparison between 2-D and 3-D simulation results, we have clarified that the growth of γ phase in 3-D is faster than in 2-D, as a result of the bigger value of SVR in 3-D. Furthermore, in 3-D simulation, the growth rate of γ phase is unequal in radial and axis direction, due to the asymmetric microstructure.

By simulating the growth of peritectic phase in Fe-C system, we have clarified the mechanisms of peritectic transition with various supersaturation, which should be helpful to understand this complex phase transition in other systems.

6. Al-C binary system: peritectic transition:

In the following, we use a phase-field model with a suitable crystalline anisotropy formulation in 3D to simulate the diffusion-reaction process, which is responsible for the growth of the intermetallic compound. The objective of our research is to show how the orientation angles influence the growth behavior of Al_4C_3, and which parameters have an impact on the critical orientation angle. By using the PF method, we simulate the evolution of a single intermetallic phase as well as the interaction of two adjacent particles. Through analyzing the concentration distribution, we clarify the underlying physics for the growth behaviors of Al_4C_3 with different orientation angles. The main part of this chapter was published in Ref. [85].

6.1. Simulation setup

We initially fill the Al_4C_3 particle as a semicircle, at the interface between the liquid and graphite phases. The interface thickness is set to be 0.06 μm, which is consistent with a typical order of the physical interface width. For the simulation stability, we set the initial size of the intermetallic phase to be at least 0.32 μm, which is much larger than the interface width of 0.06 μm. The concentrations of C in the liquid, Al_4C_3, and graphite

Symbol	Description	Value
Δt	Time step	1×10^{-8} s
Δx	Space step	1×10^{-8} m
σ_{AG}	Al_4C_3-Graphite interfacial energy	1.5 J/m^2
σ_{AL}	Al_4C_3-Liquid interfacial energy	0.3 J/m^2
σ_{LG}	Liquid-Graphite interfacial energy	1.5 J/m^2
D^s_{Al}	self-diffusivity of Al	1.02×10^{-8} m^2/s [211]
D^s_C	self-diffusivity of C	1.16×10^{-8} m^2/s [212]

Table 6.1.: Parameters for the phase-field simulations in Al-C system.

phases are set to be 0.39422, 0.42872, and 0.99932, respectively. The latter two values for Al_4C_3 and graphite are the corresponding equilibrium concentrations at peritectic temperature of 2429 K. Due to the strong anisotropy, the capillary force $\sigma\kappa$ is relatively large at the corners of the Wulff shape. In order to overcome this large capillary force, we set the C concentration in the liquid phase much higher than the equilibrium concentration at 0.1968, which provides a sufficiently large driving force for the phase growth. According to Darken's equation, the interdiffusivity can be calculated as

$$D_C = (c_C D^s_{Al} + c_{Al} D^s_C)\Phi, \tag{6.1}$$

where $D^s_{Al} = 1.02 \times 10^{-8}$ m^2/s [211] and $D^s_C = 1.16 \times 10^{-8}$ m^2/s [212] are the self-diffusivity of Al and C, respectively. According to Ref. [213], Φ is the thermodynamic factor, which is written as $\Phi = \frac{c_C c_{Al}}{RT} \frac{d^2 f}{dc_C^2}$. Other parameters for the phase-field simulations are tabulated in Table 6.1.

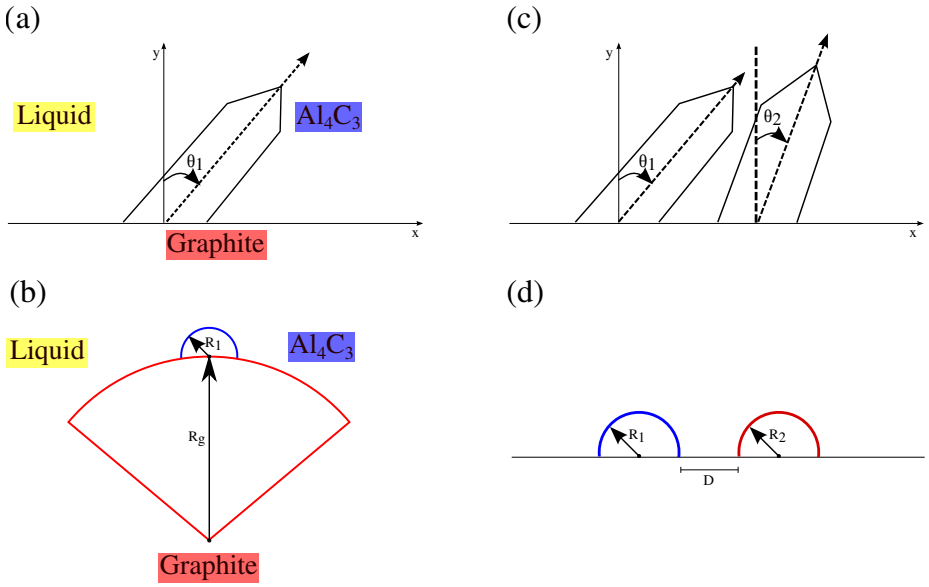

Figure 6.1.: (a), (c) Schematic illustration of the rotation angles θ_1, θ_2. (b) Radius of graphite particle R_g and radius of single Al_4C_3 nucleus R_1. (d) Radius of the Al_4C_3 nuclei R_1, R_2, and distance D between two nuclei.

A schematic illustration of the simulation configuration with geometric parameters is illustrated in Fig. 6.1. For the growth of a single Al_4C_3 crystal, the parameters θ_1, R_1, and R_g are defined in Fig. 6.1(a) and (b). Here, θ_1 represents the growth orientation angle of the Al_4C_3 particle, while R_1 and R_g are the radii of the Al_4C_3 nucleus and the graphite particle, respectively. In Fig. 6.1(c) and (d), the parameters θ_1, θ_2, R_1, R_2, and D are setups for the growth of two adjacent Al_4C_3 particles. The subscripts 1 and 2 respectively represent particle 1 and 2 (from left to right). D is the distance between the center of two Al_4C_3 nuclei.

6.2. The growth of a single Al_4C_3 particle on the graphite surface

As observed in experimental microstructures, the aluminum carbides form and grow on the Al/C interface with unknown orientation angles. The phase-field model is applied to simulate the isothermal solidification in Al-C alloys, in a 2D domain with a space step of $\Delta x = 1 \times 10^{-8}$ m. The time scale of the simulations is $\Delta t = 1 \times 10^{-8}$ s. In the present study, we set up a number of uniformly sized Al_4C_3 nuclei with random orientations on a planar graphite phase, surrounded by a supersaturated liquid phase (see Fig. 6.2(a)). Because of the imposed supersaturation, all Al_4C_3 nuclei should grow with time. In Fig. 6.2(b) it is

shown, however, that some Al_4C_3 nuclei with small absolute orientation angles can survive and grow, whereas other nuclei with big rotations vanish. Among all those growing Al_4C_3 nuclei, the growth velocity decreases with the absolute orientation angle. For the evolution of the Al_4C_3 nuclei, this observation indicates the existence of a critical orientation angle.

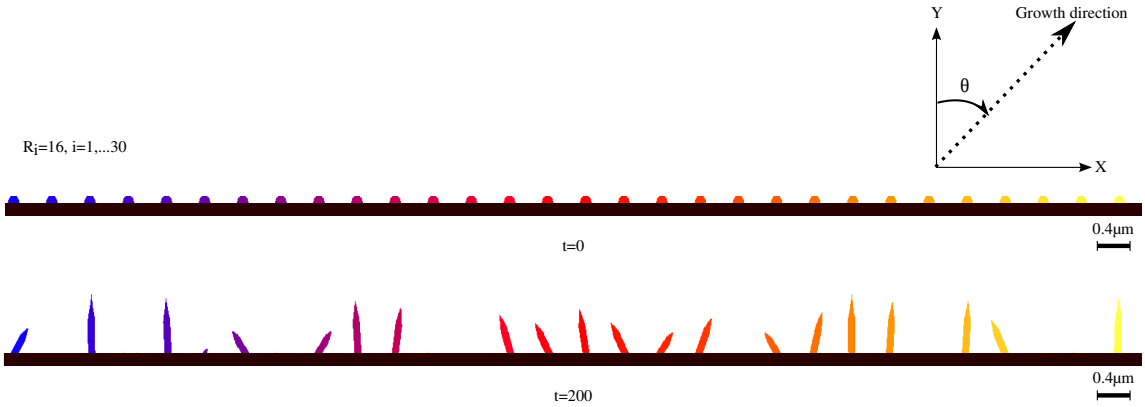

Figure 6.2.: The growth of Al_4C_3 crystals on the surface of graphite with different orientation angles θ.

Aiming to clarify the influence factors of the critical orientation angle, we simulate the growth of aluminum carbide with different orientations and its development on graphite particles in various sizes. For the following discussion in this paper, we concentrate on the orientation in the range of $[0°, 90°]$, which is due to the axisymmetry with respect to $\theta = 0°$. Fig. 6.3(a) portrays the time evolution of the microstructures for two different setups: $\theta_1 = 59°$ and $60°$. In both cases, the radii of the graphite and the aluminum carbide are fixed at $R_g = 40$ and $R_1 = 16$, respectively. In the former case, the aluminum carbide gradually grows with time, whereas in the latter case, the aluminum carbide diminishes and vanishes eventually. A comparison of these two cases quantifies the critical orientation for $R_g = 40$. For this setup, we have also examined the critical orientation angles for a series of R_1, e.g., $R_1 = 17$ and $R_1 = 18$, and the results show the increase of $\theta_{1,\text{crit}}$, with the radius R_1. For a fixed $R_1 = 17$, the critical orientation is $66°$ when $R_g = 40$. An effect of the base radius R_g on the critical orientation is depicted in Fig. 6.3(b). When $R_g = 40$, the Al_4C_3 nuclei with $66°$ can grow at the graphite surface. However, when the size of graphite expands a thousand times, the aluminum carbide finally disappears. This setup is closer to the experimental observation (Fig. 2.16(a)), and such a setup, with a high ratio of R_g/R_1, shall be focused on in the following sections. Fig. 6.3(c) illustrates the critical growth angle as a function of the initial nucleus radius. The green, red, blue, and black dashed lines correspond to graphite with a base radius of 40, 200, 400, and 40000, respectively. In all four cases, the critical orientation angle increases with the initial radius R_1. The critical growth angle of the aluminum carbide is determined by two factors: one is the supersaturation, which is responsible for the growth, and the other is the surface energy (capillary force) against the growth. As the supersaturation is set constant, the driving force for the growth is fixed. The capillary force $\sigma(\theta)\kappa$ decreases with an increase in the radius of the aluminum carbide. Hence the anti-force for the growth of the aluminum carbide is inversely proportional to the radius of the Al_4C_3 nucleus.

A comparison between the four cases, with different R_g for a constant R_1, shows that the critical angle has a negative correlation with the radius of graphite. It is noteworthy that the critical angle shows a relatively larger difference between $R_g = 40$ and $R_g = 40000$, for the case R_1=19, than for the other three cases. This difference is discussed later in this section. Next, we shed light on the underlying mechanism for the critical orientations, by analyzing the concentration distribution of carbon.

Fig. 6.4 presents the morphological evolutions and the corresponding concentration distributions with time for three cases: (a) R_1=17, $R_g = 400$, $\theta_1 = 0°$, (b) R_1=17, $R_g = 400$, $\theta_1 = 65°$, and (c) R_1=17, $R_g = 40000$, $\theta_1 = 65°$. As illustrated in Fig. 6.4(a)-i, the Al_4C_3 particle grows along the normal direction of the graphite surface. The concentration distributions around the Al_4C_3 phase at the time $t = 150$ and $t = 500$, are shown in Fig. 6.4(a)-ii. The yellow dashed lines represent the contour of the Al_4C_3 phase, i.e., $\varphi_{Al_4C_3} = 0.5$, and the solid lines describe the isoconcentration. The symmetric configuration of Al_4C_3 engenders a symmetric concentration distribution, while the concentration distribution becomes asymmetric for the cases (b) and (c). The asymmetric concentration distribution is caused by the growth of the Al_4C_3 phase, with a non-zero orientation angle. As a result, the concentration gradient on the right side of the Al_4C_3 phase is greater than the one on the other side. With an increase in R_g, the distance between the right interface of the Al_4C_3 particle and the graphite surface is decreased. Thus, the concentration gradient on the right side of the Al_4C_3 phase is more pronounced than the one in case (b). Because of these different concentration distributions, the Al_4C_3 particle facilitates the fastest growth rate in case (a), a medium growth rate in (b), and shrinks eventually in case (c).

As discussed in section 2, the deviation of the interfacial concentration from the equilibrium concentration leads to a difference in the grand chemical potential, which provides the driving force for the phase transition. We use the tip concentration of Al_4C_3 to characterize the driving force for its morphological evolution. Fig. 6.5 describes the tip concentration as a function of time. In Fig. 6.4, the blue, green, and red lines respectively correspond to the cases (a), (b) and (c). It is observed that the tip concentration in case (a) maintains a constant, as well as the supersaturation concentration. This supersaturation is sufficient to surmount the surface energy, giving rise to the growth of Al_4C_3. In the case (b), the tip concentration descends at the beginning and increases after a certain time. The decrease in the concentration emanates from the concentration gradient on the right side of Al_4C_3, which leads to a diffusion flux of carbon from the tip of Al_4C_3 to the graphite surface (see Fig. 6.4(b)). With the growth of aluminum carbide, the tip is far from the graphite and the concentration gradient is decreased, so that more C-atoms accumulate ahead of Al_4C_3. Since the tip concentration in case (b) is always less than the one in case (a), the evolution rate in (b) is slower than in (a). It is noteworthy that the concentration in the case (c) drops down quickly. This quick decline in the concentration is due to the same reason as in (b), but the concentration gradient is larger than that in (b), so that the tip concentration in (a) decreases faster than in (b). This pronounced concentration gradient is engendered from the fact that the distance between the tip of Al_4C_3 and the graphite is reduced when increasing R_g. Since the tip concentration cannot provide sufficient driving force for the phase transition, the needle structure shrinks and vanishes eventually.

In a similar way, we explain the difference of the critical orientation angle between $R_g = 40$ and $R_g = 40000$, enlarging with R_1, shown in Fig. 6.3(c). Fig. 6.6 depicts the tip concentra-

tion of the Al_4C_3 crystal as a function of time for different radii of graphite. The green, red, blue, and black lines correspond to graphite with a base radius of 40, 200, 400, and 40000, respectively. Fig. 6.6(a) and (b) represent the distinct cases for $R_1 = 16$, $\theta = 59°$ and $R_1 = 19$, $\theta = 78°$, respectively. In both cases, the Al_4C_3 nucleus grows for $R_g = 40$ and shrinks for other base radii. A comparison between the two cases shows that the tip concentration in (b) declines faster than the one in (a), for each graphite radius. These two different decreasing rates are attributed to the fact that the concentration distribution in (b) is more asymmetrical, due to a larger orientation angle. The faster reduction speed of the tip concentration in (b) results in a bigger tip concentration difference between $R_g = 40$ and $R_g = 40000$ at the same time. In order to rise the tip concentration, to ensure the growth of the nuclei, the difference of the critical orientation angle between $R_g = 40$ and $R_g = 40000$ is greater in (b) than the one in (a), as observed in Fig. 6.3(c). In Fig. 6.6(b), the red, blue, and black lines almost overlap with each other, which implies the same critical orientation angle for different graphite radii.

6.3. The growth of two adjacent Al_4C_3 particles on the graphite surface

When two Al_4C_3 nuclei in proximity grow at the surface of graphite, the concentration fields may overlap with each other, affecting the critical orientation angle. In this section, we investigate the growth of two Al_4C_3 particles on a flat graphite surface, influenced by three factors: the distance D between them and the orientations θ_1 and θ_2. As an exemplary study, the radius of the aluminum carbide is set as $R_1 = R_2 = 18$, where the individual critical orientation angle is 67°.

Figs. 6.7(a)-(d) illustrate the growth behaviors of Al_4C_3 under different conditions: (a) $\theta_1 = 35°$, $\theta_2 = 64°$, and $D = 40$, (b) $\theta_1 = 45°$, $\theta_2 = 64°$, and $D = 40$, (c) $\theta_1 = 45°$, $\theta_2 = 64°$, and $D = 60$, (d) $\theta_1 = 45°$, $\theta_2 = 63°$, and $D = 40$. In the case (a), both particles grow with time. When increasing θ_1 from 35° to 45° (case (b)), particle 2 firstly grows for a relatively short while and then shrinks with time. However, varying D from 40 (case (b) to 60 (case (c)) or decreasing θ_2 from 64° to 63° (case (d)) again leads to the growth of particle 2. Changing the distance D for a series of θ_2, i.e., $\theta_2 = 63°, 64°, 65°, 66°$, we obtain the critical orientation angle $\theta_{1,\mathrm{crit}}$, with which both particles can grow simultaneously, as shown in Fig. 6.7(e). In all cases, $\theta_{1,\mathrm{crit}}$ is less than the individual critical orientation angle 67° and increases with D. When $\theta_2 = 63°$ (red circles), there is an upper critical distance D^*_{max}, above which the growth of the two particles is independent from each other, and the critical angle follows the individual one. When $\theta_2 = 66°$ (green triangles), we observe a lower critical distance D^*_{min}, below which particle 2 cannot survive for all $\theta_1 \in [0°, 90°]$. For θ_2 between 63° and 66°, $\theta_{1,\mathrm{crit}}$ linearly increases with D. It is noted that in these cases, upper and lower critical distances exist in principle. The lower critical distance is expected to be less than D^*_{min}. But a further decrease in D leads to an overlap of the diffuse interfaces of the adjacent particles, preventing them from precisely determining the lower critical distance.

6.4. Microstructures for two adjacent Al_4C_3 particles

In the previous section, we set $R_1 = R_2 = 18$ and find that the growth of particle 2 is inhibited with an increasing θ_1. According to the discussion in section 6.2, the radius of aluminum carbide also has an influence on the particle growth. In this section, we study different morphological evolutions for three cases, as shown in Fig. 6.8(a)-(c): (a) $R_1 = R_2 = 18$, (b) $R_1 = 18$, $R_2 = 16$, and (c) $R_1 = 16$, $R_2 = 18$. In each case, we increase θ_1 while fixing θ_2 and D: (a) $\theta_1 = 35^\circ \longrightarrow 45^\circ \longrightarrow 55^\circ$, $D = 40$ and $\theta_2 = 64^\circ$, (b) $\theta_1 = 46^\circ \longrightarrow 56^\circ \longrightarrow 59^\circ$, $D = 35$ and $\theta_2 = 47^\circ$, (c) $\theta_1 = 30^\circ \longrightarrow 40^\circ \longrightarrow 50^\circ$, $D = 35$ and $\theta_2 = 64^\circ$.

In case (a), where $R_1 = R_2$, the growth of particle 2 is suppressed by particle 1, with an increase in θ_1. Meanwhile, the growth velocity of particle 1 declines. In case (b), where $R_1 > R_2$, an increase in θ_1 leads to a transition of particle 2, from growth to shrinkage, and then to growth. In case (c), where $R_1 < R_2$, the growth of particle 2 is inhibited in (c)-(i) and (c)-(ii), while increasing θ_1. A further increase in θ_1 results in the shrinkage of particle 1 itself, while particle 2 thrives. The underlying mechanisms for the particle competition effect are as follows: On the one hand, the increase in θ_1 leads to a decreased tip distance between the two particles. As a result, the suppression of particle 1 on particle 2 becomes more pronounced, as demonstrated in (a)-(ii), (a)-(iii), and (b)-(ii). With an increase in θ_1, the growth velocity of particle 1, on the other hand, is significantly reduced, which thus weakens the influence of particle 1 on particle 2. This effect is observed in case (b)-(iii), where the tip of particle 2 surpasses the one of particle 1, before a complete suppression by the latter one. It is emphasized that the impact of particle 2 on particle 1 is also of significance. As depicted in case (c)-(iii), particle 1 should grow by itself, but vanishes thoroughly under the constraint of the vying particle 2.

In order to provide insight into the competing effect between the two particles, we scrutinize the concentration distribution around the Al_4C_3 particles. Fig. 6.9(a) maps the concentration fields of carbon for the case where particle 1 completely suppresses particle 2, corresponding to Fig. 6.8(a)-(ii). As can be seen in Fig. 6.9(a), the tip concentration of particle 1 is greater than that of particle 2, at the time $t = 1000$ (left image). Due to the suppression, the difference in the tip concentrations is enlarged at $t = 1800$ (right image). The tip concentrations for particle 1 and 2 with time are displayed by the blue and black lines in Fig. 6.9(d). While the tip concentration of particle 2 quickly drops down, the one for particle 1 almost remains a constant. When the declining tip concentration is below the threshold, whose driving force is not sufficient to surmount the capillary force, the particle cannot survive. Fig. 6.9(b) illustrates the concentration distribution for Fig. 6.8(b)-(iii). At the time $t = 1000$, the tip concentrations of both particles are comparable. When the tip of the right particle surpasses the left one, the right particle gains more carbon species from the liquid phase, so that its tip concentration is greater than the one of the left particle. In this case, the movement of the left particle is governed by two mechanisms. One is the supersaturation, which allows the motion of the particle-liquid interface. The other one is Young's law which drives the evolution of the triple junction of the two particles with the liquid. Although the supersaturation for the left particle is less than the supersaturation for the right one, it still can move forward, driven by the triple junction. The concentration distribution corresponding to Fig. 6.8(c)-(iii) is depicted in Fig. 6.9(c). The tip concentration

of the left particle declines rapidly, and the left particle shrinks prior to the formation of a triple junction.

6.5. Summary

By using a phase-field method, we have investigated the growth of the anisotropic intermetallic phase in an Al-C binary system, with inputs from the CALPHAD database. It has been shown that a concentration or chemical potential gradient is required for the formation and growth of the intermetallic phase, in contrast to the ideal assumption for the stoichiometric phase in the phase diagram. Due to the anisotropy of Al_4C_3, this intermetallic phase forms a needle-like structure, which is different from the emblematic microstructure of peritectic transition. By imitating the classical nucleation theory, we have presented and verified that the Al_4C_3 phase grows with a critical orientation angle.

Our simulation results show that the critical orientation angle for a single Al_4C_3 particle depends on the radius itself and on the base radius of the parent graphite phase. The critical orientation angle decreases as the base radius increases. The reason is that the increasing base radius enhances the concentration gradient, which causes a diffusion obstacle for carbon from liquid to Al_4C_3. As a result, the concentration in front of Al_4C_3 declines with time. When the driving force is less than the capillary force, the needle structure begins to shrink and eventually disappears. With the size reduction of Al_4C_3, the increasing capillary force has a negative impact on the growth of this intermetallic phase, and therefore the critical orientation angle decreases.

Moreover, we have elucidated that when two needle structures with the same size are in proximity, as a result of the competing effect and the superimposed concentration fields between the particles, the critical orientation angle is less than the individual one. An additional parameter which affects the competing effect and therefore the critical orientation angle is the apart distance between the particles. It has been revealed that the critical orientation angle linearly increases with the distance. Most importantly, upper and lower critical distances have been identified with a variation in the orientation angle of particle 2(see Fig. 6.7). In addition, by varying the difference in the radii of the two particles and the orientation of particle 1, three typical competing effects have been obtained: (i) Particle 1 completely suppresses particle 2. (ii) Particle 2 surpasses particle 1. (iii) Particle 2 inhibits particle 1 conversely. By simulating the diffusion-reaction process in the Al-C system, we have clarified the mechanisms of the orientation selection in the phase transition from the energetic aspect, which is helpful to understand the growth orientation of the phase in other systems. In the future, we will investigate the orientation angle by using 3D simulations. In comparison with 2D simulations, an extra orientation angle shall be considered in the third dimension (see Fig. 2.16(d)).

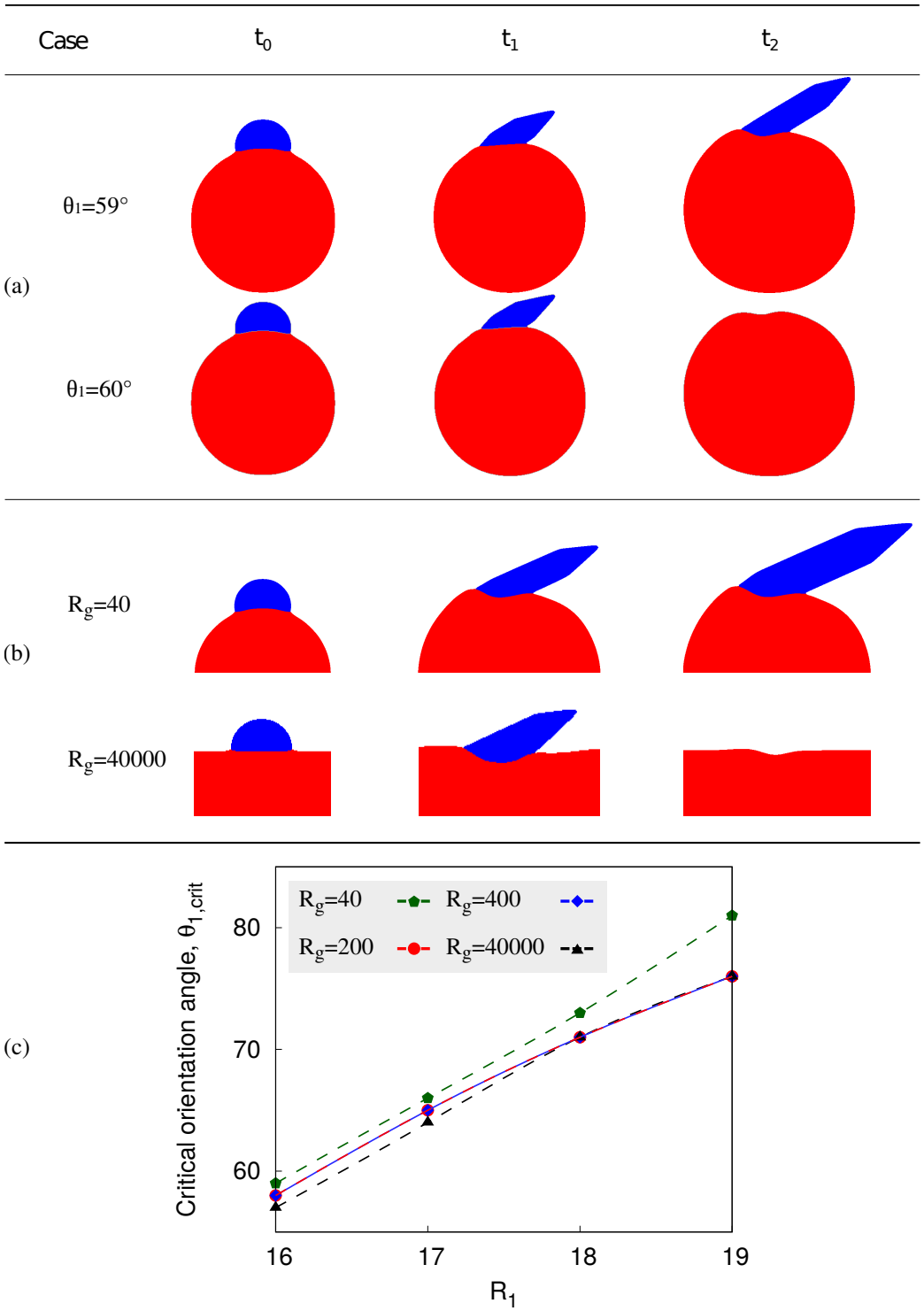

Figure 6.3.: The morphological evolution of Al_4C_3 under two different conditions: (a) Different orientation angles and (b) distinctly sized graphites. t_0, t_1, and t_2 represent the dimensionless time 0, 500, and 1000, respectively. (c) The critical orientation angle of Al_4C_3 $\theta_{1,\mathrm{crit}}$, as a function of its initial radius R_1, for different radii of graphite.

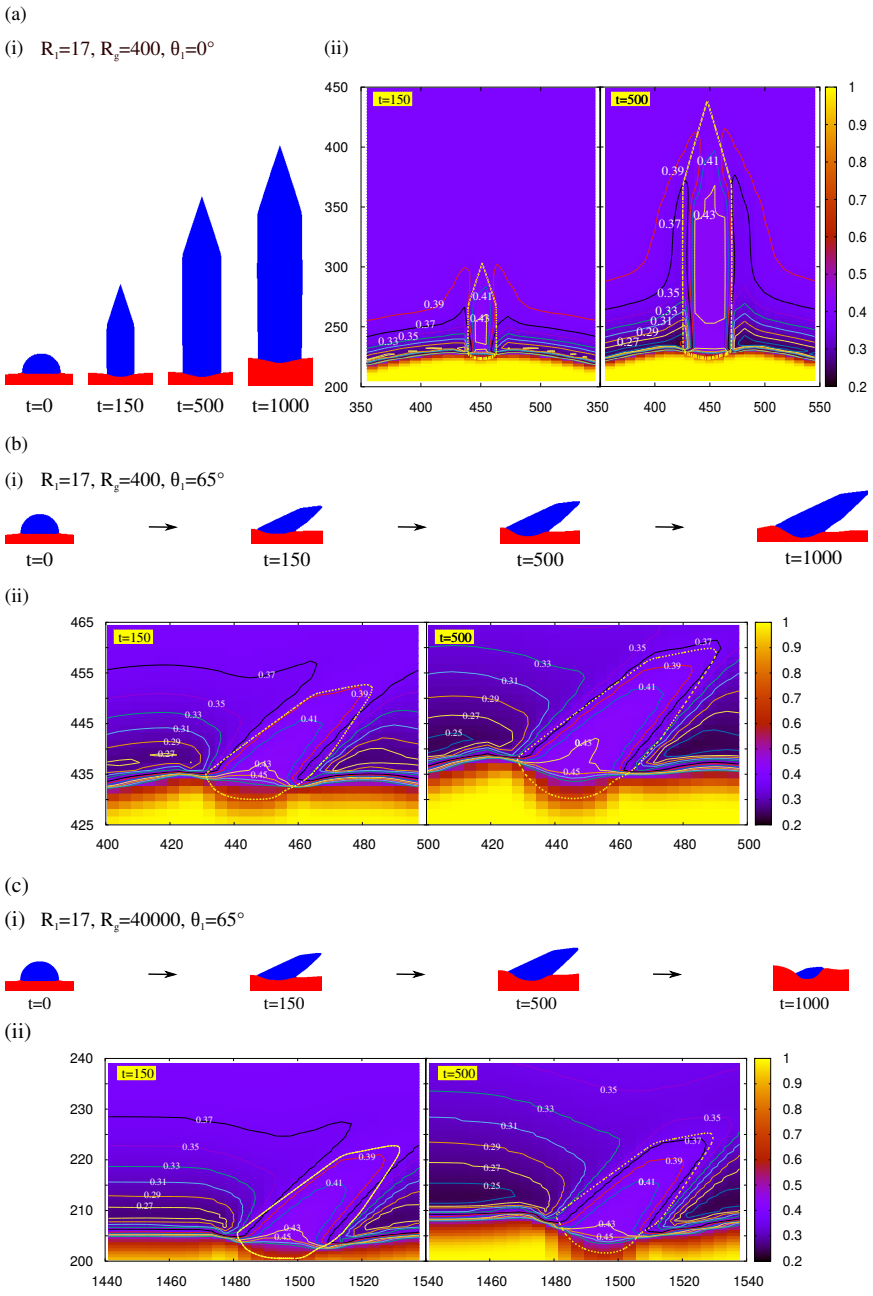

Figure 6.4.: The morphological evolution of Al_4C_3 on the graphite and the corresponding concentration distributions for three cases: (a) R_1=17, R_g = 400, and θ_1 = 0°, (b) R_1=17, R_g = 400, and θ_1 = 65°, (c) R_1=17, R_g = 40000, and θ_1 = 65°.

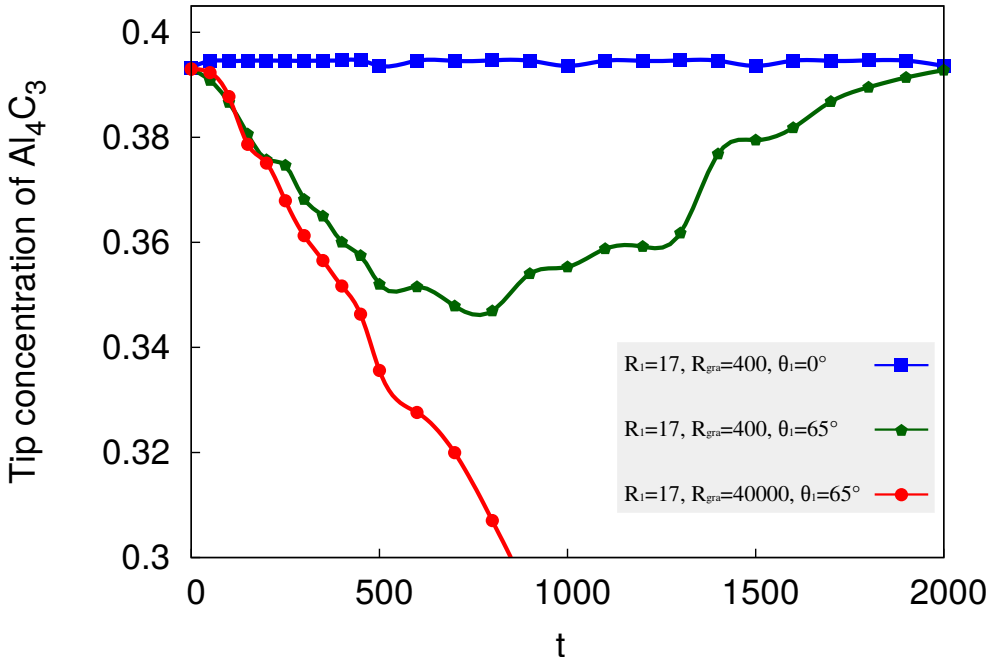

Figure 6.5.: The tip concentration of the Al_4C_3 crystal, as a function of time corresponding to the morphological evolutions in Fig. 6.4.

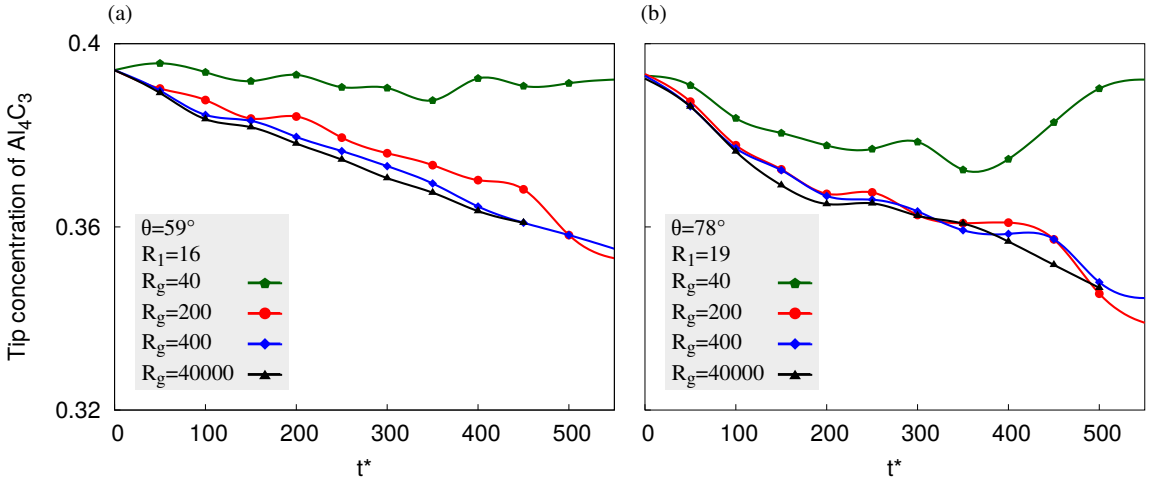

Figure 6.6.: The tip concentration of the Al_4C_3 crystal, as a function of time, for different radii of graphite: (a) $\theta = 59°$, R_1=16 and (b) $\theta = 78°$, R_1=19.

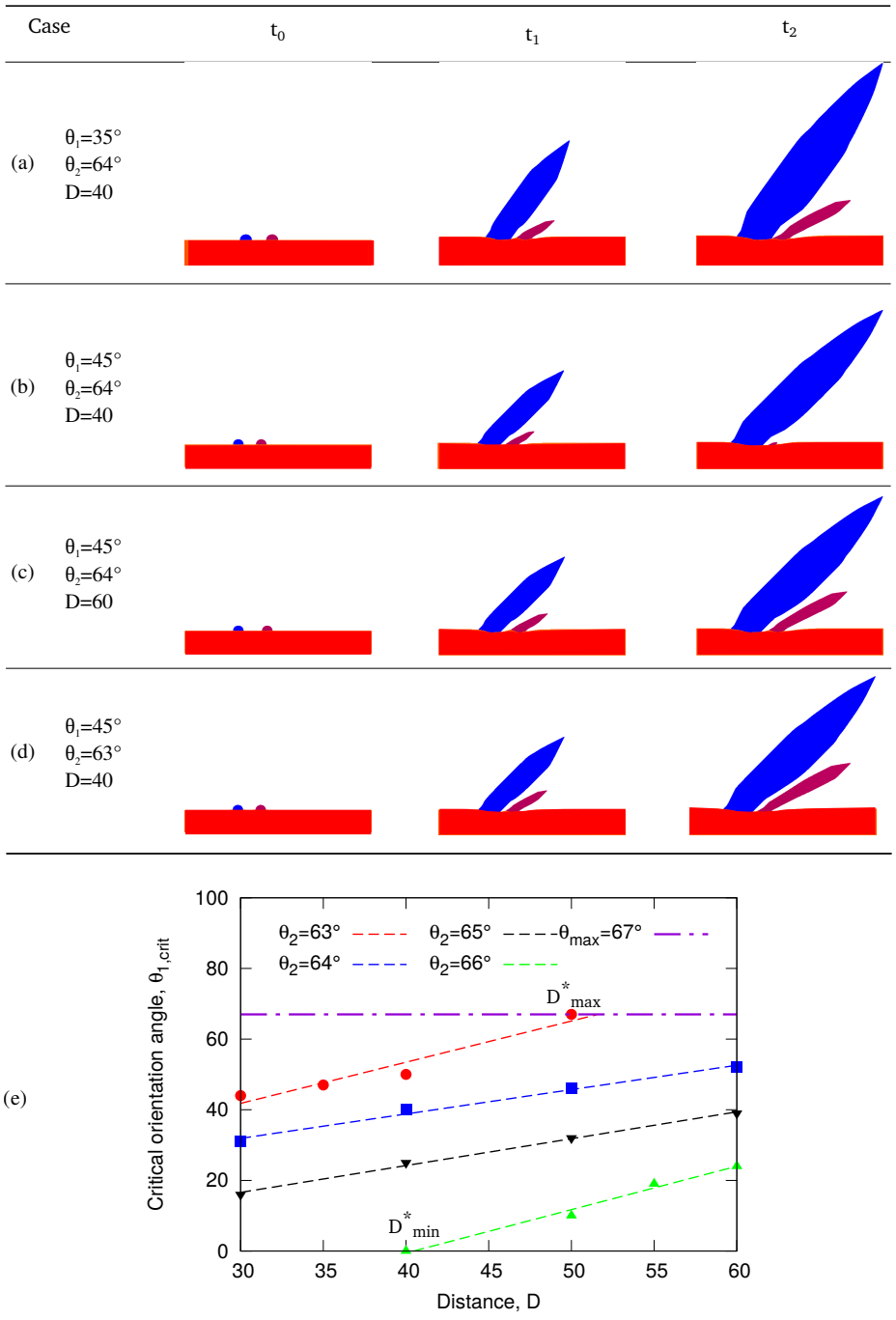

Figure 6.7.: (a)-(d) Morphological evolutions of two adjacent Al_4C_3 particles for four cases: (a) $\theta_1 = 35°$, $\theta_2 = 64°$, and $D = 40$, (b) $\theta_1 = 45°$, $\theta_2 = 64°$, and $D = 40$, (c) $\theta_1 = 45°$, $\theta_2 = 64°$, and $D = 60$, (d) $\theta_1 = 45°$, $\theta_2 = 63°$, and $D = 40$. t_0, t_1, and t_2 represent the dimensionless time 0, 1000, and 1800, respectively. (e) The critical growth angle of particle 1, as a function of the distance between two particles, for different orientation angles of particle 2.

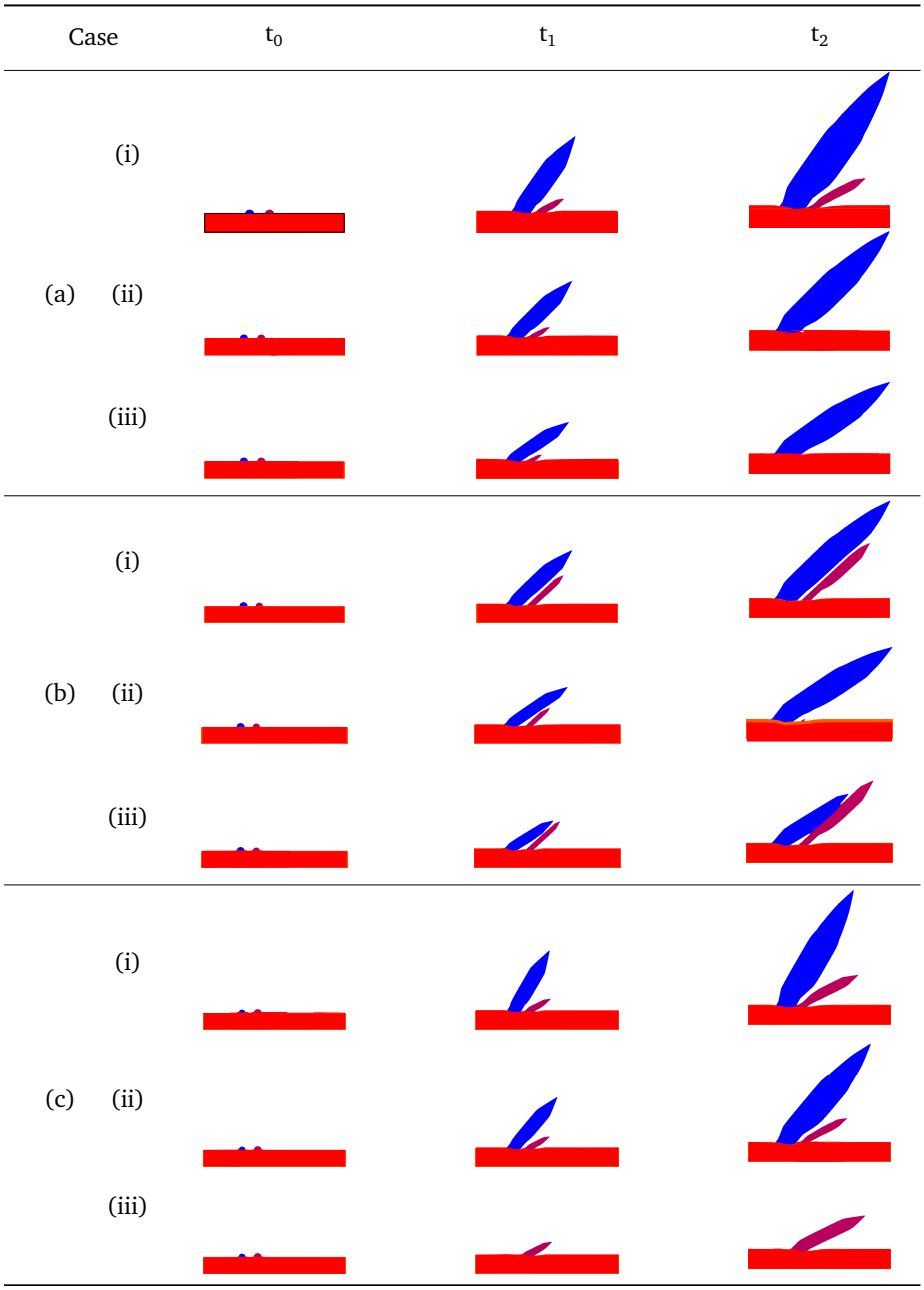

Figure 6.8.: Competing effect of two adjacent particles. t_0, t_1, and t_2 represent the dimensionless time 0, 1000, and 1800, respectively: (a) $R_1 = R_2 = 18$, $D = 40$, and $\theta_2 = 64°$, (i) $\theta_1 = 35°$ (ii) $\theta_1 = 45°$ (iii) $\theta_1 = 55°$, (b) $R_1 = 18$, $R_2 = 16$, $D = 35$, and $\theta_2 = 47°$, (i) $\theta_1 = 46°$ (ii) $\theta_1 = 56°$ (iii) $\theta_1 = 59°$, (c) $R_1 = 16$, $R_2 = 18$, $D = 35$, and $\theta_2 = 64°$, (i) $\theta_1 = 30°$ (ii) $\theta_1 = 40°$ (iii) $\theta_1 = 50°$.

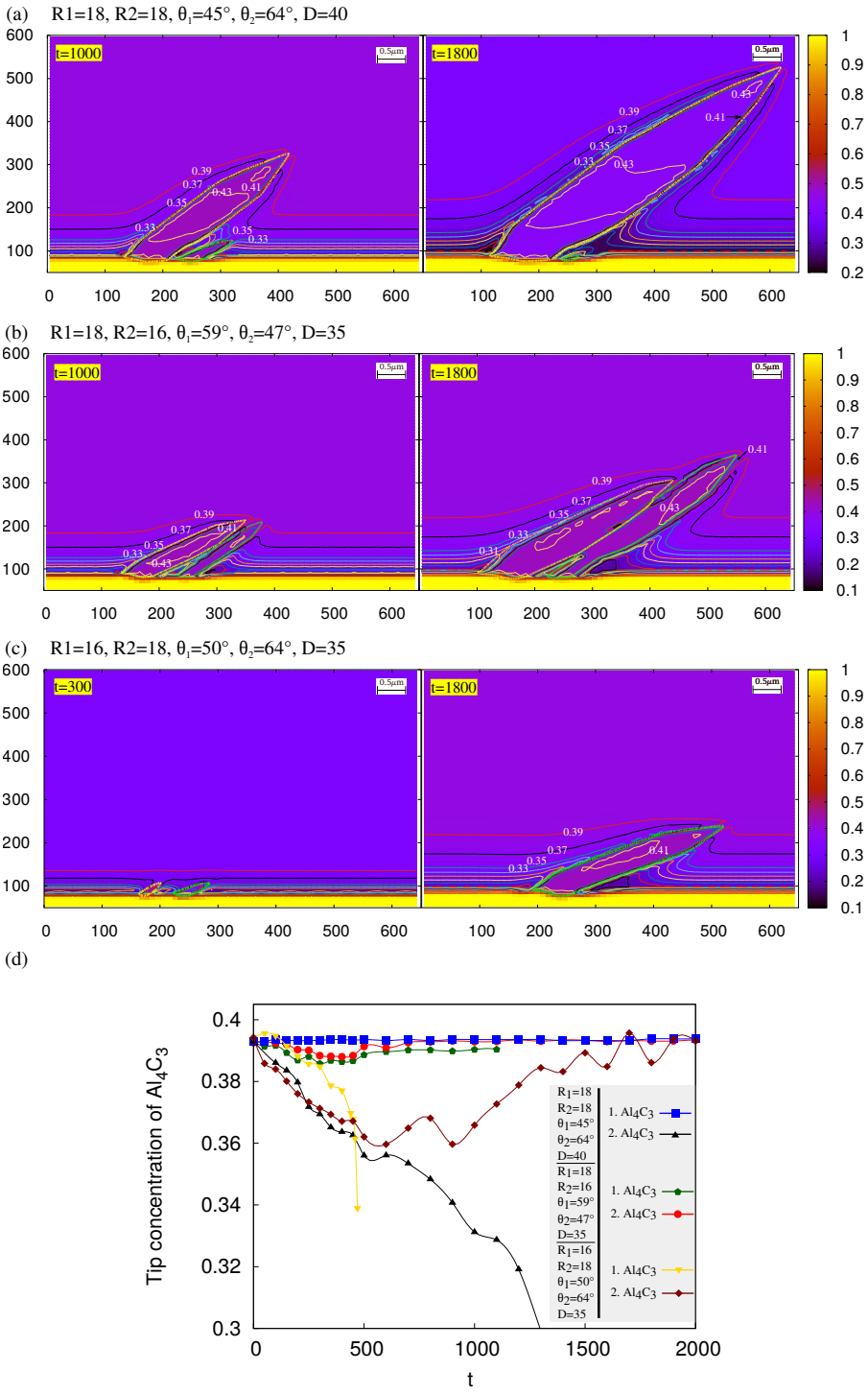

Figure 6.9.: The morphological evolution of two adjacent Al_4C_3 particles on the surface of graphite, and the corresponding concentration distributions for three cases: (a) $\theta_1 = 59°$, $\theta_2 = 47°$, $D = 35$, $R_1 = 18$, and $R_2 = 16$, (b) $\theta_1 = 45°$, $\theta_2 = 64°$, $D = 40$, $R_1 = 18$, and $R_2 = 18$. (c) The tip concentration as a function of time for (a)-(c).

7. Mo-Si-Ti ternary system: eutectic transformation and quasi-peritectic reaction

According to the previous study [136], the formation of the lamellar pair (TS and β) occurs at the surface of two different particles: the primary solidified β phase and the MS phase. The former one is caused by a eutectic transformation ($L \rightarrow Ti(Mo)_5Si_3 + \beta(Mo,Si,Ti)$) and the latter one arises from a four-phase reaction ($L + Mo(Ti)_3Si \rightarrow Ti(Mo)_5Si_3 + \beta(Mo,Si,Ti)$). Aiming to explore the influencing factors of the microstructure of the lamellar pair (TS and β) formed by different phase transition processes, we simulate isothermal eutectic transformation as well as the four-phase reaction of Mo-Si-Ti alloy by using the phase-field model in 2-D and 3-D domains. A 3-D phase-field model with an anti-trapping current, coupled with the diffusion equation, is utilized to simulate the occurrence of phase transitions and the growth of intermetallic compounds. For both phase transformation processes, we shed light on the microstructural evolution of the lamellar pair with different supersaturations in liquid and with different lamellar spacings. Since the 3-D simulations are closer to the reality, we simulate the rod eutectic growth in 3-D domains to clarify the influence of neighboring particles. The main part of this chapter was published in Ref. [186].

7.1. Simulation setup

In the following discussion, we simulate the growth of lamellar pair ($Ti(Mo)_5Si_3$ and β(Mo,Si,Ti) phases) with different melt compositions and their evolution with various lamellar spacing during a eutectic transformation and a four-phase reaction. The interface thickness is set to be 0.06 μm in order to keep the simulation stable. The reason for this setting is explained in supplementary document. For the eutectic transformation, we establish a cooling situation at fixed composition along the equilibrium phases in the phase diagram and initially fill a semicircular $Ti(Mo)_5Si_3$ nucleus at the interface between the liquid and β(Mo,Si,Ti) phases. For the four-phase reaction, two semicircular particles $Ti(Mo)_5Si_3$ and β(Mo,Si,Ti) are placed at some distance next to each other on top of the $Mo(Ti)_3Si$ phase and surrounded by the liquid. The other simulation parameters are listed in Table 7.1. We use the following way to obtain the diffusion coefficients for the lack of direct experimental data in Mo-Si-Ti system. According to Ref. [214], the diffusion coefficients of molybdenum and tantalum in the melt are related to their melting points and show almost the same dependence on the homologous temperature T_h, which is defined as $T_h = T/T_m$ (T_m is the melting temperature). Based on this result, we assume that titanium

Symbol	Description	Value
Δt	Time step	0.5×10^{-7} s
Δx	Space step	0.5×10^{-8} m
$\sigma_{i/j}$	Interfacial energy	$1\,\mathrm{J\,m^{-2}}$
D^L_{Mo}	Diffusion coefficient of Mo in the liquid phase	$6.6 \times 10^{-9}\,\mathrm{m^2\,s^{-1}}$ [214]
D^L_{Ti}	Diffusion coefficient of Ti in the liquid phase	$6.6 \times 10^{-9}\,\mathrm{m^2\,s^{-1}}$
D^L_{Si}	Diffusion coefficient of Si in the liquid phase	$6.6 \times 10^{-9}\,\mathrm{m^2\,s^{-1}}$
D^S_{Mo}	Diffusion coefficient of Mo in the solid phases	$0.5 \times 10^{-9}\,\mathrm{m^2\,s^{-1}}$ [216]
D^S_{Ti}	Diffusion coefficient of Ti in the solid phases	$0.5 \times 10^{-9}\,\mathrm{m^2\,s^{-1}}$ [216]
D^S_{Si}	Diffusion coefficient of Si in the solid phases	$0.5 \times 10^{-9}\,\mathrm{m^2\,s^{-1}}$

Note: i, j = liquid, $Ti(Mo)_5Si_3$, β(Mo,Si,Ti), $Mo(Ti)_3Si$

Table 7.1.: Parameters for the phase-field simulations in Mo-Si-Ti system.

and silicon have similar dependence on T_h, and calculate their diffusion coefficients in melt for the present study by D^L_{Ti} =D^L_{Si} =$6.6 \times 10^{-9}\,\mathrm{m^2\,s^{-1}}$ (2216 K). Through comparing D^L_{Ti} with the data $5.3 \times 10^{-9}\,\mathrm{m^2\,s^{-1}}$ (2000 K) from [215], it is reliable to set the diffusion coefficient for all three components (Mo, Si, Ti) in liquid phase with the same value $6.6 \times 10^{-9}\,\mathrm{m^2\,s^{-1}}$. For the diffusion coefficients in solid phases, we use the value based on the data from [216]. In Ref. [216], the self-diffusion of titanium D^s_{Ti} and impurity diffusion coefficients of molybdenum D^i_{Mo} in β-Ti matrix with body-centered cubic structure are calculated, which has the same crystalline structure as the β(Mo,Si,Ti) phase. After a linear extrapolation to the temperature 2216 K, we obtain $D^s_{Ti} = 1 \times 10^{-9}\,\mathrm{m^2\,s^{-1}}$ and $D^i_{Mo} = 1 \times 10^{-10}\,\mathrm{m^2\,s^{-1}}$ approximately. Due to the great difference in the diffusion coefficient between liquid and solid phases and the fact that the phase transformation in the present study is caused by a supersaturation in liquid, we set the diffusion coefficients in all solid phases of all components with the same value for simplification. In addition, assumptions referring to the common interfacial energy $1\,\mathrm{J\,m^{-2}}$ in alloy system [217, 218] are made to assign a suitable value for the interfacial energies between each two phases. The influence of different interfacial energies on the morphological evolution is investigated in a forthcoming paper.

In the following study, the Neumann boundary condition for all fields is applied at the solidified end of the domain. An infinite domain perpendicular to the solidification front is modeled by periodic boundary condition. At the liquid end of the domain, a constant flux of melt is realized by the Dirichlet boundary condition. Considering this infinite flux of melt, the negligible evolution of the solidified phases, and the reduction in the computational effort, we only simulate the region around the solidification front. This is achieved by a moving window technique [219], which is controlled by the height of solidification front.

7.2. 2-D Simulation: morphological evolution of lamellar pair

In this section, we focus on the growth of lamellar pair, when the TS nucleus sits on the surface of β particle. As λ increases, the radius of TS nucleus maintains at $r = 0.05$ µm, which is the critical nucleation size for TS particle under the smallest supersaturation

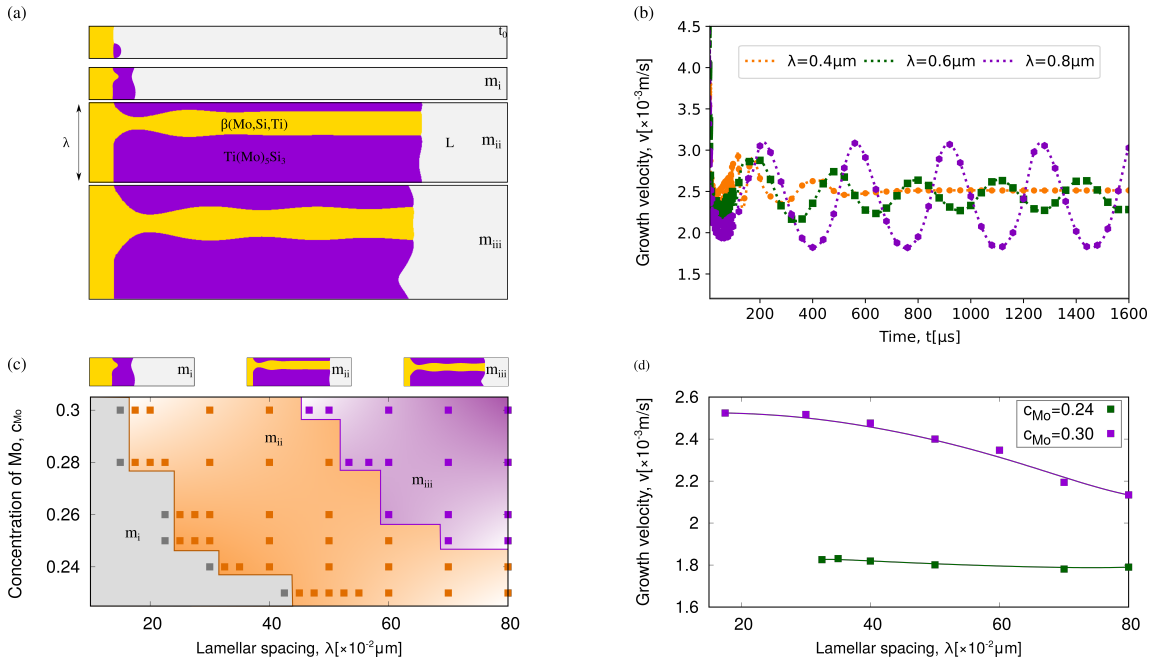

Figure 7.1.: (a) Three typical morphologies of the lamellar pair: (m_i) The engulfment of β particle by the TS phase (unstable growth mode), (m_{ii}) The lamellar structure with a planar TS-β interface (stable growth mode), and (m_{iii}) The lamellar structure with an oscillatory TS-β interface (metastable growth mode). (b) Growth velocity of β phase v as a function of time for the cases with lamellar spacing λ =0.4 µm, 0.6 µm, and 0.8 µm, respectively. (c) The morphology regime diagram describing the three growth modes for six different liquid compositions: 23Mo-56Ti-21Si, 24Mo-55Ti-21Si, 25Mo-54Ti-21Si, 26Mo-53Ti-21Si, 28Mo-51Ti-21Si, and 30Mo-49Ti-21Si and for different lamellar spacings from 0.1-0.8 µm. (d) Growth velocity as a function of lamellar spacing λ for the cases with c_{Mo} = 0.24 and 0.30.

based on the classical nucleation theory. Fig. 7.1(a) portrays the morphological evolution of the lamellar pair with different lamellar spacings λ. A semicircular nucleus of the TS phase is initially placed on the L-β interface. With increasing λ, three possible final morphologies are observed: (m_i) The engulfment of β particle by the TS phase (unstable growth mode), (m_{ii}) The lamellar structure with a planar TS-β interface (stable growth mode), and (m_{iii}) The lamellar structure with an oscillatory TS-β interface (metastable growth mode). When λ is relatively small, the distance between adjacent TS particles decreases and the growth competition between the β phase and the neighboring TS phase is more pronounced. As a result, the β particle is overgrown by the adjacent TS grains resulting in an unstable growth mode (type m_i). To better explore the underlying physical mechanism for the stable and metastable growth modes, we analyze the variation of the growth velocity of β phase with time. Fig. 7.1(b) exemplifies its growth velocity v as a function of time for the cases with lamellar spacing λ =0.4 µm, 0.6 µm, and 0.8 µm, which are shown by the orange, green, and violet lines, respectively. The composition of melt for all three cases is fixed at 30Mo-49Ti-21Si. For the case with λ =0.4 µm, the growth rate of β phase

converges to a constant value after the initial oscillation, whereas the growth rates for other two cases with larger λ oscillate around a particular value. With increasing lamellar spacing, the growth velocity shows a transformation from no oscillation to oscillation corresponding to the change from stable (type m_{ii}) to metastable (type m_{iii}) growth modes. The amplitude for the velocity of the oscillation increases with λ. In the present study, the eutectic transformation is caused by the supersaturation in melt, which indicates the concentration deviation in liquid from the equilibrium concentration with respect to TS- and β-phase. Hence, this phase transformation is mainly controlled by the diffusion of atoms from liquid. The whole diffusion process consists of two parts: one is the diffusion along the growth direction called axial diffusion, the other is the diffusion perpendicular to the growth direction called lateral diffusion. Due to the constant composition of melt for the three different lamellar spacings, λ =0.4 µm, 0.6 µm, and 0.8 µm, the variation of axial diffusion between these three cases can be ignored. For the lateral diffusion, its diffusion path increases with an enlargement in lamellar spacing. As a result, the coupling of these two diffusion processes exhibits a metastable state instead of the steady state like the case with relatively smaller λ. The underlying mechanism of this oscillation phenomenon in eutectic patterns has been investigated systematically in other papers [220, 221, 222].
In addition, we explore the influence of supersaturation in liquid on the growth of lamellar pair. The considered initial concentrations in liquid phase are 23Mo-56Ti-21Si, 24Mo-55Ti-21Si, 25Mo-54Ti-21Si, 26Mo-53Ti-21Si, 28Mo-51Ti-21Si, and 30Mo-49Ti-21Si. Here, the initial concentration of silicon in the liquid phase is constant in all six cases, hence there is only one independent component in the present study and the concentration of molybdenum c_{Mo} is used to represent the supersaturation in liquid. Fig. 7.1(c) portrays a regime diagram describing the three growth modes for the six considered liquid compositions. The regions marked by gray, orange, and violet correspond to the unstable (m_i), stable (m_{ii}), and metastable (m_{iii}) growth regions, respectively (see Fig. 7.1(a)). The boundaries between unstable and stable as well as between stable and metastable growth mode shift towards the direction of λ reduction as the supersaturation increases. Furthermore, the growth mode of lamellar pair for the case with a larger supersaturation in melt is more sensitive to the variation in lamellar spacing. In order to explain this finding, we compare the relationship between v and λ for the cases with c_{Mo} =0.24 and 0.30, as depicted by green and violet lines in Fig. 7.1(d). For the case of lamellar pair with oscillatory interface, we use an average growth velocity to represent its growth rate. With an enlarging λ, the growth rate decreases for both cases, which are in accordance with the prediction of Jackson-Hunt theory for the case with large lamellar spacing [223]. For the case with c_{Mo} =0.24, the growth velocity decreases slightly with increasing λ, whereas the growth velocity for the case with c_{Mo} =0.30 reduces rapidly. Moreover, the growth rate in the former case is always slower than the latter case. With increasing λ, the lateral diffusion becomes weaker, whereas the axial diffusion due to the same initial supersaturation in liquid remains almost unchanged. For small supersaturation, the axial diffusion is comparable with the lateral diffusion in a wide range of λ. In this case, the coupling of axial and lateral diffusion leads to a stable growth of the lamellar pair. In contrast, for large supersaturations, only when λ is relatively small where the lateral diffusion is pronounced. The axial diffusion is comparable with the lateral diffusion, resulting in stable growth. When λ increases, the lateral diffusion becomes weaker and cannot give rise to a steady diffusion process because

of strong diffusion in the axial direction. By this way, oscillatory growth is achieved when the supersaturation and the lamellar spacing are relatively large.

7.3. 3-D Simulation: rod eutectic growth

Next, we perform 3-D simulations to compare with 2-D simulations. The additional curvature contribution in 3-D affects the microstructural evolution in the eutectic transformation, which is not considered in 2-D simulation. In addition, the effect of neighboring particles on the rod eutectic growth should also be taken into account. In this section, we investigate the eutectic phase transformation in 3-D by varying the lamellar spacing in x and z directions. The differences between 2-D simulations and 3-D simulations are discussed.

Fig. 7.2(a) and (b) portray side views of the morphological evolution for the cases: (i) with same lamellar spacing $\lambda_x = \lambda_z = 0.5$ µm and (ii) with different lamellar spacing $\lambda_x = 0.5$ µm and $\lambda_z = 0.7$ µm, respectively. For both cases, a hemisphere TS particle with a radius of 0.125 µm is placed initially on the surface of β phase surrounded by the melt with the same composition 26Mo-53Ti-21Si. From the side view, a stable eutectic growth at the time $t_3 = 1540$ µs is observed in case (i), whereas the elimination of β phase and the split of TS phase are shown in case (ii). A comparison of the height for the solidification front between cases (i) and (ii) at the same time shows that a larger lamellar spacing in z dimension leads to a slower axial growth in case (ii). As a result, an unstable growth in x-y plane, namely the engulfment of β phase by TS phase, is observed in case (ii), instead of the stable growth in case (i). Fig. 7.2(c) depicts the top view of the rod eutectic growth corresponding to cases (i) and (ii). During this eutectic transformation, the growth of these two phases exhibits an anisotropic behaviour. The results show that the morphology depends on the ratio of the lamellar distances. Due to the unequal lamellar spacing in x and z directions, these two cases show distinguish morphological evolution.
For comparison, Fig. 7.2(d) and (g) illustrate 2-D simulation results of two cases: (1) The lamellar structure with a planar β/TS interface, when $\lambda = 0.5$ µm and (2) the lamellar structure with an oscillatory β/TS interface, when $\lambda = 0.7$ µm, respectively. The x-y cross section of the 3D case (i) is shown in Fig. 7.2(e). The x-y and y-z cross sections of the 3D case (ii) are illustrated in Fig. 7.2(f) and Fig. 7.2(h), respectively. All the cross sections from 3-D simulations are through the center of TS particle. A comparison between Fig. 7.2(d), Fig. 7.2(e), and Fig. 7.2(f) demonstrates that the engulfment of β phase occurs in 3-D, whereas the lamellar pair is stable in 2-D. For the cases with larger lamellar spacing, the eutectic growth in 2-D exhibits an oscillatory interface between the lamellar pair (see Fig. 7.2(h)), while the eutectic growth in 3-D reaches a steady state after a certain time and shows lamellar structure with a planar β/T interface finally. Under the same supersaturation in liquid and with the same lamellar spacing, the eutectic growth in 3-D displays the microstructure corresponding to the cases with smaller lamellar spacing or with lower supersaturation in 2-D. Owing to that the heights of solidification front are almost identical in cases with the same simulation conditions, for instance cases shown in Fig. 7.2(d), (e) and (f), the axial diffusion process is almost identical for all cases. The difference between 2-D and 3-D simulations is induced by the lateral diffusion. A

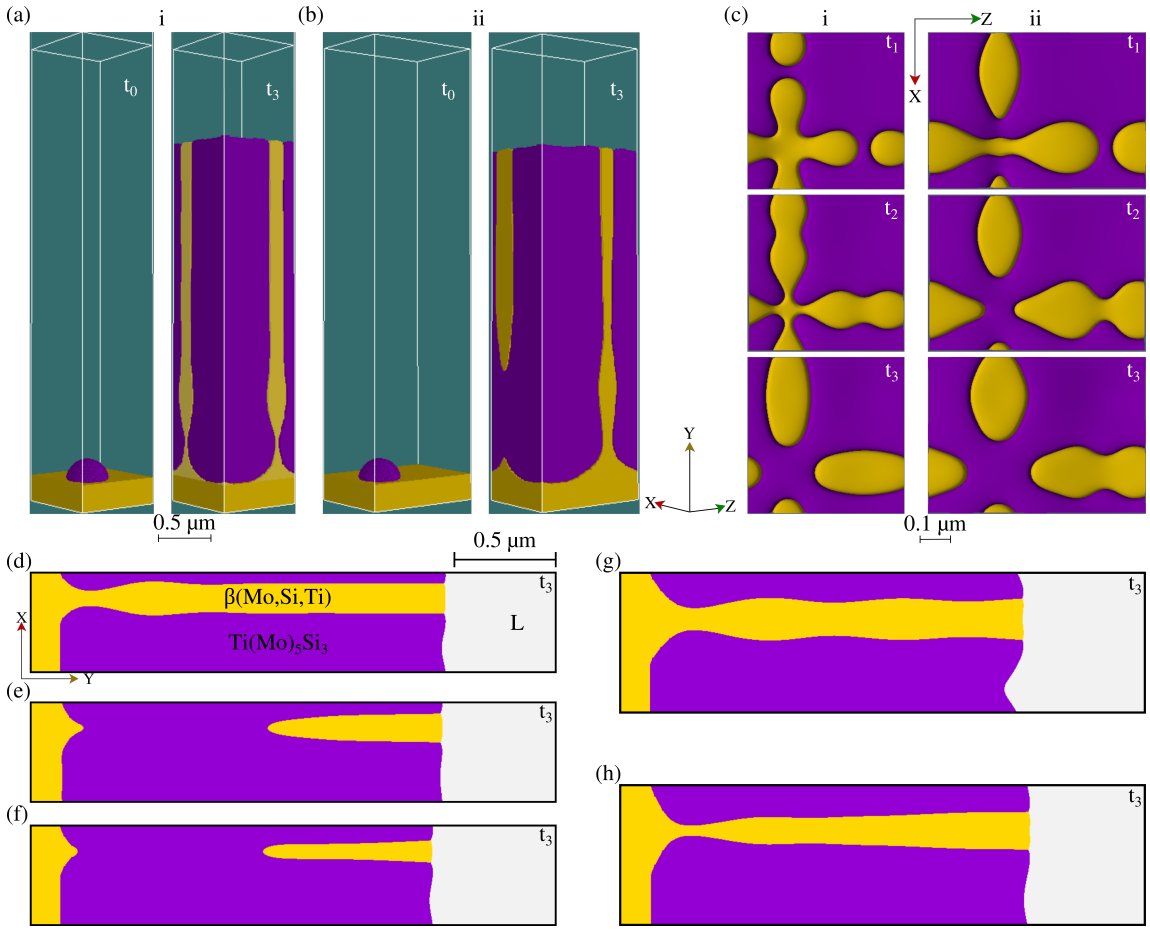

Figure 7.2.: (a) and (b) Side views of the morphological evolution for the cases: (i) with same lamellar spacing $\lambda_x = \lambda_z = 0.5$ µm and (ii) with different lamellar spacing $\lambda_x = 0.5$ µm and $\lambda_z = 0.7$ µm, respectively. (c) Top views of the rod eutectic growth corresponding to cases (i) and (ii). (d) and (g) 2-D simulation results of two cases: (1) The lamellar structure with a planar interface and (2) the lamellar structure with an oscillatory interface, respectively. The cross section of 3-D simulations corresponding to the cases: (e) The rod eutectic growth with $\lambda_x = \lambda_z$ in x-y plane, (f) the rod eutectic growth with $\lambda_x \neq \lambda_z$ in x-y plane, and (h) the rod eutectic growth with $\lambda_x \neq \lambda_z$ in y-z plane.

schematic illustration of the difference between 2-D and 3-D simulations is depicted in Fig. 7.3. The domain in our simulation is represented by solid lines and the adjacent domains are complemented by the dashed lines due to the periodic boundary condition. In 2-D simulations, only the diffusion flux in x direction is taken into consideration for lateral diffusion, whereas in 3-D, not only the fluxes in x and z directions, but also the fluxes from other directions, for example $\boldsymbol{j}_3$. The flux vector $\boldsymbol{j}_3$ can be split into a x- ($\boldsymbol{j}_{3,x}$) and a z-component ($\boldsymbol{j}_{3,z}$). This extra flux contribution in x direction leads to a faster lateral growth in x-y plane.

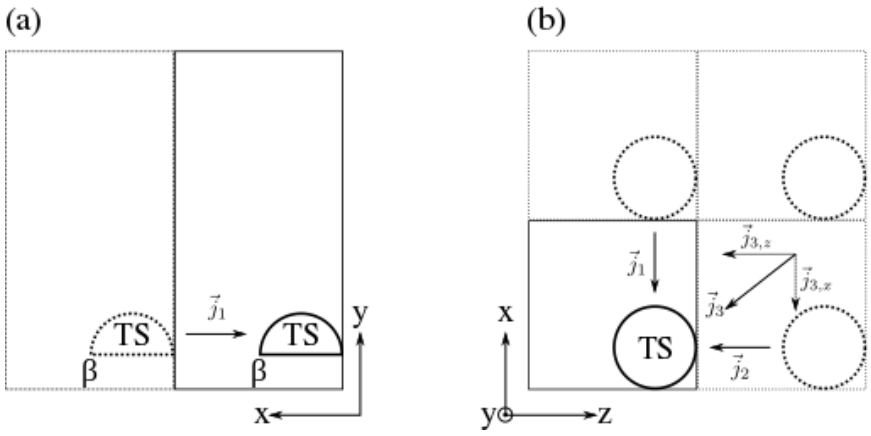

Figure 7.3.: Schematic illustration of the differences between 2-D and 3-D simulations.

7.4. Interfacial energy

The interfacial energy is defined as the required energy involved in creating unit area of new interface at constant temperature, volume and total number of moles [224]. In general, the interfacial energies between different phases are different and are challenging to be measured experimentally. Due to lack of precise experimental data for the interfacial energy between each two phases in Mo-Si-Ti system, we investigate how the morphological evolution of the lamellar pair is affected by the interfacial energies in this section. The

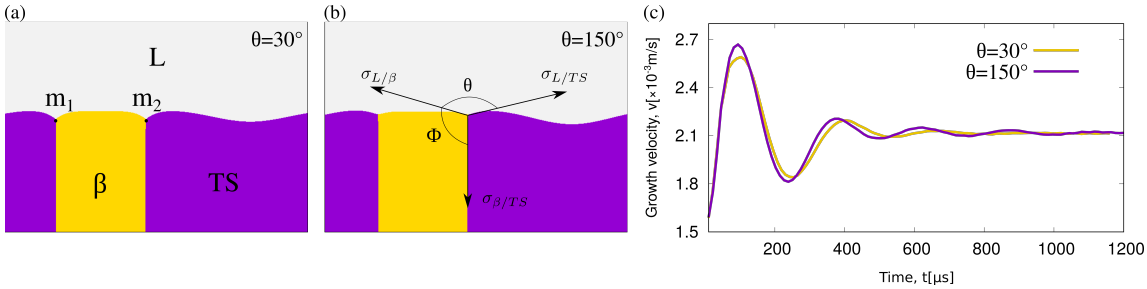

Figure 7.4.: (a) and (b) are the morphology of the solidification front of lamellae (TS and β phases) for the cases with the dynamic contact angle $\theta = 30°$ and 150°, respectively. (c) The temporal change of the growth velocity of β phase for the cases with different contact angle θ.

lamellar spacing is maintained as 0.5 µm, which ensures a stable lamellar structure for the considered melt compositions (see Fig.7.1(c)). Fig. 7.4(a) and (b) depict the morphology of the solidification front of lamellae (TS and β phases) for the cases with the equilibrium contact angle $\theta = 30°$ and 150°, respectively. The lamellar pair is surrounded by the melt with the composition 26Mo-53Ti-21Si. The contact angle θ is defined as the angle between the interfacial tension vectors $\sigma_{L/\beta}$ and $\sigma_{L/TS}$, as shown in Fig. 7.4(b). Through changing $\sigma_{\beta/TS}$, the equilibrium value of θ is manipulated, while keeping $\sigma_{L/\beta} = \sigma_{L/TS} = 1\,\mathrm{J\,m^{-2}}$. For the two cases of $\theta = 30°$ and 150°, the solidification morphology is almost same; the growth velocity of β phase converges to the same value after the initial oscillation (Fig. 7.4(c)).

Φ (°)	30	60	90	120	150
$\sigma_{L/TS}$ (J m^{-2})	1.93	1.73	1.41	1.00	0.52

Table 7.2.: The contact angle Φ and corresponding interfacial energy $\sigma_{L/TS}$.

The similar behavior in microstructure and growth velocity for the cases with different θ reveals that the interfacial energy between two solid phases has no significant influence on the morphological evolution of lamellae. When the interfacial energies between liquid

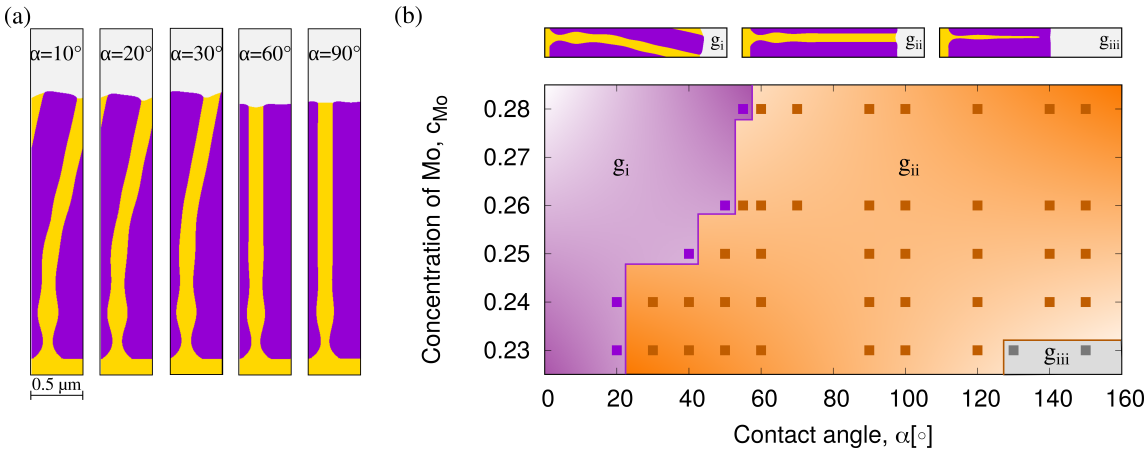

Figure 7.5.: (a) The solidification morphology for the cases with contact angle Φ = 10, 20, 30, 60, 90°. (b) The morphology regime diagram describing the three growth modes for five different liquid compositions: 23Mo-56Ti-21Si, 24Mo-55Ti-21Si, 25Mo-54Ti-21Si, 26Mo-53Ti-21Si, and 28Mo-51Ti-21Si and for different contact angle α.

and solid phases are unequal, namely $\sigma_{L/\beta} \neq \sigma_{L/TS}$, the solidification morphology is affected by the interfacial energy ratio. As an exemplary illustration in Fig. 7.5(a), different solidification morphologies are observed in the simulations with different equilibrium angle of Φ. The angle Φ is defined as the one between the interfacial energies $\sigma_{L/\beta}$ and $\sigma_{\beta/TS}$ (see Fig. 7.4(b)); the contact angel Φ is manipulated by changing $\sigma_{L/TS}$, while keeping $\sigma_{L/\beta} = \sigma_{L/TS} = 1\,\mathrm{J\,m^{-2}}$. The five representative contact angles Φ and the corresponding interfacial energies are listed in Table 7.2. With increasing Φ, the lamellae growth changes from curving to stable growth modes. In Fig. 7.5(b), a regime diagram describes the three growth modes for the five considered melt compositions. The violet, orange, and gray regions represent the curving (g_i), stable (g_{ii}), and unstable (g_{iii}) growth modes, respectively. The boundary between curving and stable growth region shifts towards the direction of increasing in Φ. The growth of solid phase is determined by two factors: one is the supersaturation in melt, which provides the driving force for the growth, and the other is the capillary force $\sigma\kappa$ against the growth (κ is the surface curvature). For the cases with same melt composition, the supersaturated melt provides the same driving force for the lamellae growth. Due to the asymmetric geometry in the two sides of β phase, the capillary force of the TS phases at two sides is unequal, giving rise to the different

growth velocities at two triple points m_1 and m_2 (see Fig. 7.4(a)). For the case with large Φ, $\sigma_{L/TS}$ is small and therefore the difference in the capillary forces of two adjacent TS phases is small, resulting in a small difference in the growth velocity at m_1 and m_2. In this case, the unequal growth rate at m_1 and m_2 can be balanced by lateral diffusion. As a result, the lamellae exhibits a stable growth. With decreasing Φ, the interfacial energy $\sigma_{L/TS}$ increases and the difference in capillary force enhances. The effect of capillary force on the lamellae growth is pronounced, leading to a largely distinct growth rate at m_1 and m_2. Hence, the lamellae exhibits a tilt growth. In addition, an excessive growth velocity difference between two solid phases gives rise to the engulfment of one solid phase by the other one, corresponding to unstable growth of the lamellae, as shown in the gray region in Fig. 7.5(b). As expected, this engulfment can also be observed when a contact angle cannot be formed between these three phases. Similarly, for the cases with large supersaturation, the fast growth causes the growth rate difference to be compensated by diffusion with difficulty. Hence, the lamellae growth surrounded by high supersaturation melt is more sensitive to the difference in the interfacial energy between liquid and two solid phases.

7.5. Quasi-peritectic reaction

Based on the experimental observation in the previous study [136], the formation of the lamellar pair can also take place at the L-MS interface, that is produced by a four-phase reaction. In this section, we investigate the four-phase reaction under different supersaturations and with various lamellar spacings.

Fig. 7.6(a)-(d) portray the morphological evolution of the four-phase reaction for the cases with distinct supersaturations in melt. The initial melt composition in Fig. 7.6(a)-(d) is set to 22Mo-57Ti-21Si, 23Mo-56Ti-21Si, 26Mo-53Ti-21Si, and 28Mo-51Ti-21Si, respectively. For all four cases, the TS and β particles are initially placed on the surface of MS phase with the same radius of 0.1 µm. To better explore the four phase reaction, these two particles are separated with a distance of 0.2 µm. Due to the periodic boundary condition used at the boundaries perpendicular to the solidification front, the initial setup for the four-phase reaction is identical to that in the study of eutectic transformation in previous section. With time, TS and β phases grow towards liquid phase as well as along the L/MS interface simultaneously. For the case shown in Fig. 7.6(a) with the lowest supersaturation in liquid, the L/MS interface remains quasiplanar at the beginning and is bent towards the MS phase to form a ‶groove″, when TS and β phases approach each other. This grooving indicates the melting of the MS phase during the growth of these two solid phases as both solid phases β and TS require Mo, which is provided by dissolving the MS phase via short-range diffusion in the liquid. With increasing supersaturation, this melting phenomenon weakens and the L/MS interface moves towards liquid phase to form a ‶ridge″ for the cases illustrated in Fig. 7.6(c) and (d). The overall growth process of these two solid phases involves the following three parts. The first part is the direct solidification from liquid phase, namely $L \rightarrow TS$ and $L \rightarrow \beta$, that leads to the axial growth of TS and β phase. The second part consists of two peritectic transformations near the L/TS/MS and L/β/MS triple junctions that continues as long as the TS and β particles are far apart from each other.

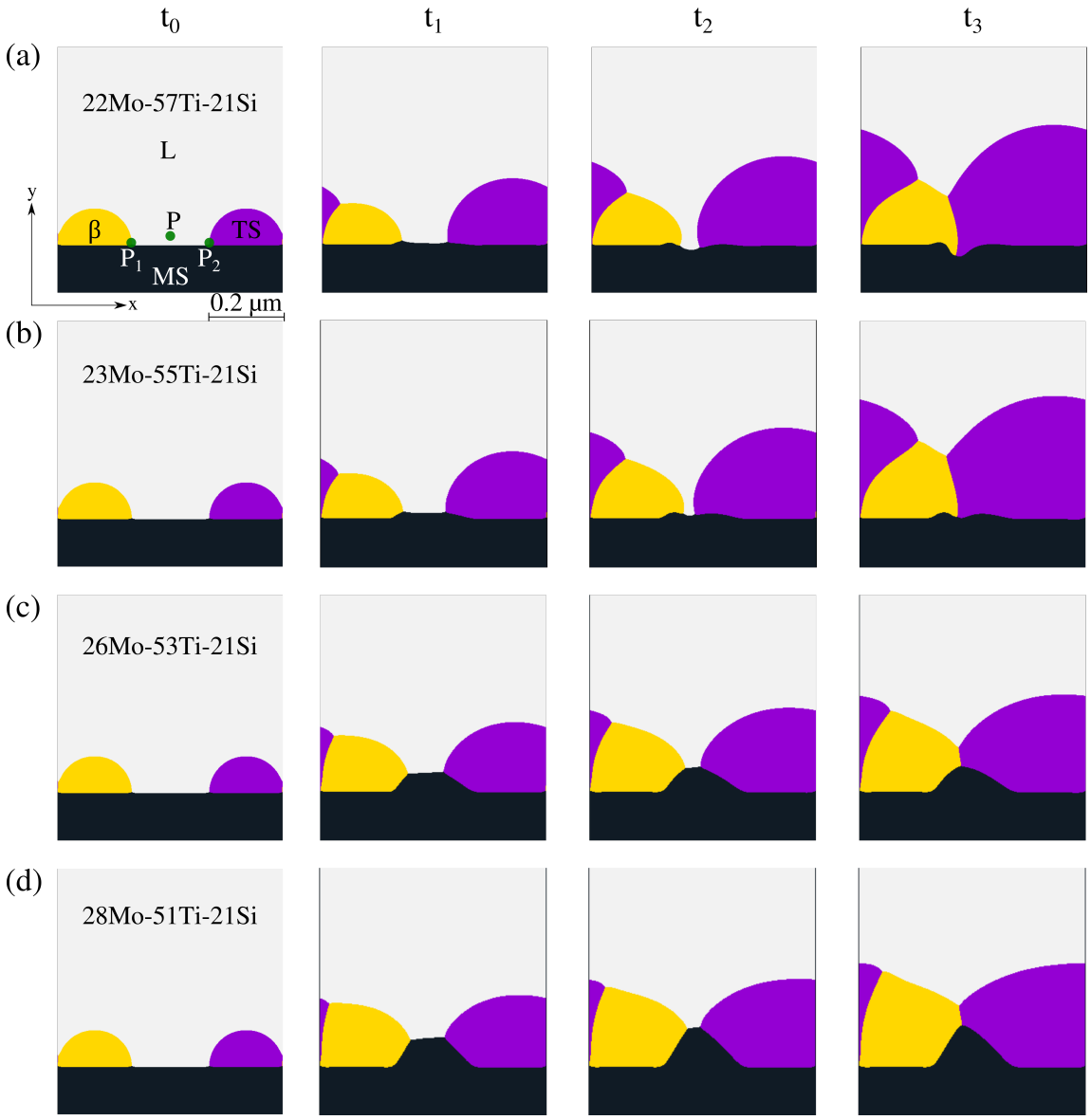

Figure 7.6.: (a)-(d) The morphological evolution of four-phase reaction at proceeding times t_0-t_3 for the cases with liquid concentration of 22Mo-57Ti-21Si, 23Mo-56Ti-21Si, 26Mo-53Ti-21Si, and 28Mo-51Ti-21Si, respectively.

These peritectic transformations give rise to their growth along L/MS interface. The third part is the four-phase reaction, namely L + $Mo(Ti)_3Si \rightarrow Ti(Mo)_5Si_3 + \beta$(Mo,Si,Ti), when TS and β grains have established an interface of TS-β. As a result, the MS phase melts forming a "groove" in low Mo melt compositions of cases (a) and (b). A similar melting phenomenon of parent solid phase is observed in peritectic transformation in other alloy systems, for example in Fe-C alloy [40]. For cases (c) and (d), a sufficient amount of atoms for the growth of TS and β phases come directly from the melt with higher supersaturation instead of consuming MS phase.

To explain the underlying mechanism for the formation of ‵groove″ and ‵ridge″ on the surface of the MS phase, we analyze the concentration variation of a representative spatial point p in the liquid phase under different supersaturations. The point p is defined at the position with 5 grid cells along y direction away from the midpoint of two triple junctions p_1 and p_2 to ensure that the point p is not inside the diffuse interface (see Fig. 7.6(a)). Fig. 7.7(a)-(c) depict the variation of three components (Mo, Si, and Ti) with time for the cases with melt composition 22Mo-57Ti-21Si (violet line) and 28Mo-51Ti-21Si (orange line). Since the point p disappears when the MS phase is completely covered by the TS and β phases, we consider only the concentration variation before the MS phase is engulfed. In the case with a higher supersaturation (orange curve), the concentration of three components eventually converges to a constant value. In contrast, in the case with a lower supersaturation, the concentration of Mo increases at the beginning and decreases after a certain time, the concentration of Si reduces and the concentration of Ti enriches. As the sum of the three concentrations is unity, this system is characterized by two independent components Mo and Si. A comparison between these two cases demonstrates that a higher supersaturation leads to a larger concentration of Mo and Si that provides the driving force for phase transformation $L \rightarrow MS$, while the phase transformation $MS \rightarrow L$ occurs in the other case, where the concentrations of Mo and Si are lower. As a consequence, L/MS interface shifts towards liquid phase in the case with a higher supersaturation, whereas L/MS interface moves towards MS phase in the case with a lower supersaturation.

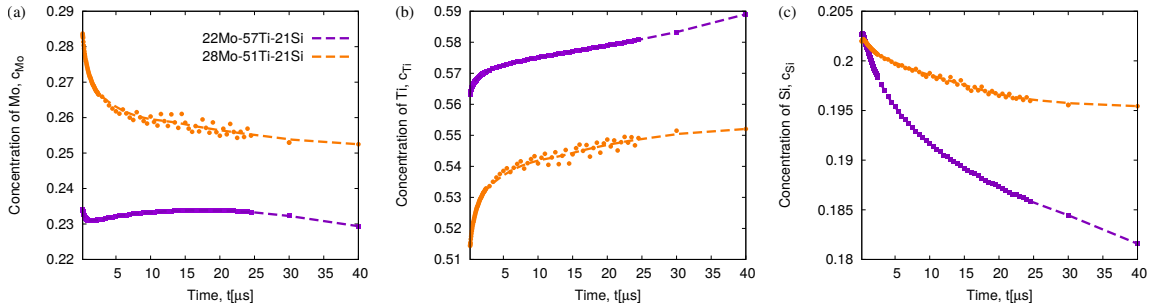

Figure 7.7.: (a)-(c) The variation of the concentration of Mo, Si, and Ti with time for the cases with melt composition 22Mo-57Ti-21Si and 28Mo-51Ti-21Si.

When the TS and β phases cover the MS phase completely, the four-phase reaction is inhibited and subsequently eutectic transformation takes place. In the following, we investigate the influence of the preceding four-phase reaction on the morphological evolution of the eutectic lamellae.

The initial setup for the simulations with melt composition 24Mo-55Ti-21Si and 26Mo-53Ti-21Si is illustrated in Fig. 7.8(a) and (f), respectively. Two semicircular particles TS and β with the same radius of 0.1 µm are placed tangentially to each other on the L/MS interface. Due to the periodic boundary condition used at the boundaries perpendicular to the solidification front, the selected volume is identical to that in the previous discussion of four-phase reaction in this section. By adjusting the lamellar spacing, we control the contact between liquid and MS phase and thus manipulate the four-phase reaction. Fig. 7.8(b)-(e) show the microstructure of the eutectic lamellae for the cases with $\lambda = 0.4$,

Cases \ λ (μm)	0.4	0.5	0.6	0.7
24Mo-55Ti-21Si	0°	0.9°	2.2°	3.7°
26Mo-53Ti-21Si	0°	1.3°	4.4°	9.5°

Table 7.3.: The orientation angle of the lamellae for the cases with melt composition 24Mo-55Ti-21Si and 26Mo-53Ti-21Si.

0.5, 0.6, and 0.7 μm at the time t= 1540 μs, respectively. For all the four cases, the lamellar structure forms on the MS surface. In the case (b), the MS phase is completely covered by the two solid phases at the beginning, which prevents the four-phase reaction. In this case, the formation of lamellar structure is only caused by eutectic transformation. For the cases involving with four phase reaction (Fig. 7.8(c)-(e)), the eutectic lamellae grows with an orientation angle deviating from y-direction. In contrast, the lamellar structure formed only by eutectic transformation in the case (b) grows along y-direction without orientation angle. In the same manner, we investigate the morphology of the lamellar pair with melt composition 26Mo-53Ti-21Si at the time t= 1860 μs, as illustrated in Fig. 7.8(g) to (j). In case (g) only with eutectic transformation, the lamellar pair exhibits a straight growth after reaching a steady state, while in other three cases, an oblique growth of the eutectic lamellae caused by the active four-phase reaction is observed. In order to characterize the tilted growth of the lamellar pair, we measure the angle between the TS/β interface and y-direction, when the growth reaches a steady state (see Fig. 7.8(i)). For the cases with an oscillatory TS/β interface, we connect all peaks and all valleys of the interface by two lines, and calculate the orientation angle by using the average tangent of these two lines. The orientation angles for the cases (b) to (e) and (g) to (j) are listed in Table 7.3. For the cases under same supersaturation, the orientation angle of the lamellar growth increases with λ. As discussed in section 2, the deviation of the interfacial concentration from the equilibrium concentration leads to a difference in the grand chemical potential, which provides the driving force for the phase transition. Therefore, we explain the reasons for the tilted growth by analyzing the concentration distribution ahead of the solidification front. Fig. 7.9(a) shows the concentration profile of the three components along the black dashed line (see Fig. 7.8(b)) for the four cases with λ = 0.4, 0.5, 0.6, and 0.7 μm. As an exemplary explanation, we choose the concentration profile of the cases with melt composition 24Mo-55Ti-21Si at the time t= 1540 μs. For all three components, their concentration distributions along the black dashed line become more asymmetrical with respect to the growth direction and the difference between maximum and minimum concentration becomes larger, when λ increases. The asymmetrical composition profile is caused by the asynchronous movements of triple points L/TS/β on both side of TS phase, which in turn is affected by the liquid concentration ahead of them. Hence, we use the temporal concentration variation of p_1 and p_2 after occurrence of eutectic transformation, as shown in Fig. 7.9(b), to characterize the motions of two triple points. The points p_1 and p_2 are defined at the position in liquid phase, which are 5 grid cells away in the y-direction from the triple point L/TS/β on either side of the TS phase (see Fig. 7.8(e)). The violet and orange lines in Fig. 7.9(b) represent the concentration of point p_1 and p_2 varying

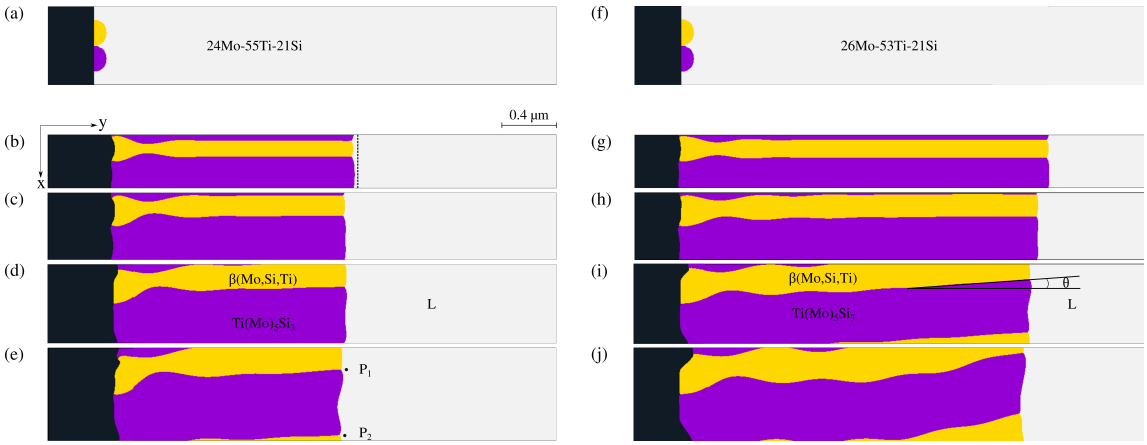

Figure 7.8.: (a) and (f): The initial setup for the simulations with melt composition 24Mo-55Ti-21Si and 26Mo-53Ti-21Si. (b)-(e): The microstructure of eutectic lamellae with melt composition 24Mo-55Ti-21Si for the cases with λ = 0.4, 0.5, 0.6, and 0.7 µm at the time t= 1540 µs, respectively. (g)-(j): The microstructure of eutectic lamellae with melt composition 26Mo-53Ti-21Si for the cases with λ = 0.4, 0.5, 0.6, and 0.7 µm at the time t= 1860 µs, respectively.

with time, respectively. For both points, the concentrations of Mo and Si decrease at the beginning and then increase with time, while the Ti concentration increases initially and decreases after a certain time. A comparison between the concentration variation of the two points shows that the Ti concentration at two points maintain identical, the concentration of Mo increases faster at p_2 than p_1, whereas the opposite tendency is observed for Si concentration with time. According to the previous discussion, two different peritectic transitions occurs at the L/TS/MS and L/β/MS triple points at the beginning. When the MS phase is completely covered by TS and β grains, L/TS/MS and L/β/MS triple points disappear and two new L/TS/β triple points appear indicating the beginning of the eutectic transformation. Under the influence of two different peritectic transitions, the concentrations in front of these triple points are not the same. This difference gives rise to the different movement velocity of triple points. As a result, the lamellar pair grows with an orientation angle. Examplarily, we study the morphological evolution of the lamellar pair during the four-phase reaction with the melt composition 26Mo-53Ti-21Si in 3-D, as shown in Fig. 7.10. For a better observation, Fig. 7.10(b)-(d) portray the cross section of the 3-D simulation. In Fig. 7.10, the tilted growth of the lamellar pair is also observed in 3-D. Compared with the 2-D simulation, the morphology of the lamellar pair is more complex due to the additional contribution in the third dimension. The detailed discussion and systematic analysis of the lamellar growth morphologies in 3-D will be addressed in a forthcoming work.

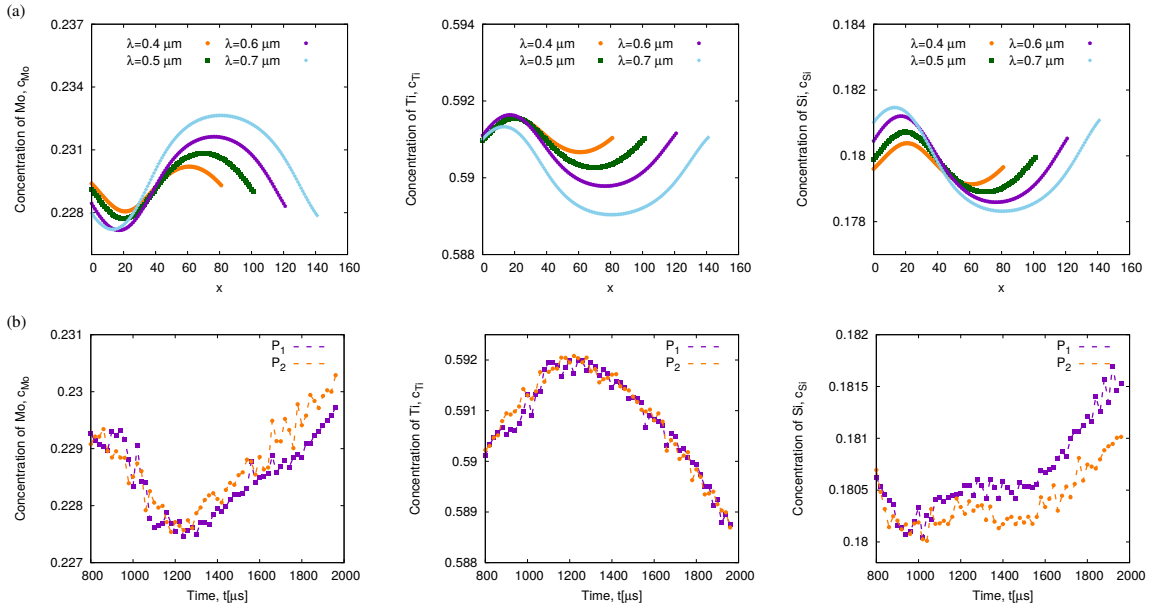

Figure 7.9.: (a) The concentration profile of three components along the black dashed line in Fig. 7.8(b), for the four cases with λ = 0.4, 0.5, 0.6, and 0.7 μm. (b) The temporal concentration variation of p_1 and p_2.

7.6. Summary

In this study, we have systematically studied the lamellae growth caused by a eutectic transformation as well as by a four-phase reaction in Mo-Si-Ti alloy through 2-D and 3-D simulations, with inputs from the CALPHAD database.

For the eutectic transformation, the 2-D simulation results show that the microstructural evolution of lamellar pair is affected by the supersaturation and the lamellar spacing, which is consistent with Jackson-Hunt theory. The lamellae growth exhibits a transformation from unstable to metastable through stable growth mode with increasing lamellar spacing. Through the simulations with different supersaturation and with various lamellar spacing, we obtain a microstructure selection map for distinct growth morphologies. In 3-D simulation, the eutectic growth of the rods under the influence of neighbor particles in the third dimension displays a distinct microstructure compared to 2-D simulation. In addition, the stable growth of lamellae in 3-D is restricted in a region with smaller lamellar spacing than in 2-D. The reason for the difference between 2-D and 3-D is that an additional diffusion flux in 3-D leads to faster growth in the plane perpendicular to the solidification direction. When the TS phases are set asymmetrically at the two sides of β phase, the solidification morphology of the lamellar pair under different supersaturations in melt or with distinct solid-liquid interfacial energies shows three different types: curving, stable, and unstable growth modes. The final morphology is determined by the combining effect of diffusion, reaction as well as the capillary force.

In the four-phase reaction, we observe the formation of "groove" and "ridge" of $Mo(Ti)_3Si$ phase in the melt with lower and higher supersaturation, respectively. These phenomena indicate that the remelting of this phase at lower supersaturation provides the

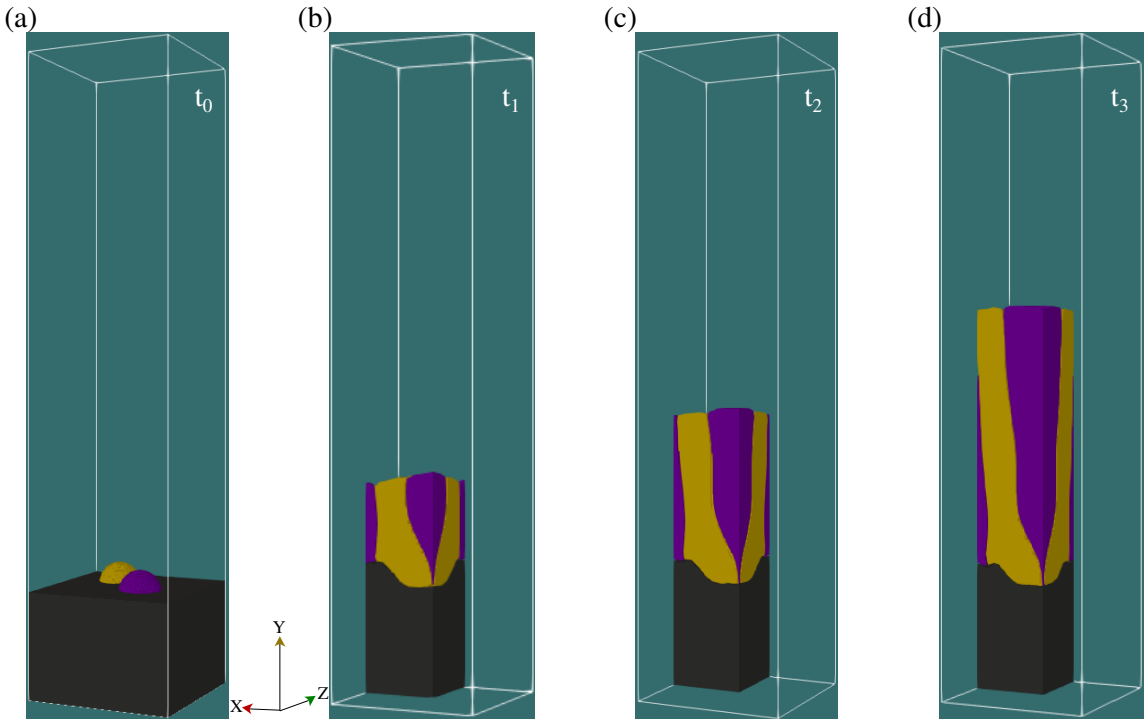

Figure 7.10.: Side view of the morphological evolution for the four-phase reaction.

solute for the lamellae growth, while the melt with higher supersaturation directly offers a sufficient amount of atoms for its growth. Furthermore, the lamellar pair on the surface of $Mo(Ti)_3Si$ grain grows with a certain orientation angle during the four-phase reaction and the orientation angle increases with the enlarging lamellar spacing. The tilted growth is caused by two different peritectic transitions and the associated asymmetric concentration profiles in the vicinity of two triple junctions, namely $L/Ti(Mo)_5Si_3/Mo(Ti)_3Si$ and $L/\beta(Mo,Si,Ti)/Mo(Ti)_3Si$.

By simulating the lamellae growth during a eutectic transformation in Mo-Si-Ti alloy, we have constructed a microstructure selection map, which should be helpful to the experimental studies and the industrial applications in the development of new tailored materials by new designing the microstructural morphology. Our computational investigation on the four-phase reaction provides additional insight into the underlying growth mechanism for the formation of the lamellae pair in Mo-Si-Ti alloy. The study on the bending growth of lamellae explains two possible reasons for this phenomenon found in experiments.

8. Conclusion and outlook

8.1. Conclusion and remarks

In this work, we presented a comprehensive investigative chain on the alloy solidification process, encompassing the modeling of material systems, conducting representative phase field simulations, and analyzing the microstructural evolution.

To ensure the thermodynamic consistence of PF-simulation, we coupled the thermodynamic information based on the published CALPHAD database with PF-model. In this coupling process, we described the free energy of single phase by a parabolic function and explained the reason for this treatment. However, the data of stoichiometric phase in CALPHAD database is limited. Therefore, the correct expression of its free energy as a function of concentration is still challenge. To solve this problem, we proposed a novel expression of its free energy, in which the solute solubility is assumed. By utilizing a fitting program (code provided in the Appendix), we automated the generation of the free energy of the stoichiometric phase. Based on the fitted free energy function of each phase, we reconstructed the phase diagram and calculated the required thermodynamic information. Through the comparison of them with that obtained based on CALPHAD database, we validated this coupling method and proved that this approach can be used in PF-simulation for a quantitative investigation. By using this coupling method, the thermodynamic model of three alloy systems, namely Fe-C, Al-C, and Mo-Si-Ti, was rebuilt and coupled in PF-equation.

In Fe-C binary system, we focused on the peritectic transition between liquid, austenite (γ), and ferrite (δ). By using phase-field method, we systematically elucidated the growth of γ phase on the surface of δ phase with different microstructure during the peritectic transition. The 2D and 3D simulation results reveal that the growth of γ platelet involves the contributions from peritectic transformation between L/γ and δ/γ interfaces, and from peritectic reaction in the vicinity of the triple point. This understanding of the underlying mechanism of peritectic transition under various processing conditions is helpful to understand this complex phase transition in other systems. In addition, the dynamic contact angle differs from the steady contact angle. As described by Young's law, the steady contact angle should follow the thermodynamic equilibrium relation, whereas the dynamic contact angle has an extra dynamic contribution and therefore its value deviates from the value calculated by Young's law. In this dissertation, we presented a new measurement method to precisely define a dynamic contact angle during a peritectic transition.

Owing to the anisotropic property of Al_4C_3, this intermetallic compound exhibits a needle-like growth pattern, which differs from the emblematic microstructure observed in peritectic transition (e.g. as seen in Fe-C system). By imitating the classical nucleation the-

ory, we have presented and verified that the Al_4C_3 phase grows with a critical orientation angle. Through the PF-simulations, the critical orientation angle for a single Al_4C_3 particle is affected by its nucleation radius and by the size of the parent graphite phase. Furthermore, we've elucidated that when two needle-like structures of equal size are in close proximity, the critical orientation angle decreases due to competing effects and the overlapping concentration fields between the particles, in contrast to the angle observed for an individual particle. For this case, the competing effect between two neighboring particles will be affected by the nucleation distance between them. The variation in the orientation angle of particle 2 led to the identification of both the upper and lower critical distances. Three typical competing effects have been observed by varying the difference in the radii of two particles and the orientation of particle 1. By simulating the diffusion-reaction process in the Al-C system, we have elucidated the underlying mechanisms of the orientation selection during phase transition from the energetic point of view that is beneficial to understand the orientation selection of phase growth in other system. In Mo-Si-Ti system, we paid attention to the microstructural development of the lamellar pair consisting of $Ti(Mo)_5Si_3$ and β phases during the eutectic transformation as well as the quasi-peritectic reaction. This attention was motivated by the exceptional properties exhibited by this alloy with a lamellar microstructure, particularly in high-temperature applications. For the study on eutectic transformation, we firstly scrutinized the influence of supersaturation and lamellar spacing on the development of the lamellar pair. The simulation results show a good agreement with the Jackson-Hunt theory, indicating that the rebuilt the model of this ternary system can be used to study this eutectic transformation quantitatively. Three growth modes for the lamellae growth were observed in the PF-simulations: unstable, stable, and metastable growth mode. By varying the supersaturations and the lamellar spacing, we obtained a microstructure selection map for distinct growth morphology. Moreover, accurately measuring the interfacial energy between different phases through experiments is highly challenging, leading to a lack of research discussing its influence on the solidified morphology. In present work, we systematically studied the influence of the interfacial energy between each two phases on the solidification morphology and observed three different growth modes:curving, stable, and unstable growth modes. In the four-phase reaction, we observe the formation of "groove" and "ridge" of $Mo(Ti)_3Si$ phase in the melt with lower and higher supersaturation, respectively. These phenomenon indicates that the remelting of this phase at lower supersaturation provides the solute for the lamellae growth, while the melt with higher supersaturation directly offers a sufficient amount of atoms for its growth. This finding of the "groove" formation is similar to the remelting behavior observed in peritectic transition in Fe-C alloy. After the complete cover of $Mo(Ti)_3Si$ phase by the lamellar pair ($Ti(Mo)_5Si_3$ and β phases), the lamellae on the surface of $Mo(Ti)_3Si$ grain grows with an certain orientation angle, that is different from the microstructure formed by the primary eutectic transformation. Our computational investigation of the eutectic and the quasi-peritectic reaction offers valuable insights into the growth mechanism underlying the formation of lamellae pairs in Mo-Si-Ti alloys. The analysis of the bending growth of lamellae sheds light on two potential reasons for this observed phenomenon in experiments.

This thesis focuses on comprehensively analyzing the morphological evolution during diverse phase transformation processes across various alloy systems. It commences

with fundamental and frequently observed transitions, such as the three-phase peritectic transition and eutectic transformation, and progresses towards more intricate reaction, exemplified by the quasi-peritectic four-phase reaction. Through a detailed investigation of solidification processes in distinct alloy systems employing a phase-field model, we attain a profound understanding of the processing-microstructure relationship in these alloys. This understanding provides valuable insights for industrial applications and can be used as a guideline for designing new tailored materials with outstanding properties.

8.2. Future directions

In future research, attention should be directed towards the following three key aspects: (1) the material models developed in present work can be applied to carry out a sensitivity analysis of morphological evolution during directional solidification process in these alloys. Experimental conditions such as alloy composition, temperature gradient, pulling velocity will be incorporated in simulations and the relationship between them and solidified morphology will be studied. In addition, the influence of the solidification conditions that are difficult to be controlled in experiments, e.g., interfacial energy and nucleation, will also be explored by simulation. Based on the sufficient amount of simulation results, machine learning techniques will be employed to improve the accuracy and efficiency of phase-field simulations. (2) Establishing a robust connection between microstructure and material properties is crucial, with the objective of constructing a comprehensive processing-microstructure-properties relationship applicable for industrial applications. (3) Addressing a potential limitation identified in this study, future efforts should aim to mitigate the influence of simulation boundaries. This may involve devising new boundary conditions to maintain physical consistency in simulations within a more confined domain, thus reducing computational effort.

Bibliography

[1] D. Tourret, H. Liu, and J. LLorca. "Phase-field modeling of microstructure evolution: Recent applications, perspectives and challenges". In: *Progress in Materials Science* 123 (2022). A Festschrift in Honor of Brian Cantor, p. 100810. ISSN: 0079-6425. DOI: https://doi.org/10.1016/j.pmatsci.2021.100810. URL: https://www.sciencedirect.com/science/article/pii/S0079642521000347.

[2] R. J. Hebert. "Chapter Two - Processing-microstructure-property relationship for AM metals and the effect of thermal properties". In: *Quality Analysis of Additively Manufactured Metals*. Ed. by J. Kadkhodapour, S. Schmauder, and F. Sajadi. Elsevier, 2023, pp. 25–72. ISBN: 978-0-323-88664-2. DOI: https://doi.org/10.1016/B978-0-323-88664-2.00012-9. URL: https://www.sciencedirect.com/science/article/pii/B9780323886642000129.

[3] A. Colthorpe. *BloombergNEF: China dominates global battery supply chain again with followers in flux*. https://www.energy-storage.news/bloombergnef-china-dominates-global-battery-supply-chain-again-with-followers-in-flux/. Accessed on 08.09.2023. 2022.

[4] D. Schliephake et al. "Constitution, oxidation and creep of eutectic and eutectoid Mo-Si-Ti alloys". In: *Intermetallics* 104 (2019), pp. 133–142. ISSN: 0966-9795. DOI: https://doi.org/10.1016/j.intermet.2018.10.028. URL: https://www.sciencedirect.com/science/article/pii/S0966979518304400.

[5] C. Belda. https://mmta.co.uk/hafnium-prices-surge-as-concerns-build/. Accessed on 08.09.2023.

[6] https://www.seshagirigears.com/bevel-gear.html. Accessed on 08.09.2023.

[7] https://www.felgenoutlet.de/de/alufelgen-reifen. Accessed on 08.09.2023.

[8] J. Tang et al. "Unique surface patterns emerging during solidification of liquid metal alloys". In: *Nature Nanotechnology* 16.4 (2021), pp. 431–439. ISSN: 1748-3395. DOI: 10.1038/s41565-020-00835-7. URL: https://doi.org/10.1038/s41565-020-00835-7.

[9] X. Zhang et al. "Atypical pathways for lamellar and twinning transformations in rapidly solidified TiAl alloy". In: *Acta Materialia* 227 (2022), p. 117718. ISSN: 1359-6454. DOI: https://doi.org/10.1016/j.actamat.2022.117718. URL: https://www.sciencedirect.com/science/article/pii/S1359645422001045.

[10] P. Shi et al. "Hierarchical crack buffering triples ductility in eutectic herringbone high-entropy alloys". In: *Science* 373.6557 (2021), pp. 912–918. DOI: 10.1126/science.abf6986. eprint: https://www.science.org/doi/pdf/10.1126/science.abf6986. URL: https://www.science.org/doi/abs/10.1126/science.abf6986.

[11] L.-Q. Chen and Y. Wang. "The continuum field approach to modeling microstructural evolution". In: *JOM* 48.12 (1996), pp. 13–18. ISSN: 1543-1851. DOI: 10.1007/BF03223259. URL: https://doi.org/10.1007/BF03223259.

[12] L.-Q. Chen. "Phase-Field Models for Microstructure Evolution". In: *Annual Review of Materials Research* 32.1 (2002), pp. 113–140. DOI: 10.1146/annurev.matsci.32.112001.132041. eprint: https://doi.org/10.1146/annurev.matsci.32.112001.132041. URL: https://doi.org/10.1146/annurev.matsci.32.112001.132041.

[13] M. Ode, S. G. Kim, and T. Suzuki. "Recent Advances in the Phase-field Model for Solidification". In: *ISIJ International* 41.10 (2001), pp. 1076–1082. DOI: 10.2355/isijinternational.41.1076.

[14] W. J. Boettinger et al. "Phase-Field Simulation of Solidification". In: *Annual Review of Materials Research* 32.1 (2002), pp. 163–194. DOI: 10.1146/annurev.matsci.32.101901.155803. eprint: https://doi.org/10.1146/annurev.matsci.32.101901.155803. URL: https://doi.org/10.1146/annurev.matsci.32.101901.155803.

[15] I. Steinbach. "Phase-field models in materials science". In: *Modelling and Simulation in Materials Science and Engineering* 17.7 (2009), p. 073001. DOI: 10.1088/0965-0393/17/7/073001. URL: https://dx.doi.org/10.1088/0965-0393/17/7/073001.

[16] A. Karma. "Phase-field model of eutectic growth". In: *Phys. Rev. E* 49 (3 1994), pp. 2245–2250. DOI: 10.1103/PhysRevE.49.2245. URL: https://link.aps.org/doi/10.1103/PhysRevE.49.2245.

[17] A. A. Wheeler, G. McFadden, and W. Boettinger. "Phase-field model for solidification of a eutectic alloy". In: *Proceedings of the Royal Society of London. Series A: Mathematical, Physical and Engineering Sciences* 452.1946 (1996), pp. 495–525.

[18] I. Steinbach et al. "A phase field concept for multiphase systems". In: *Physica D: Nonlinear Phenomena* 94.3 (1996), pp. 135–147.

[19] J. Tiaden et al. "The multiphase-field model with an integrated concept for modelling solute diffusion". In: *Physica D: Nonlinear Phenomena* 115.1-2 (1998), pp. 73–86.

[20] B. Nestler and A. Wheeler. "A multi-phase-field model of eutectic and peritectic alloys: numerical simulation of growth structures". In: *Physica D: Nonlinear Phenomena* 138.1 (2000), pp. 114 –133. ISSN: 0167-2789. DOI: https://doi.org/10.1016/S0167-2789(99)00184-0. URL: http://www.sciencedirect.com/science/article/pii/S0167278999001840.

[21] A. Choudhury et al. "Growth morphologies in peritectic solidification of Fe–C: A phase-field study". In: *Acta Materialia* 58.10 (2010), pp. 3815 –3823. ISSN: 1359-6454. DOI: https://doi.org/10.1016/j.actamat.2010.03.030. URL: http://www.sciencedirect.com/science/article/pii/S1359645410001758.

[22] A. Choudhury and B. Nestler. "Grand-potential formulation for multicomponent phase transformations combined with thin-interface asymptotics of the double-obstacle potential". In: *Phys. Rev. E* 85 (2 2012), p. 021602. DOI: 10.1103/PhysRevE.85.021602. URL: https://link.aps.org/doi/10.1103/PhysRevE.85.021602.

[23] Y. Chen et al. “Quantitatively comparing phase-field modeling with direct real time observation by synchrotron X-ray radiography of the initial transient during directional solidification of an Al–Cu alloy”. In: *Acta Materialia* 60.1 (2012), pp. 199–207.

[24] H. Xing et al. “Degenerate seaweed to tilted dendrite transition and their growth dynamics in directional solidification of non-axially oriented crystals: a phase-field study”. In: *Scientific reports* 6 (2016), p. 26625.

[25] R Folch and M Plapp. “Quantitative phase-field modeling of two-phase growth”. In: *Physical Review E* 72.1 (2005), p. 011602.

[26] A. Karma. “Phase-field formulation for quantitative modeling of alloy solidification”. In: *Physical Review Letters* 87.11 (2001), p. 115701.

[27] J. Y. Huh et al. “Phase field simulations of intermetallic compound growth during soldering reactions”. In: *Journal of electronic materials* 33.10 (2004), pp. 1161–1170.

[28] M. S. Park, S. L. Gibbons, and R Arróyave. “Phase-field simulations of intermetallic compound evolution in Cu/Sn solder joints under electromigration”. In: *Acta Materialia* 61.19 (2013), pp. 7142–7154. ISSN: 1359-6454. DOI: https://doi.org/10.1016/j.actamat.2013.08.016. URL: https://www.sciencedirect.com/science/article/pii/S1359645413006125.

[29] F. Wang and B. Nestler. “A phase-field study on the formation of the intermetallic Al2Au phase in the Al–Au system”. In: *Acta Materialia* 95 (2015), pp. 65 –73. ISSN: 1359-6454. DOI: https://doi.org/10.1016/j.actamat.2015.05.002. URL: http://www.sciencedirect.com/science/article/pii/S1359645415003146.

[30] D.-C. Kim et al. “Establishment of a theoretical model based on the phase-field method for predicting the γ phase precipitation in Fe–Cr–Ni ternary alloys”. In: *Materials Today Communications* 26 (2021), p. 101932. ISSN: 2352-4928. DOI: https://doi.org/10.1016/j.mtcomm.2020.101932. URL: https://www.sciencedirect.com/science/article/pii/S2352492820329433.

[31] M. Berghoff and B. Nestler. “Phase field crystal modeling of ternary solidification microstructures”. In: *Computational Condensed Matter* 4 (2015), pp. 46–58. ISSN: 2352-2143. DOI: https://doi.org/10.1016/j.cocom.2015.08.002. URL: https://www.sciencedirect.com/science/article/pii/S235221431530006X.

[32] S. Gyoon Kim et al. “Phase-field modeling of eutectic solidification”. In: *Journal of Crystal Growth* 261.1 (2004), pp. 135–158. ISSN: 0022-0248. DOI: https://doi.org/10.1016/j.jcrysgro.2003.08.078. URL: https://www.sciencedirect.com/science/article/pii/S0022024803017974.

[33] M. Apel et al. “2D and 3D phase-field simulations of lamella and fibrous eutectic growth”. In: *Journal of Crystal Growth* 237-239 (2002). The thirteenth international conference on Crystal Growth in conj unction with the eleventh international conference on Vapor Growth and Epitaxy, pp. 154–158. ISSN: 0022-0248. DOI: https://doi.org/10.1016/S0022-0248(01)01895-4. URL: https://www.sciencedirect.com/science/article/pii/S0022024801018954.

[34] F. m. c. Drolet et al. “Phase-field modeling of eutectic growth”. In: *Phys. Rev. E* 61 (6 2000), pp. 6705–6720. DOI: 10.1103/PhysRevE.61.6705. URL: https://link.aps.org/doi/10.1103/PhysRevE.61.6705.

[35] A. Karma and A. Sarkissian. “Morphological instabilities of lamellar eutectics”. In: *Metallurgical and Materials Transactions A* 27.3 (1996), pp. 635–656.

[36] D. Phelan, M. Reid, and R. Dippenaar. “Kinetics of the peritectic phase transformation: In-situ measurements and phase field modeling”. In: *Metallurgical and Materials Transactions A* 37.3 (2006), pp. 985–994.

[37] J. Tiaden. “Phase field simulations of the peritectic solidification of Fe–C”. In: *Journal of Crystal Growth* 198-199 (1999), pp. 1275 –1280. ISSN: 0022-0248. DOI: https://doi.org/10.1016/S0022-0248(98)01009-4. URL: http://www.sciencedirect.com/science/article/pii/S0022024898010094.

[38] S. Pan, M. Zhu, and M. Rettenmayr. “A phase-field study on the peritectic phase transition in Fe-C alloys”. In: *Acta Materialia* 132 (2017), pp. 565–575. ISSN: 1359-6454. DOI: https://doi.org/10.1016/j.actamat.2017.04.053. URL: https://www.sciencedirect.com/science/article/pii/S1359645417303452.

[39] M. Ohno and K. Matsuura. “Diffusion-controlled peritectic reaction process in carbon steel analyzed by quantitative phase-field simulation”. In: *Acta Materialia* 58.18 (2010), pp. 6134–6141. ISSN: 1359-6454. DOI: https://doi.org/10.1016/j.actamat.2010.07.031. URL: https://www.sciencedirect.com/science/article/pii/S1359645410004659.

[40] Y. Cai et al. “Phase-field investigation on the peritectic transition in Fe-C system”. In: *Acta Materialia* 219 (2021), p. 117223. ISSN: 1359-6454. DOI: https://doi.org/10.1016/j.actamat.2021.117223. URL: https://www.sciencedirect.com/science/article/pii/S1359645421006030.

[41] D. M. Stefanescu et al. “On the stable eutectic solidification of iron–carbon–silicon alloys”. In: *Acta Materialia* 103 (2016), pp. 103–114. ISSN: 1359-6454. DOI: https://doi.org/10.1016/j.actamat.2015.09.043. URL: https://www.sciencedirect.com/science/article/pii/S1359645415007247.

[42] C. Gu, M. P. Moodispaw, and A. A. Luo. “Cellular automaton simulation and experimental validation of eutectic transformation during solidification of Al-Si alloys”. In: *npj Computational Materials* 8.1 (2022), p. 134. ISSN: 2057-3960. DOI: 10.1038/s41524-022-00824-5. URL: https://doi.org/10.1038/s41524-022-00824-5.

[43] M. Kellner, S. N. Enugala, and B. Nestler. “Modeling of stoichiometric phases in off-eutectic compositions of directional solidifying NbSi-10Ti for phase-field simulations”. In: *Computational Materials Science* 203 (2022), p. 111046. ISSN: 0927-0256. DOI: https://doi.org/10.1016/j.commatsci.2021.111046. URL: https://www.sciencedirect.com/science/article/pii/S0927025621007278.

[44] P. Steinmetz et al. “Quantitative comparison of ternary eutectic phase-field simulations with analytical 3D Jackson–Hunt approaches”. In: *Metallurgical and Materials Transactions B* 49.1 (2018), pp. 213–224.

[45] M. Kellner et al. "Phase-field study of eutectic colony formation in NiAl-34Cr". In: *Acta Materialia* 182 (2020), pp. 267–277. ISSN: 1359-6454. DOI: https://doi.org/10.1016/j.actamat.2019.10.028. URL: https://www.sciencedirect.com/science/article/pii/S1359645419306901.

[46] Z. Tu et al. "A phase-field study of lamellar eutectic growth with solid-solid boundary anisotropy". In: *Journal of Crystal Growth* 532 (2020), p. 125439. ISSN: 0022-0248. DOI: https://doi.org/10.1016/j.jcrysgro.2019.125439. URL: https://www.sciencedirect.com/science/article/pii/S0022024819306542.

[47] J Valloton et al. "Modeling of peritectic coupled growth in Cu–Sn alloys". In: *Acta materialia* 61.15 (2013), pp. 5549–5560.

[48] H. Ha and J. Hunt. "A numerical and experimental study of the rate of transformation in three directionally grown peritectic systems". In: *Metallurgical and Materials Transactions A* 31.1 (2000), pp. 29–34.

[49] N. Liu et al. "Peritectic solidification of undercooled Fe–Co alloys". In: *Journal of alloys and compounds* 465.1-2 (2008), pp. 391–395.

[50] T. Shing Lo, A. Karma, and M. Plapp. "Phase-field modeling of microstructural pattern formation during directional solidification of peritectic alloys without morphological instability". In: *Phys. Rev. E* 63 (3 2001), p. 031504. DOI: 10.1103/PhysRevE.63.031504. URL: https://link.aps.org/doi/10.1103/PhysRevE.63.031504.

[51] S Dobler et al. "Peritectic coupled growth". In: *Acta Materialia* 52.9 (2004), pp. 2795–2808.

[52] G. Azizi, B. G. Thomas, and M. A. Zaeem. "Review of Peritectic Solidification Mechanisms and Effects in Steel Casting". In: *Metallurgical and Materials Transactions B* 51.5 (2020), pp. 1875–1903.

[53] S. Griesser, C. Bernhard, and R Dippenaar. "Effect of nucleation undercooling on the kinetics and mechanism of the peritectic phase transition in steel". In: *Acta materialia* 81 (2014), pp. 111–120.

[54] H Shibata et al. "Kinetics of peritectic reaction and transformation in Fe-C alloys". In: *Metallurgical and Materials Transactions B* 31.5 (2000), pp. 981–991.

[55] S. Akamatsu and M. Plapp. "Eutectic and peritectic solidification patterns". In: *Current Opinion in Solid State and Materials Science* 20.1 (2016), pp. 46–54.

[56] G Sha et al. "Quasi-peritectic solidification reactions in 6xxx series wrought Al alloys". In: *Acta Materialia* 51.7 (2003), pp. 1883–1897. ISSN: 1359-6454. DOI: https://doi.org/10.1016/S1359-6454(02)00595-5. URL: https://www.sciencedirect.com/science/article/pii/S1359645402005955.

[57] Y. Wang et al. "Research progress on solidification structure of alloys by synchrotron X-ray radiography: A review". In: *Journal of Magnesium and Alloys* 8.2 (2020), pp. 396–413. ISSN: 2213-9567. DOI: https://doi.org/10.1016/j.jma.2019.08.003. URL: https://www.sciencedirect.com/science/article/pii/S2213956720300360.

[58] Y. S. Kim et al. “Influence of Nb on microstructure and mechanical properties of Ti-Sn ultrafine eutectic alloy”. In: *Metals and Materials International* 23 (2017), pp. 20–25.

[59] B. Chalmers. “Principles of Solidification”. In: *Applied Solid State Physics*. Ed. by W. Low and M. Schieber. Boston, MA: Springer US, 1970, pp. 161–170. ISBN: 978-1-4684-1854-5. DOI: 10.1007/978-1-4684-1854-5_5. URL: https://doi.org/10.1007/978-1-4684-1854-5_5.

[60] F. Czerwinski and B. Shalchi Amirkhiz. “On the Al–Al11Ce3 Eutectic Transformation in Aluminum–Cerium Binary Alloys”. In: *Materials* 13.20 (2020). ISSN: 1996-1944. DOI: 10.3390/ma13204549. URL: https://www.mdpi.com/1996-1944/13/20/4549.

[61] K. Nogita et al. “Engineering the Mg–Mg2Ni eutectic transformation to produce improved hydrogen storage alloys”. In: *International Journal of Hydrogen Energy* 34.18 (2009), pp. 7686–7691. ISSN: 0360-3199. DOI: https://doi.org/10.1016/j.ijhydene.2009.07.036. URL: https://www.sciencedirect.com/science/article/pii/S0360319909010970.

[62] C. Zhu et al. “Pattern formation mechanism of directionally-solidified MoSi2/Mo5Si3 eutectic by phase-field simulation”. In: *Intermetallics* 116 (2020), p. 106590. ISSN: 0966-9795. DOI: https://doi.org/10.1016/j.intermet.2019.106590. URL: https://www.sciencedirect.com/science/article/pii/S0966979519304819.

[63] L. Rátkai et al. “Phase-field modeling of eutectic structures on the nanoscale: the effect of anisotropy”. In: *Journal of Materials Science* 52.10 (2017), pp. 5544–5558.

[64] S. Akamatsu and M. Plapp. “Eutectic and peritectic solidification patterns”. In: *Current Opinion in Solid State and Materials Science* 20.1 (2016). Recent Advances in Solidification Microstructure- Experiments and Computational Analysis, pp. 46–54. ISSN: 1359-0286. DOI: https://doi.org/10.1016/j.cossms.2015.10.002. URL: https://www.sciencedirect.com/science/article/pii/S1359028615300085.

[65] S. Griesser, C. Bernhard, and R. Dippenaar. “Mechanism of the peritectic phase transition in Fe–C and Fe–Ni alloys under conditions close to chemical and thermal equilibrium”. In: *ISIJ international* 54.2 (2014), pp. 466–473.

[66] S. Griesser. “In-situ study of the influence of alloying elements on the kinetics and mechanism of the peritectic phase transition in steel”. In: (2013).

[67] T. Lo et al. “Two-phase microstructure selection in peritectic solidification: from island banding to coupled growth”. In: *Acta Materialia* 51.3 (2003), pp. 599–611. ISSN: 1359-6454. DOI: https://doi.org/10.1016/S1359-6454(02)00440-8. URL: https://www.sciencedirect.com/science/article/pii/S1359645402004408.

[68] H. Fredriksson and U. Akerlind. *Materials processing during casting*. Vol. 210. Wiley Online Library, 2006.

[69] H. Fredriksson et al. *Solidification and crystallization processing in metals and alloys*. John Wiley & Sons, 2012.

[70] H. W. Kerr and W. Kurz. "Solidification of peritectic alloys". In: *International Materials Reviews* 41.4 (1996), pp. 129–164. DOI: 10.1179/imr.1996.41.4.129. eprint: https://doi.org/10.1179/imr.1996.41.4.129. URL: https://doi.org/10.1179/imr.1996.41.4.129.

[71] M Hillert. "Solidification and casting of metals". In: *The Metals Society, London* 81 (1979).

[72] W. P. Bosze and R. Trivedi. "On the kinetic expression for the growth of precipitate plates". In: *Metallurgical transactions* 5.2 (1974), pp. 511–512. ISSN: 2379-0083. DOI: 10.1007/BF02644122. URL: https://doi.org/10.1007/BF02644122.

[73] H. Fredriksson and T. Nylén. "Mechanism of peritectic reactions and transformations". In: *Metal Science* 16.6 (1982), pp. 283–294. DOI: 10.1179/030634582790427370. eprint: https://doi.org/10.1179/030634582790427370. URL: https://doi.org/10.1179/030634582790427370.

[74] A. P. Titchener and J. A. Spittle. "A Solid–Liquid Diffusion Couple Study of Peritectic Reactions". In: *Metal Science* 8.1 (1974), pp. 112–116. DOI: 10.1179/msc.1974.8.1.112. eprint: https://doi.org/10.1179/msc.1974.8.1.112. URL: https://doi.org/10.1179/msc.1974.8.1.112.

[75] D. Fisher, M. Rappaz, and W. Kurz. "Fundamentals of solidification". In: *Fundamentals of Solidification* (2023), pp. 1–353.

[76] F. Abraham. *Homogeneous Nucleation Theory; The pretransition Theory of Vapor Condensation (Supplement 1).* New York, Academic Press, 1974.

[77] R Kuziak, R. Kawalla, and S. Waengler. "Advanced high strength steels for automotive industry". In: *Archives of civil and mechanical engineering* 8.2 (2008), pp. 103–117.

[78] B. De Cooman. "Structure–properties relationship in TRIP steels containing carbide-free bainite". In: *Current Opinion in Solid State and Materials Science* 8.3-4 (2004), pp. 285–303.

[79] P. Jacques. "Transformation-induced plasticity for high strength formable steels". In: *Current Opinion in Solid State and Materials Science* 8.3-4 (2004), pp. 259–265.

[80] A Grill, K Sorimachi, and J. Brimacombe. "Heat flow, gap formation and break-outs in the continuous casting of steel slabs". In: *Metallurgical Transactions B* 7.2 (1976), pp. 177–189.

[81] M. Suzuki and Y. Yamaoka. "Influence of carbon content on solidifying shell growth of carbon steels at the initial stage of solidification". In: *Materials transactions* 44.5 (2003), pp. 836–844.

[82] J. Xu et al. "Analysis of crack susceptibility of regular carbon steel slabs using volume-based shrinkage index". In: *ISIJ international* 53.10 (2013), pp. 1812–1817.

[83] H. W. Kerr and W Kurz. "Solidification of peritectic alloys". In: *International materials reviews* 41.4 (1996), pp. 129–164.

[84] H. Nassar and H. Fredriksson. "On peritectic reactions and transformations in low-alloy steels". In: *Metallurgical and materials transactions A* 41.11 (2010), pp. 2776–2783.

[85] Y. Cai et al. "Phase-field investigation on the growth orientation angle of aluminum carbide with a needle-like structure at the surface of graphite particles". In: *Modelling and Simulation in Materials Science and Engineering* 27.6 (2019), p. 065010.

[86] D. Phelan, M. Reid, and R. Dippenaar. "Experimental and modelling studies into high temperature phase transformations". In: *Computational Materials Science* 34.3 (2005). Computational Microstructure Evolution in Steels, pp. 282 –289. ISSN: 0927-0256. DOI: https://doi.org/10.1016/j.commatsci.2005.02.006. URL: http://www.sciencedirect.com/science/article/pii/S0927025605000637.

[87] G. Boussinot, E. Brener, and D. Temkin. "Kinetics of isothermal phase transformations above and below the peritectic temperature: Phase-field simulations". In: *Acta Materialia* 58.5 (2010), pp. 1750 –1760. ISSN: 1359-6454. DOI: https://doi.org/10.1016/j.actamat.2009.11.017. URL: http://www.sciencedirect.com/science/article/pii/S1359645409007964.

[88] R. E. Johnson Jr, R. H. Dettre, and D. A. Brandreth. "Dynamic contact angles and contact angle hysteresis". In: *Journal of Colloid and Interface science* 62.2 (1977), pp. 205–212.

[89] P. A. Thompson and M. O. Robbins. "Simulations of contact-line motion: slip and the dynamic contact angle". In: *Physical review letters* 63.7 (1989), p. 766.

[90] Š Šikalo et al. "Dynamic contact angle of spreading droplets: Experiments and simulations". In: *Physics of Fluids* 17.6 (2005), p. 062103.

[91] J. Banhart. "Light-Metal Foams—History of Innovation and Technological Challenges". In: *Advanced Engineering Materials* 15.3 (2013), pp. 82–111.

[92] D. Lehmhus et al. *Structural materials and processes in transportation*. John Wiley & Sons, 2013.

[93] M. F. Ashby et al. *Metal foams: a design guide*. Elsevier, 2000.

[94] H. P. Degischer and B. Kriszt. *Handbook of cellular metals: production, processing, applications*. Wiley-vch, 2002.

[95] J. Banhart and H.-W. Seeliger. "Aluminium foam sandwich panels: Manufacture, metallurgy and applications". In: *Advanced Engineering Materials* 10.9 (2008), pp. 793–802.

[96] I. Duarte et al. "Manufacturing and bending behaviour of in situ foam-filled aluminium alloy tubes". In: *Materials & Design* 66 (2015), pp. 532–544.

[97] I. Duarte et al. "Static and dynamic axial crush performance of in-situ foam-filled tubes". In: *Composite structures* 124 (2015), pp. 128–139.

[98] S. R. Bakshi et al. "Interface in carbon nanotube reinforced aluminum silicon composites: Thermodynamic analysis and experimental verification". In: *Journal of Alloys and Compounds* 481.1-2 (2009), pp. 207–213.

[99] T. Kuzumaki et al. “Processing of carbon nanotube reinforced aluminum composite”. In: *Journal of materials Research* 13.9 (1998), pp. 2445–2449.

[100] D. L. McDanels. “Analysis of stress-strain, fracture, and ductility behavior of aluminum matrix composites containing discontinuous silicon carbide reinforcement”. In: *Metallurgical transactions A* 16.6 (1985), pp. 1105–1115.

[101] L. Yolshina et al. “Novel aluminum-graphene and aluminum-graphite metallic composite materials: Synthesis and properties”. In: *Journal of alloys and compounds* 663 (2016), pp. 449–459.

[102] T Etter et al. “Aluminium carbide formation in interpenetrating graphite/aluminium composites”. In: *Materials Science and Engineering: A* 448.1-2 (2007), pp. 1–6.

[103] C Hu and T. Baker. “A new aluminium silicon carbide formed in laser processing”. In: *Journal of materials science* 32.19 (1997), pp. 5047–5051.

[104] H.-D. Steffens et al. “Carbide formation in aluminium-carbon fibre-reinforced composites”. In: *Journal of materials science* 32.20 (1997), pp. 5413–5417.

[105] Y. Zhang and G. Wu. “Comparative study on the interface and mechanical properties of T700/Al and M40/Al composites”. In: *Rare metals* 29.1 (2010), pp. 102–107.

[106] S.-H. Li and C.-G. Chao. “Effects of carbon fiber/Al interface on mechanical properties of carbon-fiber-reinforced aluminum-matrix composites”. In: *Metallurgical and Materials Transactions A* 35.7 (2004), pp. 2153–2160.

[107] M. Yang and V. Scott. “Interface and fracture of carbon fibre reinforced Al-7 wt% Si alloy”. In: *Journal of materials science* 26.6 (1991), pp. 1609–1617.

[108] M. Pech-Canul, R. Katz, and M. Makhlouf. “Optimum parameters for wetting silicon carbide by aluminum alloys”. In: *Metallurgical and Materials Transactions A* 31.2 (2000), pp. 565–573.

[109] W. Lacom, H. P. Degischer, and P. A. Schulz. “Assessment and control of surface reactions of carbon fibres in light weight metal matrix composites”. In: *Key Engineering Materials*. Vol. 127. Trans Tech Publ. 1997, pp. 679–686.

[110] V Ocelik, J. Vreeling, and J. T. M. De Hosson. “EBSP study of reaction zone in SiC/Al metal matrix composite prepared by laser melt injection”. In: *Journal of materials science* 36.20 (2001), pp. 4845–4849.

[111] J. Vreeling et al. “In-situ microscopy investigation of failure mechanisms in Al/SiC {sub p} metal matrix composite produced by laser embedding”. In: *Scripta Materialia* 42.6 (2000).

[112] S Kleiner et al. “Effect of diamond crystallographic orientation on dissolution and carbide formation in contact with liquid aluminium”. In: *Scripta Materialia* 55.4 (2006), pp. 291–294.

[113] B. Liu and E. S. Aydil. “Growth of oriented single-crystalline rutile TiO2 nanorods on transparent conducting substrates for dye-sensitized solar cells”. In: *Journal of the American Chemical Society* 131.11 (2009), pp. 3985–3990.

[114] S. Akamatsu and T. Ihle. "Similarity law for the tilt angle of dendrites in directional solidification of non-axially-oriented crystals". In: *Physical Review E* 56.4 (1997), p. 4479.

[115] J. Deschamps, M. Georgelin, and A. Pocheau. "Growth directions of microstructures in directional solidification of crystalline materials". In: *Physical Review E* 78.1 (2008), p. 011605.

[116] A. O. Mekhrabov and M. V. Akdeniz. "Modelling and Monte Carlo simulation of the atomic ordering processes in Ni3Al intermetallics". In: *Modelling and Simulation in Materials Science and Engineering* 15.2 (2006), p. 1.

[117] A Jacot and M Rappaz. "A pseudo-front tracking technique for the modelling of solidification microstructures in multi-component alloys". In: *Acta Materialia* 50.8 (2002), pp. 1909–1926.

[118] M. Rebow, D. J. Browne, and Y. Fautrelle. "Combined analytical and numerical front tracking approach to modeling directional solidification of a TiAl-based intermetallic alloy for design of microgravity experiments". In: *Materials Science Forum*. Vol. 649. Trans Tech Publ. 2010, pp. 243–248.

[119] A. Lis et al. "Early stage growth characteristics of Ag 3 Sn intermetallic compounds during solid–solid and solid–liquid reactions in the Ag–Sn interlayer system: Experiments and simulations". In: *Journal of Alloys and Compounds* 617 (2014), pp. 763–773.

[120] S. Tang et al. "Phase field modeling the growth of Ni3Al layer in the β/γ diffusion couple of Ni–Al binary system". In: *Intermetallics* 19.3 (2011), pp. 229–233.

[121] J. Guo et al. "Phase-field simulation of structure evolution at high growth velocities during directional solidification of Ti55Al45 alloy". In: *Intermetallics* 13.3-4 (2005), pp. 275–279.

[122] F. Wang and B. Nestler. "A phase-field study on the formation of the intermetallic Al2Au phase in the Al–Au system". In: *Acta Materialia* 95 (2015), pp. 65–73.

[123] F. Wang et al. "Numerical and Experimental Investigations on the Growth of the Intermetallic Mg2Si Phase in Mg Infiltrated Si-Foams". In: *Advanced Engineering Materials* 19.10 (2017), p. 1700063.

[124] M. Park, S. Gibbons, and R Arróyave. "Phase-field simulations of intermetallic compound evolution in Cu/Sn solder joints under electromigration". In: *Acta Materialia* 61.19 (2013), pp. 7142–7154.

[125] T. Haxhimali et al. "Orientation selection in dendritic evolution". In: *Nature materials* 5.8 (2006), p. 660.

[126] H. Xing et al. "Orientation dependence of columnar dendritic growth with side-branching behaviors in directional solidification: insights from phase-field simulations". In: *Metallurgical and Materials Transactions B* (2018), pp. 1–13.

[127] D. Tourret et al. "Grain growth competition during thin-sample directional solidification of dendritic microstructures: a phase-field study". In: *Acta Materialia* 122 (2017), pp. 220–235.

[128] G. Demange et al. “A phase field model for snow crystal growth in three dimensions”. In: *npj Computational Materials* 3.1 (2017), p. 15.

[129] A. Karma and W.-J. Rappel. “Quantitative phase-field modeling of dendritic growth in two and three dimensions”. In: *Physical review E* 57.4 (1998), p. 4323.

[130] G. McFadden et al. “Phase-field models for anisotropic interfaces”. In: *Physical Review E* 48.3 (1993), p. 2016.

[131] R. F. Sekerka. “Analytical criteria for missing orientations on three-dimensional equilibrium shapes”. In: *Journal of crystal growth* 275.1-2 (2005), pp. 77–82.

[132] J. A. Lemberg and R. O. Ritchie. “Mo-Si-B Alloys for Ultrahigh-Temperature Structural Applications”. In: *Advanced Materials* 24.26 (2012), pp. 3445–3480.

[133] J. H. Perepezko. “The hotter the engine, the better”. In: *Science* 326.5956 (2009), pp. 1068–1069.

[134] M. A. Azim et al. “Creep resistance and oxidation behavior of novel Mo-Si-B-Ti alloys”. In: *JOM* 67.11 (2015), pp. 2621–2628.

[135] S. Obert, A. Kauffmann, and M. Heilmaier. “Characterisation of the oxidation and creep behaviour of novel Mo-Si-Ti alloys”. In: *Acta Materialia* 184 (2020), pp. 132–142. ISSN: 1359-6454. DOI: https://doi.org/10.1016/j.actamat.2019.11.045. URL: https://www.sciencedirect.com/science/article/pii/S1359645419307840.

[136] Y Yang et al. “Experimental investigation and thermodynamic descriptions of the Mo–Si–Ti system”. In: *Materials Science and Engineering: A* 361.1-2 (2003), pp. 281–293.

[137] V. V. Podolinsky, Y. Taran, and V. G. Drykin. “Eutectic solidification in organic systems”. In: *Journal of Crystal Growth* 74.1 (1986), pp. 57–66. ISSN: 0022-0248. DOI: https://doi.org/10.1016/0022-0248(86)90248-4. URL: https://www.sciencedirect.com/science/article/pii/0022024886902484.

[138] K. Dargahi Noubary, M. Kellner, and B. Nestler. “Rotating Directional Solidification of Ternary Eutectic Microstructures in Bi-In-Sn: A Phase-Field Study”. In: *Materials* 15.3 (2022). ISSN: 1996-1944. DOI: 10.3390/ma15031160. URL: https://www.mdpi.com/1996-1944/15/3/1160.

[139] B. Nestler, H. Garcke, and B. Stinner. “Multicomponent alloy solidification: Phase-field modeling and simulations”. In: *Phys. Rev. E* 71 (4 2005), p. 041609. DOI: 10.1103/PhysRevE.71.041609. URL: https://link.aps.org/doi/10.1103/PhysRevE.71.041609.

[140] O Kazemi et al. “Phase field simulation of a directional solidification of a ternary eutectic Mo-Si-B Alloy”. In: *IOP Conference Series: Materials Science and Engineering* 118.1 (2016), p. 012028. DOI: 10.1088/1757-899X/118/1/012028. URL: https://dx.doi.org/10.1088/1757-899X/118/1/012028.

[141] M. Rahul, S. Samal, and G. Phanikumar. "Metastable microstructures in the solidification of undercooled high entropy alloys". In: *Journal of Alloys and Compounds* 821 (2020), p. 153488. ISSN: 0925-8388. DOI: https://doi.org/10.1016/j.jallcom.2019.153488. URL: https://www.sciencedirect.com/science/article/pii/S0925838819347346.

[142] J. Park, J.-H. Kang, and C.-S. Oh. "Phase-field simulations and microstructural analysis of epitaxial growth during rapid solidification of additively manufactured AlSi10Mg alloy". In: *Materials & Design* 195 (2020), p. 108985. ISSN: 0264-1275. DOI: https://doi.org/10.1016/j.matdes.2020.108985. URL: https://www.sciencedirect.com/science/article/pii/S0264127520305190.

[143] M. Apel et al. "Grain growth simulations including particle pinning using the multiphase-field concept". In: *ISIJ international* 49.7 (2009), pp. 1024–1029.

[144] J. Eiken. "Discussion of the Accuracy of the Multi-Phase-Field Approach to Simulate Grain Growth with Anisotropic Grain Boundary Properties". In: *ISIJ International* 60.8 (2020), pp. 1832–1834. DOI: 10.2355/isijinternational.ISIJINT-2019-722.

[145] J. Kundin, E. Pogorelov, and H. Emmerich. "Phase-field modeling of the microstructure evolution and heterogeneous nucleation in solidifying ternary Al–Cu–Ni alloys". In: *Acta Materialia* 83 (2015), pp. 448–459. ISSN: 1359-6454. DOI: https://doi.org/10.1016/j.actamat.2014.09.057. URL: https://www.sciencedirect.com/science/article/pii/S135964541400754X.

[146] J. D. Van der Waals. "The thermodynamic theory of capillarity under the hypothesis of a continuous variation of density". In: *Journal of Statistical Physics* 20.2 (1979), pp. 200–244.

[147] V. L. Ginzburg and L. D. Landau. "On the Theory of Superconductivity". In: *On Superconductivity and Superfluidity: A Scientific Autobiography*. Berlin, Heidelberg: Springer Berlin Heidelberg, 2009, pp. 113–137. ISBN: 978-3-540-68008-6. DOI: 10.1007/978-3-540-68008-6_4. URL: https://doi.org/10.1007/978-3-540-68008-6_4.

[148] J. W. Cahn and J. E. Hilliard. "Free Energy of a Nonuniform System. I. Interfacial Free Energy". In: *The Journal of Chemical Physics* 28.2 (Aug. 2004), pp. 258–267. ISSN: 0021-9606. DOI: 10.1063/1.1744102. eprint: https://pubs.aip.org/aip/jcp/article-pdf/28/2/258/11106115/258_1_online.pdf. URL: https://doi.org/10.1063/1.1744102.

[149] J. W. Cahn. "Free Energy of a Nonuniform System. II. Thermodynamic Basis". In: *The Journal of Chemical Physics* 30.5 (Aug. 2004), pp. 1121–1124. ISSN: 0021-9606. DOI: 10.1063/1.1730145. eprint: https://pubs.aip.org/aip/jcp/article-pdf/30/5/1121/7404897/1121_1_online.pdf. URL: https://doi.org/10.1063/1.1730145.

[150] J. W. Cahn and J. E. Hilliard. "Free Energy of a Nonuniform System. III. Nucleation in a Two-Component Incompressible Fluid". In: *The Journal of Chemical Physics* 31.3 (Aug. 2004), pp. 688–699. ISSN: 0021-9606. DOI: 10.1063/1.1730447. eprint: https://pubs.aip.org/aip/jcp/article-pdf/31/3/688/10945650/688_1_online.pdf. URL: https://doi.org/10.1063/1.1730447.

[151] J. Hilliard and J. Cahn. "On the nature of the interface between a solid metal and its melt". In: *Acta Metallurgica* 6.12 (1958), pp. 772–774. ISSN: 0001-6160. DOI: https://doi.org/10.1016/0001-6160(58)90052-X. URL: https://www.sciencedirect.com/science/article/pii/000161605890052X.

[152] S. M. Allen and J. W. Cahn. "A microscopic theory for antiphase boundary motion and its application to antiphase domain coarsening". In: *Acta Metallurgica* 27.6 (1979), pp. 1085–1095. ISSN: 0001-6160. DOI: https://doi.org/10.1016/0001-6160(79)90196-2. URL: https://www.sciencedirect.com/science/article/pii/0001616079901962.

[153] B. I. Halperin, P. C. Hohenberg, and S.-k. Ma. "Renormalization-group methods for critical dynamics: I. Recursion relations and effects of energy conservation". In: *Phys. Rev. B* 10 (1 1974), pp. 139–153. DOI: 10.1103/PhysRevB.10.139. URL: https://link.aps.org/doi/10.1103/PhysRevB.10.139.

[154] P. C. Hohenberg and B. I. Halperin. "Theory of dynamic critical phenomena". In: *Rev. Mod. Phys.* 49 (3 1977), pp. 435–479. DOI: 10.1103/RevModPhys.49.435. URL: https://link.aps.org/doi/10.1103/RevModPhys.49.435.

[155] A. A. Wheeler, W. J. Boettinger, and G. B. McFadden. "Phase-field model for isothermal phase transitions in binary alloys". In: *Phys. Rev. A* 45 (10 1992), pp. 7424–7439. DOI: 10.1103/PhysRevA.45.7424. URL: https://link.aps.org/doi/10.1103/PhysRevA.45.7424.

[156] A. A. Wheeler, W. J. Boettinger, and G. B. McFadden. "Phase-field model of solute trapping during solidification". In: *Phys. Rev. E* 47 (3 1993), pp. 1893–1909. DOI: 10.1103/PhysRevE.47.1893. URL: https://link.aps.org/doi/10.1103/PhysRevE.47.1893.

[157] J. B. Collins and H. Levine. "Diffuse interface model of diffusion-limited crystal growth". In: *Phys. Rev. B* 31 (9 1985), pp. 6119–6122. DOI: 10.1103/PhysRevB.31.6119. URL: https://link.aps.org/doi/10.1103/PhysRevB.31.6119.

[158] R. Kobayashi. "Modeling and numerical simulations of dendritic crystal growth". In: *Physica D: Nonlinear Phenomena* 63.3 (1993), pp. 410–423. ISSN: 0167-2789. DOI: https://doi.org/10.1016/0167-2789(93)90120-P. URL: https://www.sciencedirect.com/science/article/pii/016727899390120P.

[159] H. Garcke, B. Nestler, and B. Stoth. "On anisotropic order parameter models for multi-phase systems and their sharp interface limits". In: *Physica D: Nonlinear Phenomena* 115.1 (1998), pp. 87–108. ISSN: 0167-2789. DOI: https://doi.org/10.1016/S0167-2789(97)00227-3. URL: https://www.sciencedirect.com/science/article/pii/S0167278997002273.

[160] B. Stinner, B. Nestler, and H. Garcke. "A Diffuse Interface Model for Alloys with Multiple Components and Phases". In: *SIAM Journal on Applied Mathematics* 64.3 (2004), pp. 775–799. DOI: 10.1137/S0036139902413143. eprint: https://doi.org/10.1137/S0036139902413143. URL: https://doi.org/10.1137/S0036139902413143.

[161] B. Nestler. "A 3D parallel simulator for crystal growth and solidification in complex alloy systems". In: *Journal of Crystal Growth* 275.1 (2005). Proceedings of the 14th International Conference on Crystal Growth and the 12th International Conference on Vapor Growth and Epitaxy, e273–e278. ISSN: 0022-0248. DOI: https://doi.org/10.1016/j.jcrysgro.2004.10.121. URL: https://www.sciencedirect.com/science/article/pii/S002202480401437X.

[162] P.-R. Cha, D.-H. Yeon, and J.-K. Yoon. "Phase-field model for multicomponent alloy solidification". In: *Journal of Crystal Growth* 274.1 (2005), pp. 281–293. ISSN: 0022-0248. DOI: https://doi.org/10.1016/j.jcrysgro.2004.10.002. URL: https://www.sciencedirect.com/science/article/pii/S0022024804012539.

[163] J. Eiken, B. Böttger, and I. Steinbach. "Multiphase-field approach for multicomponent alloys with extrapolation scheme for numerical application". In: *Phys. Rev. E* 73 (6 2006), p. 066122. DOI: 10.1103/PhysRevE.73.066122. URL: https://link.aps.org/doi/10.1103/PhysRevE.73.066122.

[164] O. Penrose and P. C. Fife. "Thermodynamically consistent models of phase-field type for the kinetic of phase transitions". In: *Physica D: Nonlinear Phenomena* 43.1 (1990), pp. 44–62. ISSN: 0167-2789. DOI: https://doi.org/10.1016/0167-2789(90)90015-H. URL: https://www.sciencedirect.com/science/article/pii/016727899090015H.

[165] G. Caginalp. "Stefan and Hele-Shaw type models as asymptotic limits of the phase-field equations". In: *Phys. Rev. A* 39 (11 1989), pp. 5887–5896. DOI: 10.1103/PhysRevA.39.5887. URL: https://link.aps.org/doi/10.1103/PhysRevA.39.5887.

[166] P. Steinmetz et al. "Large-scale phase-field simulations of ternary eutectic microstructure evolution". In: *Computational Materials Science* 117 (2016), pp. 205–214. ISSN: 0927-0256. DOI: https://doi.org/10.1016/j.commatsci.2016.02.001. URL: https://www.sciencedirect.com/science/article/pii/S0927025616300180.

[167] A. Karma and W.-J. Rappel. "Phase-field method for computationally efficient modeling of solidification with arbitrary interface kinetics". In: *Physical review E* 53.4 (1996), R3017.

[168] S. Gyoon Kim, W. Tae Kim, and T. Suzuki. "Phase-field model with a reduced interface diffuseness". In: *Journal of Crystal Growth* 263.1 (2004), pp. 620–628. ISSN: 0022-0248. DOI: https://doi.org/10.1016/j.jcrysgro.2003.12.003. URL: https://www.sciencedirect.com/science/article/pii/S0022024803021729.

[169] S. G. Kim et al. "Computer simulations of two-dimensional and three-dimensional ideal grain growth". In: *Phys. Rev. E* 74 (6 2006), p. 061605. DOI: 10.1103/PhysRevE.74.061605. URL: https://link.aps.org/doi/10.1103/PhysRevE.74.061605.

[170] W. Boettinger et al. “Prediction of solute trapping at high solidification rates using a diffuse interface phase-field theory of alloy solidification”. In: *Materials Science and Engineering: A* 178.1 (1994). NATO-Advanced Research Workshop on Undercooled Metallic Melts: Properties, Solidification and Metastable Phases, pp. 217–223. ISSN: 0921-5093. DOI: https://doi.org/10.1016/0921-5093(94)90546-0. URL: https://www.sciencedirect.com/science/article/pii/0921509394905460.

[171] N. A. Ahmad et al. “Solute trapping and solute drag in a phase-field model of rapid solidification”. In: *Phys. Rev. E* 58 (3 1998), pp. 3436–3450. DOI: 10.1103/PhysRevE.58.3436. URL: https://link.aps.org/doi/10.1103/PhysRevE.58.3436.

[172] M. Conti and M. Fermani. “Interface dynamics and solute trapping in alloy solidification with density change”. In: *Phys. Rev. E* 67 (2 2003), p. 026117. DOI: 10.1103/PhysRevE.67.026117. URL: https://link.aps.org/doi/10.1103/PhysRevE.67.026117.

[173] H. Wang et al. “Application of the maximal entropy production principle to rapid solidification: A multi-phase-field model”. In: *Acta Materialia* 61.7 (2013), pp. 2617–2627. ISSN: 1359-6454. DOI: https://doi.org/10.1016/j.actamat.2013.01.041. URL: https://www.sciencedirect.com/science/article/pii/S1359645413000682.

[174] B. Echebarria et al. “Quantitative phase-field model of alloy solidification”. In: *Phys. Rev. E* 70 (6 2004), p. 061604. DOI: 10.1103/PhysRevE.70.061604. URL: https://link.aps.org/doi/10.1103/PhysRevE.70.061604.

[175] S. G. Kim. “A phase-field model with antitrapping current for multicomponent alloys with arbitrary thermodynamic properties”. In: *Acta Materialia* 55.13 (2007), pp. 4391–4399. ISSN: 1359-6454. DOI: https://doi.org/10.1016/j.actamat.2007.04.004. URL: https://www.sciencedirect.com/science/article/pii/S1359645407002467.

[176] A. Carré, B. Böttger, and M. Apel. “Implementation of an antitrapping current for a multicomponent multiphase-field ansatz”. In: *Journal of Crystal Growth* 380 (2013), pp. 5–13. ISSN: 0022-0248. DOI: https://doi.org/10.1016/j.jcrysgro.2013.05.032. URL: https://www.sciencedirect.com/science/article/pii/S0022024813003874.

[177] A. Mullis. “Quantification of mesh induced anisotropy effects in the phase-field method”. In: *Computational Materials Science* 36.3 (2006), pp. 345–353. ISSN: 0927-0256. DOI: https://doi.org/10.1016/j.commatsci.2005.02.017. URL: https://www.sciencedirect.com/science/article/pii/S0927025605001837.

[178] B. Nestler, D. Danilov, and P. Galenko. “Crystal growth of pure substances: Phase-field simulations in comparison with analytical and experimental results”. In: *Journal of Computational Physics* 207.1 (2005), pp. 221–239. ISSN: 0021-9991. DOI: https://doi.org/10.1016/j.jcp.2005.01.018. URL: https://www.sciencedirect.com/science/article/pii/S0021999105000240.

[179] G. B. McFadden et al. “Phase-field models for anisotropic interfaces”. In: *Phys. Rev. E* 48 (3 1993), pp. 2016–2024. DOI: 10.1103/PhysRevE.48.2016. URL: https://link.aps.org/doi/10.1103/PhysRevE.48.2016.

[180] H. Garcke, B. Nestler, and B. Stoth. “A MultiPhase Field Concept: Numerical Simulations of Moving Phase Boundaries and Multiple Junctions”. In: *SIAM Journal on Applied Mathematics* 60.1 (1999), pp. 295–315. DOI: 10.1137/S0036139998334895. eprint: https://doi.org/10.1137/S0036139998334895. URL: https://doi.org/10.1137/S0036139998334895.

[181] G. Caginalp and P. Fife. “Phase-field methods for interfacial boundaries”. In: *Phys. Rev. B* 33 (11 1986), pp. 7792–7794. DOI: 10.1103/PhysRevB.33.7792. URL: https://link.aps.org/doi/10.1103/PhysRevB.33.7792.

[182] G. Caginalp and P. Fife. “Higher-order phase field models and detailed anisotropy”. In: *Phys. Rev. B* 34 (7 1986), pp. 4940–4943. DOI: 10.1103/PhysRevB.34.4940. URL: https://link.aps.org/doi/10.1103/PhysRevB.34.4940.

[183] R. Folch and M. Plapp. “Towards a quantitative phase-field model of two-phase solidification”. In: *Phys. Rev. E* 68 (1 2003), p. 010602. DOI: 10.1103/PhysRevE.68.010602. URL: https://link.aps.org/doi/10.1103/PhysRevE.68.010602.

[184] B. Nestler, H. Garcke, and B. Stinner. “Multicomponent alloy solidification: phase-field modeling and simulations”. In: *Physical Review E* 71.4 (2005), p. 041609.

[185] M. Plapp. “Unified derivation of phase-field models for alloy solidification from a grand-potential functional”. In: *Phys. Rev. E* 84 (3 2011), p. 031601. DOI: 10.1103/PhysRevE.84.031601. URL: https://link.aps.org/doi/10.1103/PhysRevE.84.031601.

[186] Y. Cai et al. “Phase-field investigation on the microstructural evolution of eutectic transformation and four-phase reaction in Mo-Si-Ti system”. In: *Acta Materialia* 258 (2023), p. 119178. ISSN: 1359-6454. DOI: https://doi.org/10.1016/j.actamat.2023.119178. URL: https://www.sciencedirect.com/science/article/pii/S1359645423005098.

[187] B. Echebarria et al. “Quantitative phase-field model of alloy solidification”. In: *Physical review E* 70.6 (2004), p. 061604.

[188] O. Tschukin et al. “Concepts of modeling surface energy anisotropy in phase-field approaches”. In: *Geothermal Energy* 5.1 (2017), p. 19.

[189] I. Steinbach et al. “CALPHAD and Phase-Field Modeling: A Successful Liaison”. In: *Journal of Phase Equilibria and Diffusion* 28.1 (2007), pp. 101–106. ISSN: 1863-7345. DOI: 10.1007/s11669-006-9009-2. URL: https://doi.org/10.1007/s11669-006-9009-2.

[190] S. G. Fries et al. “Upgrading CALPHAD to microstructure simulation: the phase-field method”. In: *International Journal of Materials Research* 100.2 (2009), pp. 128–134. DOI: doi:10.3139/146.110013. URL: https://doi.org/10.3139/146.110013.

[191] L. Zhang et al. "Incorporating the CALPHAD sublattice approach of ordering into the phase-field model with finite interface dissipation". In: *Acta Materialia* 88 (2015), pp. 156–169. ISSN: 1359-6454. DOI: https://doi.org/10.1016/j.actamat.2014.11.037. URL: https://www.sciencedirect.com/science/article/pii/S1359645414008908.

[192] T. Wang et al. "Coarsening kinetics of γ precipitates in the Ni–Al–Mo system". In: *Acta Materialia* 56.19 (2008), pp. 5544–5551. ISSN: 1359-6454. DOI: https://doi.org/10.1016/j.actamat.2008.07.024. URL: https://www.sciencedirect.com/science/article/pii/S1359645408005259.

[193] K Wu, Y. Chang, and Y Wang. "Simulating interdiffusion microstructures in Ni–Al–Cr diffusion couples: a phase field approach coupled with CALPHAD database". In: *Scripta Materialia* 50.8 (2004), pp. 1145–1150. ISSN: 1359-6462. DOI: https://doi.org/10.1016/j.scriptamat.2004.01.025. URL: https://www.sciencedirect.com/science/article/pii/S1359646204000429.

[194] Q. Chen et al. "Quantitative phase field modeling of diffusion-controlled precipitate growth and dissolution in Ti–Al–V". In: *Scripta Materialia* 50.4 (2004), pp. 471–476. ISSN: 1359-6462. DOI: https://doi.org/10.1016/j.scriptamat.2003.10.032. URL: https://www.sciencedirect.com/science/article/pii/S135964620300719X.

[195] R. D. Ramdan, T. Takaki, and Y. Tomita. "Free Energy Problem for the Simulations of the Growth of Fe₂B Phase Using Phase-Field Method". In: *MATERIALS TRANSACTIONS* 49.11 (2008), pp. 2625–2631. DOI: 10.2320/matertrans.MRA2008158.

[196] H.-S. Kim et al. "Three-dimensional simulation of intermetallic compound layer growth in a binary alloy system". In: *Acta Materialia* 57.4 (2009), pp. 1254–1262. ISSN: 1359-6454. DOI: https://doi.org/10.1016/j.actamat.2008.11.006. URL: https://www.sciencedirect.com/science/article/pii/S1359645408008148.

[197] O. Redlich and A. Kister. "Algebraic representation of thermodynamic properties and the classification of solutions". In: *Industrial & Engineering Chemistry* 40.2 (1948), pp. 345–348.

[198] K. Dargahi Noubary et al. "Data workflow to incorporate thermodynamic energies from Calphad databases into grand-potential-based phase-field models". In: *Journal of Materials Science* 56.20 (2021), pp. 11932–11952. ISSN: 1573-4803. DOI: 10.1007/s10853-021-06033-7. URL: https://doi.org/10.1007/s10853-021-06033-7.

[199] P. Gustafson. "A Thermodynamic Evaluation of the Fe–C System". In: *Scand. J. Metall.* 14.5 (1985), pp. 259–267.

[200] J. Gröbner, H. L. Lukas, and F. Aldinger. "Thermodynamic calculation of the ternary system Al-Si-C". In: *Calphad* 20.2 (1996), pp. 247–254.

[201] R. Siegel. "Vacancy concentrations in metals". In: *Journal of Nuclear Materials* 69 (1978), pp. 117–146.

[202] F. Wang et al. "Phase-field study on the growth of magnesium silicide occasioned by reactive diffusion on the surface of Si-foams". In: *Acta Materialia* (2019).

[203] Y. Yang et al. "Multiphase equilibria in the metal-rich region of the Mo–Ti–Si–B system: thermodynamic prediction and experimental validation". In: *Acta Materialia* 53.6 (2005), pp. 1711–1720. ISSN: 1359-6454. DOI: https://doi.org/10.1016/j.actamat.2004.12.020. URL: https://www.sciencedirect.com/science/article/pii/S1359645404007578.

[204] S. Obert et al. "On the chemical and microstructural requirements for the pesting-resistance of Mo–Si–Ti alloys". In: *Journal of Materials Research and Technology* 9.4 (2020), pp. 8556–8567. ISSN: 2238-7854. DOI: https://doi.org/10.1016/j.jmrt.2020.06.002. URL: https://www.sciencedirect.com/science/article/pii/S2238785420314034.

[205] S. Majumdar et al. "Kinetics of oxide scale growth on a (Ti, Mo)$_5$Si$_3$ based oxidation resistant Mo-Ti-Si alloy at 900-1300°C". In: *High Temperature Materials and Processes* 38.2019 (2019), pp. 533–540. DOI: doi:10.1515/htmp-2019-0056. URL: https://doi.org/10.1515/htmp-2019-0056.

[206] H Fredriksson and T Nylen. "Mechanism of peritectic reactions and transformations". In: *Metal Science* 16.6 (1982), pp. 283–294.

[207] W. Villanueva et al. "Effect of phase change and solute diffusion on spreading on a dissolving substrate". In: *Acta Materialia* 57.20 (2009), pp. 6022–6036. ISSN: 1359-6454. DOI: https://doi.org/10.1016/j.actamat.2009.08.033. URL: https://www.sciencedirect.com/science/article/pii/S1359645409005412.

[208] H W. Kerr, J Cisse, and G. Bolling. "On equilibrium and non-equilibrium peritectic transformations". In: *Acta Metallurgica* 22.6 (1974), pp. 677 –686. ISSN: 0001-6160. DOI: https://doi.org/10.1016/0001-6160(74)90077-7. URL: http://www.sciencedirect.com/science/article/pii/0001616074900777.

[209] S. Griesser, C. Bernhard, and R. Dippenaar. "Mechanism of the Peritectic Phase Transition in Fe–C and Fe–Ni Alloys under Conditions Close to Chemical and Thermal Equilibrium". In: *ISIJ International* 54.2 (2014), pp. 466–473. DOI: 10.2355/isijinternational.54.466.

[210] R. W. Balluffi, S. M. Allen, and W. C. Carter. *Kinetics of materials*. John Wiley & Sons, 2005.

[211] N. Peterson. "Self-diffusion in pure metals". In: *Journal of Nuclear Materials* 69 (1978), pp. 3–37.

[212] K Tapasa et al. "Computer simulation of carbon diffusion and vacancy–carbon interaction in α-iron". In: *Acta materialia* 55.1 (2007), pp. 1–11.

[213] H. Mehrer. "Diffusion in intermetallics". In: *Materials Transactions, JIM* 37.6 (1996), pp. 1259–1280.

[214] Q.-L. Cao et al. "Transport Properties and the Entropy-Scaling Law for Liquid Tantalum and Molybdenum under High Pressure". In: *Chinese Physics Letters* 31.6 (2014), p. 66202. DOI: 10.1088/0256-307x/31/6/066202. URL: https://doi.org/10.1088/0256-307x/31/6/066202.

[215] A. Meyer et al. "Self Diffusion in Liquid Titanium: Quasielastic Neutron Scattering and Molecular Dynamics Simulation". In: *Diffusion in Materials - DIMAT2008*. Vol. 289. Defect and Diffusion Forum. Trans Tech Publications Ltd, May 2009, pp. 609–614. DOI: 10.4028/www.scientific.net/DDF.289-292.609.

[216] Y. Liu et al. "Microstructures and mechanical behavior of PM Ti-Mo alloy". In: *Journal of Central South University of Technology* 10.2 (2003), pp. 81–86.

[217] C. Fu and M. Yoo. "Interfacial energies in two-phase TiAl-Ti3Al alloy". In: *Scripta Materialia* 37.10 (1997), pp. 1453–1459. ISSN: 1359-6462. DOI: https://doi.org/10.1016/S1359-6462(97)00313-8. URL: https://www.sciencedirect.com/science/article/pii/S1359646297003138.

[218] G. Kaptay. "Modelling interfacial energies in metallic systems". In: *Materials Science Forum*. Vol. 473. Trans Tech Publ. 2005, pp. 1–10.

[219] A. Vondrous et al. "Parallel computing for phase-field models". In: *The International Journal of High Performance Computing Applications* 28.1 (2014), pp. 61–72. DOI: 10.1177/1094342013490972. eprint: https://doi.org/10.1177/1094342013490972. URL: https://doi.org/10.1177/1094342013490972.

[220] M. Ginibre, S. Akamatsu, and G. Faivre. "Experimental determination of the stability diagram of a lamellar eutectic growth front". In: *Phys. Rev. E* 56 (1 1997), pp. 780–796. DOI: 10.1103/PhysRevE.56.780. URL: https://link.aps.org/doi/10.1103/PhysRevE.56.780.

[221] Karma Alain and Sarkissian Armand. "Morphological instabilities of lamellar eutectics". In: *Metallurgical and Materials Transactions A* 27.3 (1996), pp. 635–656. ISSN: 1543-1940. DOI: https://doi.org/10.1007/BF02648952.

[222] M. Perrut et al. "Dynamic instabilities of rod-like eutectic growth patterns: A real-time study". In: *Acta Materialia* 61.18 (2013), pp. 6802–6808. ISSN: 1359-6454. DOI: https://doi.org/10.1016/j.actamat.2013.07.054. URL: https://www.sciencedirect.com/science/article/pii/S1359645413005740.

[223] K. A. Jackson and J. D. Hunt. "Lamellar and Rod Eutectic Growth". In: *Dynamics of Curved Fronts*. Ed. by P. Pelcé. San Diego: Academic Press, 1988, pp. 363–376. ISBN: 978-0-12-550355-6. DOI: https://doi.org/10.1016/B978-0-08-092523-3.50040-X. URL: https://www.sciencedirect.com/science/article/pii/B978008092523350040X.

[224] G. H. Meier. "Introduction to surface quantities". In: *Thermodynamics of Surfaces and Interfaces: Concepts in Inorganic Materials*. Cambridge University Press, 2014, 40–72. DOI: 10.1017/CBO9781139047029.003.

A. Appendix

A.1. Phase diagram

Here, we show the temperature dependence of all coefficients in free energy function for all three phases in Mo-Si-Ti system. When the eutectic phase transformation occurs in a relatively small temperature range, the temperature-dependence of coefficients are fitted by a linear function. Fig. A.1 and Fig. A.2 illustrate the six coefficients as a function of temperature for liquid phase and β phase, respectively. All coefficients are formulated in a general formula as

$$x^L = a_0^L + a_1^l T. \tag{A.1}$$

x represents a, b, d, e, g, and h in free energy function.

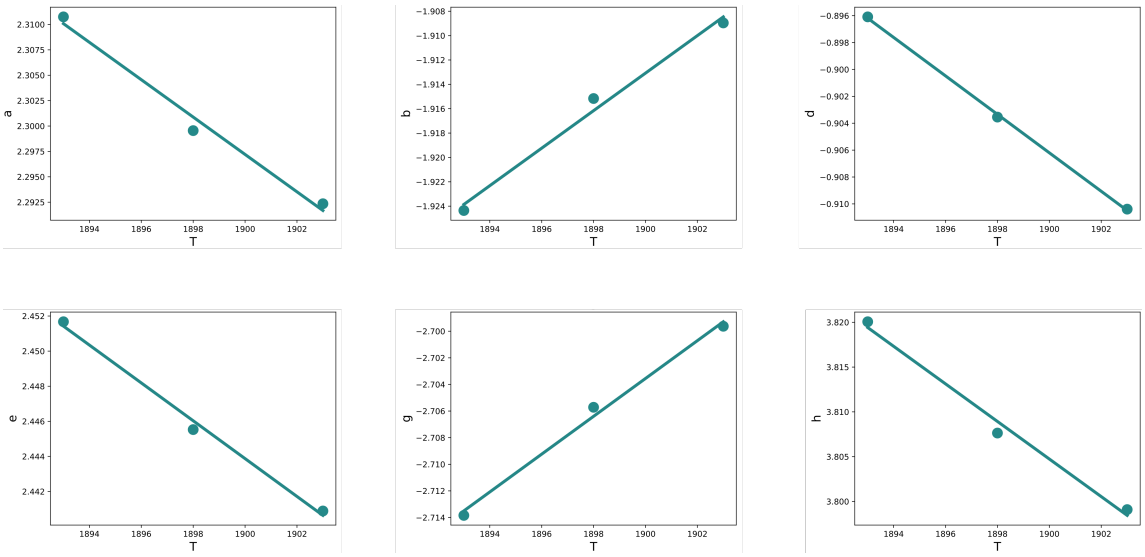

Figure A.1.: The six coefficients in free energy function of liquid phase as a function of temperature.

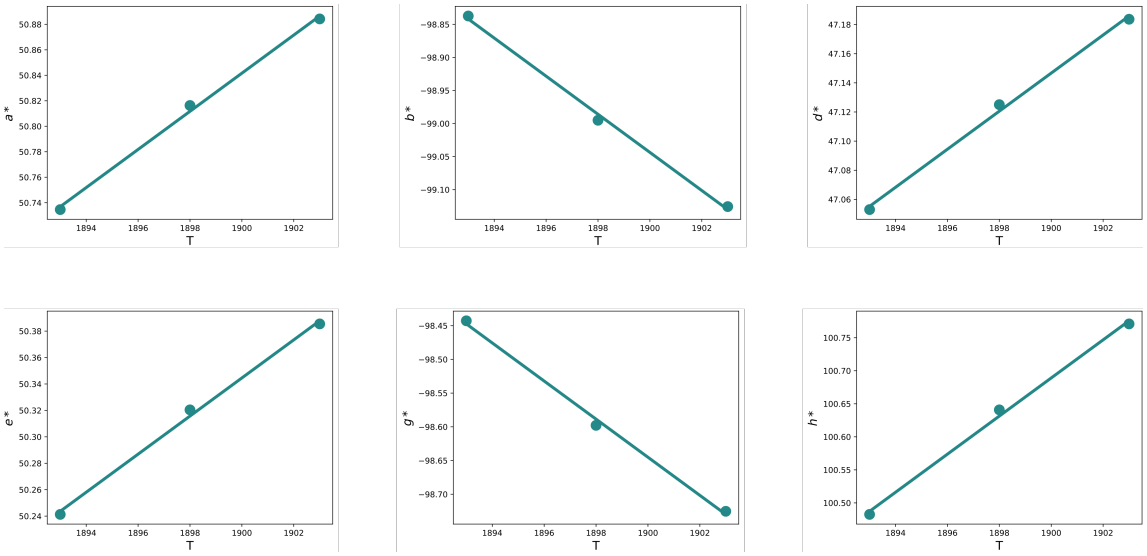

Figure A.2.: The six coefficients in free energy function of β phase as a function of temperature.

When the eutectic phase transformation occurs in a relatively large temperature range, the temperature-dependence of coefficients are written as a power series in temperature

$$x^L = a_0^L + a_1^L T + a_2^L T ln(T) + a_3^L T^2 + a_4^L T^3. \tag{A.2}$$

x represents a, b, d, e, g, and h in free energy function. In this case, all coefficients as a function of temperature for liquid and β phases are illustrated in Fig. A.3 and Fig. A.4, respectively.

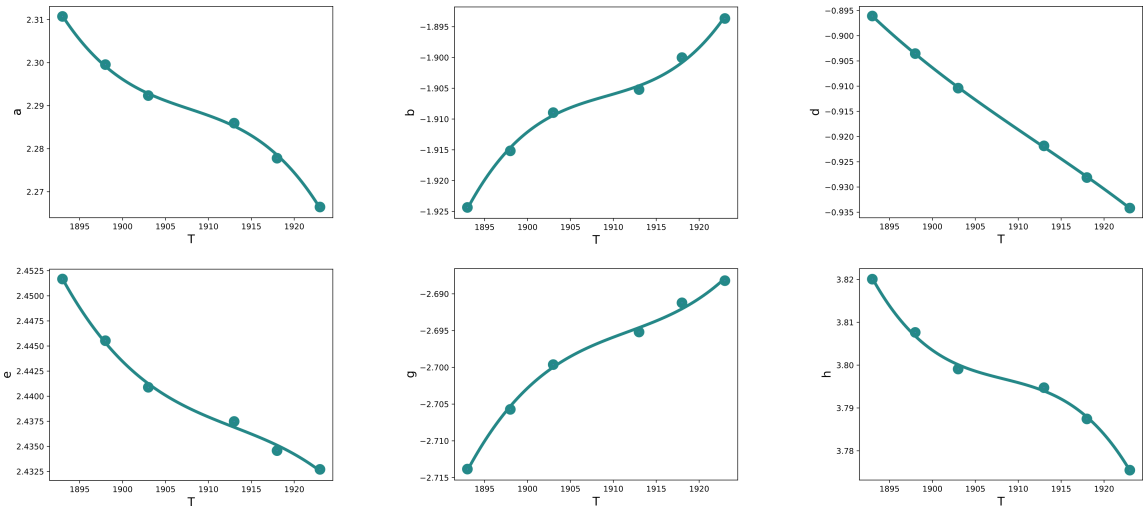

Figure A.3.: The six coefficients in free energy function of liquid phase as a function of temperature.

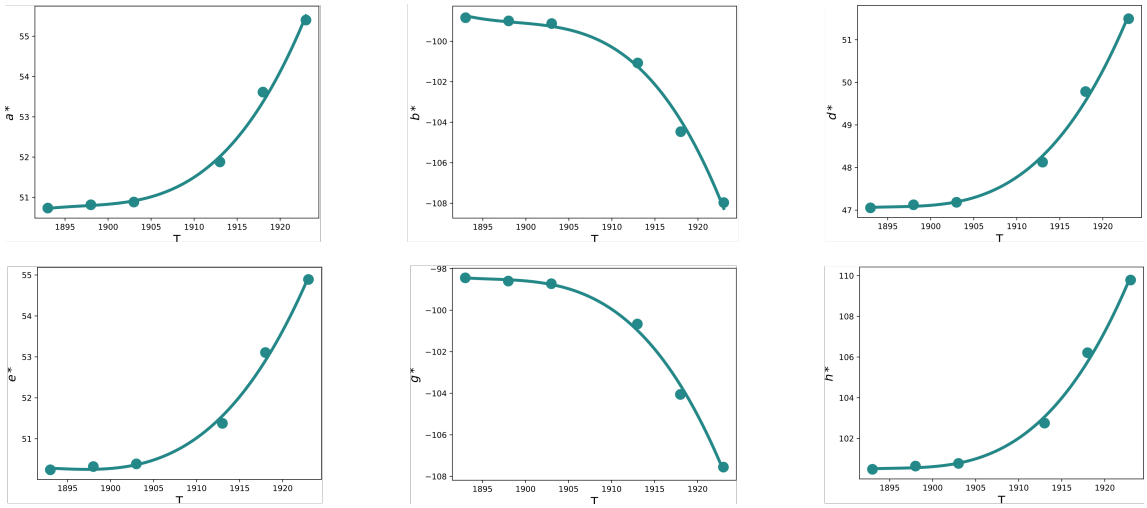

Figure A.4.: The six coefficients in free energy function of β phase as a function of temperature.

A.2. Calculation of dynamic contact angle

The code for calculating the dynamic contact angle is presented as follows.

```
import pandas as pd
from IPython.display import display
import ast
from scipy.interpolate import griddata
import numpy as np
import math

# extract concentration data from "concentration.dat"
# columns=['x','y','c','t']
df_concen=pd.read_csv("./FeC_Gab2_R20_c019/concentration.dat",sep=" ",index_col=None,header=None)
df_concen.columns=['x','y','c','timestamp','time']
display(df_concen.head())

df_tp=pd.read_csv("./xxx.csv",delimiter=",",index_col=0,converters={"TP":
ast.literal_eval,"p1": ast.literal_eval,"p2": ast.literal_eval,"p3": ast.literal_eval})
df_p1=pd.read_csv("./xxx.csv",delimiter=",",index_col=0,converters={"p1": ast.literal_eval})
df_p2=pd.read_csv("./xxx.csv",delimiter=",",index_col=0,converters={"p2": ast.literal_eval})

def get_neighber_points(tp):
    np1=(int(tp[0]),int(tp[1]))
    np2=(int(tp[0]+1),int(tp[1]))
    np3=(int(tp[0]),int(tp[1]+1))
    np4=(int(tp[0]+1),int(tp[1]+1))
    #print(np1,np2,np3,np4)
    return [np1,np2,np3,np4]

for i in df_tp.index:
    tp=df_tp.loc[i,"TP"]
    np_list=get_neighber_points(tp)
    #print(np_list)
    locations=np.asarray([[np[0] for np in np_list],[np[1] for np in np_list]]).T
    try:
        cs=list(map(lambda a: df_concen.loc[(df_concen["x"]==a[0])&(df_concen["y"]==a[1])
        &(df_concen["timestamp"]==i)]['c'].values[0],np_list))

        # use 4 neighbor points around TP to intepolate the concentration of TP point
        c_predict = griddata(locations, cs, tp, method='cubic')

        c_predict=round(float(c_predict),6)

        df_tp.loc[i,'tp-c']=c_predict

    except:
        df_tp.loc[i,'tp-c']=None

def cal_tp10(p2,p3,tp):
```

```
    try:
        k=(p3[1]-p2[1])/(p3[0]-p2[0])
        # case 1
        x_1=tp[0]-math.sqrt(64*k**2/(1+k**2))
        y_1=1/k*math.sqrt(64*k**2/(1+k**2))+tp[1]
        # case 2
        x_2=tp[0]+math.sqrt(64*k**2/(1+k**2))
        y_2=-1/k*math.sqrt(64*k**2/(1+k**2))+tp[1]

        # using Ax+By+C > or < 0
        value_1=k*(x_1-p2[0])+p2[1]-y_1
        #value_2=k(x_2-p1[0])+p1[1]-y_2
        value_tp=k*(tp[0]-p2[0])+p2[1]-tp[1]

        #tp and p10 candidate_1 locate on the same side
        if value_1*value_tp>0:
            x=x_2
            y=y_2

        else:
            x=x_1
            y=y_1

    # when k --> unlimit
    except:

        if tp[0]>p2[0]:
            x=tp[0]-8
            y=tp[1]

        else:
            x=tp[0]+8
            y=tp[1]

    print(x,y)

    return x,y


for i in df_tp.index:
    tp=df_tp.loc[i,"TP"]
    p2=df_tp.loc[i,"p2"]
    p3=df_tp.loc[i,"p3"]
    x,y=cal_tp10(p2,p3,tp)

    try:
        c=df_concen.loc[(df_concen["x"]==int(x))&(df_concen["y"]==int(y))&
        (df_concen["timestamp"]==i)]['c'].values[0]
        c=round(float(c),6)
```

```
        df_tp.loc[i,'tp__10']=c

    except:
        df_tp.loc[i,'tp__10']=None



for i in df_p1.index:
    p1=df_p1.loc[i,"p1"]
    np_list=get_neighber_points(p1)
    #print(np_list)
    locations=np.asarray([[np[0] for np in np_list],[np[1] for np in np_list]]).T
    try:
        cs=list(map(lambda a: df_concen.loc[(df_concen["x"]==a[0])&
        (df_concen["y"]==a[1])&(df_concen["timestamp"]==i)]['c'].values[0],np_list))

        # use 4 neighbor points around TP to intepolate the concentration of TP point
        c_predict = griddata(locations, cs, p1, method='cubic')

        c_predict=round(float(c_predict),6)

        df_tp.loc[i,'p1-c']=c_predict

    except:
        df_tp.loc[i,'p1-c']=None

for i in df_p2.index:
    p2=df_p2.loc[i,"p2"]
    np_list=get_neighber_points(p2)
    #print(np_list)
    locations=np.asarray([[np[0] for np in np_list],[np[1] for np in np_list]]).T
    try:
        cs=list(map(lambda a: df_concen.loc[(df_concen["x"]==a[0])&(df_concen["y"]==a[1])&
        (df_concen["timestamp"]==i)]['c'].values[0],np_list))

        # use 4 neighbor points around p2 to intepolate the concentration of TP point
        c_predict = griddata(locations, cs, p2, method='cubic')

        c_predict=round(float(c_predict),6)

        df_tp.loc[i,'p2-c']=c_predict

    except:
        df_tp.loc[i,'p2-c']=None

display(df_tp)
df_tp.to_csv("xxxx.csv")
```

A.3. Fitting the free energy in a ternary system

The code for fitting the free energy of single phase in a ternary system is presented as follows.

```
"""This is a module that performs coefficients fitting of gibbs' free energy."""
import os
import pandas as pd
import numpy as np
from scipy.optimize import curve_fit, minimize
from sympy import symbols, Eq, nonlinsolve

EQUI = {1893: [0.0671069, 0.77151, 0.0534117, 0.571588, 0.370401, 0.609583],
        1898: [0.0686863, 0.769248, 0.0542365, 0.570764, 0.375683, 0.604046],
        1903: [0.0702927, 0.766959, 0.0550656, 0.569934, 0.380921, 0.598549],
        1908: [0.0719272, 0.764643, 0.0558993, 0.569101, 0.386114, 0.593091],
        1913: [0.0735906, 0.762299, 0.0567378, 0.568262, 0.391264, 0.587673],
        1918: [0.0752838, 0.759926, 0.0575814, 0.567419, 0.396371, 0.582294],
        1923: [0.0770079, 0.757523, 0.0584303, 0.56657, 0.401436, 0.576954]}


def read_all_data(path):
    """Read all the calphad data in a folder and store them in the variable "valus"."""
    files = os.listdir(path)
    values = []
    for file in files:
        data = pd.read_excel(path + '/' + file, engine='odf', skiprows=0, decimal=',')
        value = data.values
        values.append(value)
    return values


def _f_l(x, a, b, d, e, g, h):
    """Use an equation of the form _f_l to fit the free gibbs' energy in liquid phase."""
    return a * np.power(x[:, 0], 2) + b * x[:, 0] + d + e * np.power(x[:, 1], 2) +
    g * x[:, 1] + h * x[:, 0] * x[:, 1]


def _f_ts_b(x, a, b, d):
    """Use an equation of the form _f_ts_b to fit the free gibbs' energy in ts/beta phase."""
    return a * np.power(x + b, 2) + d


def _fitting_data(value):
    """
    Fit the coefficients of free gibbs' energy under one speicific temperature without the
    assumption of n.

    Notice: The energy here is dimensionless.
    """
```

```
    length = len(value[:, 1])
    mo_l = [value[j, 1] for j in range(length) if not np.isnan(value[j, 10])]
    ti_l = [value[j, 3] for j in range(length) if not np.isnan(value[j, 10])]
    g_l = [val / 100000 for val in value[:, 10] if not np.isnan(val)]
    c_l = np.column_stack((mo_l, ti_l))
    popt_l, _ = curve_fit(_f_l, c_l, g_l)
    mo_ts = [value[j, 4] for j in range(length) if not np.isnan(value[j, 11])]
    g_ts = [val / 100000 for val in value[:, 11] if not np.isnan(val)]
    popt_ts, _ = curve_fit(_f_ts_b, mo_ts, g_ts)
    mo_b = [value[j, 7] for j in range(length) if not np.isnan(value[j, 12])]
    g_b = [val / 100000 for val in value[:, 12] if not np.isnan(val)]
    popt_b, _ = curve_fit(_f_ts_b, mo_b, g_b)
    return np.concatenate((popt_l, popt_ts, popt_b))


def _equi_error(params, *args):
    """
    Calculate the three-phase equilibrium concentrations of Mo and Ti.

    Return the error between the calculated point and the experimental value.
    """
    n_ts, n_b = params
    a_l, b_l, d_l, e, g, h, a_ts, b_ts, d_ts, a_b, b_b, d_b = args[0]
    equi = args[1]
    mo_l, ti_l, mo_ts, ti_ts, mo_b, ti_b = symbols('mo_l ti_l mo_ts ti_ts mo_b ti_b', real=True)
    u_1 = 2 * a_l * mo_l + b_l + h * ti_l
    u_2 = 2 * e * ti_l + g + h * mo_l
    u_3 = 2 * a_ts * (mo_ts + b_ts) - 2 * n_ts * (0.625 - mo_ts - ti_ts)
    u_4 = - 2 * n_ts * (0.625 - mo_ts - ti_ts)
    g_l = a_l * np.power(mo_l, 2) + b_l * mo_l + d_l + e * np.power(ti_l, 2) +
    g * ti_l + h * mo_l * ti_l
    gts = a_ts * np.power(mo_ts + b_ts, 2) + d_ts + n_ts * np.power(0.625 - mo_ts - ti_ts, 2)
    u_5 = 2 * a_b * (mo_b + b_b) - 2 * n_b * (0.9797 - mo_b - ti_b)
    u_6 = - 2 * n_b * (0.9797 - mo_b - ti_b)
    g_b = a_b * np.power(mo_b + b_b, 2) + d_b + n_b * np.power(0.9797 - mo_b - ti_b, 2)
    eq1 = Eq(u_1, u_3)
    eq2 = Eq(u_2, u_4)
    eq3 = Eq(g_l - u_1 * mo_l - u_2 * ti_l, gts - u_3 * mo_ts - u_4 * ti_ts)
    eq4 = Eq(u_1, u_5)
    eq5 = Eq(u_2, u_6)
    eq6 = Eq(g_l - u_1 * mo_l - u_2 * ti_l, g_b - u_5 * mo_b - u_6 * ti_b)
    sol = nonlinsolve((eq1, eq2, eq3, eq4, eq5, eq6), mo_l, ti_l, mo_ts, ti_ts, mo_b, ti_b)
    error = (equi[0] - sol.args[0][0])**2 + (equi[1] - sol.args[0][1])**2 +
    (equi[2] - sol.args[0][2])**2\ + (equi[3] - sol.args[0][3])**2 +
    (equi[4] - sol.args[0][4])**2 + (equi[5] - sol.args[0][5])**2
    print("error: ", error)
    return error


def fitting_all_data(path):
```

```
    """
    Fit the coefficients of free gibbs' energy under all temperatures together with n.

    Step 1: Find the optimal coefficients (without n) by using function "_fitting_data(value)"
    Step 2: Find the optimal n that minimizing the error from "_equi_error(params, *args)"
    """
    values = read_all_data(path)
    values.sort(key=lambda x: x[0, 0])  # sort the values by temperature
    coes = []
    for value in values:
        coe = _fitting_data(value)
        init_guess = [1, 1]
        temp = value[0, 0]  # temperature
        args = (coe, EQUI[temp])
        bounds = [(0, None), (0, None)]
        result = minimize(_equi_error, init_guess, args=args, bounds=bounds,
        options={'ftol': 1e-30})
        opt_n_ts, opt_n_b = result.x
        all_coe = np.append(coe, [opt_n_ts, opt_n_b, temp])
        coes.append(all_coe)
        print(f"{temp}: ", all_coe)
    return coes


if __name__ == "__main__":
    PATH = "data/Gibbs_energy_data"
    SAVE_PATH = "result/"
    all_coes = fitting_all_data(PATH)
    np.save(SAVE_PATH + 'gibbs_result', all_coes)
```

B. Publications

- **Article 1: Y. Cai**, F. Wang, M. Selzer, and B. Nestler. “Phase-field investigation on the growth orientation angle of aluminum carbide with a needle-like structure at the surface of graphite particles”. In: *Modelling and Simulation in Materials Science and Engineering* 27.6 (2019), p. 065010.
- **Article 2: Y. Cai**, F. Wang, Z. Zhang, and B. Nestler. “Phase-field investigation on the peritectic transition in Fe-C system”. In: *Acta Materialia* 219 (2021), p. 117223.
- **Article 3: Y. Cai**, F Wang, A Czerny, HJ Seifert, B Nestler “Phase-field investigation on the microstructural evolution of eutectic transformation and four-phase reaction in Mo-Si-Ti system”. In: *Acta Materialia* 258 (2023), p. 119178.
- **Article 4: Y. Cai**, F Wang, B Nestler “Phase-field study on the formation of tilted lamellar eutectics in Mo-Si-Ti alloy ”. *In preparation*